Series in BioEngineering

Hongliang Ren
Jinji Sun *Editors*

Electromagnetic Actuation and Sensing in Medical Robotics

Springer

Series in BioEngineering

More information about this series at http://www.springer.com/series/10358

Hongliang Ren · Jinji Sun
Editors

Electromagnetic Actuation and Sensing in Medical Robotics

Springer

Editors
Hongliang Ren
Department of Biomedical Engineering
National University of Singapore
Singapore
Singapore

Jinji Sun
Department of Biomedical Engineering
National University of Singapore
Singapore
Singapore

ISSN 2196-8861 ISSN 2196-887X (electronic)
Series in BioEngineering
ISBN 978-981-10-6034-2 ISBN 978-981-10-6035-9 (eBook)
https://doi.org/10.1007/978-981-10-6035-9

Library of Congress Control Number: 2017951424

Printed on acid-free paper

This Springer imprint is published by Springer Nature
The registered company is Springer Nature Singapore Pte Ltd.
The registered company address is: 152 Beach Road, #21-01/04 Gateway East, Singapore 189721, Singapore

Contents

A Preface in Electromagnetic Robotic Actuation and Sensing in Medicine

Hongliang Ren and Hritwick Banerjee

Abstract With the advancement in robotics technology, medical field is evolving more with minimally invasive to noninvasive procedures. Minimally invasive surgical procedures have gained ever-increasing popularity over the past decades due to many of their advantages compared to traditional open operations, such as smaller incisions, faster recoveries, fewer complications, and shorter hospital stays. Robot-assisted minimally invasive surgery promises to improve the precision, dexterity, and stability of delicate procedures. Among these technologies, there is a demanding clinical need to progress the field of medical robotics in connection with noninvasive surgery. For this, the actuation and sensing in the future robotic surgery systems would be desired to be more wireless/untethered. Out of many promising wireless actuation and sensing technologies, one of the most patient friendly techniques to use is electromagnetic or magnetic actuation and sensing for feedback control and manipulation. In this book, we have intended to elucidate the recent related research and developments behind the electromagnetic actuation and sensing implemented in medical robotics and therein.

1 Electromagnetic Actuation

In a magnetically controlled actuation, the core components can typically be the actuator (moving portion) and the stators which are typically the external magnetic field generators. This is analogous to active magnetic bearings (Chap. 5) where the actuators are the rotors, and the magnetic fields are generated from the stators. Common field generation setup includes Helmholtz and Maxwell variations (Chap. 2) or arbitrary multipole electromagnetic coils (Chap. 5). The actuated region can be in the form of distal tips for catheters (Chap. 4) or small microparticles/microrobots (Chap. 2).

As discussed in Chap. 2, Helmholtz coil is a specific configuration to generate an uniform field at a region of interest (ROI) where EM field is usually referred

H. Ren (✉) · H. Banerjee
Department of Biomedical Engineering, National University of Singapore, Singapore, Singapore
e-mail: ren@nus.edu.sg

H. Ren and J. Sun (eds.), *Electromagnetic Actuation and Sensing in Medical Robotics*, Series in BioEngineering, https://doi.org/10.1007/978-981-10-6035-9_1

to as the alignment field. Maxwell coil generates a gradient field where the scalar contribution at the ROI is near zero. In general, the alignment fields exhibit a torque on the permanent magnet or soft magnetic target such that it rotates to align and associates with the magnetic fields generated about the moment of inertia [7].

Maxwell gradient coils provide the displacement force to move the particle. The number and type of coils can be designed according to the requirements in degrees of freedom (DOFs) needed. The total contribution is popularly arranged in a matrix [7]. The electromagnetic fields generated are in turn controlled by the current flowing through the coils. More complex variations of Helmholtz Maxwell designs include the Halbach cylinder [18], saddle coils [15], and square coils [12]. The increasing complexity of the coil design aims to either increase field uniformity or field strength. In general, the most primitive Helmholtz Maxwell combination is an easier to manufacture setup but requires a more robust controller for precision. It is also noteworthy that current designs which require closing the control loop present a limitation in terms of the sensor. More prominent techniques utilize sensors, which are eddy current sensors and hall effect sensors, to feedback position information to the controller; hence these methods are preferable over image processing alternative which requires an external camera [35].

Other than Helmholtz and Maxwell designs, alternative multiple electromagnet pole designs have been proposed (US7173507, US20120143127A1). Octamag [19] uses eight electromagnets to control the 5DOF microrobot for use in ocular surgery. A microelectronic [10] fabricated design was also able to do particle filtering and separation by generating unique field from the complex electronic circuit design. These methods generate less uniform field which could be an issue for control [2]. In a more recently published paper [22], a combination of electromagnetic coils and permanent magnets was demonstrated for camera positioning in laparoscopic surgery.

2 Magnetic Actuated Robots

In Chap. 2, it is worth looking into the field of magnetically actuated microrobots/particles, and it is also highly similar to magnetic catheter actuation (Chap. 4), which can also be seen as a particle control if only the distal tip contributes to magnetic actuation. Developments in magnetically actuated microrobots have potential to contribute improvements toward present methodologies in magnetic catheter actuation. The magnetic manipulation of the small particle does have some differences, for example, having a fabricated tail to assist motion [1, 24]. The tail is usually of a helical form which does not have apparent use in guide wires, but it has been shown that it could have potential value in mediating calcified arteries [17]. Common materials that have been considered are NdFeB permanent magnet, Ni, and iron oxide for microparticle fabrication. Further, for small robots, piezoelectrics have been implemented for locomotion [5, 20]. Other than magnetic propulsion, acoustics such as from piezoelectric can serve an additional function to deliver drugs [34]. The oscillatory magnetic field which is required for piezoelectric stimulation could also be used for steering control depending on the phase lag [21]. For specific fabrication, SU-8 with dispersed magnetic particles was shown to be viable [14]. Octomag's microparticle manipulation is demonstrated to be robust even without Helmholtz and Maxwell coils [23].

3 Magnetic Guide Wire/Catheter

Chapter 4 specifically investigates certain roles of magnetic actuation in clinical procedures particularly for controlling the guide wire or catheter in very complicated cardiovascular environments. The manipulators or catheters bend due to specific magnetic domains along the axis of the guide wire under an imposed magnetic field which could be of a specific configuration. Historically, the bending resulted from the magnet tip can be controlled by introducing a compliant hinge to reduce the force required to bend the guide wire [30]. These manipulators usually have magnetic responsive elements which could be in the form of particle suspensions (Chap. 2), or flexible magnetic material (Chaps. 4 and 6). It was noted that the increase in the number of segments increased the difficulty to control the catheter but enabled a more stable and linear distal portion [31]. There are many geometrical designs of such distal remotely controlled elements, for example, balls, rings, or helical elements to induce bending. Such elements could also be used for guide wire alignment or inducing restrictions to assist bending and positioning of the guide wire. Other than bending manipulation, these elements are also shown to be able to perform lateral advancement, transmission of force, and assist visual feedback.

Additionally, the magnetic navigation system was also simulated to be able to improve the operative procedure and save the fluoroscopy time [28]. By using a glass model of liver and choosing to navigate a highly tortuous path, the magnetic guidance system outperforms the traditional manual methods, both in time taken and the number of bends it is able to achieve. A specific application to ventricular ablation was reported [4, 6, 29], demonstrating the manipulability of a magnetic navigation system in a biophysical environment. Magnetic navigation was argued to be an improvement over traditional manual control for the ablation procedure [27]. The catheter was implanted with a permanent magnet which aligns with the external field generated by the StereotaxisTM system with a field strength of 0.15 tesla at the homogeneous region [9]. Another novel advantage of magnetic navigation is the ability of the catheter to be attracted into the vessel rather than being pushed in, which allows the catheter to be very soft and compliant increasing the safety of the procedure [8]. Other catheters have also been developed to clear plaque and use a combination of Helmholtz, Maxwell, and Maxwell gradient and saddle coils [16] unlike the previous StereotaxisTM [33] which uses two electromagnets. The StereotaxisTM [31] is known to work as an open-loop system, and they have also proposed a closed-loop methodology utilizing the equilibrium equations from the potential energy in the work space. The specific model used can also be referred from this publication [32]. There are also some associated risks of magnetic navigation that are noteworthy. Using MRI, it was studied that heat generated from the magnetic resonance could cause heating of the catheter [26], indicating that traditional guide wires will not be suitable for these applications [25].

4 Electromagnetic Sensing

Magnetic biosensing and detection pose a fertile field of research in the realm of biomedical engineering applications. A potential way to receive a feedback signal from the human body is to use an electromagnetic sensor that is capable of sensing the downstream physiology and processes. For example, biological cells triggered by magnetic micro/nanobeads accelerate traction force for mechanotransduction, which can be sensed by external magnetic sensors. In addition to the microscale, macroscale diagnostic and point of care (POC) applications need sensing mechanism for better health care, faster diagnostics, and therapeutics. Tactile sensing and rehabilitation robotics are some of the exciting paradigms where electromagnetic sensing elements can play a pivotal role and beyond. To make the mechanoreceptors work aptly, the electromagnetic sensor can portray an exciting new regime for flexible electronics and skin prosthetics. Magnetorheological elastomer (MRE) has promising applications in soft, flexible robotics for better human–machine interaction and cooperative control. MRE also has similar mechanical property to that of natural muscle for which can be further served as rehabilitation and tactile sensing in biomedical engineering. On the same hand, minimally invasive surgical robotics and force control in mechanical counterpart need sensor actuation for better motion navigation and planning algorithm as described hereunder.

Overall, the automatic and reliable navigation and motion control or compensation of surgical robots are depending on the motion tracking of surgical instruments and also the surrounding anatomic structures. Many technology advancements have been achieved to address this problem, and we are focusing on magnetic sensing technologies, because of its advantages in terms of size, remotely sensing, flexible passive or active configurations, and also, free of line-of-sight requirement.

To achieve online motion control and planning, it is necessary to gain the real-time position and shape information of the flexible surgical robot. To acquire this information, the flexible surgical robots can be mounted with electromagnetic sensors. The shape estimation algorithm has been developed based on either quadratic or cubic Bézier curves as presented in [3, 11, 13]. Besides electromagnetic sensors, microcameras can also be utilized to assist the navigation procedure. Then with the position and shape information acquired for the flexible surgical robot, the online motion planning can be achieved by modifying the offline planned trajectory based on the feedbacks provided by the sensors in the future.

5 Brief Outline of the Chapters

The flow of the chapters in this book will mostly adhere a bottom-up approach and will be starting from submillimeter microrobotic device driven by external magnetic field to submillimeter magnetic sensing devices. For example, in the initial part of the book, we constrict in the microscale untethered robots and application in the medical community with the help of electromagnetic actuations.

Chapter 2 investigates the field of microbots, which is exponentially advancing its impact on the medical healthcare industry with its ever-increasing potential. It may happen in near future when the sci-fi movie fantastic voyage will be a reality with the help of electromagnetic actuation and precise control. To make this microbot a reality, there still is a huge amount of research needed in order to overcome many different challenges such as (1) smart manipulation with changing *in vivo* pH environment, (2) to sense a cancer cell from healthy counterpart, (3) smooth access to near and farthest abnormal tissues from point of injection, and (4) most importantly to overcome toxicity and biocompatibility issues. In parallel to investigating the microcapsules, we have initiated tracking of microparticle using contrast agent microbubble in the vicinity of medical ultrasound. Magnetic microbubbles which can be controlled by an external magnetic field have been explored as a method for precise and efficient drug delivery. In our lab, a technique for the fabrication of microbubbles encapsulated in magnetic spheres is presented. The resultant magnetic spheres were subsequently imaged using ultrasound, and the encapsulated microbubbles proved to appear as bright spots and resulted in enhanced ultrasound image contrast, as compared to the solid magnetic spheres which appeared dull. A tracking algorithm was then developed for the tracking of the magnetic microbubbles based on optical flow tracking. Further development of the magnetic microbubbles and tracking algorithm can lead to future use of the tracking algorithm in the case of *in vivo* injection of the magnetic microbubbles.

Chapter 3 represents a state-of-the-art approach for magnetically induced soft flexible robots for diverse biomedical applications. Soft, flexible yet resilient, adaptable polymers can be introduced with magnetic micro/nanoparticles for changing mechanical dimensions upon magnetic actuation. Soft force sensors are very much needed for the biomedical rehabilitation patients in general for light and efficient tracking with the outside environments. In this aspect, MRE has potential applications for force sensing and tracking which has been focused in this chapter in general. To support our design and hypothesis, we have given some initial experimental results for proof of concept and future scope to dig more into this realm. Soft magnetic polymer has an inherent property of high remanence like permanent magnets which can be refined to meet ever-increasing demands in safe regulated medical environments. The grating-based sensors like the Low Period Fiber Grating (LPFG) and Fiber Bragg Grating (FBG) are commonly used to measure the intensity or wavelength variation. These require a complex signal processing technique and difficult to minimize the effect of temperature and nonlinearities with simple fabrication. To solve the above problems and for wider applications, e.g., in rehabilitation and assistive biomedical device, bend sensors need to be more flexible, stable, cost-effective, and human friendly. Taking advantage of this soft magnetic polymer, in Chap. 3, we propose a novel soft-squishy and flexible bend sensor by determining the relationship between inductive changes and bending angle. This bend sensor employs flexible wire embedded in a silicone elastomer with different permeable core. The principle notion is to have a comprehensive analysis of the change in the morphology of the sensor with bending angle which can be translated to the inductance generated therein.

Chapter 4 concentrates on progressing the existing medically proven concept of catheter and guide wire robotic system under magnetic actuation. Surgical robotics is a growing field with substantial benefits to professionals and patients but one limit of conventional key-hole surgical robotic systems is the requirement for mechanical information to be conducted along the path of the robot. This can result in complications such as buckling and entanglement due to the tortuous environments. In this realm of catheter and guide wire system, the electromagnetic actuation holds a promising chapter. This chapter will discuss the method of using a tether-less electromagnetic coupling to transmit the mechanical information. Our lab has devised a small-scale prototype demonstrating electromagnetic deflection principle. In addition, when compared to the larger devices, this prototype is more portable and easier to integrate with existing equipment without the need for bulky equipment. This chapter presents an overview of electromagnetic actuated system which will further cover the design principles of magnetic actuated catheter robot taking example from in-house prototypes, such that the reader will be capable of designing and fabricating a similar art. A key parameter of electromagnetic catheter systems is the bending angle and will be addressed. The key considerations for an electromagnetic actuation and brief clinical perspectives are introduced for the design considerations of an electromagnetic catheterization system.

Chapter 5 has introduced a novel microrobot system based on magnetic levitation techniques for better handheld precise motion control in surgical applications. This chapter in part is to counterbalance the persisting challenges in (1) economy, (2) complexity, and (3) space requirement of a bulky traditional master–slave remote operation. In this chapter, at first, the primary components and working principle of magnetic suspension bearing system are introduced. Then, the configuration analysis of magnetic actuator is presented, and the design method of magnetic bearing with current bias is introduced in detail. The design of 1DOF, 3DOF, and 4DOF magnetic actuator system is described in detail. Finally, the expectation of magnetic actuator system is presented for the small volume and self-sensing destination (Fig. 1).

Chapter 6 will give a comprehensive overview of magnetic sensing applied to surgical environments, discover recent developments, and show a possible future of the magnetic tracking research. The chapter will first give an overview of how the magnetic sensing technology works. After that, the sensing applications will be given in detail in the context of three typical medical applications: (1) magnetic sensing for wireless capsule robots; (2) magnetic sensing for in clinical particles; and (3) magnetic sensing for flexible surgical robots.

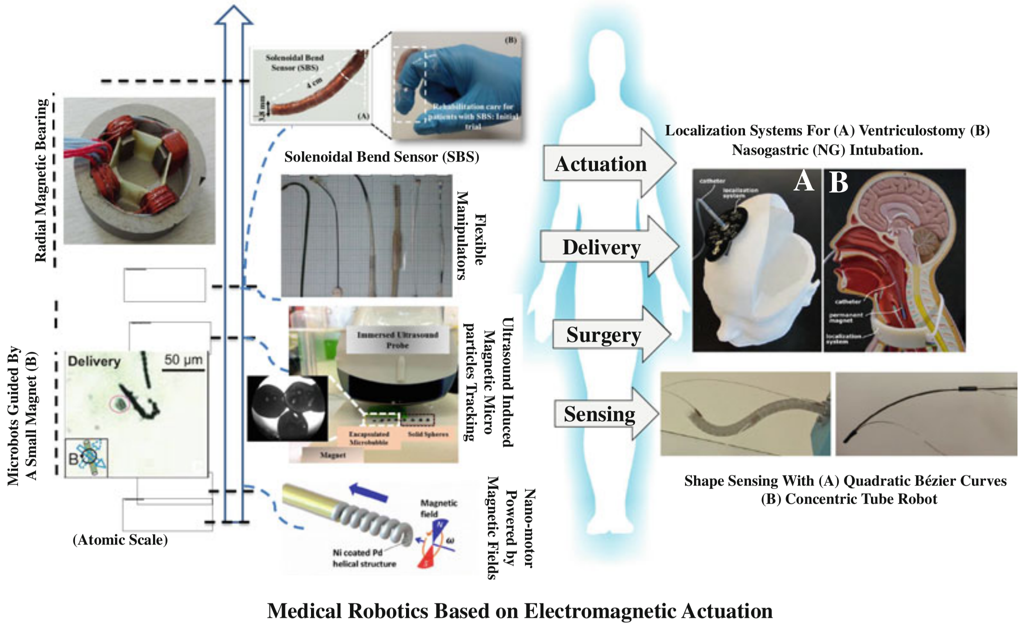

Fig. 1 A scaled-up view with dimension to show the distribution and arrangement of book chapters. This illustrates organization of the book chapters in the context of electromagnetic actuation and sensing in biorobotics. *Bottom left*: microbots in Chap. 2; *Upper most*: (a) Soft Solenoidal Bend Sensor (SBS) with flexible coil embedded in polymer and Sensor used to detect the bending angles of finger Distal Interphalangeal joints (DIP) joint as illustrated in Chap. 3. *Upper Middle*: Magnetic actuated catheterization in Chap. 4; *Upper left*: Magnetic bearing for micromanipulations in Chap. 5; *Right*: Magnetic sensing in Chaps. 6 and 7; and finally ultrasound based magnetic microparticle tracking using contrast agent described in Chap. 8.

Chapter 7 will introduce more advanced topics involving magnetic tracking, signal estimation, artificial intelligence techniques in motion tracking, and navigation systems, which are paramount for both safety and efficacy in a variety of medical interventions and procedures. Magnetic field-based tracking technology becomes appealing for many applications. It utilizes the phenomenon that the distance and orientation of the magnetic source will change the amplitude and direction of the local magnetic field in space. By mapping the measurements of the local magnetic field to the distribution of the magnetic source, it can estimate up to six degrees of freedom (DOFs) positional information (both position and orientation). Because the magnetic fields are of a low field strength and can safely pass through human tissue with least interference, it can be used for tracking instruments/tools inside the human body without line-of-sight restrictions. In this final book chapter, the magnetic field model often used in passive magnetic tracking is first reviewed. Along with this, an overview of the working principle and methods of the passive magnetic tracking technology is presented. Then, two different localization methods are described, namely, the inverse optimization method and the direct ANN (artificial neural network) method; the advantages and disadvantages of the two methods are discussed using two actual medical intervention procedures for practical illustration. Lastly, some limitations and challenges faced by the passive magnetic tracking are discussed. Conclusively, through this chapter, implementation of the technology in actual medical interventions was also be demonstrated, and the challenges in the development of this technology are explored and discussed therein.

Ultrasound transducer has been used extensively since last few decades for monitoring living organism in medical diagnostics as well as in therapeutic applications. The non-thermal effects of ultrasound like cavitation and microstreaming are well regarded for therapeutic applications than only for medical imaging and tumor ablation processes. Here, in Chap. 8, we unveil motion of magnetic particles captured using ultrasound imaging with contrast-enhanced microbubbles. Ultrasound videos were captured and analyzed by image tracking algorithm to determine the efficiency and accuracy of the algorithm. It is necessary to ensure an efficient and accurate tracking method of the particles in order to evaluate future *in vitro* or *in vivo* applications of the microbubbles, when implanted into an enclosed system and imaged using ultrasound. Microbubble-generated therapy in deep tissue with ultrasound-induced non-invasive administration is envisioned to be ongoing popular choice as long as we can safely administer drugs using accurate magnetic navigation, control. Encapsulated microbubbles enhance the ultrasound imaging contrast, allowing the fabricated magnetic particles to be effectively tracked using the created algorithm. For future development, *in vivo* like conditions can be used, such as the presence of other particles, for example, red blood cells. The fabricated magnetic microbubbles could be further used as test particles for external manipulation systems for drug delivery.

References

1. Abbott, Jake J., et al. 2009. How should microrobots swim? *The International Journal of Robotics Research* 28 (11–12): 1434–1447.
2. Abbott, Jake J., et al. 2007. Modeling magnetic torque and force for controlled manipulation of soft-magnetic bodies. *IEEE Transactions on Robotics* 23 (6): 1247–1252.
3. Albert, Matthew R., et al. 2013. Transanal minimally invasive surgery (TAMIS) for local excision of benign neoplasms and early-stage rectal cancer: efficacy and outcomes in the first 50 patients. *Diseases of the Colon & Rectum* 56 (3): 301–307.
4. Bauernfeind, Tamas, et al. 2011. The magnetic navigation system allows safety and high efficacy for ablation of arrhythmias. *Europace* 13 (7): 1015–1021.
5. Bouchebout, Soukeyna, et al. 2012. An overview of multiple DoF magnetic actuated micro-robots. *Journal of Micro-Nano Mechatronics* 7 (4): 97–113.
6. Bradfield, Jason, et al. 2012. Catheter ablation utilizing remote magnetic navigation: a review of applications and outcomes. *Pacing and Clinical Electrophysiology* 35 (8): 1021–1034.
7. Cao, Quanliang, et al. 2012. Analysis and optimal design of magnetic navigation system using Helmholtz and Maxwell coils. *IEEE Transactions on Applied Superconductivity* 22 (3): 4401504–4401504.
8. Chun, Julian Kyoung-Ryul et al. 2007. Remote-controlled catheter ablation of accessory pathways: results from the magnetic laboratory. *European Heart Journal*.
9. Faddis, Mitchell N. and Bruce D. Lindsay. 2003. Magnetic catheter manipulation. *Coronary Artery Disease* 14 (1): 25–27.
10. Fusco, Stefano, et al. 2014. Microrobots: a new era in ocular drug delivery. *Expert Opinion on Drug Delivery* 11 (11): 1815–1826.
11. Gutwein, Luke G., et al. 2011. Utilization of minimally invasive breast biopsy for the evaluation of suspicious breast lesions. *The American Journal of Surgery* 202 (2): 127–132.
12. Ha, Yong H., Byung H. Han, and Soo Y. Lee. 2010. Magnetic propulsion of a magnetic device using three square-Helmholtz coils and a square-Maxwell coil. *Medical & Biological Engineering & Computing* 48 (2): 139–145.
13. Hamad, Giselle G., and Myriam Curet. 2010. *Minimally Invasive Surgery*.
14. Jacot-Descombes, Loïc et al. 2014. Inkjet printing of high aspect ratio superparamagnetic SU-8 microstructures with preferential magnetic directions. *Micromachines* 5 (3): 583–593.
15. Jeon, Seungmun, et al. 2010. Magnetic navigation system with gradient and uniform saddle coils for the wireless manipulation of micro-robots in human blood vessels. *IEEE Transactions on Magnetics* 46 (6): 1943–1946.
16. Jeon, S.M., and G.H. Jang. 2012. Precise steering and unclogging motions of a catheter with a rotary magnetic drill tip actuated by a magnetic navigation system. *IEEE Transactions on Magnetics* 48 (11): 4062–4065.
17. Jeong, Semi, et al. 2011. Enhanced locomotive and drilling microrobot using precessional and gradient magnetic field. *Sensors and Actuators A: Physical* 171 (2): 429–435.
18. Knopp, Tobias, et al. 2010. Generation of a static magnetic field-free line using two Maxwell coil pairs. *Applied Physics Letters* 97 (9): 092505.
19. Kummer, Michael P., et al. 2010. OctoMag: An electromagnetic system for 5-DOF wireless micromanipulation. *IEEE Transactions on Robotics* 26 (6): 1006–1017.
20. Kwon, Jun O. et al. 2013. A novel drug delivery method by using a microrobot incorporated with an acoustically oscillating bubble. In *IEEE 26th International Conference on Micro Electro Mechanical Systems (MEMS)*, 2013, 1157–1160, IEEE.
21. Li, Yan-Hom, He-Ching Lin, and Ching-Yao Chen. 2013. Steering of magnetic micro-swimmers. *IEEE Transactions on Magnetics* 49 (7): 4120–4123.
22. Liu, Xiaolong, Gregory J. Mancini and Jindong Tan. 2015. Design and analysis of a magnetic actuated capsule camera robot for single incision laparoscopic surgery. In *International conference on Intelligent Robots and Systems (IROS), 2015 IEEE/RSJ*, 229–235, 2015, IEEE.

23. Marino, Hamal, Christos Bergeles and Bradley J. Nelson. 2014. Robust electromagnetic control of microrobots under force and localization uncertainties. *IEEE Transactions on Automation Science and Engineering* 11 (1): 310–316.
24. Mhanna, Rami, et al. 2014. Artificial bacterial flagella for remote-controlled targeted single-cell drug delivery. *Small* 10 (10): 1953–1957.
25. Mukherjee, Debabrata et al. 2010. *Cardiovascular catheterization and intervention: A textbook of coronary, peripheral, and structural heart disease*. CRC Press.
26. Nitz, Wolfgang R., et al. 2001. On the heating of linear conductive structures as guide wires and catheters in interventional MRI. *Journal of Magnetic Resonance Imaging* 13 (1): 105–114.
27. Proietti, Riccardo, et al. 2013. Remote magnetic with open-irrigated catheter vs. manual navigation for ablation of atrial fibrillation: a systematic review and meta-analysis. *Europace* 15 (9): 1241–1248.
28. Schiemann, Mirko, et al. 2004. Vascular GuideWire Navigation with a Magnetic Guidance System: Experimental Results in a Phantom 1. *Radiology* 232 (2): 475–481.
29. SZILI-TOROK, TAMAS et al. 2012. Catheter ablation of ventricular tachycardias using remote magnetic navigation: a consecutive case-control study. In *Journal of Cardiovascular Electrophysiology* 23 (9): 948–954.
30. Tang, Libo, Yonghua Chen and Xuejian He. 2007. Magnetic force aided compliant needle navigation and needle performance analysis. In *IEEE International Conference on Robotics and Biomimetics, 2007. ROBIO 2007*, 612–616, IEEE.
31. Thornton, A.S., et al. 2006. Magnetic navigation in AV nodal re-entrant tachycardia study: early results of ablation with one-and three-magnet catheters. *Europace* 8 (4): 225–230.
32. Tunay, Ilker. 2004. Modeling magnetic catheters in external fields. In *26th Annual International Conference of the IEEE Engineering in Medicine and Biology Society, 2004. IEMBS'04*, vol. 1, 2006–2009, IEEE.
33. Tunay, Ilker. 2004. Position control of catheters using magnetic fields. In *Proceedings of the IEEE International Conference on Mechatronics, 2004, ICM'04*, 392–397, IEEE.
34. Yim, Sehyuk, Kartik Goyal, and Metin Sitti. 2013. Magnetically actuated soft capsule with the multimodal drug release function. *IEEE/ASME Transactions on Mechatronics* 18 (4): 1413–1418.
35. Yim, Sehyuk and Metin Sitti. 2012. Design and rolling locomotion of a magnetically actuated soft capsule endoscope. *IEEE Transactions on Robotics* 28 (1): 183–194.

Magnetically Actuated Minimally Invasive Microbots for Biomedical Applications

Hritwick Banerjee, Shen Shen and Hongliang Ren

Abstract This chapter elucidates comprehensive overview of magnetically actuated microbots for various biomedical applications, discover recent developments and show a possible future scope and challenges therein. We confine our biomedical applications and present state of the art mostly related to translational research and near term deliverable possibilities to make *in vivo* applications. We will first demonstrate a brief overview of the potential medical applications and recent state of the art magnetically actuated microbots. After that, we will briefly touch upon various aspects of magnetically driven magneto-responsive microcapsules for targeted Drug Delivery (TDD) applications. In this part, we will provide a brief literature review in the nexus of magnetic micro robotics with design specifications for drug delivery. Finally, we will illustrate magnetically manipulated self-propelled microjets for biosensing as future perspectives.

1 Introduction

Microbots that are associate with molecular machine have given birth to a new paradigm in biomedicine and healthcare as indicated by 2016 Nobel Prize in Chemistry to Nanomachines [25, 66]. The governing challenges now and the major point of consideration is how to power these molecular devices so that they can be used as *in vitro* molecular diagnosis and biochemical assays as well as interacting with human body *in vivo* [68]. Powering these microbots is a nontrivial challenge typically boiling down to (1) on-board supply, (2) Energy harvesting, and (3) Energy or power transmission. As many biomedical applications inside human bodies will be for intervention delivery, surgery delivery, targeted drug delivery (TDD), separations, cell sorting, and biosensing, the power and the mechanical motion are ideal to be transmitted wirelessly.

H. Banerjee · S. Shen · H. Ren (✉)
Department of Biomedical Engineering, National University of Singapore,
Singapore, Singapore
e-mail: ren@nus.edu.sg

H. Ren and J. Sun (eds.), *Electromagnetic Actuation and Sensing in Medical Robotics*,
Series in BioEngineering, https://doi.org/10.1007/978-981-10-6035-9_2

The wireless motion and power transmission approach that we will cover in this chapter, is to use magnetic fields. Researchers in magnetically actuated self-propelled micro/nanomachines have started to apply this technology in many new avenues from biosensing, microfluidics, robotics, and environmental fields with many others [96, 97]. As for example, self-propelled microrobots [55] using closed loop control algorithm in a fluidic microchannel (Width: 500 μm, Depth: 300 μm) are believed to be integrated further for targeted drug delivery (TDD), separations, cell sorting, and biosensing applications [90, 100]. Here, self-propelled microjets used microfluidic confinement with flow rate of 0–7.5 μL/min (for and against the flow mimicking blood circulation) [55, 63, 83, 85] in line with the consideration that microfluidic channels mimic the confinement effects induced by micro confinements of downstream physiological pathways [6]. Moreover, U-turn [3, 52] and the rotating magnetic field technique [113] characterization implemented in [55] to determine average magnetic dipole moment poses inconsistencies as: (i) Hydrogen peroxide and water dynamic viscosities are assumed to be comparable but not same (H_2O_2 viscosity: 1.245 cP and Water viscosity: 1 cP at 20°C) [103], while bubble dynamics incorporation is nontrivial for further development of robust self-propelled microjet magnetic setup (ii) rotating magnetic field is an optimal choice but time consuming. There is significant research where magnetically driven biomedical microbots used their helical flagella rotating like a cork screw to move onward and backward in a viscous fluid mimicking human blood circulatory systems [27]. For future research, it is hypothesized that ultrasound (US) can even be integrated with imaging and generating acoustic waves simultaneously for sonoporation and TDD incorporating established self-propelled catalytic decomposed oxygen bubbles [8, 9, 55, 58]. Further developments incorporating magnetic actuation and ultrasound guidance methods could manipulate swarms of micro robotic agents and magnetic catheters. In this regard, study in [123] uses ultrasound driven propulsion mechanism in micro/nanoscale in fuel-driven and fuel-free conditions. Conclusively, although there are studies to implement magnetically driven microbots for different biomedical applications we are still facing significant challenges for implementing the state of the art technique in real-life applications. Therefore, substantial effort needs to be established for characterizing new propulsion mechanism based on closed loop feedback control framework [124].

2 Potential Impact of Magnetically Induced Medical Microbots

The transition from macro to micro scale robotics follows fundamental law of physics but the scale length provides a sense of priority and disturbances comparing to macro scale. As for example, in micro robotics the surface to volume ratio, surface tension, and viscosity effect predominantly exhibit main counter stones in making a perfect actuation. To illustrate more, to function in the human circulatory system, a microbot must overcome the challenges of varying diameter of blood vessel (a couple of centimeters for Aorta down to several microns in capillaries) [74] and pulsatile flow of blood in contrary to its tethered counterparts. Therefore, in order to apply magnetically driven microrobot for TDD applications, the prospective system has to pass at least three main challenges (1) the ability to continually monitor propulsion force so that the microrobot can maintain its movement against time varying blood flow inside human body (2) along with magnetic control there has to be a provision for imaging modality which will further provide the motion control of microrobot and (3) the magnetically driven micromotor control system need to be robust enough to counter balance the deviation like time varying flow, viscosity, and many others. All these challenges need to be overcome before this microbot can be used in biomedical applications.

2.1 Potential Medical Application Areas

As we discussed earlier, due to the challenges medical microbots are still far from reality. Therefore, in this section, we will illustrate the near term feasible microbots application converging to biomedical fields with relevant literature focussed on electromagnetic actuations.

2.1.1 The Blood Circulatory System

The benefits of minimally to noninvasive surgery (MIS) includes less operative pain, truncated hospitalization cost, reduced recovery period, and many others. Therefore, there are huge scientific discourses in the realm of medical trials to work on electromagnetically driven jet pumps in human circulatory systems [93]. In this paradigm, a magnetic resonance imaging (MRI) based control mechanism for micro particle tracking inside human circulatory systems *in vivo* [73, 93] proved that microparticle tracking and control against blood flow is possible with several challenges to overcome.

2.1.2 The Central Nervous System (CNS)

In the recent past, an investigation was established for successful trials of remotely controlled and guidance of magnetic seeds in the brain and several prototype systems have been developed [33, 34, 77, 78]. There was a carry forward research where the amount of forces required for the magnetic seeds were investigated within a human brain [82]. With the advent of MEMS fabrication for neurosurgery [92] in the distant future a bridge can be overlaid where magnetically driven wireless microbot can further be incorporated in neurosurgery. In this regard, noninvasive control of microbot for endoscopy in the subarachnoid space of the spine [60] lay out a platform for future researches to investigate in this realm.

2.1.3 The Urinary System and the Prostate

Urolithiasis causes blockage of the ureter resulting in painful urination with blood and if untreated tissue damage with renal dysfunction can occur. It is a multi-factorial disorder with ever increasing prevalence leading to a disproportionate misery in human life and morbidity worldwide [35, 61]. The advancement in biomedical engineering and medical devices cemented the necessity for microbots to treat kidney stone diseases (KSD) by optimal access to the stone sites. In this regard, a biopolymer coated microbot can swim up the ureter to crash kidney stones with least harms and side effects [23]. In addition, the microbot can also be administered as a soluble capsule for temperature, pressure and pH sensor *in vivo* for long-term bladder monitoring. On the other hand, as discussed in the earlier section the advancements of MEMS (Micro-Electro-Mechanical Systems) and NMES (Nano-Electro-Mechanical Systems) devices can be integrated with wireless mocrobots for applications in urology [62] and allied fields.

Nowadays prostate cancer has become an epidemic such that millions of males encounter a prostate biopsy yearly only in USA. The lone available treatment now is to use an insertion needle through the perineum, during which 20% of the prostate cancer tumors are missed [19, 88, 114]. Another feasible option is to gain access through colon but at the cost of much complex maneuver and a much-controlled manipulation. Therefore, in this regime, microbots can take a huge step forward to minimize the complexity of guide wires and will produce less infections. At the same time, the microbot can carry radioactive seed to various distributed tumor locations for delivery of radiation dosage. There is an alternate path through urethra for delivering microbot to the desired prostate cancer tumor regions. The use of magnetically controlled microbots will significantly cut down the possibility of nerve damage, and noninvasive treatment will induce altogether a new paradigm of TDD [130].

2.1.4 The Eye

Despite sufficient efforts in optimizing ocular drug delivery, the progress in this domain is still in infancy in comparison to other delivery routes such as oral, transdermal, and transmucosal. Though a small volume of drug is required, to achieve the same amount using a dropper is extremely difficult to design. In addition to this, patients usually are unable to absorb small concentration of drugs required. These factors resulted in transcorneal absorption of 1% or less when applied as a solution [94] (Fig. 1). Conclusively, the amount of loss of drugs from the eyes vary 500–700 times the rate of absorption into the anterior chamber [17]. In this realm, microbots

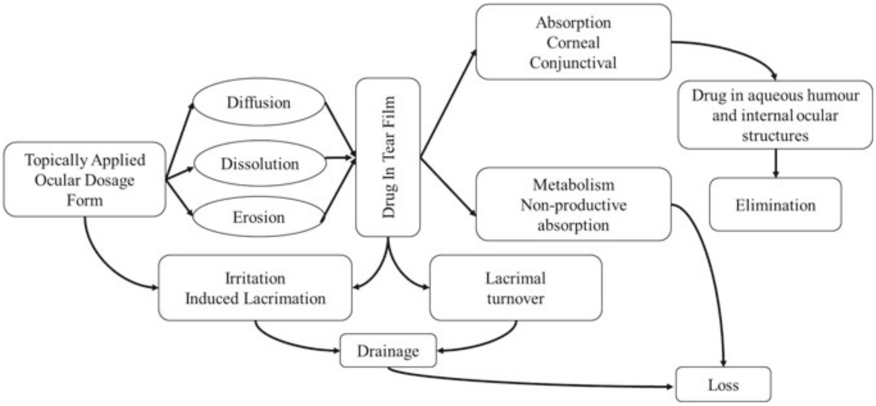

Fig. 1 Schematic illustration of the ocular disposition of topically applied constructions.

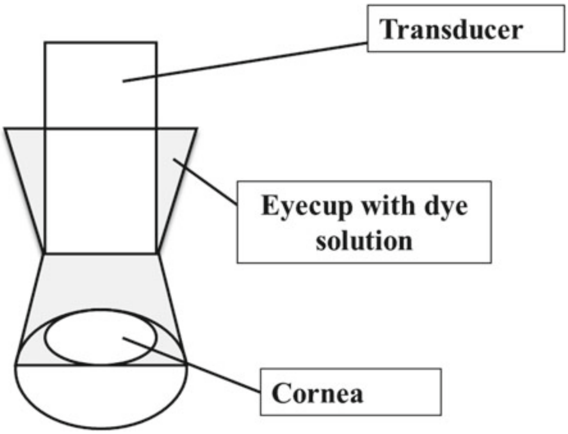

Fig. 2 A sample figure for effective ocular drug delivery.

robots can be interfaced for controlled drug delivery from anterior to posterior chambers [111].

With ever increasing advances of wirelessly controlled magnetic field, there are scientific reports where microbots have been used for intraocular procedures while tracking was possible through the pupil [129]. On the other hand, a controlled retinal therapy using magnetic microparticle tracking emerged for optimal drug delivery [42] (Fig. 2). Despite the current advances, challenges related to biocompatibility and toxicity issues need to be overcome before successful clinical trials.

2.1.5 The Fetus

Presently, 0.6–1.9% of the world population is suffering badly from Congenital Cardiovascular Malfunctions (CCM) [40]. CCM is causing birth defects, which ultimately turns into death [128]. The time of CCM detection by fetal ultrasound [28], abnormalities were already stabilized instigating progressive challenge to repair them in general. It is reported in an animal study which explains any alteration of amniotic fluid especially deficiency or low volume may be one of the causes of CCM [41, 45].

Fetal surgery is in its preliminary stage with minimum success rates and few organizations practicing it, though promising [59, 118]. In the future, micro robots,

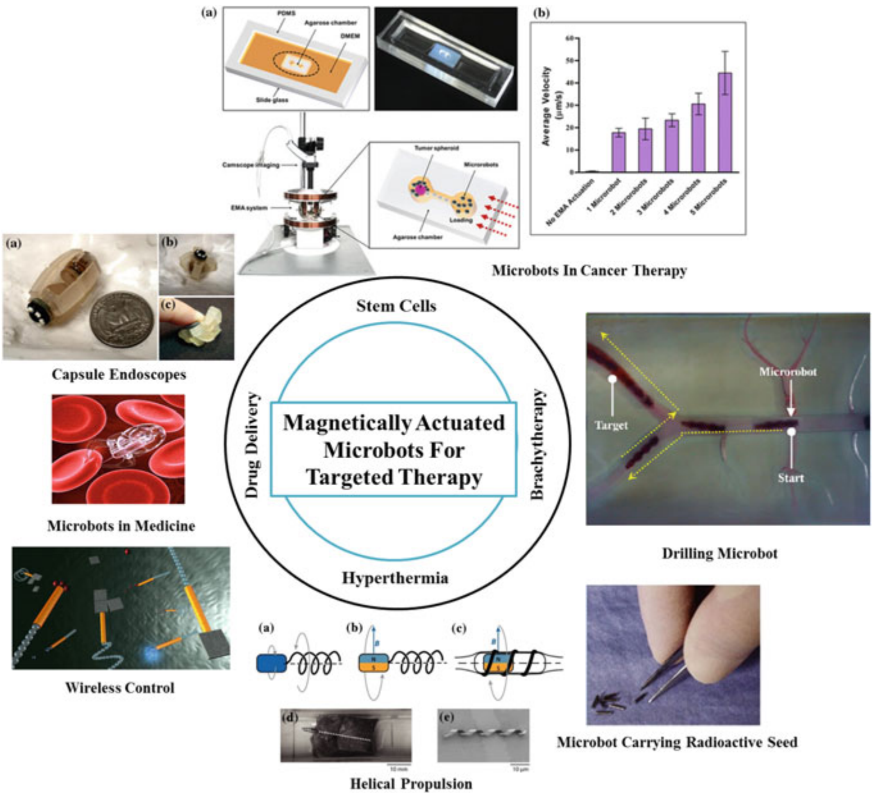

Fig. 3 Potential magnetically actuated microrobots in various medical application areas such as (i) Drug Delivery, (ii) Hyperthermia, (iii) Brachytherapy, and (iv) Stem cells research. (i) In targeted drug delivery, there are cases where soft, squishy bot controlled wirelessly used for capsule endoscope passing through human blood vessel. (ii) In hyperthermia treatment, microbots optimally controlled can be used for helical propulsion where body tissue will be exposed to rise in temperature (iii) In brachytherapy, microbots wirelessly controlled used for carrying radioactive seeds in treating tumor. (iv) In stem cells research, microbots controlled in noninvasive manner are used for cell motility enhancement and increasing potential for cancer therapy [14, 29–31, 36, 49, 50, 64, 85, 99, 117].

can be replacements to the current techniques as researchers are developing new concepts of the minimally invasive fetal surgical system. For example, procedures to insert microbots through the cervix to uterus [7, 26]. It can clear the obstruction of the urinary tract in the fetus, in cases of congenital cystic adenomatous malformation, microbots can remove extra tissues and prevent hydrops and procedures of amniocentesis and cordocentesis can go needless with the use of microbots. Figure 3 shows potential magnetically actuated microrobots in various medical application areas such as (i) Drug Delivery, (ii) Hyperthermia, (iii) Brachytherapy, and (iv) Stem cells research.

3 Magnetically Driven Magneto-Responsive Microcapsules for Targeted Therapy

The microcapsule fabrication processes are based on the principles of calcium alginate gelation. The microcapsules are generated in bulk by encapsulation. This section is going to elucidate the following points briefly: First, the setup of the microcapsule fabrication system is described; secondly, the chemical principles of the gelation processes are introduced and finally, the detailed fabrication methodology is discussed for the three calcium alginate microcapsule designs.

In contrary to the magnetic nano particles, larger particle in microns (e.g., agglomerates of superparamagnetic microspheres, 1 micron in diameter) are more effective in sustaining with the flow dynamics of the human circulatory system—mostly in larger aortic veins and arteries (Fig. 4). Like rolling down a steep hill, the steeper the gradient is, the total force will be placed on the particle. Table 1 gives typical B field values and gives a sense of what values are realizable for a working magnetically controlled microsphere guidance system.

Table 1 Typical B field values for retention at flow speeds corresponding to capillary blood flow [105].

Distance of flow tube center from pole face (cm)	Local magnetic field strength (Oe)	Local magnetic field strength gradient (Oe/cm)	Observed particle retention (%)	Longitudinal flow speed, computed for full retention (cm/sec)
1.0	1150	770	99	0.207
1.9	670	370	98	0.095
2.7	460	170	26	0.039
4.6	240	66	14	0.015

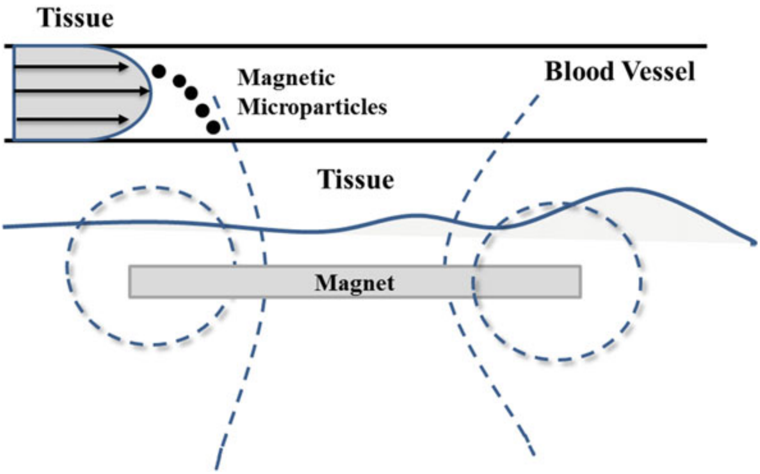

Fig. 4 A concept of magnetic actuated drug delivery system. The magnets or electromagnetic coils positioned optimally outside the body so that the generated magnetic field will influence the magnetic-responsive micro particles inside the blood vessel for manipulation and control [32, 86].

3.1 Design of Magneto-Responsive Microcapsules

3.1.1 General Mechanism of B-390 Encapsulation

Generally, the B-390 Encapsulator is a machinery that utilizes the charged vibration nozzle to generate droplets of the liquid flowing through it. As illustrated in Fig. 5, after the liquid is pumped in with a syringe pump, it is vibrated into small droplets, where the frequency is selectable between 0–6000 Hz. The droplets are charged by an electric field, which is selectable between 0–2500 V at the same time. The charged droplets are dispersed because they possess the same charge, then fall into the coagulation solution for gelation [16, 104].

Figure 5 presents the mechanism of the Encapsulator B-390 and step by step procedure for encapsulation. Here, Step 1 is mixing of active ingredient and polymer while Step 2 signifies pumping of mixture with syringe pump or air pressure. Step 3 defines superimposition of vibration and Step 4 is the droplet formation. After droplets accumulate Electrostatic charge dispersion followed as demonstrated in Step 5. Thereafter, Step 6 defines the online process control of droplet formation in the light of the stroboscope lamp and Step 7 proposes Bead formation in polymerization solution or by gelatination. Finally, the beads (matrix) are collected in Step 8 [16].

There is flow vibration nozzle set and concentric nozzle set for microbeads generation and core-shell beads generation respectively. Apart from the nozzle size, beads size is affected by other parameters. Per the operation manual, beads size decreases when (1) Electrostatic potential increases; (2) Gelling ion (Ca2+ in this case) concentration increases; (3) Alginate concentration decreases; (4) Alginate viscosity

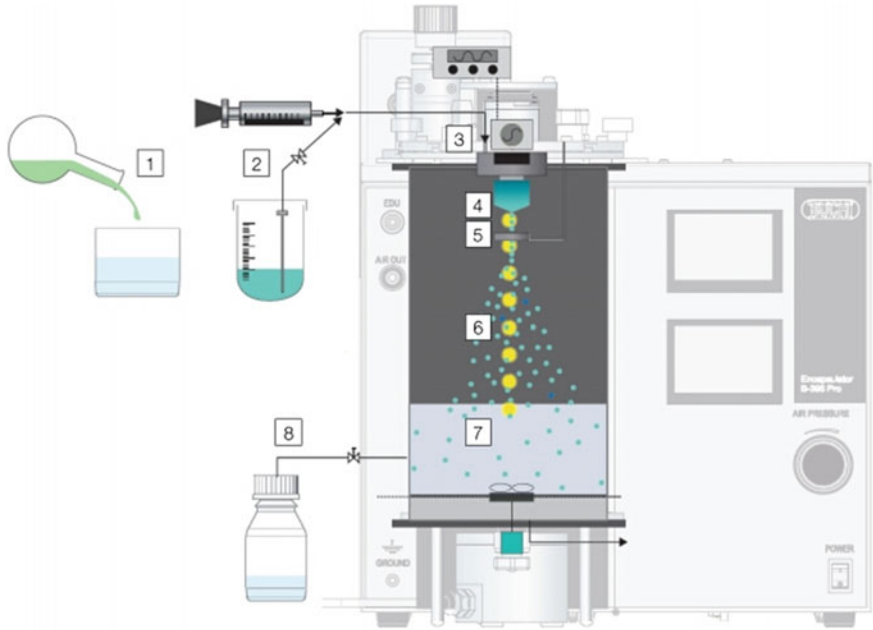

Fig. 5 Mechanism of the encapsulator B-390 and step by step procedure for encapsulation.

decreases and flow rate increases. Among those parameters, the flow rate, electrostatic potential, and viscosity influence the dispersion of the fluid the most, thus affecting the quality of magnetic beads.

3.1.2 Calcium Alginate Gelation Process

Calcium alginate hydrogel bind when covalent bonds form between alginic acids and calcium ions. As described in Fig. 6, alginate is a linear co-polymer composed of two monomeric units. When sodium alginate droplets fall into calcium chloride solution, covalent bonds form between alginic acids and calcium ions. These inter-chain associations can be either permanent or temporary, depending on the concentration of the calcium ions. In this chapter, high concentration of calcium chloride solution is chosen to be optimal and calcium alginate hydrogel beads form permanently in the solution [106, 133]. Figure 6 illustrates the Gelation Processes of the Calcium Alginate.

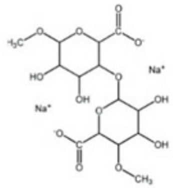

Ca2+

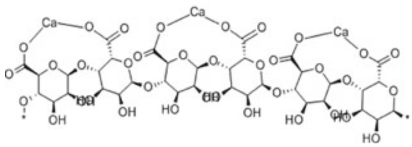

Sodium Alginate + Ca2+ ↔ Calcium Alginate

Fig. 6 Gelation processes of the calcium alginate.

3.1.3 Microcapsule Design

The design of microcapsules has been proposed in this chapter and the design rationales is discussed consecutively. The primary design proposed herein is simple in fabrication processes when applied to the locomotion control experiments. The other designs can be utilized to include thermal sensitive properties to the microcapsules, regarding the materials used.

It has been reported that polymer coated magnetic micro/nanoparticles demonstrate excellent *in vitro* and *in vivo* hyperthermia, which is a phenomenon where magnetic nanoparticles oscillate under high frequency alternating magnetic field (HF-AMF) [106, 133] and generate heat. This phenomenon indicates the potential of internal local heating of the microcapsules containing magnetic nanoparticles, hence triggering the hydrophilicity change of the thermosensitive nanogel particles from inside of the microcapsules and increasing the drug release rate.

Briefly, in the proposed design, the calcium alginate core of the microcapsule will contain bovine serum albumin (BSA) as a model drug, carbonyl iron particles for magneto-responsive properties and PNIPAM for thermal sensitive properties. The core will be coated by a layer of chitosan for controlled drug release. This core-shell structured microcapsule design will utilize thermal sensitive property of the material. PNIPAM is a kind of thermal sensitive polymer that changes hydrophilicity when crossing its transition temperature. Therefore, the assumption is made that when the environment temperature rises above the transition point, the PNIPAM hydrogel becomes hydrophobic and dehydrated, this changes the permeability of the microcapsule and increases the release rate of the drug, which is loaded in the core.

Table 2 Specifications of the EMF generator model of the 1D coil system.

D: Diameter T: Thickness L: Length W: Width

Diameter of the Maxwell coils:	2 * 55.6 mm(D) * 11 mm(T)
Diameter of the Helmholtz coils:	2 * 65.6 mm(D) * 11 mm(T)
Inter-coils wall:	100 mm(L) * 100 mm(W) * 3.622 mm(T)
Platform:	87.62 mm(L) * 100 mm(W) * 5 mm(T)

3.2 Fabrication of Magnetic Actuation Systems

The proposed coil systems consist of coil supporters, microcapsule container, and platforms. After the models were printed, copper wires of diameter 0.9 mm will be wined to the coil supporters, followed by the assembly of all the components.

3.2.1 One-Dimensional Coil System

The one-dimensional coil system consists of one pair of Helmholtz coils to generate homogeneous magnetic field and one pair of Maxwell coils to generate magnetic gradient field. A simple prototype will be fabricated with a 3D printer and copper wires of diameter 0.9 mm. The printed components will include two identical coil supporters, one particle container and one platform. The wires will be winded on the coil supporters, followed by fixing the supporters to the platform. Table 2 is going to demonstrate sample specifications of the magnetic field generator model of this one-dimensional coil system.

Table 2 is a list of the Specifications of the EMF Generator model of the 1D coil system.

The one-dimensional coil system was connected directly to the power supply. A 5 A–10 A current was fed to the Helmholtz coils and the Maxwell coils. Different magnetic particles were put into the container and an endoscope camera was fixed above the EMA system to record the locomotion of those particles in the container.

3.2.2 Two-Dimensional Coil System

The two-dimensional magnetic field generation system consists of two pairs of Helmholtz coils and two pairs of Maxwell coil. Theoretically, it will be able to control the locomotion of magnetic particles in two dimensions within the Region of interest (ROI). The two-dimensional coil system will be integrated with a current control system to realize current control, hence magnetic field control and finally the locomotion control via programming. The next Section will show the details of the current control system.

Table 3 Specifications of the EMF generator model of the 2D coil system.

D: Diameter T: Thickness	Helmholtz X	Maxwell X	Helmholtz Y	Maxwell Y
D of the core	2 * 36 mm(D)	2 * 40 mm(D)	2 * 90 mm(D)	2 * 50 mm(D)
Inter-coils wall	6 * 68 mm(D) * 2 mm(T)		6 * 160 mm(D) * 2 mm(T)	

Instead of using a platform, this design will include screws and nuts for better stability. The materials for the two-dimensional coil system will be changed from Acrylonitrile butadiene styrene (ABS), which is a very common material for 3D printing, to aluminium. Compared to ABS, aluminium has a higher melting point and better heat transfer ability. Therefore, deformation of the structure can be avoided and changes, for instance, the varying resistance of the coil caused by the heat generated when current passing through, are decreased.

Table 3 is the list of Specifications of the EMF generator model of the 2D coil system.

3.2.3 Power Supply and Current Control System

As proposed, AQMD3620NS DC motor governors receive input power (9–36 V) from the DC power supply and serial signals from the RS485 system to generate respective output power. There are two input points (AI 1 and AI 2) to receive signals for motor speed control and one input point (DE) to receive signals for motor direction control. There are eight system DIP switches for setting of modes, of which the eighth switch defines the control mode. If it is ON, the motor governor is set as a serial communication mode, where each governor is given an address by setting different combinations of the other seven switches. The USB to RS485 converter enables direct communication between the system and the programming environment. Figure 7 sketches the Principle of magnetic actuation over the microcapsules.

3.3 *Proposed Design and Materials*

The materials going to be used in this following proposed design will include alginic acid sodium salt (Alg, viscosity 15–20 cP in 1% solution) calcium chloride dehydrate ($CaCl2{\cdot}2H2O$), and carbonyl iron (CI) powder (BASF). Fabrication with Carbonyl iron (Fe (CO) n) particles can be irregular shaped dark grey particles with high iron content. Therefore, they are quite sensitive to magnetic fields. It is widely used in the fabrication of Magnetorheological (MR) fluid, coil cores and dietary supplements to discuss in the later stage. Microscale carbonyl iron particles are insoluble in neutral solvents, indicating its stability during transportation. The particles can be added into sodium alginate solution and the mixture can be injected through the encapsulator and vibrated into micro droplets for gelation processes.

3.3.1 Electromagnetic Actuation (EMA) System

The EMA system mainly consists of two parts: the coil system to generate magnetic field per the current provided and the current control system including the power supply, coil driver based on motor governor, data processor, and routine algorithms.

3.3.2 Coil System

The coil systems are utilized to emanate magnetic fields by the current flux applied through them. With different magnetic coiling parameters, such as the loop diameter and the wire diameter, the emanated field strength and patterns are changed accordingly. In this proposed design, a one-dimensional coil system and a two-dimensional coil system have been proposed for testing. Both consists of Helmholtz pairs and Maxwell pairs are described in the earlier design part.

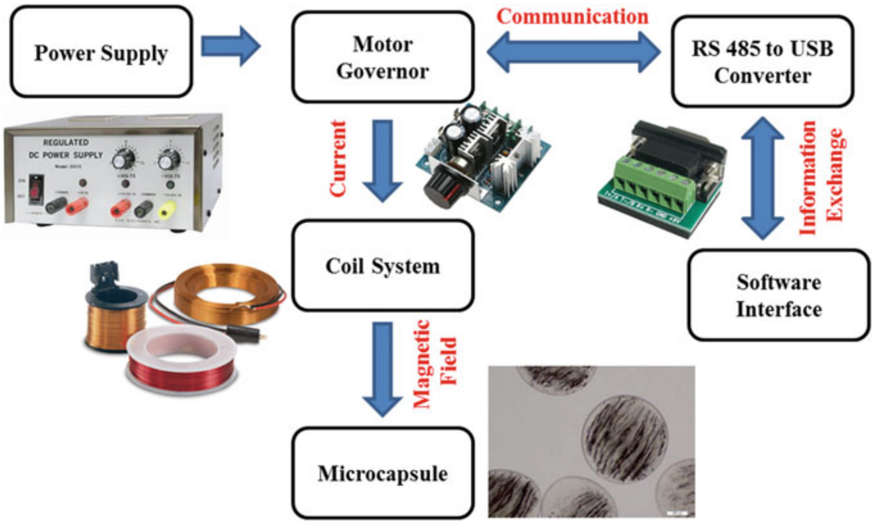

Fig. 7 Principle of magnetic actuation over the microcapsules.

3.3.3 Design Rationale

In general, for the principles, Helmholtz coil pairs generate uniform magnetic field between them along their common axis within the range of interest (ROI), while Maxwell coil pairs emanate constant gradient magnetic field. The Helmholtz coil pairs determine the orientation of the magnetic particles, while the Maxwell coil pairs drive the locomotion of them. With the currents flowing through the coil pairs, the desired magnetic fluxes can be generated. Superposition of the coil pairs generates multidimensional flux vectors.

Helmholtz coil pairs are two parallel identical coils connected to current sources of the same direction and equal flux. The distance between their centers is equal to the coil diameter. According to the Biot-Savart theory, for current flowing through a single wire loop, the magnetic field generated to a point on the axis at a distance x can be derived as in (1):

$$B(x) = \frac{\mu_0 \mu_r I R^2}{2(R^2 + x^2)^{\frac{3}{2}}} \tag{1}$$

where μ_0 is the magnetic permeability of free space and μ_r is the permeability of the environment where the magnetic particle is located. I is the current flowing through the loop and R is the radius of the wire loop. For a point at the center of the axis of the two identical Helmholtz coils with n turns each, the magnetic flux density B_M can be calculated as:

$$\begin{aligned} B_H(\frac{R}{2}) &= 2\frac{\mu_0 \mu_r n I R^2}{2(R^2 + (\frac{R}{2})^2)^{\frac{3}{2}}} \\ &= \frac{8}{5\sqrt{5}} \frac{\mu_0 \mu_r n I}{R} \end{aligned} \tag{2}$$

From formula (2), it can be concluded that the uniform magnetic field density is proportional to the current density.

Helmholtz coils are designed to generate uniform magnetic field between them along their common axis. When a magnetic particle is located in the region of interest and not aligned with the direction of the field, torque τ is generated as (3):

$$\tau = VM \times B_H \tag{3}$$

Where V is the volume of the magnetic particle and M is the magnetization of the particle. Therefore, the misaligned particle experiences torque until it is aligned to the direction of the field, where the angle between M and B_M is zero.

Figure 8 is a sketch of the Structure and the Induced Magnetic Field of a Helmholtz Coil Pair.

Similar in structure with the Helmholtz coils, Maxwell coil pairs are parallel identical coils connected to currents with equal flux but opposite directions. As illustrated in Fig. 9, the distance between their centers equals to $\sqrt{3}$ times of the coil diameter.

Figure 9 portraits the Structure and the Induced Magnetic Field of a Maxwell Coil Pair. Maxwell coils usually generate constant gradient magnetic field between them, along not only the axis, but also all directions perpendicular to the axis. The force applied to the magnetic particles inside the region of interest is described as (4):

$$F = V(M \cdot \nabla)B_M \tag{4}$$

Here, V is the volume of the magnetic particle and M is the magnetization. Magnetic flux B_M is described as:

$$B_M = [-0.5g_x, -0.5g_y, g_z] \tag{5}$$

Here, x, y, z are the respective dimensional value of the interested point and g is the magnetic flux gradient calculated as (6):

$$g = \frac{16}{3}\left(\frac{3}{7}\right)^{\frac{5}{2}} \frac{i_m \times n \times \mu_0}{(r_m)^2} \tag{6}$$

Here, μ_0 is the magnetic permeability of free space, n, i_m, r_m are the turns, current, and radius of each coil, respectively. From the formula 6, the gradient magnetic field density is proportional to the current density.

Here in Table 4, we have portrayed few of the significant papers reported from 2009 year and ahead from Prof. Sukho Park Research Group, Chonnam National University, Gwangju, Korea and Prof. Bradley Nelson Research Group, ETH Zurich,

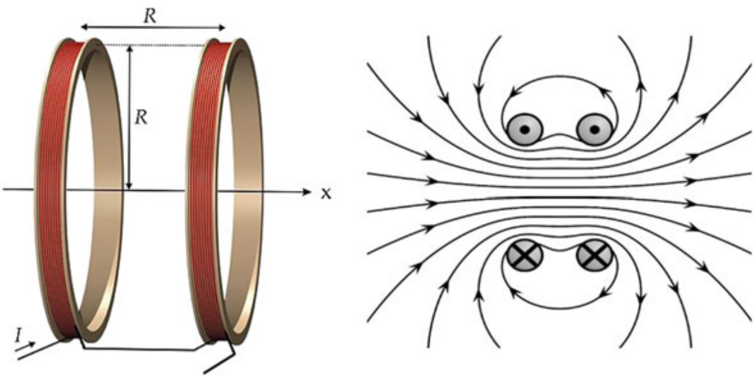

Fig. 8 Structure and the induced magnetic field of a Helmholtz coil pair.

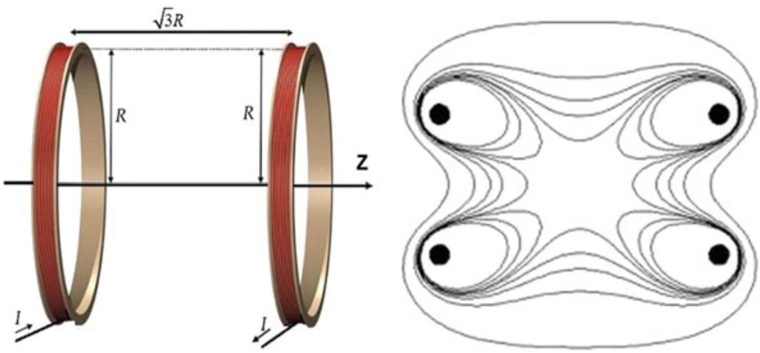

Fig. 9 Structure and the induced magnetic field of a Maxwell coil pair.

Switzerland. This is just to give an initial fragmented idea of the microbots and their design and control strategy in a listed format for ease of the reader, especially who is going to initiate a fresh research in this realm.

Table 4 Brief review of literature in magnetic micro robotics for biomedical applications (Sukho Park research group some selected publications).

Year	Application	Robot	Size Material	Magnetic system	Control	ROI	DOF(T+R)	Remarks
2009	Locomotive	Rod	um size (Permenent Magnet)		Open LoopCa-meraLab-VIEWNI PXI Controller	<35*35mm	2+1(2H2M)	——
2009	Intravascular	Rod	um size (Nd)		OpenLoop… Joystick	D+=60mm	3(1H1M)	Roll-Pitch-RollPosition recognition
2010	Intravascular	Rod	um size (Nd)		OpenLoop… Joystick	<+32mm	3+1(2H2M)	Rotational coil pairs
2010	Intravascular with drilling	Sphere 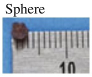	mm size (Nd Al2O3)		Open Loop	<43mm	3+3(3H2M)	1 Rotational; M coil pair
2010	with ROI developed	Rod	um size (Nd)		NG	NG	2+1(1H1M+ 1HS+ 1MS)	More efficient
2013	.. with ROI and power developed	Sphere	mm size (Nd Al2O3)		Open Loop	440% Bigger than (4)	3+3(3H1M)	440% bigger WS and 49% less power
2015	Target Ther-apy	Bacteriobot 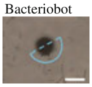	5-10um (CaAlg beads as1.) live bacteria)		(same Open Loop LabVIEW NI PXI Controller	(app <35*35mm)	2+1(2H2M)	Bacterial MagHybrid

Table 5 Brief review of literature in magnetic micro robotics for biomedical applications (Bradley Nelson research group some selected publications).

Year	Application	Robot	Size & Material	Magnetic System	ROI	DOF(T+R)	Remarks
2010	5-DOF wireless micromanipulation	Ni Magnetic 	L: 500um		NG(D<130mm)	3+2C)	—
2012	Cell Attachment	Helical micromachine 	L:8.8um D:2.0um CSS:290nmCSL: 900nm	NG	NG	3+3	DLWThin Film Deposition
2012	Wireless Mag Manipulation	Helical microstructure 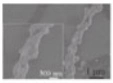	D:0.5umL:um scale	NA	NA	NA	Cavity
2012	Biomanipulations	Nanowires 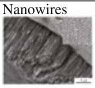	D: 100nm/200nmL: 7um	3H coils	20mm*5mm*2m	3m+3(3H)	Cell tests with microbeads
2013	TDD & Localized manipulations	Flagellum with mastigonemes 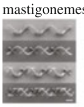	D:5um CS:0.7um(SU8Fe layer)	3H coils	NG	3+3(3H)	Speed depend on Length and Spacing Ratio of the mastigonemes
2013	3D Cell Culture & Targeted Transportation	3D porous niches 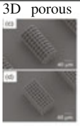	L:arnd 150umD:arnd 73umPore size:arnd 20um(photocurable polymerTi & Ni layer)	Minimag (Aeon Scientific, Switzerland)	NG	NG	HEK 293 cells attachment
2014	Triggered Drug Release	Temperature Sensitive ABF 	L:16um D:5um(Ti layer DPPC liposomes)	NA	NA	NA	——
2014	TDD & Triggered Release	Encapsulated Magnetic Microbeads 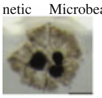	D:10um(Alginate)	OctoMag	OctoMag	3+2	Near Infrared Light Triggered Drug Release
2015	Screening	Magnetic FluorescenceABF 	L:8um(Ni/Ti layer Photosensitive polymers NIR-797 dye)	9mT and 90Hz 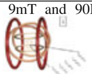	NG	3+3(3H)	DLWThin film deposition
2015	TDD & MIS Posterior part of eye	Microtubes 	OD:300um ID:125um L:3.4mm(CoNi layer)	OctoMag 40mT-500mT/m 1.186T	OctoMag	3+2	In vivo Release Study

Table 4 is a Brief Review of literature in magnetic micro robotics for biomedical applications from Prof. Sukho Park's Research Group (Selected Publications).

Table 5 is a brief review of literature in magnetic micro robotics for biomedical applications from Prof. Bradley Nelson's Research Group (Selected Publications).

4 Electromagnetically Actuated Self-driven Microjet for Biosensing Applications

Artificial micromachines have fascinated researchers around the world for last few decades with the advancements in areas of chemistry, physics, and nanotechnology [70, 109]. Hydrogen peroxide (H_2O_2) has widely been used as fuel to propel tiny motors in the presence of precise electromagnetic motion control. This electromagnetic motion controller can contain different functionalities for diverse applications, including biosensors. Bimetallic nanowires first and more recently microtubular jet engines are two of the most promising candidates to perform useful tasks at the micro/nanoscale. The transport of microparticles in controlled electromagnetic environment into a microfluidic chip was achieved by nanowires and microjets. However, only microtubular jets can self-propel in complex biological samples near EM field. Thus, the controlled transport of cells is significant since it is clearly the next step towards the use of artificial micro/nanomachines in future biomedical applications [101, 127]. In the recent past, efficient isolation of biomaterials such as nucleic acids, proteins, and cancer cells from raw biological samples was achieved by functionalized microjet engines [12]. The rapid development of this research area paves the way for designing new detection platforms and biosensing systems with the need of optical microscopes and tracking methods to measure the speeds of the micro-nanomotors [98].

4.1 Breakthrough and Innovative Aspects

4.1.1 Lab-In-A-Tube

The study of cell behaviors (division time, DNA damage, spindle reorientation, etc.) in 2D confinements represents a pioneering and unique paradigm in cell biology, chemistry, and biotechnology fields. Up to date, most of the studies on cellular behaviors have been explored only on planar 2D patterns, which do not mimic the *in vivo* microenvironment of the cells. The rolled-up microtubes not only serve as 2D microreactors for live cell studies but also as on-chip integrated sensors (optical, electric, or magnetic), which distinguishes the rolled-up nanotechnology from other technologies [38, 108]. In addition, the tubular size is scalable and easily tuned on-demand [69].

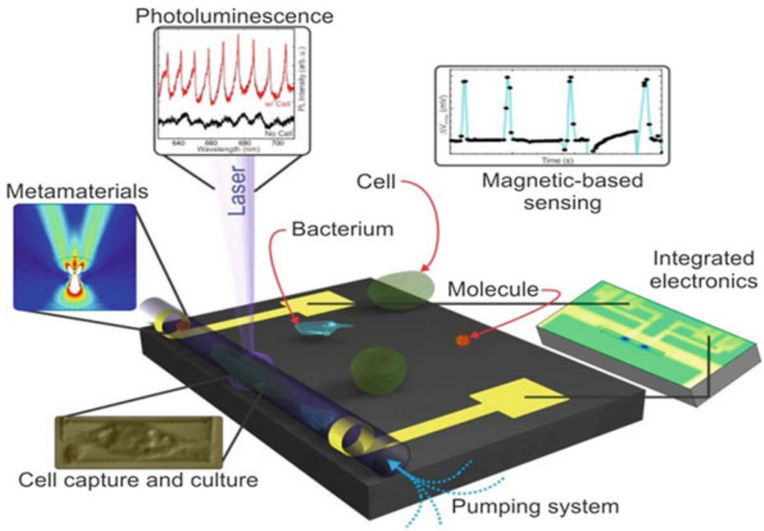

Fig. 10 Lab-in-a-tube device. Capturing and sensing of cells and cellular behaviors [11].

Figure 10 shows a Lab-in-a-tube device capturing and sensing of cells and cellular behaviors [11].

4.1.2 Catalytic Micro/Nanomotors

These tiny machines have demonstrated interesting capabilities to transport cargoes to specific targets in an accurate manner [69]. Despite the increasing number of publications, no reports have clearly proven the biocompatibility of the fuel-machine couple in the presence of EM filed [71]. Thus, major future challenges for scientists are (1) effective motion control of micro/nanomotors in vivo; (2) to seek for other biocompatible and clean sources of motion to expand the field of micro/nanomotors to real biomedical and environmental applications. The effective motion control of micro/nanomotors utilizing strong EM field for selective biosensors will surely be of ground-breaking nature [53].

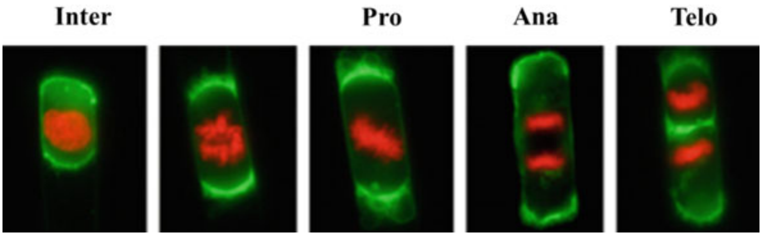

Fig. 11 Different phases of mitosis (cells into tubes) [2].

4.2 EM Field Motion Control Potential Applications Area: Future Perspectives

4.2.1 Single Cell Studies into Confined Spaces

• Cell division of animal cells has been studied in detail during the last years (Fig. 11) [18]. However, the relation between cellular morphology and its orientation during division still is mostly under study [20]. Up to now, only flat patterned surfaces have been employed for those studies concluding that the spindle orients in a specific position during the division cycle [57]. There is a great need to bring these investigations into a new concept which resembles the *in vivo* microenvironment that surrounds the cells [5, 72].

(I) Study of Mechanical (Physical) and (Bio) Chemical Stress on DNA Damage

DNA damage and recovery is nowadays a hot topic in cell biology and genetics. DNA damage in cells can be caused by several factors, including chemical or mechanical stress [51, 76]. By scaling the dimensions of the microtubes there is a great need to discriminate the threshold (in microscale size) where the cells sense mechanical stress. In addition, to gain more insight into the influence of external sources for DNA damage [48], there is a need to study several methods of trapping cells [91].

(II) The ability to integrate electrodes within the integrated on-chip tubular structure is a unique feature of the rolled-up nanotechnology. Up to date, off-chip manipulation and sensing of cells have been reported and the glass pipettes containing electrodes are the most common devices to obtain electrical signal from cells. However, those often damage the cells under study. Conclusively, there is a need to establish manipulation, control, and sensing of confined cells by means of electrochemical signals and capacitance difference on-chip. Thereafter, a detailed investigation needed for the magnetic detection of nanoparticles uptake by cells will serve as novel magneto-biosensors completing the Lab-in-a-tube concept [38, 56].

4.2.2 Rolled-Up Microtube as Microreactors for Different Types of Cells and Proteins

The mass production of parallel microtubular structures on-chip will facilitate the separation of different kinds of cells, bacteria, and proteins for bioanalytical and biosensing applications. Magnetically controlled on-chip microbots will simplify several steps of the analytical process since they can separate, isolate and concentrate the desired species (cells). Because of their biocompatibility and transparency, the microtubes will act as microreactors [46, 80] and as sensors for live imaging towards integrative lab-in-a-tube systems [22, 81].

(I) Integration of Optofluidic (Bio) Sensors into Microfluidic Chips

Up to date, rolled-up microtubes have been employed as optofluidic sensors [89], capable of distinguishing different kinds of liquids based on their refractive indexes [24]. Rolled-up SiOx microtubes [37, 112] can act as optical ring resonators [79] confining light at defined wavelengths in small volumes. The thin walls from rolled-up microtubes can act as optical microcavities since Whispering Gallery Modes (WGMs) [75] are observed in the photoluminescence spectra from the rolled-up nanomembranes. The optical rolled-up resonators can couple the light into the resonant mode of the cross section of the tube. Therefore, changes in the fluid composition or molecules bound to the inner wall surface of the tubes lead to a spectral shift of the resonant modes. As a next step, there is a huge thirst to design microtubes with comparable diameter to the studied cell size (i.e., 15 μm diameter). Once the cells were trapped into the microtubes they sharpened the Quality factor and shifting of the WGMs. It is well known that cancer and normal cell lines have different stiffness and the rigidity and morphology of the cell changes [4] during the division cycle and more drastically during apoptosis [115]. With these optical resonators, there can be an aim to sense these changes optically in confined cells.

Figure 12 demonstrates an optofluidic sensor for detection of cells.

(II) Development of Smart Self-Propelled Micro/Nanomotors For Biosensing, Biomedical, and Environmental Applications

Despite the great success and rapid development of this field, several key questions need to be addressed such as the scalability or the biocompatibility of these tiny machines [15, 123]. How small can the jet engines be and still being self-propelled in fluid? [110] Can they really perform useful bio-related applications? [102, 126] For that purpose, the supreme need is to reduce the toxicity of the fuel down to levels where the cells are viable for long periods. One straightforward method towards this aim has been carried out by warming up the solution to physiological temperatures in which the cells grow. Other sources of motion need to be studied such as light and enzymatic reactions. Moreover, the immunoresponse towards the micro-nanojets will be investigated by incubating the microtubes with macrophages. Understanding on the engulfment process will enable the optimization of the size of the microtubes and material composition to avoid the immunoresponse. These findings will be essential to understand phagocytosis of natural and artificial tubular targets. There is a need to design microjets which can be functionalized with drugs, proteins, specific antibodies, and DNA on their walls to be employed as biosensors or drug delivery systems [107, 119].

Figure 13 sketches the self-powered microbots remotely guided by a small magnet (B) [1, 87, 100].

4.3 Guidance in Magnetic Actuation

Magnetic robotic microbots or microbubbles which can be controlled by an external magnetic field have been explored as a method for precise and efficient drug delivery. With the increased usage of microbots as a system for drug delivery using ultrasound imaging *in vivo* and using microscopes *in vitro*, there is an interest to develop a tracking and guidance algorithm to locate the position of the microbots during the actuation process. By incorporating real time imaging feedback, better and accurate closed loop robot control, namely visual servoing, can be accomplished.

Typically, the visual servoing algorithm falls into three categories: position-based visual servoing [13], image-based visual servoing [13], and hybrid visual servoing [43, 44]. Since position-based visual servoing calculates the control inputs using the 3D data retrieved from the image features, it is quite sensitive to calibration and reconstruction errors. Both position-based and hybrid methods require the informa-

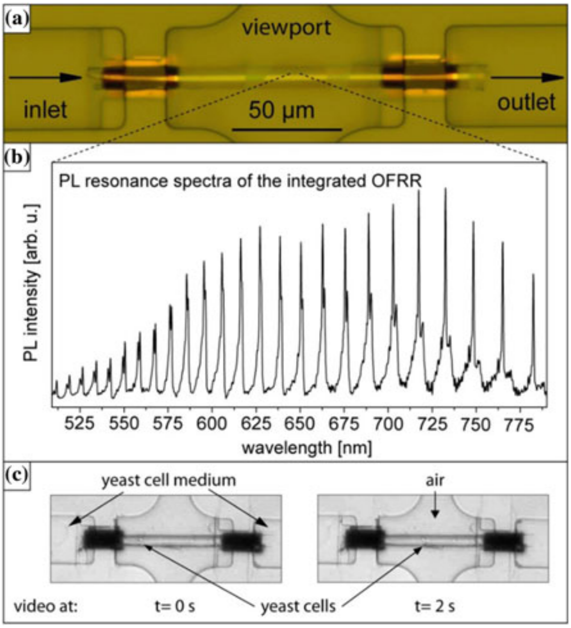

Fig. 12 Optofluidic sensor for detection of cells.

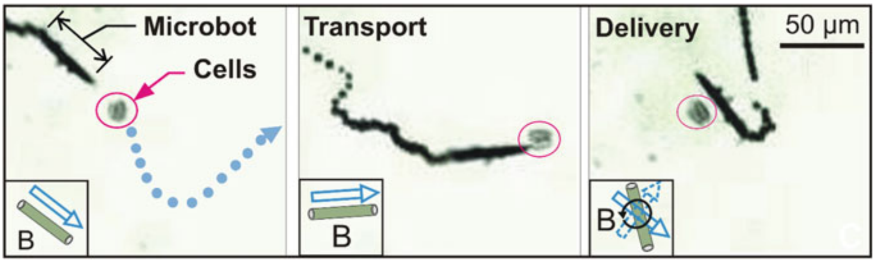

Fig. 13 The self-powered microbots can be remotely guided by a small magnet (B) [1, 87, 100].

tion of the kinematic models of the robots while the current models for surgical robots are complicated and quite inaccurate in constrained surgical environments. Hence, image-based visual servoing is preferable in this application because it can be tailored to utilize only the 2D image features as the feedback to calculate the control inputs while no prior knowledge on robot kinematics is required.

4.4 Control System Design: Future Perspective

In the past decades, several milestones have been attained in the realm of micro/nano scale drug delivery system (as described briefly in the earlier sections) including lab-on-a-chip devices and endoscopic capsules, and for minimally invasive medicines. With the increasing development of micro/nanoscale engineering, it is now possible to batch process nanoscale drug carriers including nanotubes, nanoparticles, and nanowires. A major concern now with the development of this untethered devices *in vivo* is to power them and to control effectively. In this realm, we propose a control strategy for faithful mechanism and manipulation.

Proposed Design and Future Perspectives

Figure 14 is a schematic for proposed magnetic control of self-propelled microjets under ultrasound image guidance. (A) Two sets of electromagnetic coils to be used for generation of controlled magnetic fields [54]. (B) Glass-PDMS hybrid microfluidic device which contains a microchannel using a standard Soft Lithography technique [5, 21]. (C) Microjets move along the magnetic field lines using the propulsion force that is generated due to the ejecting oxygen bubbles from one of their ends [54, 55]. (D) A camera with microscope system will acquire self-propelled microjet real-time images for validation with ultrasound. (E) Ultrasound probe embedded with transducers to acquire images in 3D plane (preferably).

Figure 15 proposed a self-propelled microjets control algorithm. The control system uses the model of self-propelled microjets in a feed forward configuration [54]. Based on the nonlinearity of the system we will use Fuzzy Logic PID Controller or

MPC for better accuracy. The magnetic field strength (B) can be computed as the summation of feed forward controller and MPC. The real-time position tracking algorithm is used to capture ultrasound images (P). The position error E=P(Reference)-P will be used to initiate PID/MPC closed loop control [10].

Proposed Ultrasound-based Tracking of Self-propelled Jets

In contrast to single carrier short duration pulse [10, 95], the proposed technique will use Chirp (Frequency Modulated Signal) coded excitation for better resolution and penetration [39]. Using Chirp as test signal is believed to counteract the long lasting inverse relation (resolution and penetration inversely proportional) trade-off determining accurately noise removal for de-noising in medical US imaging realm [67]. Finally, it is proposed to use Fractional Fourier Transform (FRFT) which is reported to be more flexible for image edge extraction and recognition scenario [116, 131].

Due to the sparsity and multi-resolution property, incorporating wavelet-transform is another novel way which is reported to have emerging potential for speckle noise reduction in 2D and 3D US images [46]. As reported, this will eventually minimize the speckle noise while preserving sharp edges [47, 120].

5 Concluding Remarks and Future Scope

The advances of MRI based diagnosis which falls in the regime of electromagnetically driven actuation is not a new concept. The selling point to use magnetic actuation

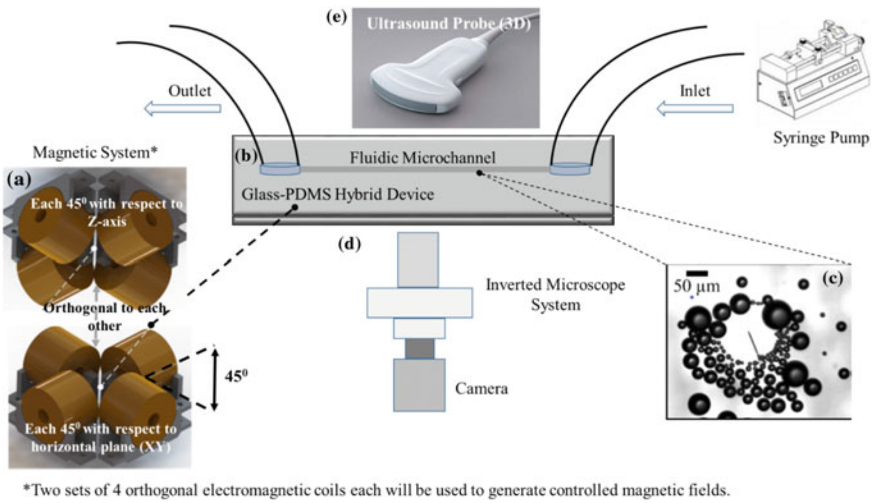

Fig. 14 Schematic for proposed magnetic control of self-propelled microjets under ultrasound image guidance.

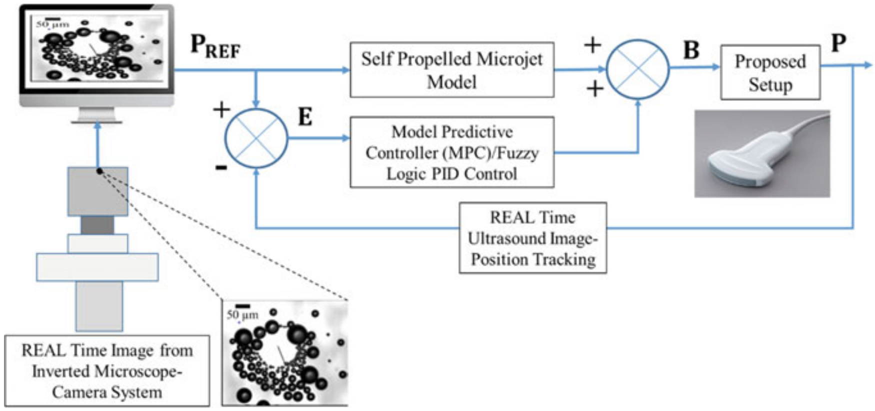

Fig. 15 Proposed self-propelled microjets control algorithm.

for noninvasive drug delivery is multifunctional. The advantages of minimally invasive techniques offer less postoperative pain, less infection, quick recovery time, less hospitalization cost, and overall much higher quality of life. There is no doubt that magnetically driven microbots are going to bring noninvasive drug delivery to a new level but somehow presently the market for commercialization is missing. To dig in more into the problem of functional commercialization there is still a gap in research which needs to be filled beforehand. There are huge number of challenges, e.g., the pH of the media, the heart flow rate and many more to overcome before this Fantastic Voyage turns into reality. Finally, we should be optimistic and constantly work towards building advanced micro motors for biomedical applications when safety is concerned in magnetically driven microbots *in vivo* medical applications.

Acknowledgements This work was in part supported by the Singapore Academic Research Fund under Grant R-397-000-173-133 (Magnetically Actuated Micro Robotics), R-397-000-227-112, and National Natural Science Foundation of China NSFC grant 51405322, NUSRI China Jiangsu Provincial Grant BK20150386 and BE2016077 awarded to Dr. Hongliang Ren.

References

1. Ahmed, Suzanne, et al. 2013. Steering acoustically propelled nanowire motors toward cells in a biologically compatible environment using magnetic fields. *Langmuir* 29 (52): 16113–16118.
2. Alberts, Bruce, et al. 2013. Essential cell biology. Garland Science.
3. Bahaj, A.S., and P.A.B. James. 1993. Characterisation of magnetotactic bacteria using image processing techniques. *IEEE Transactions on Magnetics* 29 (6): 3358–3360.
4. Baker, Erin L., Roger T. Bonnecaze, and Muhammad H. Zaman. 2009. Extracellular matrix stiffness and architecture govern intracellular rheology in cancer. *Biophysical Journal* 97 (4): 1013–1021.

5. Banerjee, Hritwick. 2014. Frequency driven alteration in cellular morphology during ultrasound pulsing in a microfluidic confinement. PhD thesis, Indian Institute of Technology, Gandhinagar.
6. Banerjee, Hritwick and Babji Srinivasan. 2013. Modelling, optimization and control of droplet based microfluidic technology for single-cell high-throughput screening.
7. Berris, M., and M. Shoham. 2006. Febotics-a marriage of fetal surgery and robotics. *Computer Aided Surgery* 11 (4): 175–180.
8. Bose, Nilanjana. 2015. The role of acoustofluidics in targeted drug delivery. *Biomicrofluidics* 9 (5): 052609.
9. Bose, Nilanjana, et al. 2011. The role of cell membrane strain in sonoporation characterised by microfluidic-based single-cell analysis. In *15th International conference on miniaturized systems for chemistry and life sciences*, 1743–1745, Seattle, Washington, USA.
10. Boskma, Klaas Jelmer, Stefano Scheggi and Sarthak Misra. 2016. Closed-loop control of a magnetically-actuated catheter using two-dimensional ultrasound images. In *2016 6th IEEE international conference on biomedical robotics and biomechatronics (BioRob)*, 61–66, IEEE.
11. Burdick, Jared, et al. 2008. Synthetic nanomotors in microchannel networks: Directional microchip motion and controlled manipulation of cargo. *Journal of the American Chemical Society* 130 (26): 8164–8165.
12. Campuzano, S., et al. 2011. Motion-driven sensing and biosensing using electrochemically propelled nanomotors. *Analyst* 136 (22): 4621–4630.
13. Chaumette, Francois. 1998. Potential problems of stability and convergence in image-based and position-based visual servoing. In *The confluence of vision and control*, 66–78.
14. Cheung, Eugene, et al. 2005. A new endoscopic microcapsule robot using beetle inspired microfibrillar adhesives. In *Proceedings, 2005 IEEE/ASME international conference on advanced intelligent mechatronics*, 551–557, IEEE.
15. Chng, Elaine Lay Khim, Guanjia Zhao, and Martin Pumera. 2014. Towards biocompatible nano/microscale machines: self-propelled catalytic nanomotors not exhibiting acute toxicity. *Nanoscale* 6 (4): 2119–2124.
16. Cho, Ah Ra, et al. 2014. Preparation of chitosan-TPP microspheres as resveratrol carriers. In *Journal of Food Science* 79 (4).
17. Collins, James F Jr, et al. 2011. Ophthalmic drug delivery system. US Patent 7,883,031, Feb. 2011.
18. Croce, Carlo M., and George A. Calin. 2005. miRNAs, cancer, and stem cell div. *Cell* 122 (1): 6–7.
19. Croswell, Jennifer M., David F. Ransohoff, and Barnett S. Kramer. 2010. Principles of cancer screening: Lessons from history and study design issues. *Seminars in oncology*, 202–215. Elsevier.
20. Darnell, James E., Harvey Lodish, David Baltimore, et al. 1990. *Molecular cellbiology*. New York: Scientific American Books.
21. Das, Tamal, Tapas K. Maiti, and Suman Chakraborty. 2011. Augmented stressresponsive characteristics of cell lines in narrow confinements. *Integrative Biology* 3 (6): 684–695.
22. Duan, Ruixue, et al. 2013. Lab in a tube: Ultrasensitive detection of microRNAs at the single-cell level and in breast cancer patients using quadratic isothermal amplification. *Journal of the American Chemical Society* 135 (12): 4604–4607.
23. Edd, Jon, et al. 2003. Biomimetic propulsion for a swimming surgical microrobot. In *Proceedings 2003 IEEE/RSJ international conference on intelligent robots and systems (IROS 2003)*, vol. 3, 2583-2588, IEEE.
24. Fan, Xudong. 2011. Optofluidic microsystems for chemical and biological analysis. *Nature Photonics* 5 (10): 591–597.
25. Feringa, Ben L. 2007. The art of building small: From molecular switches to molecular motors. *The Journal of Organic Chemistry* 72 (18): 6635–6652.
26. Flake, Alan W. 2003. Surgery in the human fetus: The future. *The Journal of Physiology* 547 (1): 45–51.

27. Frankel, Richard, Timothy, Williams, and Dennis Bazylinski. 2007. Magnetoaerotaxis. In: *Magnetoreception and magnetosomes in bacteria*, 1–24.
28. Garne, E., C. Stoll, and M. Clementi. 2001. Evaluation of prenatal diagnosis of congenital heart diseases by ultrasound: experience from 20 European registries. *Ultrasound in Obstetrics and Gynecology* 17 (5): 386–391.
29. Glass, Paul, Eugene Cheung, and Metin Sitti. 2008. A legged anchoring mechanism for capsule endoscopes using micropatterned adhesives. *IEEE Transactions on Biomedical Engineering* 55 (12): 2759–2767.
30. Glass, Paul, Metin Sitti, and Ragunath Appasamy. 2007. A new biomimetic adhesive for therapeutic capsule endoscope applications in the gastrointestinal tract. *Gastrointestinal Endoscopy* 65 (5): AB91.
31. Glass, Paul, et al. 2008. A motorized anchoring mechanism for a tethered capsule robot using fibrillar adhesives for interventions in the esophagus. In *2nd IEEE RAS & EMBS international conference on biomedical robotics and biomechatronics, BioRob*, 758–764, IEEE.
32. Glass, Paul, et al. 2009. A swallowable tethered capsule endoscope for diagnosing Barrett's Esophagus. *Gastrointestinal Endoscopy* 69 (5): AB106.
33. Grady, M.S., et al. 1989. Preliminary experimental investigation of in vivo magnetic manipulation: Results and potential application in hyperthermia. *medical Physics* 16 (2): 263–272.
34. Grady, M.S., et al. 1990. Nonlinear magnetic stereotaxis: Three-dimensional, in vivo remote magnetic manipulation of a small object in canine brain. *Medical Physics* 17 (3): 405–415.
35. Guha, Manalee, et al. 2015. Polymorphisms in CaSR and CLDN14 Genes Associated with Increased Risk of Kidney Stone Disease in Patients from the Eastern Part of India. *PloS one* 10 (6): e0130790.
36. Han, Jiwon, et al. 2016. Hybrid-actuating macrophage-based microrobots for active cancer therapy. *Scientific Reports* 6.
37. Harazim, Stefan M., et al. 2012. Fabrication and applications of large arrays of multifunctional rolled-up SiO/SiO 2 microtubes. *Journal of Materials Chemistry* 22 (7): 2878–2884.
38. Harazim, Stefan M., et al. 2012. Lab-in-a-tube: On-chip integration of glass optofluidic ring resonators for label-free sensing applications. *Lab on a Chip* 12 (15): 2649–2655.
39. Harput, Sevan. 2012. *Use of chirps in medical ultrasound imaging*. University of Leeds.
40. Hoffman, Julien I.E., and Samuel Kaplan. 2002. The incidence of congenital heart disease. *Journal of the American college of cardiology* 39 (12): 1890–1900.
41. Hogers, B., et al. 1995. Intracardiac blood flow patterns related to the yolk sac circulation of the chick embryo. *Circulation Research* 76 (5): 871–877.
42. Holligan, D.L., G.T. Gillies, and J.P. Dailey. 2003. Magnetic guidance of ferrofluidic nanoparticles in an in vitro model of intraocular retinal repair. *Nanotechnology* 14 (6): 661.
43. Hosoda, Koh, Katsuji Igarashi, and Minoru Asada. 1996. Adaptive hybrid visual servoing/force control in unknown environment. In *Proceedings of the 1996 IEEE/RSJ international conference on intelligent robots and systems' 96, IROS 96*, vol. 3, 1097–1103, IEEE.
44. Hosoda, Koh, Katsuji Igarashi, and Minoru Asada. 1998. Adaptive hybrid control for visual and force servoing in an unknown environment. *IEEE Robotics & Automation Magazine* 5 (4): 39–43.
45. Hove, Jay R., et al. 2003. Intracardiac fluid forces are an essential epigenetic factor for embryonic cardiogenesis. *Nature* 421 (6919): 172–177.
46. Huang, Gaoshan, et al. 2009. Rolled-up transparent microtubes as two-dimensionally confined culture scaffolds of individual yeast cells. *Lab on a Chip* 9 (2): 263–268.
47. Jaber, Alaa Abdulhady and Robert Bicker. 2014. A simulation of non-stationary signal analysis using wavelet transform based on LabVIEW and Matlab. In *2014 European, Modelling Symposium (EMS)*, 138–144, IEEE.
48. Jackson, Stephen P., and Jiri Bartek. 2009. The DNA-damage response in human biology and disease. *Nature* 461 (7267): 1071–1078.
49. Jeong, Semi, et al. 2011. Enhanced locomotive and drilling microrobot using precessional and gradient magnetic field. *Sensors and Actuators A: Physical* 171 (2): 429–435.

50. Karagozler, Mustafa Emre, et al. 2006. Miniature endoscopic capsule robot using biomimetic micro-patterned adhesives. In *The first IEEE/RAS-EMBS international conference on biomedical robotics and biomechatronics, 2006, BioRob*, 105–111, IEEE.
51. Kasai, Hiroshi. 1997. Analysis of a form of oxidative DNA damage, 8-hydroxy- 2-deoxyguanosine, as a marker of cellular oxidative stress during carcinogenesis. *Mutation Research/Reviews in Mutation Research* 387 (3): 147–163.
52. Khalil, Islam S.M., et al. 2013. Characterization and control of biological microrobots. In *Experimental robotics*, 617–631. Springer.
53. Khalil, Islam S.M., et al. 2013. Magnetic control of potential microrobotic drug delivery systems: nanoparticles, magnetotactic bacteria and self-propelled microjets. In *2013 35th annual international conference of the IEEE, engineering in medicine and biology society (EMBC)*, 5299–5302, IEEE.
54. Khalil, Islam S.M., et al. 2013. Three-dimensional closed-loop control of selfpropelled microjets. *Applied Physics Letters* 103 (17): 172404.
55. Khalil, Islam S.M., et al. 2014. The control of self-propelled microjets inside a microchannel with time-varying flow rates. *IEEE Transactions on Robotics* 30 (1): 49–58.
56. Khalil, Islam S.M., et al. 2014. Wireless magnetic-based closed-loop control of self-propelled microjets. *PloS one* 9 (2): e83053.
57. Kihlman, Bengt A. 1966. Actions of chemicals on dividing cells.
58. Klibanov, Alexander L. 2006. Microbubble contrast agents: targeted ultrasound imaging and ultrasound-assisted drug-delivery applications. *Investigative radiology* 41 (3): 354–362.
59. Kohl, Thomas, et al. 2000. World experience of percutaneous ultrasound-guided balloon valvuloplasty in human fetuses with severe aortic valve obstruction. *The American Journal of Cardiology* 85 (10): 1230–1233.
60. Kosa, Gbor, Moshe Shoham, and Menashe Zaaroor. 2007. Propulsion method for swimming microrobots. *IEEE Transactions on Robotics* 23 (1): 137–150.
61. Kossoff, Eric H., et al. 2002. Kidney stones, carbonic anhydrase inhibitors, and the ketogenic diet. *Epilepsia* 43 (10): 1168–1171.
62. Kristo, Blaine, et al. 2003. Microelectromechanical systems in urology. *Urology* 61 (5): 883–887.
63. Kummer, Michael P., et al. 2010. OctoMag: An electromagnetic system for 5- DOF wireless micromanipulation. *IEEE Transactions on Robotics* 26 (6): 1006–1017.
64. Kwon, Jiwoon, et al. 2006. Friction enhancement via micro-patterned wet elastomer adhesives on small intestinal surfaces. *Biomedical Materials* 1 (4): 216.
65. Latombe, Jean-Claude. 2012. Robot motion planning, vol. 124. Springer Science & Business Media.
66. Leigh, David A. 2016. Genesis of the nanomachines: The 2016 nobel prize in chemistry. *Angewandte Chemie International Edition* 55 (47): 14506–14508.
67. Lizzi,Frederic L, and Ernest J Feleppa. 2000. Image processing and pre-processing for medical ultrasound. In *2000 29th Proceedings applied imagery pattern recognition workshop*, 187–192, IEEE.
68. Lymberis, Andreas. 2010. Micro-nano-biosystems: An overview of European research. *Minimally Invasive Therapy & Allied Technologies* 19 (3): 136–143.
69. Ma, Xing, Kersten Hahn, and Samuel Sanchez. 2015. Catalytic mesoporous Janus nanomotors for active cargo delivery. *Journal of the American Chemical Society* 137 (15): 4976.
70. Magdanz, Veronika, Samuel Sanchez, and Oliver G. Schmidt. 2013. Development of a sperm-flagella Driven Micro-Bio-Ro. *Advanced Materials* 25 (45): 6581–6588.
71. Magdanz, Veronika, et al. 2014. Stimuli-responsive microjets with reconfigurable shape. *Angewandte Chemie International Edition* 53 (10): 2673–2677.
72. Mak, Michael, Cynthia A. Reinhart-King, and David Erickson. 2013. Elucidating mechanical transition effects of invading cancer cells with a subnucleusscaled microfluidic serial dimensional modulation device. *Lab on a Chip* 13 (3): 340–348.
73. Martel, Sylvain, et al. 2007. Automatic navigation of an untethered device in the artery of a living animal using a conventional clinical magnetic resonance imaging system. *Applied Physics Letters* 90 (11): 114105.

74. Mathieu, J.-B., Gilles Beaudoin, and Sylvain Martel. 2006. Method of propulsion of a ferromagnetic core in the cardiovascular system through magnetic gradients generated by an MRI system. *IEEE Transactions on Biomedical Engineering* 53 (2): 292–299.
75. Matsko, Andrey B., and Vladimir S. Ilchenko. 2006. Optical resonators with whispering gallery modes I: basics. *IEEE Journal of Selected Topics in Quantum Electronics* 12 (3): 3.
76. Mayr, Manuel, et al. 2002. Mechanical stress-induced DNA damage and racp38MAPK signal pathways mediate p53-dependent apoptosis in vascular smooth muscle cells. *The FASEB Journal* 16 (11): 1423–1425.
77. McNeil, Robert G., et al. 1995. Functional design features and initial performance characteristics of a magnetic-implant guidance system for stereotactic neurosurgery. *IEEE Transactions on Biomedical Engineering* 42 (8): 793–801.
78. Meeker, David C., et al. 1996. Optimal realization of arbitrary forces in a magnetic stereotaxis system. *IEEE Transactions on Magnetics* 32 (2): 320–328.
79. Mei, Yongfeng, et al. 2008. Versatile approach for integrative and functionalized tubes by strain engineering of nanomembranes on polymers. *Advanced Materials* 20 (21): 4085–4090.
80. Mei, Yongfeng, et al. 2011. Rolled-up nanotech on polymers: from basic perception to self-propelled catalytic microengines. *Chemical Society Reviews* 40 (5): 2109–2119.
81. Min, Xuehong, et al. 2015. Lab in a tube: Sensitive detection of MicroRNAs in urine samples from bladder cancer patients using a single-label DNA probe with AIEgens. *ACS Applied Materials & Interfaces* 7 (30): 16813–16818.
82. Molloy, J.A., et al. 1990. Experimental determination of the force required for insertion of a thermoseed into deep brain tissues. *Annals of Biomedical Engineering* 18 (3): 299–313.
83. Nacev, A., et al. 2010. Magnetic nanoparticle transport within flowing blood and into surrounding tissue. *Nanomedicine* 5 (9): 1459–1466.
84. Nadeau, Caroline, et al. 2015. Intensity-based visual servoing for instrument and tissue tracking in 3D ultrasound volumes. *IEEE Transactions on Automation Science and Engineering* 12 (1): 367–371.
85. Nelson, Bradley J., Ioannis K. Kaliakatsos, and Jake J. Abbott. 2010. Microrobots for minimally invasive medicine. *Annual Review of Biomedical Engineering* 12: 55–85.
86. Pankhurst, Quentin A., et al. 2003. Applications of magnetic nanoparticles in biomedicine. *Journal of Physics D: Applied Physics* 36 (13): R167.
87. Patra, Debabrata, et al. 2013. Intelligent, self-powered, drug delivery systems. *Nanoscale* 5 (4): 1273–1283.
88. Plante, Jean-Sébastien, Lauren M Devita, and Steven Dubowsky. 2007. A road to practical dielectric elastomer actuators based robotics and mechatronics: discrete actuation. In *The 14th international symposium on smart structures and materials & nondestructive evaluation and health monitoring, International Society for Optics and Photonics*, 652406– 652406.
89. Psaltis, Demetri, and Stephen R. Quake. 2006. Developing optofluidic technology through the fusion of microfluidics and optics. *Nature* 442 (7101): 381–386.
90. Ren, Liqiang, et al. 2015. A high-throughput acoustic cell sorter. *Lab on a Chip* 15 (19): 3870–3879.
91. Rettig, Jacqueline R. 2005. Large-scale single-cell trapping and imaging using microwell arrays. *Analytical Chemistry* 77 (17): 5628–5634.
92. Roy, Shuvo, et al. 2006. MEMS and neurosurgery. In *BioMEMS and biomedical nanotechnology*, 95–123. Springer.
93. Rubinstein, Leslie. 2000. A practical nanorobot for treatment of various medical problems. In *Draft paper for the 8th foresight conference on molecular nanotechnology*, Bethesda, Maryland.
94. Saettone, Marco Fabrizio. 2002. Progress and problems in ophthalmic drug delivery. *Business Briefing: Pharmatech* 1: 167–71.
95. Sánchez, Alonso, et al. 2014. Magnetic control of self-propelled microjets under ultrasound image guidance. In *2014 5th IEEE RAS & EMBS international conference on biomedical robotics and biomechatronics*, 169–74, IEEE.
96. Sánchez, Samuel. Chemical nanomachines as active drug nanovehicles.

97. Samuel Sánchez. Hybrid micro and nanoBots as future active drug carriers.
98. Sánchez, Samuel, Lluıs Soler, and Jaideep Katuri. 2015. Chemically powered micro-and nanomotors. *Angewandte Chemie International Edition* 54 (5): 1414–1444.
99. Sanchez, Samuel, et al. 2010. Dynamics of biocatalytic microengines mediated by variable friction control. *Journal of the American Chemical Society* 132 (38): 13144–13145.
100. Sanchez, Samuel, et al. 2010. Microbots swimming in the flowing streams of microfluidic channels. *Journal of the American Chemical Society* 133 (4): 701–703.
101. Sanchez, Samuel, et al. 2011. Controlled manipulation of multiple cells using catalytic microbots. *Chemical Communications* 47 (2): 698–700.
102. Sánchez, Samuel, et al. 2014. Tubular micro-nanorobots: smart design for biorelated applications. In *Small-scale robotics. From nano-to-millimeter- sized robotic systems and applications*, 16–27. Springer.
103. Satterfield, Charles N, Ralph L Wentworth, and Sterge T Demetriades. 1953. The viscosity of vapor mixtures of hydrogen peroxide and water. Technical Report, MASSACHUSETTS INST OF TECH CAMBRIDGE HYDROGEN PEROXIDE LABS.
104. Seiffert, Sebastian. 2013. Small but smart: Sensitive microgel capsules. *Angewandte Chemie International Edition* 52 (44): 11462–11468.
105. Senyei, Andrew, Kenneth Widder, and George Czerlinski. 1978. Magnetic guidance of drug-carrying microspheres. *Journal of Applied Physics* 49 (6): 3578–3583.
106. Shi, Jun, Natalia M Alves, and Joao F Mano. 2008. Chitosan coated alginate beads containing poly (N-isopropylacrylamide) for dual-stimuli-responsive drug release. *Journal of Biomedical Materials Research Part B: Applied Biomaterials* 84 (2): 595–603.
107. Sitti, Metin, et al. 2015. Biomedical applications of untethered mobile milli/microrobots. *Proceedings of the IEEE* 103 (2): 205–224.
108. Smith, Elliot J., et al. 2010. Lab-in-a-tube: detection of individual mouse cells for analysis in flexible split-wall microtube resonator sensors. *Nano Letters* 11 (10): 4037–4042.
109. Soler, Lluıs, et al. 2013. Self-propelled micromotors for cleaning polluted water. *Acs Nano* 7 (11): 9611.
110. Solovev, Alexander A., et al. 2009. Catalytic microtubular jet engines self-propelled by accumulated gas bubbles. *Small* 5 (14): 1688–1692.
111. Solovev, Alexander A., et al. 2010. Magnetic control of tubular catalytic microbots for the transport, assembly, and delivery of micro-objects. *Advanced Functional Materials* 20 (15): 2430–2435.
112. Songmuang, R., et al. 2007. From rolled-up Si microtubes to SiO x/Si optical ring resonators. *Microelectronic Engineering* 84 (5): 1427–1430.
113. Steinberger, Bernhard, et al. 1994. Movement of magnetic bacteria in time-varying magnetic fields. *Journal of Fluid Mechanics* 273: 189–211.
114. Stroumbakis, Nicholas, et al. 1997. Clinical significance of repeat sextant biopsies in prostate cancer patients. *Urology* 49 (3): 113–118.
115. Suresh, Subra. 2007. Biomechanics and biophysics of cancer cells. *Acta Materialia* 55 (12): 3989–4014.
116. Tao, Ran, Lin Qi, and Yue Wang. 2004. *Theory and applications of the fractional Fourier transform*. Beijing: Publisher of Tsinghua University.
117. Temel, Fatma Zeynep and Serhat Yesilyurt. 2011. Magnetically actuated micro swimming of bio-inspired robots in mini channels. In *2011 IEEE international conference on mechatronics (ICM)*, 342–347, IEEE.
118. Tobita, Kimimasa, and Bradley B Keller. 2000. Right and left ventricular wall deformation patterns in normal and left heart hypoplasia chick embryos. *American Journal of Physiology-Heart and Circulatory Physiology* 279 (3): H959–H969.
119. Trewyn, Brian G., et al. 2007. Mesoporous silica nanoparticle based controlled release, drug delivery, and biosensor systems. *Chemical Communications* 31: 3236–3245.
120. Uddin, Muhammad Shahin, et al. 2016. Speckle-reduction algorithm for ultrasound images in complex wavelet domain using genetic algorithm-based mixture model. *Applied Optics* 55 (15): 4024–4035.

121. Unger, Bertram J., et al. 2002. Virtual peg-in-hole performance using a 6-dof magnetic levitation haptic device: Comparison with real forces and with visual guidance alone. In *Proceedings, 10th symposium on haptic interfaces for virtual environment and teleoperator systems, HAPTICS*, 263–270, IEEE.
122. Van, Mien, et al. 2016. Fault diagnosis in image-based visual servoing with eye-in-hand configurations using Kalman filter. *IEEE Transactions on Industrial Informatics* 12 (6): 1998–2007.
123. Wang, Joseph, and Wei Gao. 2012. Nano/microscale motors: biomedical opportunities and challenges. *ACS nano* 6 (7): 5745–5751.
124. Wang, Joseph, and Kalayil Manian Manesh. 2010. Motion control at the nanoscale. *Small* 6 (3): 338–345.
125. Wu, Keyu, Liao Wu, and Hongliang Ren. 2014. An image based targeting method to guide a tentacle-like curvilinear concentric tube robot. In *2014 IEEE international conference on robotics and biomimetics (ROBIO)*, 386–391, IEEE.
126. Yingjie, Wu, et al. 2012. Autonomous movement of controllable assembled Janus capsule motors. *ACS Nano* 6 (12): 10910–10916.
127. Xi, Wang, et al. 2013. Rolled-up magnetic microdrillers: towards remotely controlled minimally invasive surgery. *Nanoscale* 5 (4): 1294–1297.
128. Yang, Quanhe, et al. 2006. Racial differences in infant mortality attributable to birth defects in the United States, 1989–2002. *Birth Defects Research Part A: Clinical and Molecular Teratology* 76 (10): 706–713.
129. Yesin, K Berk, Karl Vollmers, and Bradley J Nelson. 2006. Modeling and control of untethered biomicrorobots in a fluidic environment using electromagnetic fields. *The International Journal of Robotics Research* 25 (5–6): 527–536.
130. Zhang, Li, et al. 2010. Controlled propulsion and cargo transport of rotating nickel nanowires near a patterned solid surface. *ACS Nano* 4 (10): 6228–6234.
131. Zhang, Xinghui, et al. 2015. Alpha stable distribution based morphological filter for bearing and gear fault diagnosis in nuclear power plant. *Science and Technology of Nuclear Installations*.
132. Zhou, Yue, et al. 2013. Robotics in natural orifice transluminal endoscopic surgery. *Journal of Mechanics in Medicine and Biology* 13 (02): 1350044.
133. Zhu, Xiaoli, et al. 2012. Preparation and characterization of nanosized P (NIPAMMBA) hydrogel particles and adsorption of bovine serum albumin on their surface. *Nanoscale Research Letters* 7 (1): 519.

Electromagnetically Responsive Soft-Flexible Robots and Sensors for Biomedical Applications and Impending Challenges

Hritwick Banerjee and Hongliang Ren

Abstract Advantages of flexible polymer materials with developments in refined magnetic actuation can be intertwined for a promising platform to work on a resilient, adaptable manipulator aimed at a range of biomedical applications. Moreover, soft magnetic material has an inherent property of high remanence like the permanent magnets which can be further refined to meet ever-increasing demands in untethered and safe-regulated medical environments. In this chapter, we focus mostly on different avenues and facets of flexible polymer materials in adaptable actuation and sensing in the context of magnetic field for range of biomedical applications.

1 Introduction

Instead of rigid, inflexible, stiff robots, the era of robotics evolving rapidly towards a soft, flexible, yet resilient and squishy counter parts. The advantage of using a soft material as active component comes with its own challenges. In theory, soft materials will pose infinite DOF, which makes control, and design an increasingly difficult problem for engineers. Therefore, we need to have a better trade-off between a combination of rigid and soft counterparts to support objective optimally. Electromagnetic actuation is widely been used to handle the movement of medical robots for decades now in the realm of biomedical field for its wireless, untethered and safe control. Along with this, soft magnetic material has an inherent property of high remanence like the permanent magnets to be used as a better regulated control [35, 39, 70]. Due to the non-linear relationship between electromagnetic torque and bending angle of the soft material, quantization of the magnetic field inside a deformable structure is a nontrivial problem to investigate [1]. In the paradigm of smart materials, magnetic fields and its field distribution have been studied, tested and used in biomedical systems such as magnetic sensors, magnetic nanoparticles for MRI and multifunctional drug releasing polymers [69]. In this chapter, we will focus on the fabrication and

H. Banerjee · H. Ren (✉)
Department of Biomedical Engineering, National University of Singapore, Singapore, Singapore
e-mail: ren@nus.edu.sg

H. Ren and J. Sun (eds.), *Electromagnetic Actuation and Sensing in Medical Robotics*,
Series in BioEngineering, https://doi.org/10.1007/978-981-10-6035-9_3

development of flexible polymer materials in an adaptable manipulator which will be magnetically actuated [52, 97].

1.1 From Magnetorheological (MR) Fluid to Magnetorheological Elastomer

The magnetorheological fluid is kind of a smart and controllable materials by mixing ferromagnetic particles in oil or water [40]. Under the magnetic field, the viscosity of the fluid changes and it becomes a viscoelastic solid. The MR fluid is affected by the difference between an elastic modulus with applied magnetics fields (on-state) and the same modulus with no field applied (off-state). The factors affect the MR effect includes the matrix's elastic modulus, the magnetic properties of the particles, size and concentration of the conductive particles [47].

To understand more in detail of the MR fluid, there is an inherent necessity to understand the inherent mechanics of the materials with magnetic micro particle (mostly in 1–10 micron range) (Table 1).

1.2 MRF Mechanical Dynamic Behaviour

When there is no electromagnetic field applied to the MR fluid, this behaves almost similar to the Newtonian fluids. Therefore, a simple Bingham model is well suitable to describe the dynamic behaviour of the field-dependent fluid characteristics. On the contrary, in the context of non-Newtonian fluids, Bingham plastic model will behave such as to increase the yield stress before there is any sort of flow imparted [16]. Along with the current scenario, there are numerous models been presently studied as referenced herein [12, 100]. Along with the line of Bingham model, the shear stress strain curve follows the behaviour as described [40].

Table 1 Summary of the properties of MR fluids (Data depicted from [40, 58]).

Property	Typical value
Initial viscosity	0.2–0.3 [Pa s] (at 250C)
Density	3–4 [g/cm^3]
Magnetic field strength	150–250 [kA/m]
Yield point	50–100 [kPa]
Reaction time	Few milliseconds
Typical supply voltage and current intensity	2–25 V, 1–2 A
Working temperature	−500 to 1500 °C

1.3 Magnetorheological Elastomer [MRE]

MR Elastomer consists of polymer media like silicon or natural rubber with materials that can be polarized. MRE exhibit similar characteristics to that of MR fluid but the MR fluid operates at post yield region whereas MR elastomer operates at pre yield. The major shortcomings faced by MR fluids like the contamination, deposition of iron particles are overcome by MRE [40]. There are various classification of MRE based on the distribution of particles, structure, electrical and magnetic properties (Fig. 1).

During curing or crosslinking of matrix, magnetic field is applied to the polymer composite. This would lock the particles in a columnar chain structure making it anisotropic [58]. When the field is not applied, the iron particles are randomly oriented making it isotropic. The choice of curing the elastomer composite is purely dependent on the type of application. Due to this columnar structure in anisotropic material, there is a low dipolar energy state. Shear modulus and the work required to displace the particle from the low energy state will require higher magnetic field.

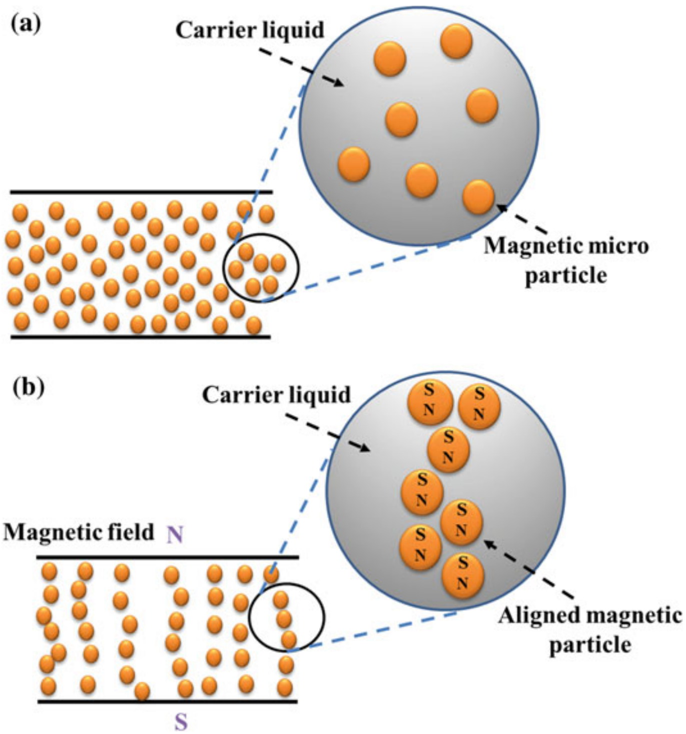

Fig. 1 MR fluid with and without magnetic field. **a** Without an external magnetic field **b** With introduction of an external magnetic field to align the magnetic micro particles.

1.4 Magnetically Responsive Stiffness Tuning in Flexible Manipulators

The advantages of flexible polymer materials with advances in refined magnetic actuation can be combined for a promising platform to work on a resilient, adaptable manipulator for a range of biomedical applications. In this realm, there are published report where microelectro-mechanical systems (MEMS) are embedded in magneto rheological polymer for different motion control [42]. In the regime of magnetorheological elastomer (MRE), experiments shown to have optimal magnetic effect with 60% carbonyl iron particles content mixed in an anisotropic solution of silicon rubber and silicon oil mixture [30]. To further optimize the whole magnetic system, researchers came up with a particle model with the help of finite element model (FEM) analysis to counteract the conjunction of ferromagnetism with viscoelasticity [60].

2 MRE for Biomedicine

MREs have the actuation properties close to that of natural muscles while the same principle can be extrapolated for peristaltic devices like micropumps. Apart from artificial muscles, MREs can also be applied widely in drug delivery as the principle mechanisms of TDD devices also based on fluid pump functioning. In the realm of drug delivery, recent advances mostly concentrated in controlled drug administration where magnetic field can take a promising action [47]. So to understand and administer in depth MRE controlled action, it is needed to appreciate the mechanical system more aptly as briefly described herein (Fig. 2).

2.1 Properties of MRE

MRE properties strongly depends on the magnetic field strength. There is a change in shear modulus and stiffness when the MRE materials are deformed [72]. Their response rate is usually in order of millisecond.

Properties of MRE materials depend on various factors.

(1) The shear or elastic modulus, density is due to the material properties of the elastomer matrix
(2) The magnetizable property depends on the micron-sized particles selected.

Hence, it is highly important in choosing the materials for MRE. The type of material used for the elastomer matrix will highly determine the viscoelasticity of MRE. Using ferromagnetic particles of size $<1.5\ \mu$m and assumed to magnetize uniformly. In these materials, the maximum change in modulus or stress for maximum

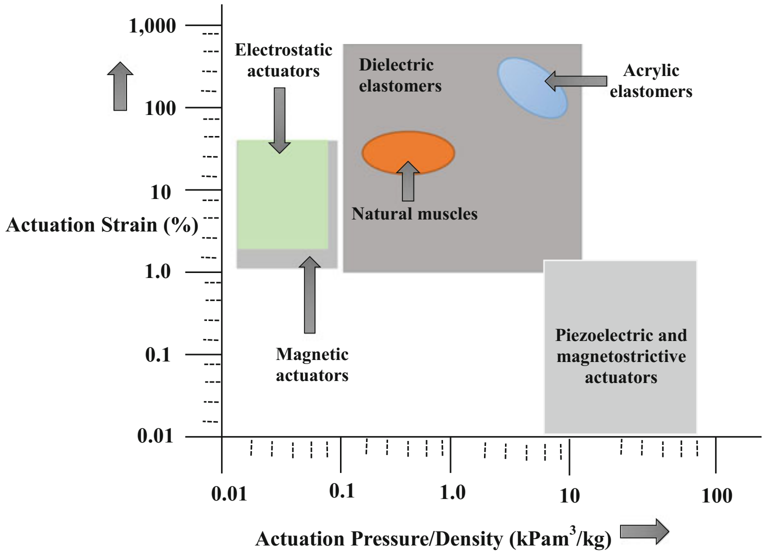

Fig. 2 Different regime of soft actuators and natural muscle [4].

magnetic field applied occurs when the magnetic particles in the MRE are saturated. The pure iron and alloys of iron exhibit this property and cobalt as these materials has high magnetic saturation. In most of these MRE materials, modulus has a significant increase when the stress applied is parallel to the magnetic particle in the elastomer and also anisotropic MRE materials exhibit a higher increase in modulus than randomly oriented magnetic particle.

The main factor that determines the property of MRE is the type of the ferromagnetic materials used like the percentage volume, type of distribution, the shape and size of the particle. It is observed that there is a low core loss and eddy current loss within the MRE.

2.2 *Change in Property Under Magnetic Field*

Properties of MRE materials like elasticity, plasticity and viscosity depends on the applied magnetic field. This study of deformation of the material under the magnetic field is required for its application. These variables can be controlled by the use of changing magnetic field. According to research result, for applied magnetic field of 0–0.3T, the range of shear strength of the material varies from 2–3 to 100kPa. There is also an influence on the composite properties due to the alignment of magnetic particles with or without external magnetic field [46]. For both anisotropic and isotropic MREs, the material properties like the stiffness and damping can be altered using an external field. With the applied magnetic field and optimizing the alignment of particle and density, the damping or the stiffness can be increased [8]. For isotropic material, the increase in stiffness or damping can be observed in applied field if the volume fraction of the filler like the iron exceeds 15% [8]. For typical elastomer, the shear modulus increase due to the magnetic forces of the inter-particle is almost 50% to the zero field shear modulus. Hence from this, the shear modulus of elastomer which are cured in the presence of magnetic field, i.e. anisotropic is no larger than the shear modulus of the same elastomer with randomly distributed particles, i.e. isotropic [99]. From various research, 27% of volume fraction of iron particles was predicted to be optimum value [36, 98].

2.3 Flexibility and Tunability

Susceptibility (or permeability) of different types of magnetic elastomers (e.g. difference between magnetic properties of elastomers with magnetic particles, phase composition) changes greatly with the electric field potential. For example, in AC magnetic fields, iron particles are continually conductive and hence heating of the devices increased up dramatically. This was due to the heating via absorption of AC magnetic field, MRE resulting in hyperthermia processes. On the contrary, high-intensity DC magnetic fields lead to hard magnetic filler, which further results in changing anisotropic properties and overall matrix elasticity.

Carbonyl iron micro particles have the highest possible saturation magnetization and high particles loading which is established up to 75 wt % with respect to polymer [28]. The relationship between saturation magnetization is that it increased linearly with particle concentration increasing. The soft magnetic and soft mechanic elastomer with 50 wt % Fe exhibited 90 emu/g saturation magnetization and 80% elongation in magnetic field of 1 T and stronger.

2.4 Sensitivity to the Magnetic Field

Thus, sensitivity to the magnetic field is important for description of the elastomer behaviour. It is of interest to compare susceptibilities (or permeability) of different types of magnetic elastomers obtained by different methods. The differences between magnetic properties of the elastomers with magnetic particles and magnetic properties of the powder of the same particles can indicate the phase composition of the composite material under investigation.

Sensitivity of the materials are governed by many distinct factors such as permeability of different type of elastomers, percentage of iron particles and voltage supplies. For example, permeability of different type of materials are affected by the geometry of the fabrication and thickness of the elastomers. The volume of iron particles, particle size, particle shape and the alignment of the iron particles inside the elastomer affects the sensitivity of the materials to the magnetic field, which in turn affects the magnetic actuation and the sensing mechanism. In addition, reports experimentally demonstrated that there is a steep difference between pulsating magnetic fields and time-independent magnetic fields and there effects therein [18, 78]. In AC magnetic fields, particles are continually conductive and this will result in the heating up the devices dramatically [18, 78]. The MRE will be heated up by absorbing the AC magnetic fields which results in hyperthermia processes [81, 82]. However, the high intensity of DC magnetic fields lead to the change anisotropic properties and overall matrix elasticity of the hard magnetic fillers inside the elastomer.

2.5 Electrical Conductivity

The current MRE materials are made of Eco-flex silicone rubber or Polydimethylsiloxane (PDMS) which do not conduct electricity [62]. This is due to the fact that the silicone and the oxygen atoms will form strong covalent bond in the giant covalent structure. Thus, these elastomers could behave as good insulators. In our work, the MRE is made of iron particles and silicone rubber. The researcher attempts to make use of the presence of iron particles, which could make the elastomer to be electrically conductive. The researcher makes a perception about the varying the percentage of iron particles will affect the electrical conductivity of the materials. Other than that, the researcher also precepts that the presence of both electrical field and magnetic field will create a motion. This could be further investigated in making a force sensor. The following fabrications have been done to improve the properties of the new materials, which includes the flexibility, sensitivity and electrical conductivity.

2.6 Viscoelastic Property

Viscoelasticity is the property of material that exhibit both viscous and elastic characteristics when undergoing deformations. Viscous materials like honey resist shear force and strain linearly when stress is applied [27]. On the other hand, elastic materials come to their original configurations when stress is been removed. Viscoelastic materials have elements of both of these properties and as such exhibit time-dependent strain where elasticity is usually the result of bond stretching crystal-like graphic planes in an ordered solids [27]. Viscosity, on the other hand, is the result of the diffusion of the atoms and molecules inside amorphous materials. When MREs are exposed to an external EM field, the shear modulus of the material can be represented in a combination of two different parts (i) Shear modulus for its own polymeric nature (G0) (ii) Shear modulus caused due to the external magnetic field (G1). While G0 corresponds the material intrinsic property, G1 changes with the external magnetic field strength [13]. As the external magnetic field intensity increases, the value of G1 increases. This increasing trend signifies higher rigidity and less ductility.

3 Electromagnetically Responsive Soft-Flexible Sensor for Biomedical Applications

Although safe and favourable technology, due to the non-linear relationship between electromagnetic torque and bending angle of the soft material, quantization of the magnetic field inside a deformable structure is still a nontrivial problem to investigate [1]. In this realm, we propose a novel soft-squishy, flexible force sensor approach for active tactile sensation that utilizes soft morphological computation [51, 64]. This research is motivated by hominoid finger's extraordinary combination of fibroblast bone tissue and flexible muscle for grabbing and sensing effective force feedback while gripping a delicate, fragile object in real-time environment [86, 87]. We intend to create an electromagnetically driven tactile sensing system that will be an integration of actuation (magnetorheological paradigm and electromagnetic) and sensing elements (electrical conductivity). The main idea of this proposal will be to have a comparative study with electrical conductivity to address the value of stress generated by the human finger with close proximity. This device when actuated will change its morphology/stiffness and generate electrical stimulus transitions for different posture of embedded sensing. As a result, the proposed device can be proactive in sensing tasks depending upon the EM field variations. Conclusively, this work will be an example of soft morphological control in sensing, and projected to open a new trend in development of tactile sensing system for medical rehabilitation device and therein [90].

The proposed prototype is a three-dimensional structure composed of a sensing coil which is fabricated using natural rubber to be used as a soft-flexible bend sensor for medical applications. The sensing coil mainly acts as an antenna, which is subjected to varying magnetic field and in turn generates electrical signals. The strength of the signal depends on the area of the coil, thickness, number of turns and the magnetic core running through the windings of the coil. The strength of the magnetic field applied to the coil would also determine the strength of the field generated.

FIGURE: Overall Objective of the whole project.

3.1 Material Fabrication

Based on the types of curing process, MR elastomers can be attributed in two distinct categories as (i) Isotropic MR elastomers and (ii) Anisotropic/Aligned MR Elastomers. For each of these two categories, silicon oil, silicone elastomer and carbonyl iron particles are mixed homogeneously to form a viscous liquid. The entrapped air bubbles need to be desiccated minutely in either vacuum chamber (preferably) [37, 83] heat treatment [48]. For isotropic elastomer preparation, the predefined viscoelastic liquid is cured without a magnetic field. On the other hand, anisotropic elastomer needs a higher magnetic field [normally higher 0.8 T] [21, 48, 75] as to align the magnetic particles in some ordered manner.

In our proposed methodology for biomedical force sensor, the copper coils are fabricated in different configurations by varying the number of turns and magnetic permeable core to compare the strength of electric field induced and the inductance of the coil [25, 26, 45]. Three different configurations were tested on the sensing coil having turns of 50, 100 and 150 by changing the core from air to hard grade carbonyl iron micro particles and 3M flexible magnetic strip. The fabrication process involves coiling of 0.25 mm copper wire in the form of solenoid keeping the length, thickness and area of cross section of the material constant for all three configuration. The outer layer of the sensing element is soft and fabricated using a cylindrical mould. The soft material (Eco-flex 00–309a natural rubber) mixture is poured in to the mould. To remove air bubbles, the mould is placed in a vacuum chamber for 5–10min. Next, the mould is placed in an oven for about 90 min at 80 °C for curing. Then, the part is removed from the oven, and the mould is removed. It can also be fabricated by leaving the mould at room temperature for about 4 h. The elastomeric structure formed after curing improves the flexibility of the coil provides a better insulation to copper windings and preserves the shape of the solenoid coil when bent or flexed at different angle. A multiple layer of silicon coating is provided by the same method of fabrication as described above for making the device robust under different working conditions. The working principle of this sensor is based on the displacement of the iron core when bent through a certain angle as shown in Fig. 3. This is because the inner curvature of the coil windings remain in contact and the outer curvature is displaced with respect to the amount of bending.

The coil will have a variable inductance when subjected to bending which can be mapped to the displacement and the angle of bending. By calculating the inductance change based on the displacement the amount of bending can be determined. Hence, the sensing determines the angle of bending by measuring inductance and displacement of the pitch in the helical coil by the application of variable magnetic field [11]. Figure 4 shows the bending in applied magnetic field.

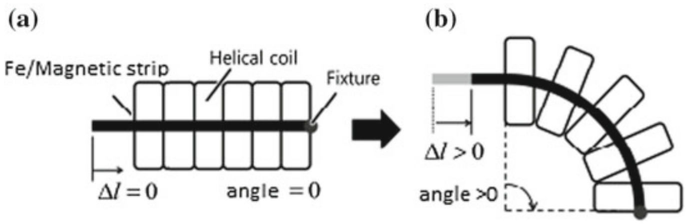

Fig. 3 Sensor working principle **a** when straight **b** when bent.

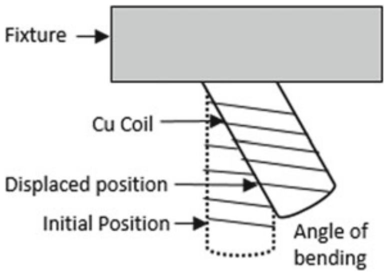

Fig. 4 Bending of the sensing coil in applied magnetic field.

3.2 Summary of Actuations in Soft Robotics and MRE

In the field of actuation in soft robotics, there are different regime of actuations. The pneumatic actuation is still widely used in soft robotics. On the other hand, there are very few well-characterized soft materials, which can be used extensively for the 3D printing—therefore, the field of soft robotics is a fertile land for future chemists to discover new polymers. To make this polymers work for a suitable desired task in most optimum manner, a well-qualitative direct actuation performance comparison is a must choice. In Table 2, we unveil the classification of actuation methods with traditional approaches like motors and cables for the sake of completeness [5].

In our proposed research for MRE-based force sensor, fabrication in making a humanoid hand-like gripper will show the advantages and disadvantages. Based on the prototype, we need to come up with the idea to make smart materials which could show magnetic actuation. In this work, silicone elastomer materials is developed to achieve the bending movement under a magnetic field. These smart materials are different form Magnetorheological elastomer (MRE) or magneto- responsive/active elastomers (MRE) materials. This new type of materials is able to conduct electricity upon actuation. It supposes to change its conductance when a force is applied on the materials. Thus, it is able to work as a sensor in future premises.

3.3 Results and Discussion: An Initial Study

An initial study related to bending flexible force MRE sensor is conducted using the finally fabricated elastomer that consists of a copper coil, iron particles and silicone rubber (details mentioned in the experimental section). In this part, we have tested the voltage difference/drop across the flexible MRE coils when bending the elastomer in different angles. To investigate more into the mechanical property paradigm, we underwent compression and tensile expansion test (Instron UTM), and recorded voltage drop across the elastomer. The experimental setup shown in the

Table 2 Type of actuations and their advantages *and* Challenges (H—High M—Medium L—low) (Data depicted from [5]).

Type of actuations	Motor	Shape-memory alloy (SMA)	Shape-memory polymer (SMP)	Dielectric elastomeric actuators (DEA)	McKibben pneumatic artificial muscles (PAMs)	Fluidic elastomeric actuator (FEAs)
Materials of use	Metals/alloys	Copper–aluminium–nickel and nickel–titanium(NiTi)	Ploy(urethane)-based thermoplastic	Silicone and Acrylic Elastomers	Fibre braid	Synthetic elastomeric films
Operating physics	Cables pulling for flexible bending	Electrical current induced Joule heating	Polymer	Electrostatic force of application	Gas chambers	Chamber network
Stress	M/L	Wires: high; Springs: medium/low	M	M	M	H
Strain	High (H)	M	M	H	H	H
Power density	Medium (M)	H	M/L	M/L	M/H	H
Scaling dimensions	Low (L)	H	H	M/L	M/L, mainly because of the pneumatic pumps	M/L
Response velocity	H	L	L	H	H	M/H
Advantages	Ease in assembly/disassembly, light moving components and low cost	High mass specific force	Less weight per unit volume of material, reversible change of elastic modulus, ease of processibility, lower cost	High strain/stress and mass specific power	Soft fabrication, quick actuation, easily integrated into three-dimensional soft actuated materials	Operated both pneumatically or hydraulically, versatile fabrication approaches to embed fibres
Challenges	Non-linear behaviour, unidirectional constraint that can only pull and not push, undesirable disturbances lead whole system uncontrollable	Relatively low (nearly 5%) strain, force generation in SMAs depends on temperature change, overheating or overstraining can cause permanent damage to the actuator	Low modulus	Requires a rigid frame for prestrains the elastomer, reliability of the compliant electrodes needs improvement. DEAs actuation requires high voltage	To achieve relatively high forces and displacements, they required high power and complex compressed air supply systems, friction between bladder and the mesh also contributes to actuator hysteresis.	Slow actions

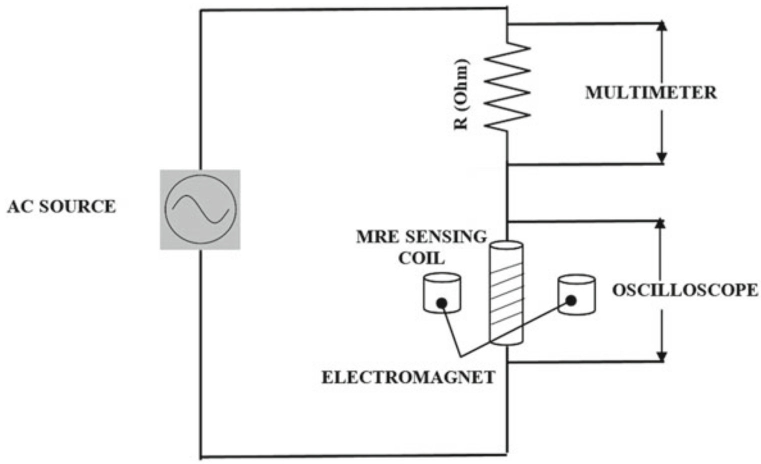

Fig. 5 Schematic of the experimental Setup.

figure includes AC Signal generator, oscilloscope and resistor to prevent our sample from short-circuiting to the supply (Fig. 5).

The principle idea behind this result and discussion subsection of this chapter is to have a comparative study with electrical conductivity to address the value of stress generated by the human finger with close proximity. To illustrate more in this paradigm, in future we will have different materials like Eco-flex, PDMS and conductive foam, Hydrogel etc. to characterize and get the comparative study with the amount of precision it can attain for force sensing. The output of electrical conductivity will be compared with the stress strain analysis (INSTRON UTM) and thus we will reverse engineer the whole system to be rugged and optimal for use in medical rehabilitation further (Fig. 6).

According to the preliminary experimental setup, when MRE elastomer is bent, the average maximum voltage across the elastomer will also change accordingly. The initial length of the MRE elastomer material is 4 cm long and the number of turns of copper coil inside the material varied from 50 turns to 150 turns. For this experiment, the frequency used is about 10 MHz. The following data are obtained from the bending angle and voltage drop across the MRE sensing coil accordingly.

Parameters	Dimensions
MRE sensing coil Length	4 cm
Diameter of the cylindrical MRE elastomer	0.56 cm
Series Resistor R	68 Ω
Supply Frequency	10 MHz

In the following experiments, we have tested preliminarily the change in voltage when bending the elastomer in different angles. In this experiment, the initial position

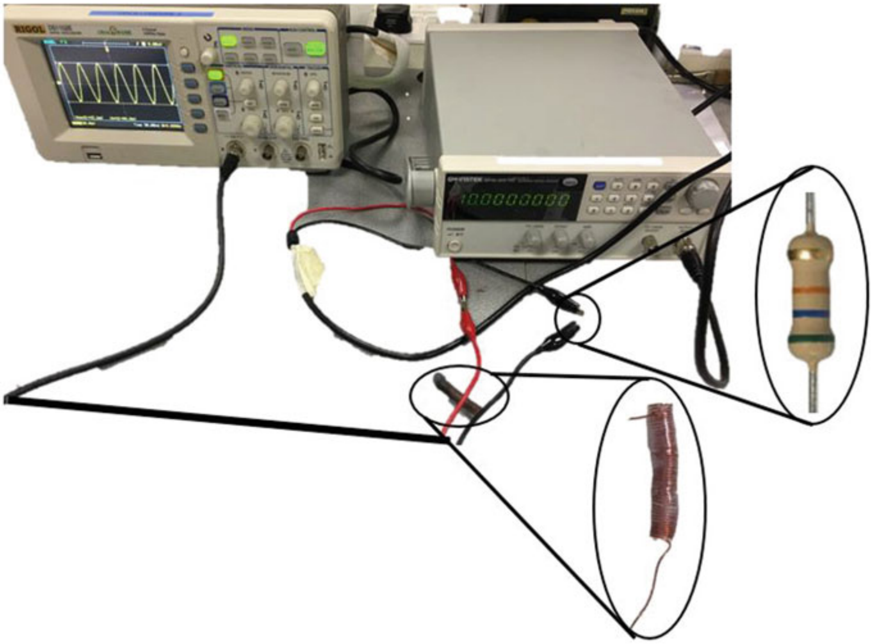

Fig. 6 The experimental setup.

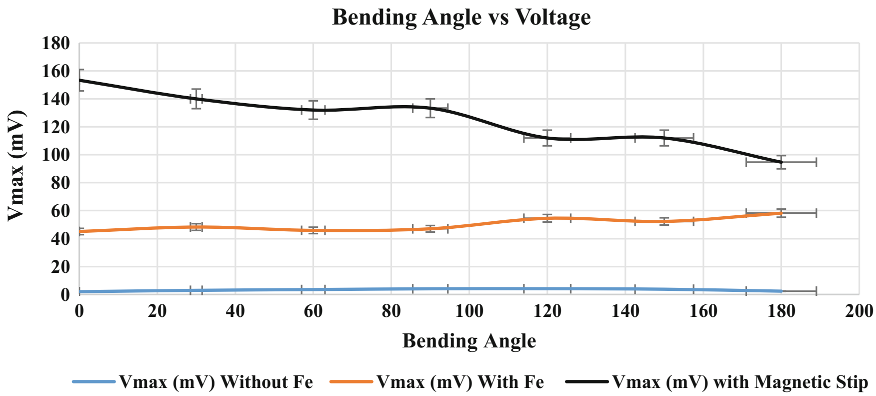

Fig. 7 Bending angle versus voltage—Average value comparison of samples with N = 50.

of the material is in a straight line, at this position, we assume the bending angle is 0 degree. The material will be bent clockwise each time and the voltage across the material will be recorded. Here we have investigated magnetic field strength in correspondence to induced voltage in the coils with three different perspectives as (i) without iron particle (ii) with iron particle and (iii) with introduction of a magnetic strip (Figs. 7 and 8).

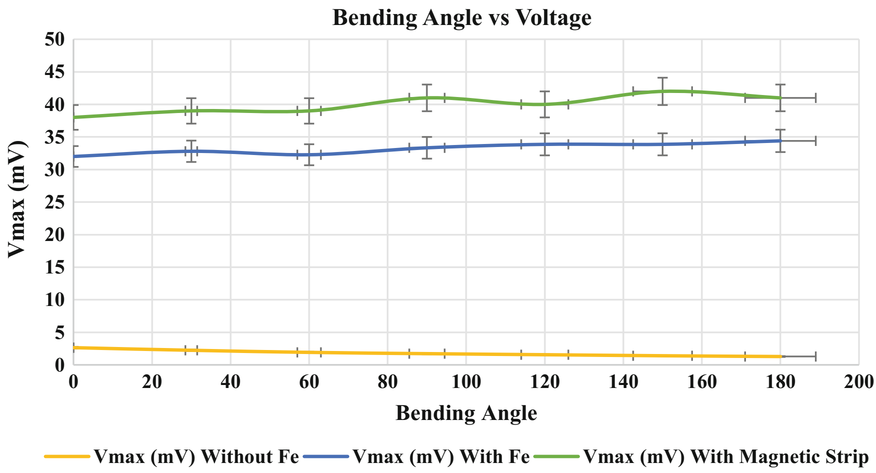

Fig. 8 Bending angle versus voltage—Average value comparison of samples with N = 100.

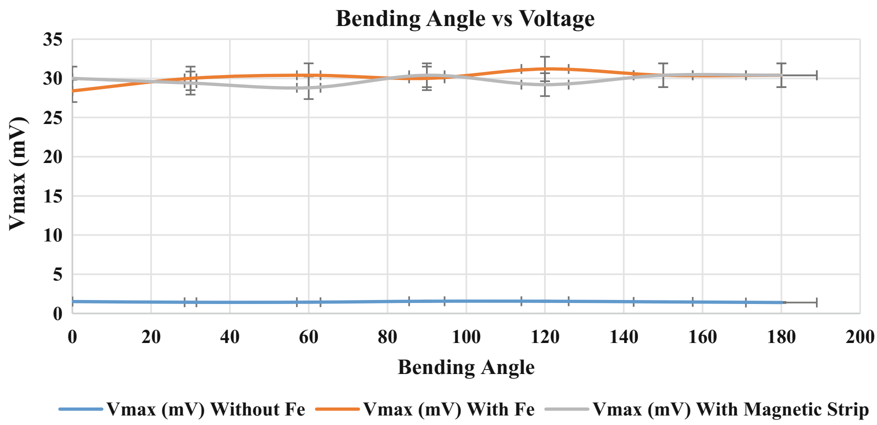

Fig. 9 Bending angle versus voltage—Average value comparison of samples with N = 150.

With the changes in the mechanical property, the EM induction also changes and in turn change the inductance of the MRE elastomers. We have calculated inductance when the coil possess only turn 50 as hereunder (Figs. 9 and 10).

From the above plots, we can extrapolate an understanding that when there is a tensile expansion force applied on the MRE-based sensing coil elastomer, the voltage across the elastomer increases exponentially and it will show a larger voltage difference across the elastomer. However, when there is a tangential compressive force applied on the material, it will cause the decrease in the voltage drop across the elastomer and follow nearly a linear trend. By comparing the plot, it is understood that, when the compressive force is applied to the elastomer, there is a linear drop

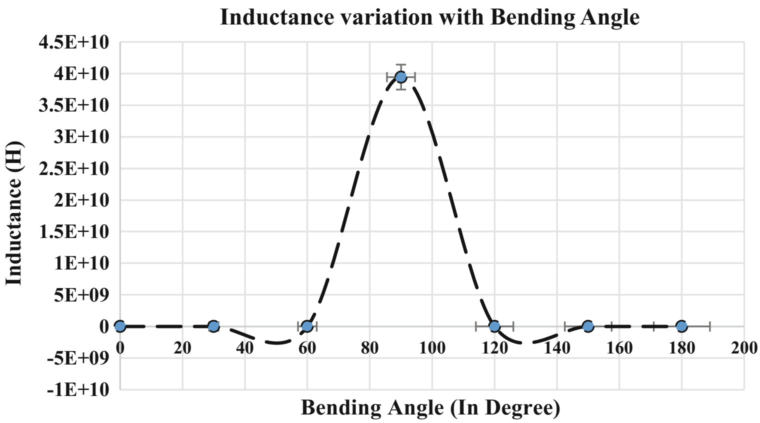

Fig. 10 Bending angle versus inductance—Average value comparison of samples with N = 50.

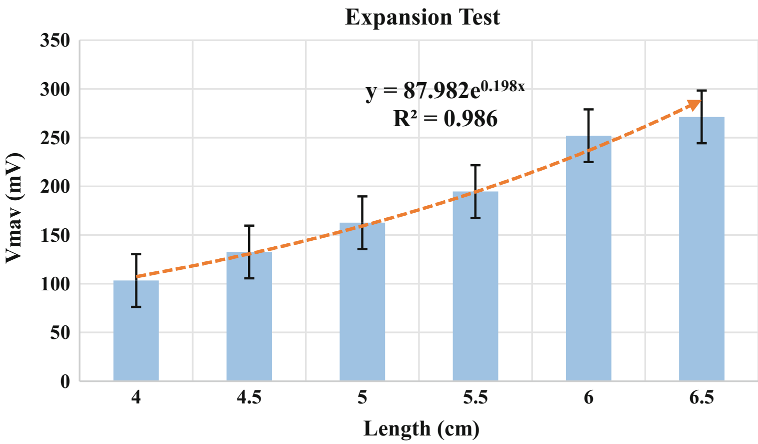

Fig. 11 When there is a tensile expansion force applied on the MRE-based sensing coil elastomer, the voltage across the elastomer increases exponentially and it will show a larger voltage difference across the elastomer.

in voltage as compared to the tension force. This shows that for our fabrication, it is more sensitive to apply compression for it work as a force sensor (Figs. 11 and 12).

3.4 Recommendations and Future Works

In this proposed research, we aimed to fabricate a new kind of MRE elastomers, which could both generate small movements under magnetic and electric field. This elastomer is believed to work as a sensor to detect the bending angles and movements.

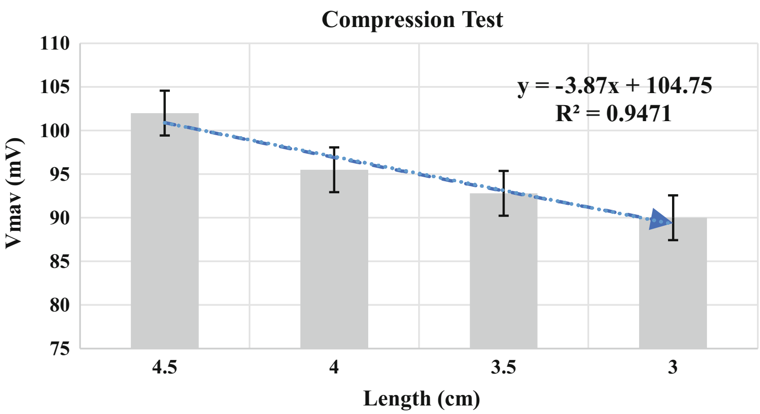

Fig. 12 When the compressive force is applied to the elastomer, there is a linear drop in voltage as compared to the tension force. This shows that for our fabrication, it is more sensitive to apply compression for it work as a force sensor.

The novel approach we have implemented herein is to use copper coil and iron particles for material fabrication to be implemented in a thin cylindrical silicone rubber layer. Compared to normal MRE materials, our approach is sensitive towards both electrical and magnetic stimuli and conductive therein. The fabrication process deployed herein is simpler solution and can be downscaled in the laboratory as per demand. We believe our setup to be conductive for flexible force sensor and thus can be implemented in medical industry and flexible wearable electronics research further. In addition to our preliminary approach the process of fabrication is cost effective and yet resilient to external electromagnetic force. By implementing our fabricated MRE elastomers in rehabilitation glove, it can work as an improvised sensor to help patients to exercise their fingers (Figs. 13 and 14).

In order to increase sensitivity of the elastomer, in future we intend to reduce diameter and hence weight in general for tracking minute differences in results. This in turn will provide a large magnetic field within the coil, which will results in the better bending motions. In addition, the copper wire that is used to make the coil is very soft which could easily deform under as strong force. Thus, a better material with the similar properties of copper wire will be chosen to make the coil. In parallel, we intend to design the MRE sensor embedded with soft skin layer and strain gauges that covers onto another soft substrate sandwiched in between [95]. The results with the strain gauges will characterize the sensor for customized rehabilitation applications. Along with this we are in a process to include conductive ink channel for same design and calculate the change of the conductivity with changing materials from composite to MRE different sample(s).

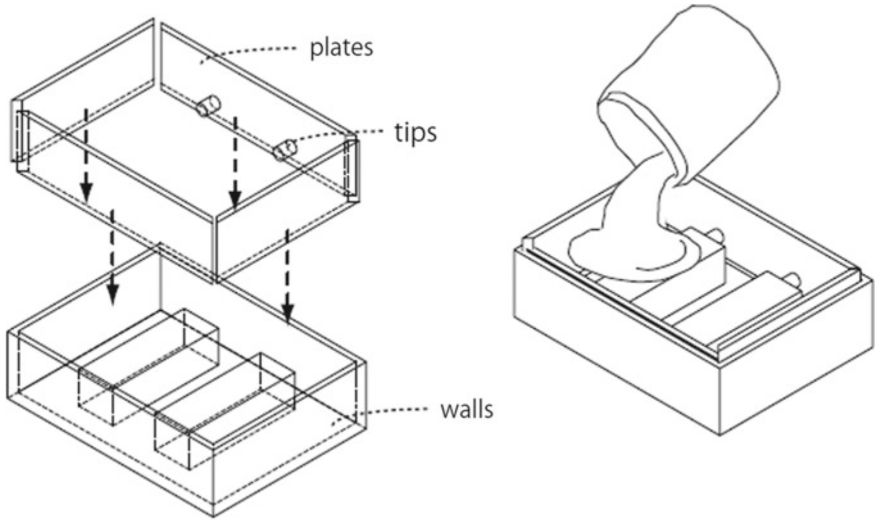

Fig. 13 Design of the sensing system prototype.

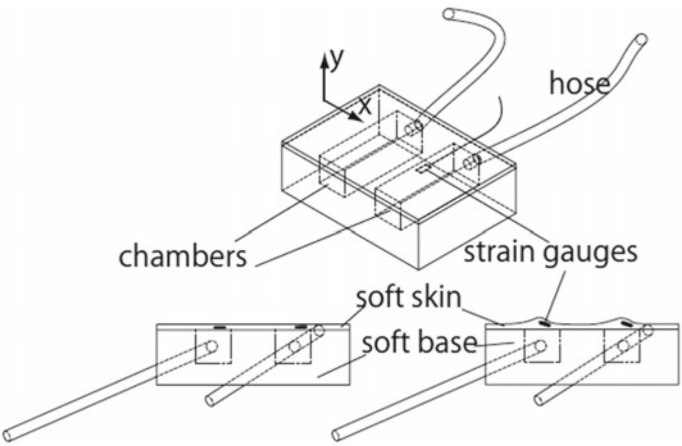

Fig. 14 Design of the sensing system prototype.

4 Proposed Design and Future Perspectives

MRE typically made with iron micro particles (~5 μm) immersed in silicon can be made softer with silicon oil. Application of a magnetic field can modulate the stiffness of the material [6]. Here exploiting geometry, we propose a saddle shape for MRE. We intend to build the saddle volume around 260 mm^3, which will fit in a 10 mm voxel comfortably. A similar volume cube will be of 6.3 mm voxel, which will exploit higher efficiency in iron particles exposed to the magnetic fields. For optimal control, changing V/V % of iron powder will affect the stiffness properties which further will allow the sample to more efficiently utilize the source B field (Fig. 15).

When we propose to apply magnetic field (B) in one direction, the magnetic micro particles will be attracted and will not only attempt to align with the magnetic field but also be attracted (gradient) towards the source permanent magnet, hence non-uniform fields. This anisotropic attraction will cause tension build up in the saddle and if we were to consider the force measurements in the orthogonal direction, this stiffness of the material should be a result of the tension induced (Fig. 16).

The uniqueness of the design is hypothesized as follows: If we apply a magnetization field in X direction where the edges of the saddle will experience a stronger magnetic field as it moves towards it [7]. Compression and tension in the Z direction should be stiffened due to the tension. The response in Y should be more special, however, compression is resisted while tension is promoted.

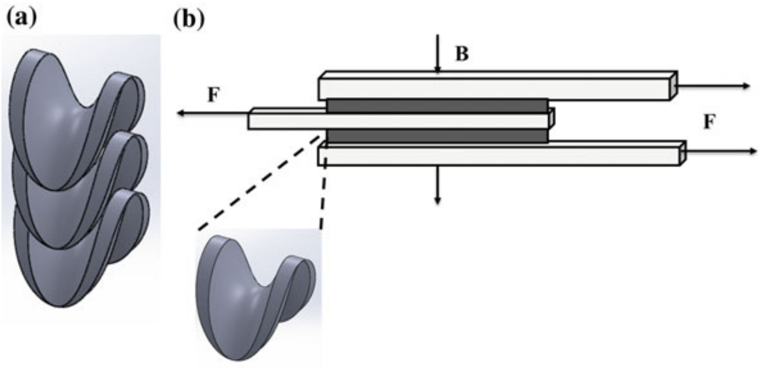

Fig. 15 MRE design exploiting geometry. **a** The design paradigm of the saddle shape MRE. **b** The aligned magnetic particles will attempt to align with the applied fields and resist shearing. Field/Flux alignment is used here to achieve stiffness modulation. The saddle should be able to achieve the same.

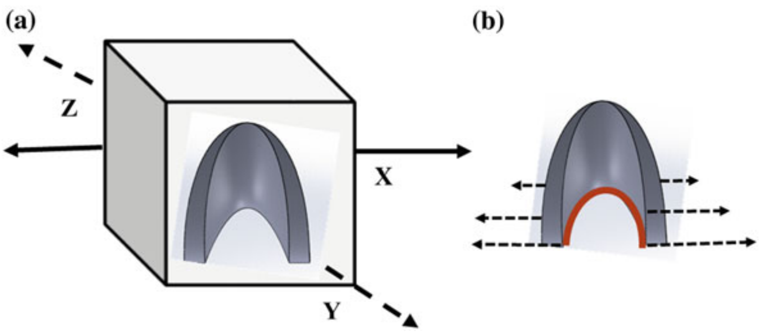

Fig. 16 The force (F) acting on a saddle in a (**a**). Three-dimensional component (**b**). The resultant stress developed in the saddle MRE material.

4.1 Magnetically Modulated/Controlled Soft and Flexible Surgical Robot

So far, the most common mode to control flexible surgical robots is teleoperation, which establishes the mapping between robot motion and movement of a master device [67]. However, the surgical robots can merely be roughly guided to the desired surgical sites with weak obstacle avoidance capability via teleoperation [66]. More precise pose control as well as the motion compensation ability are in demand to strengthen the safety when manipulating the robots during surgical procedures. To better guide the flexible surgical robots to the desired surgical sites and accomplish allotted tasks, the motion planning of the robots can be implemented first to control the robot to roughly reach the surgical sites following an obstacle free path while the visual servoing control mode can be switched on to achieve the finer pose adjustment as well as motion compensation [77]. In addition, the design and motion planning of flexible surgical robots can be assisted by the construction of statistical atlas, which contains information about the average shape and shape variation of a group of patients. This would, further guarantee and improve the performance of robots.

4.2 Magnetic Motion Planning Control (Multiple Targets)

As introduced above, flexible surgical robots are mostly controlled by teleoperation to move from one place to another. However, teleoperation can only control the position of the end effector without considering the movement of the robot body. The unexpected motion of the robot body is likely to cause harm to the patient if the robot body collides with tumours, critical blood vessels, tissues, etc. [59]. Therefore, motion planning is necessary to determine the safest and optimal paths for flexible surgical robots. These robots are desired to manoeuver along the central axes of the cavities in order to maximize the path clearance and better ensure the safety of the navigation. This goal can be achieved by incorporating the centerline extracted from statistical atlas into the motion planning algorithm. Moreover, the motion planning algorithm can be applied using different parameters of the robot [76]. By evaluating the reachability and path quality, the appropriate parameters of a flexible surgical robot can be decided. That is, the motion planning algorithms can assist the optimal designs of flexible surgical robots as well. Furthermore, it is quite hard for some classes of flexible robots, such as the concentric tube robots, to follow the leader. However, by considering the shape constraints of these robots when implementing motion planning, approximate follow-the-leader behaviour of the robots can be achieved. This is quite favourable in minimally invasive surgeries and emphasizes the significance of motion planning. Although only offline motion planning algorithm has been developed in this thesis, the online re-planning process also needs to be worked out in the future based on the real-time feedback from either the visual sensors or electromagnetic (EM) trackers.

5 Forthcoming Challenges and Future Work

A steady hand of a doctor is controlling the machine, with magnets held just above the person on the operating table. When the snake robot is at the right spot, the doctor uses the magnets to release vital drugs right where they are needed.

We are not totally there yet, but the above is not all science fiction—researchers around the world have been developing such soft robots for the past several years. In March 2017, engineers have made a big step forward in controlling soft robots—using magnetic fields to remotely move iron chains made up of tiny particles embedded in the machines. A team of researchers from North Carolina State University (NCSU) describing their research, says that using self-assembling chains that consist of iron micro particles means they can get the simple robots to perform more complex functions [73]. This could one day lead to soft robots used as remotely triggered pumps for drug delivery or robot structures that can be remotely deployed when needed for things like disaster aid, as described by them.

In the near future, we believe the onward research in this soft-flexible robotics regime will be able to advance surgery and medical treatments, while other kinds of autonomous soft robot designs can explore the real world, safely, close to humans, in a way that traditional metal robots cannot. However, researchers still need to solve a set of big challenges: how best to power and control these squidgy machines and many more as described hereunder.

5.1 Material, Design and Fabrication Challenges

The transition from a hard conventional robot to its soft counterpart depends on its underlying materials [85]. The materials, and spatial orientation of the materials, used for soft robots allow for deformable, dexterous, soft interfaces, but the fabrication process poses a challenge for robotic engineers. Currently, soft robotic researchers frequently use state-of-the-art 3D printing and soft lithography fabrication techniques [9, 15, 50, 92], stretchable electronics with wavy circuits [44, 71], soft microfluidic channel with conductive liquid [14], highly stretchable smart textiles, wearable computing, etc.

The next challenge is to 3D print active, multi-material components into a single packet for final use [19, 55, 91]. Though this 3D print technology revolution puts a milestone in the scientific community, it should be mentioned that unlike conventional rigid robots, soft robots require design and manufacturing from scratch, which makes knowledge transfer critical. For example, there are very few well-characterized soft materials which can be used extensively for the 3D printing—therefore, the field of soft robotics is a fertile land for future chemists to discover new polymers. To make this polymers work for a suitable desired task in most optimum manner, a well-qualitative direct actuation performance comparison is a must choice.

5.2 Computation and Control Challenges

In comparison with rigid, inflexible, conventional robots, soft robots theoretically possess infinite DOFs making control extremely challenging. The materials used for soft robotics are generally non-linear in nature which makes it exceedingly difficult to predict the empirical coefficient which can mimic the experimental non-linear elastic behaviour, damping coefficients, interfaces between materials, and friction [49]. As soft materials are continuous and deformable [34], the optimal control of the new generation of soft robots needs the state variables of body posture, which are missing since the design parameters are continually changing with deformations, and difficult to address with classical mechanics. The computations become even more difficult if the actuator is to generate optimum force and torque for a desired application. For example, electroactive polymers (EAPs) require very high voltage (in kV range) to operate, while low voltage ionic polymer metal composites (IPMCs) are insufficient to generate enough force and thrust. Pneumatic actuators need an extensive additional pressure infrastructure, while shape-memory alloy (SMAs) has serious trouble with overheating and surface damage. There is ongoing research in simulating continually deformable, highly compliant, flexible bodies using piecewise constant curvature (PCC) model [88], Bernoulli–Euler beam mechanics [31] for deformation prediction or inverse kinematic algorithm. Each of these standard approaches to modelling bio-inspired robotic systems comes with its own challenges. For example, PCC does not necessarily guarantee to incorporate all characteristics of soft robots, for which non-constant curvature model is being introduced recently [68]. On the other hand, inverse kinematics does not include the whole soft body and even the end effectors poses are not included in solutions. Though dynamic modelling somewhat mimics the high deformation of soft materials, interfacing control will be a great challenge as it requires a model-based prediction. So as dynamic modelling progresses, there is a great need to update control algorithms to fit real-time, complex situations.

5.2.1 Control Solutions

Controlling medical devices using magnetic fields is not a new concept and has been explored by a number of researchers. For example, teams at Vanderbilt University in the USA, the University of Leeds in the UK and in Scuola Superiore Sant'Anna in Pisa, Italy, all looked at steering and moving capsule endoscopes [17, 41, 57, 74, 80]. Researchers at the Chinese University of Hong Kong have also magnetically steered micro-robotic swarms [93, 96].

Typically, an autonomous robot must have a basic body structure, sensors, a central control system (microprocessor), actuators (motors), a power supply and a programme for its behaviour. Building a body from soft materials, like polymer, can be done by casting, injection moulding and 3D printing. Sensors and microprocessors can now be manufactured small enough to be embedded inside a soft robot without compromising its flexibility. Electronic components too can be made flexible or even stretchable. However, traditional electric motors cannot be shrunk down and embedded in the same way that sensors can, and they become less powerful the more you shrink them.

Hydraulic and pneumatic systems have been used to control soft robots but they have to be tethered to the machine—not so useful if you want a robot to travel long distances. Other options have been to use so-called soft actuators such as electroactive polymers (EAPs), macroporous gels and other phase-transition materials, but much more research needs to be done before they are effective motors. Some of the most widely used 'soft' actuators use threads of shape-memory alloy wires or foils. These are alloys that change their shape when they are heated, acting similar to muscles. So far, they have been found to be inconsistent, energy inefficient and easily affected by environmental conditions.

5.3 Energy Demand and Optimization Challenges

However, making sure these soft robots have enough power to move outdoors for hours upon end is not an easy task. Anything that is electrically powered must store energy in batteries or capacitors. Although these can be made relatively flexible, they are not widely commercially available and cannot store large amounts of energy. Researchers are instead turning to a biologically inspired solution: storing chemical energy in the soft robot and using it when needed just like fat is transformed into sugars, fats and proteins to provide energy for migrating birds.

The work [73] using magnetic field-driven soft robots is ultimately constrained. It would take incredibly large amounts of magnetic power to move larger soft robots out in the real world.

However, when it comes to autonomous soft robots controlled using the perhaps more promising approach of chemical reactions, the applications could be much wider. Robots with the muscle control and dexterity of animals and humans could be used for handling delicate items in warehouses or creating powerful exoskeletons for the elderly. The technology could even be used to create homes that could morph or change depending on its environment, like a soft robotic wall that could morph into different shapes when needed. Although it may sound far-fetched, with the field of soft robotics making strides every day, it should not be long before we start to see these ideas become a reality.

5.4 Emergence of Biobots: A New Promising Approach

The first development on hybrid bio-robots based on muscular cells have already made appearance in the form of proof-of-concept Muscular Thin Films (MTF) [79] or systems that can crawl, swim or grip [3, 20, 61, 63, 65, 89]. Most of these devices are based on cardiac muscle cells, which have the ability of self-beating, therefore reducing the need of a control mechanism [24, 89]. Nevertheless, a control of the frequency of beating can still be achieved by electric field or genetically modifying the cardiac cells to respond to a light stimulus [10, 63]. Cardiac muscle cells provide a suitable solution for proof-of-concept bio-robots or biomedical studies in heart-like constructs or organ-on-a-chip devices, since they are already differentiated into striated muscle cells. However, they are not the most convenient election for hybrid bio-robots, mainly because they contract continuously without the capacity of halting. Skeletal muscle cells do not present this problem and therefore are thought as a potential solution for hybrid soft robotics, but they have been proven more complicated to use than cardiac cells. They need to be seeded as myoblasts and differentiated into myotubes in a process that lasts several days. More developed and striated muscle tissues require the formation of sarcomeres for an optimal force generation.

Skeletal muscle cells have been used in MTF and in simple crawlers or swimmers [20, 65, 79]. However, none of these actuators discuss the formation of sarcomeric structures in their constructs, leaving only certain basic research studies to deal with that [29]. It has been shown that surface stiffness, electrical stimulation or mechanical strain can improve the development of sarcomeres [22, 23]. For instance, more mature sarcomeres can be obtained when the elastic modulus of the substrate is closer to that of real tissue. In relation to this, it has been reported that a second layer of myocytes can form well-organized sarcomeres, thanks to the mechanical compliance with the first layer of tissue [32]. Besides this, a 3D study of the formation of myotubes and striated muscle in 3D is still at a very early stage. In this regard, 3D bio-printing becomes a unique tool for the fabrication and study of well-developed muscle tissue in three dimensions as well as its integration with printable materials. Moreover, the latter could lead to the fabrication of 3D bio-robots that can produce greater power than their 2D-seeded counterparts. The state-of-the-art 3D bio-printer from RegenHU available at the institution and CELLINK's Inkredible+ 3D bio-printer already in possession by our group provide us with the necessary means for the fabrication of complex 3D Biobots. Furthermore, we will use this technique to pursue forward the study of 3D alignment of myotubes and sarcomere assembly, taking it from basic research towards real applications in the field of hybrid soft robotics and biomedical applications.

Due to the importance of the mechanical properties of substrates, a great deal of research has been carried out in the development of new hydrogels for the support or encapsulation of different kinds of cells. These materials often offer tunable mechanical properties by changes in their composition or cross-linking mechanism, making it possible to reach a better compliance and tissue-like stiffness [33]. They have also been nano-engineered with the addition of magnetic nanoparticles [94], nanofibers [43] or carbon nanotubes [2] to improve the alignment or excitation of myotubes, but it has not been pursued towards an application. 3D bio-printing has been used to obtain 3D structures of different kinds of cells encapsulated in hydrogels that are later crosslinked and it has been proven to be a biocompatible process, as well as suitable for cell survival, proliferation and differentiation [54]. Furthermore, complex architectures can be created with the help of sacrificial materials, such as hydrogels that can be removed after the construct has been crosslinked [38]. So in nutshell, the progressive research in biological cell energy stimulator will be an immediate alterative to high end energy demand and collectively in future be used as an energy harvester.

5.5 Commercial Challenges

Soft robots have great potential to be applied in industrial automation and health care realms. As per the prediction projected by ABI research, the market of personal robots may undergo a sharp fall from previous estimates to $ 6.5 billion by 2017 [53] which leaves engineers no choice but to focus more on cost-effective, flexible soft robots. However, this emerging technology has many challenges to overcome before it can be widely commercialized. First, it is extremely difficult for start-ups to sell directly to end users or to collaborate with large manufacturers, as they typically want to collaborate with companies, which already demonstrate an operational record of accomplishment and financial stability. Second, even if there is financial support for R & D and marketing activities, obtaining regulatory approval for medical applications takes a long time (5–10 years), which means investors need to commit to financial support for a long period.

There is no doubt that in the near future, market demand will influence the commercialization of soft wearable machines and medical robotics. Apart from manufacturing scalability, consumer interests and efficient and viable technical solutions, soft robots will face great pressure to be inexpensive and optimized to meet the steep market demand. The great advancement of electronics integrated chip (IC) and microfluidics network in the last few decades follow Moore's law nicely, while soft robots have yet to climb that ladder and face great challenges in the future. However, according to Bank of America Merrill Lynch (BAML) research, medical robots business is expected to grow at a much faster rate to reach $ 18b by 2022 even though compared to industrial robots, medical robots adoption is still at an early stage, with 1,224 units sold for $ 1.3b in 2014, only accounting for 5% of total robots sold [56]. On a final note to sum up, Prof. George Whitesides—in an interview with Prof. Barry Trimmer—clearly explained that the field of soft robot actuators is still in its nascent phase and will be commercially challenging for researches to explore in the near future [84].

6 Concluding Remarks

Inspired by the exceptional competence of natural organisms, researchers have been widely exploring the possibility to mimic the rich multifunctionality of soft biological species. The motivation behind this gradual shift towards soft robotics derives from the aspiration to tackle more complex, unpredictable environments, which demands higher order of mechanical intelligence. Imitating the inherent traits of their natural counterparts, these futuristic robots are designed to match the elastic and rheological properties, to facilitate easy movement through awkward surroundings. In general, soft robotics offer better mechanical compliance with biological systems than their rigid counterparts. Their biocompatibility, adaptability and capability for developing multiple and complex functions such as actuation in confined spaces, deformability, adaptation to the environment or manipulation of unmodelled objects, account for their potential towards several different applications, including biomedicine.

It is evident by now that magnetically responsive untethered soft robots bring a new way to look into robotics for future generations, which will attract investors and companies for product commercialization. It is also to be noted here that soft robotics in general for whichever actuation is posed upon, offer the potential not to compete with conventional robotics, but to tackle a set of problems that existing technologies have not been able to solve. The vast biomedical applications of soft robotics in rehabilitation, tissue engineering, soft biological cell biology, flexible surgical manipulators etc. are overwhelming and call for a serious investment in research focused on the fabrication and material synthesis of flexible, dexterous and cost-effective cross-linked polymers. There are examples of soft robotics revolutionizing areas beyond biomedical research like disaster management, rescue operations and field exploration. In all these preamble application avenues, magnetic-driven softbots are highly acknowledged as per their wireless, minute control manoeuvre. The question that stands now is whether innovations in rapid prototyping techniques like soft lithography and 3D printing will allow manufacturers to print an entire robot that will be inexpensive, easy to use and satisfy market demand. We can be optimistic to make this new technology grow faster and bring out a sustained environment in which human–robot interaction can rise to a new level.

Acknowledgements This work was in part supported by the Singapore Academic Research Fund under Grant R-397-000-173-133 (Magnetically Actuated Micro-robotics), R-397-000-227-112, and National Natural Science Foundation of China NSFC grant 51405322, NUSRI China Jiangsu Provincial Grant BK20150386 and BE2016077 awarded to Dr. Hongliang Ren.

References

1. Abbott, Jake J., et al. 2007. Modeling magnetic torque and force for controlled manipulation of soft-magnetic bodies. *IEEE Transactions on Robotics* 23 (6): 1247–1252.
2. Ahadian, Samad, et al. 2014. Hybrid hydrogels containing vertically aligned carbon nanotubes with anisotropic electrical conductivity for muscle myofiber fabrication. *Scientific reports* 4: 4271.
3. Akiyama, Yoshitake, et al. 2012. Room temperature operable autonomously moving biomicrorobot powered by insect dorsal vessel tissue. *PloS one* 7 (7): e38274.
4. Ashley, Steven. 2003. Artificial muscles. *Scientific American* 289 (4): 52–59.
5. Banerjee, Hritwick, Zion Tse, and Hongliang Ren. 2017. Soft robotics with compliance and adaptation for biomedical applications and forthcoming challenges (in press). *International Journal of Robotics and Automation* 1–20.

6. Behrooz, Majid. 2015. A controllable flexible micropump and a semi-active vibration absorber using magnetorheological elastomers. PhD thesis, University of Nevada, Reno.
7. Butta, Mattia, and Ichiro Sasada. 2013. Orthogonal fluxgate with annealed wire core. *IEEE Transactions on Magnetics* 49 (1): 62–65.
8. Cantera, M. Asun, et al. 2017. Modeling of magneto-mechanical response of magnetorheological elastomers (MRE) and MRE-based systems: a review. *Smart Materials and Structures* 26 (2): 023001.
9. Cham, Jorge G., et al. 2002. Fast and robust: Hexapedal robots via shape deposition manufacturing. *The International Journal of Robotics Research* 21 (10–11): 869–882.
10. Chan, Vincent, et al. 2015. Fabrication and characterization of optogenetic, multistrip cardiac muscles. *Lab on a Chip* 15 (10): 2258–2268.
11. Chathuranga, Damith Suresh, et al. 2016. Magnetic and mechanical modeling of a soft three-axis force sensor. *IEEE Sensors Journal* 16 (13): 5298–5307.
12. Chen, K.C., and C.S. Yeh. 2002. A mixture model for magneto-rheological materials. *Continuum Mechanics and Thermodynamics* 14 (6): 495–510.
13. Chen, Lin, X.L. Gong, and W.H. Li. 2007. Microstructures and viscoelastic properties of anisotropic magnetorheological elastomers. *Smart Materials and Structures* 16 (6): 2645.
14. Cheng, Shi, and Zhigang Wu. 2012. Microfluidic electronics. *Lab on a Chip* 12 (16): 2782–2791.
15. Cho, Kyu-Jin, et al. 2009. Review of manufacturing processes for soft biomimetic robots. *International Journal of Precision Engineering and Manufacturing* 10 (3): 171–181.
16. Cho, Young I., and Kenneth R. Kensey. 1991. Effects of the non-Newtonian viscosity of blood on flows in a diseased arterial vessel. Part 1: Steady flows. *Biorheology* 28 (3–4): 241–262.
17. Ciuti, Gastone, et al. 2010. Robotic magnetic steering and locomotion of capsule endoscope for diagnostic and surgical endoluminal procedures. *Robotica* 28 (02): 199–207.
18. Clothier, Brian L. 2001. Method and apparatus for magnetic induction heating using radio frequency identification of object to be heated. US Patent 6,320,169. Nov. 2001.
19. Cutkosky, Mark R., and Sangbae Kim. 2009. Design and fabrication of multimaterial structures for bioinspired robots. *Philosophical Transactions of the Royal Society of London A: Mathematical, Physical and Engineering Sciences* 367 (1894): 1799–1813.
20. Cvetkovic, Caroline, et al. 2014. Three-dimensionally printed biological machines powered by skeletal muscle. In *Proceedings of the National Academy of Sciences* 111 (28): 10125–10130.
21. Deng, Hua-xia, Xing-long Gong, and Lian-hua Wang. 2006. Development of an adaptive tuned vibration absorber with magnetorheological elastomer. In *Smart materials and structures* 15 (5): N111.
22. Duffy, Rebecca M., and Adam W. Feinberg. 2014. Engineered skeletal muscle tissue for soft robotics: fabrication strategies, current applications, and future challenges. *Wiley Interdisciplinary Reviews: Nanomedicine and Nanobiotechnology* 6 (2): 178–195.
23. Engler, Adam J., et al. 2004. Myotubes differentiate optimally on substrates with tissue-like stiffness. *J Cell Biol* 166 (6): 877–887.
24. Feinberg, Adam W., et al. 2007. Muscular thin films for building actuators and powering devices. *Science* 317 (5843): 1366–1370.
25. Felt, Wyatt, and C. David Remy. 2014. Smart braid: Air muscles that measure force and displacement. In *International Conference on Intelligent Robots and Systems (IROS 2014) IEEE/RSJ*, 2821–2826, 2014, IEEE.
26. Felt, Wyatt, Michelle Suen, and C. David Remy. 2016. Sensing the motion of bellows through changes in mutual inductance. In *International Conference on Intelligent Robots and Systems (IROS), 2016 IEEE/RSJ*, 5252–5257, 2016, IEEE.
27. Ferry, John D., and Henry S. Myers. 1961. Viscoelastic properties of polymers. *Journal of The Electrochemical Society* 108 (7): 142C–143C.
28. Fuhrer, Roland, et al. 2013. Soft iron/silicon composite tubes for magnetic peristaltic pumping: frequency-dependent pressure and volume flow. *Advanced Functional Materials* 23 (31): 3845–3849.

29. Fujita, Hideaki, Taku Nedachi, and Makoto Kanzaki. 2007. Accelerated de novo sarcomere assembly by electric pulse stimulation in C2C12 myotubes. *Experimental cell research* 313 (9): 1853–1865.
30. Gong, X.L., X.Z. Zhang, and P.Q. Zhang. 2005. Fabrication and characterization of isotropic magnetorheological elastomers. *Polymer testing* 24 (5): 669–676.
31. Gravagne, Ian A., Christopher D. Rahn, and Ian D. Walker. 2003. Large deflection dynamics and control for planar continuum robots. *IEEE/ASME Transactions on Mechatronics* 8 (2): 299–307.
32. Griffn, Maureen A., et al. 2004. Adhesion-contractile balance in myocyte differentiation. *Journal of Cell Science* 117 (24): 5855–5863.
33. Hutson, Che B., et al. 2011. Synthesis and characterization of tunable poly (ethylene glycol): gelatin methacrylate composite hydrogels. *Tissue Engineering Part A* 17 (13–14): 1713–1723.
34. Iida, Fumiya, and Cecilia Laschi. 2011. Soft robotics: Challenges and perspectives. *Procedia Computer Science* 7: 99–102.
35. Jiles, David. 2015. *Introduction to magnetism and magnetic materials*. CRC press.
36. Jolly, Mark R., J. David Carlson, and Beth C. Munoz. 1996. A model of the behavior of magnetorheological materials. *Smart Materials and Structures* 5 (5): 607.
37. Kallio, Marke. 2005. The elastic and damping properties of magnetorheological elastomers. VTT.
38. Kang, Hyun-Wook, et al. 2016. A 3D bioprinting system to produce human-scale tissue constructs with structural integrity. *Nature Biotechnology* 34 (3): 312–319.
39. Kasap, Safa O. 2006. *Principles of electronic materials and devices*. McGraw-Hill.
40. Kciuk, M., and R. Turczyn. 2006. Properties and application of magnetorheological fluids. *Journal of Achievements in Materials and Manufacturing Engineering* 18 (1–2): 127–130.
41. Keller, Jutta, et al. 2010. Remote magnetic control of a wireless capsule endoscope in the esophagus is safe and feasible: results of a randomized, clinical trial in healthy volunteers. *Gastrointestinal endoscopy* 72 (5): 941–946.
42. Kim, Jiyun, et al. 2011. Programming magnetic anisotropy in polymeric microactuators. *Nature materials* 10 (10): 747–752.
43. Ku, Sook Hee, Sahng Ha Lee, and Chan Beum Park. 2012. Synergic effects of nanofiber alignment and electroactivity on myoblast differentiation. *Biomaterials* 33 (26): 6098–6104.
44. Lacour, Stéphanie Périchon, et al. 2003. Stretchable gold conductors on elastomeric substrates. *Applied Physics Letters* 82 (15): 2404–2406.
45. Li, Weihua, et al. 2009. Development of a force sensor working with MR elastomers. In *AIM 2009. IEEE/ASME International Conference on Advanced Intelligent Mechatronics, 2009*, 233–238. IEEE.
46. Li, Yancheng, and Jianchun Li. 2015. Finite element design and analysis of adaptive base isolator utilizing laminated multiple magnetorheological elastomer layers. *Journal of Intelligent Material Systems and Structures* 26 (14): 1861–1870.
47. Li, Yancheng, et al. 2014. A state-of-the-art review on magnetorheological elastomer devices. *Smart Materials and Structures* 23 (12): 123001.
48. Liao, G.J., et al. 2012. Development of a real-time tunable stiffness and damping vibration isolator based on magnetorheological elastomer. *Journal of Intelligent Material Systems and Structures* 23 (1): 25–33.
49. Lipson, Hod. 2014. Challenges and opportunities for design, simulation, and fabrication of soft robots. *Soft Robotics* 1 (1): 21–27.
50. Lipson, Hod, and Melba Kurman. 2013. *Fabricated: The new world of 3D printing*. John Wiley & Sons.
51. Liu, Hu, et al. 2017. Lightweight conductive graphene/thermoplastic polyurethane foams with ultrahigh compressibility for piezoresistive sensing. *Journal of Materials Chemistry C* 5 (1): 73–83.
52. Lokander, Mattias. 2004. Performance of magnetorheological rubber materials. Ph.D thesis. Fiber-och polymerteknologi.

53. Majidi, Carmel. 2014. Soft robotics: a perspective-current trends and prospects for the future. *Soft Robotics* 1 (1): 5–11.
54. Malda, Jos, et al. 2013. 25th anniversary article: engineering hydrogels for biofabrication. *Advanced Materials* 25 (36): 5011–5028.
55. Malone, Evan, Megan Berry, and Hod Lipson. 2008. Freeform fabrication and characterization of Zn-air batteries. *Rapid Prototyping Journal* 14 (3): 128–140.
56. Masch, Vladimir A., et al. 2017. Shifting the Paradigm in Superintelligence. *Review of Economics & Finance* 8: 17–30.
57. Meng, MQ-H., et al. 2004. Wireless robotic capsule endoscopy: State-of-the-art and challenges. In *WCICA 2004. Fifth World Congress on Intelligent Control and Automation, 2004*. Vol. 6, 5561–555a. IEEE.
58. Milecki, A. 2010. Electro-and magnetorheological fluids and their applications in engineering. In *WPP, Poznań*.
59. Moerland, M.A., et al. 1994. The influence of respiration induced motion of the kidneys on the accuracy of radiotherapy treatment planning, a magnetic resonance imaging study. *Radiotherapy and Oncology* 30 (2): 150–154.
60. Murao, Shunta, Katsuhiro Hirata, and Fumikazu Miyasaka. 2016. Analysis of Variable Stiffness Magnetorheological Elastomer Employing Particle Method and FEM. *IEEE Transactions on Magnetics* 52 (3): 1–4.
61. Nawroth, Janna C., et al. 2012. A tissue-engineered jellyfish with biomimetic propulsion. *Nature biotechnology* 30 (8): 792–797.
62. Nayak, B., S.K. Dwivedy, and K.S.R.K. Murthy. 2011. Dynamic analysis of magnetorheological elastomer-based sandwich beam with conductive skins under various boundary conditions. *Journal of Sound and Vibration* 330 (9): 1837–1859.
63. Park, Sung-Jin, et al. 2016. Phototactic guidance of a tissue-engineered softrobotic ray. *Science* 353 (6295): 158–162.
64. Park, Yong-Lae, et al. 2010. Hyperelastic pressure sensing with a liquid-embedded elastomer. In *Journal of Micromechanics and Microengineering* 20 (12): 125029.
65. Raman, Ritu, et al. 2016. Optogenetic skeletal muscle-powered adaptive biological machines. *Proceedings of the National Academy of Sciences* 113 (13): 3497–3502.
66. Ren, Hongliang, and Peter Kazanzides. 2012. Investigation of attitude tracking using an integrated inertial and magnetic navigation system for hand-held surgical instruments. *IEEE/ASME Transactions on Mechatronics* 17 (2): 210–217.
67. Ren, Hongliang, et al. 2013. Computer-assisted transoral surgery with flexible robotics and navigation technologies: a review of recent progress and research challenges. In *Critical Reviews™ in Biomedical Engineering* 41 (4–5).
68. Renda, Federico, et al. 2014. Dynamic model of a multibending soft robot arm driven by cables. *IEEE Transactions on Robotics* 30 (5): 1109–1122.
69. Rivero, Guillermo, Marta Multigner, and Jorge Spottorno. 2012. Magnetic sensors for biomedical applications. In *Magnetic Sensors-Principles and Applications*. InTech.
70. Robert. C.O., and O. Handley. 2000. Modern magnetic materials: principles and applications.
71. Rogers, John A., Takao Someya, and Yonggang Huang. 2010. Materials and mechanics for stretchable electronics. *Science* 327 (5973): 1603–1607.
72. Ruddy, C., E. Ahearne, and G. Byrne. 2012. A review of magnetorheological elastomers: properties and applications. In *Advanced Manufacturing Science (AMS) Research*. http://www.ucd.ie/mecheng/ams/news_items/CillianRuddy.pdf. Accessed 20 2012.
73. Schmauch, Marissa M., et al. 2017. Chained iron microparticles for directionally controlled actuation of soft robots. *ACS Applied Materials & Interfaces* 9 (13): 11895–11901.
74. Sendoh, Masahiko, Kazushi Ishiyama, and K.-I. Arai. 2003. Fabrication of magnetic actuator for use in a capsule endoscope. *IEEE Transactions on Magnetics* 39 (5): 3232–3234.
75. Shen, Y., M. Farid Golnaraghi, and G.R. Heppler. 2004. Experimental research and modeling of magnetorheological elastomers. *Journal of Intelligent Material Systems and Structures* 15 (1): 27–35.

76. Singh, Leena, John Wen, and Harry Stephanou. 1997. Motion planning and dynamic control of a linked manipulator using modified magnetic fields. In *Proceedings of the 1997 IEEE International Conference on Control Applications, 1997*, 9–15. IEEE.
77. Song, Shuang, et al. 2014. 6-D magnetic localization and orientation method for an annular magnet based on a closed-form analytical model. *IEEE Transactions on Magnetics* 50 (9): 1–11.
78. Stauffer, Paul R., Thomas C. Cetas, and Roger C. Jones. 1984. Magnetic induction heating of ferromagnetic implants for inducing localized hyperthermia in deep-seated tumors. *IEEE Transactions on Biomedical Engineering* 2: 235–251.
79. Sun, Y., et al. 2013. Optimizing the structure and contractility of engineered skeletal muscle thin films. *Acta biomaterialia* 9 (8): 7885–7894.
80. Swain, Paul, et al. 2010. Remote magnetic manipulation of a wireless capsule endoscope in the esophagus and stomach of humans (with). *Gastrointestinal Endoscopy* 71 (7): 1290–1293.
81. Takegami, Kenji, et al. 1998. New ferromagnetic bone cement for local hyperthermia. *Journal of Biomedical Materials Research Part A* 43 (2): 210–214.
82. Tian, T.F., W.H. Li, and Gursel Alici. 2013. Study of magnetorheology and sensing capabilities of MR elastomers. *Journal of Physics: Conference Series*. 412 (1): 012037 (IOP Publishing).
83. Tian, T.F., et al. 2011. Microstructure and magnetorheology of graphite-based MR elastomers. *Rheologica Acta* 50 (9–10): 825–836.
84. Trimmer, Barry, and George Whitesides. 2014. An Interview with George Whitesides. *Soft Robotics* 1 (4): 233–235.
85. Trivedi, Deepak, et al. 2008. Soft robotics: Biological inspiration, state of the art, and future research. *Applied Bionics and Biomechanics* 5 (3): 99–117.
86. Wang, Hongbo, et al. 2016. A Low-cost soft tactile sensing array using 3D hall sensors. *Procedia Engineering* 168: 650–653.
87. Wang, Hongbo, et al. 2016. Design methodology for magnetic field-based soft tri-axis tactile sensors. *Sensors* 16 (9): 1356.
88. Webster III, Robert J., and Bryan A. Jones. 2010. Design and kinematic modeling of constant curvature continuum robots: A review. *The International Journal of Robotics Research* 29 (13): 1661–1683.
89. Williams, Brian J., et al. 2014. A self-propelled biohybrid swimmer at low Reynolds number. *Nature Communications* 5.
90. Wojewoda, K.K., et al. 2017. Hybrid position and orientation tracking for a passive rehabilitation table-top robot. In *Proceedings of the 2017 IEEERAS-EMBS International Conference on Rehabilitation Robotics (ICORR 2017)*. IEEE.
91. Wood, Robert J. 2008. The first takeoff of a biologically inspired at-scale robotic insect. *IEEE transactions on Robotics* 24 (2): 341–347.
92. Xia, Younan, and George M. Whitesides. 1998. Soft lithography. *Annual Review of Materials Science* 28 (1): 153–184.
93. Xu, Tiantian, et al. 2015. Magnetic actuation based motion control for microrobots: An overview. *Micromachines* 6 (9): 1346–1364.
94. Yamamoto, Yasunori, et al. 2009. Preparation of artificial skeletal muscle tissues by a magnetic force-based tissue engineering technique. *Journal of Bioscience and Bioengineering* 108 (6): 538–543.
95. Yamashita, Hideyasu, et al. 2016. Function-selectable tactile sensing system with morphological change. In *2016 IEEE/SICE International Symposium on System Integration (SII)*, 415–420. IEEE.
96. Yu, Jiangfan, et al. 2015. Magnetic control of AMB-1 magnetotactic bacteria for micromanipulation. In *2015 IEEE International Conference on Automation Science and Engineering (CASE)*, 1614–1619. IEEE.
97. Zhang, Wenhua, Rajashree Baskaran, and Kimberly L. Turner. 2002. Effect of cubic nonlinearity on auto-parametrically amplified resonant MEMS mass sensor. *Sensors and Actuators A: Physical* 102 (1): 139–150.

98. Zhang, Xianzhou, et al. 2008. Analysis and fabrication of patterned magnetorheological elastomers. *Smart Materials and Structures* 17 (4): 045001.
99. Zhang, Xian-zhou, et al. 2007. Existence of bound-rubber in magnetorheological elastomers and its influence on material properties. *Chinese Journal of Chemical Physics* 20 (2): 173.
100. Zhou, Lei, Weijia Wen, and Ping Sheng. 1998. Ground states of magnetorheological fluids. *Physical review letters* 81 (7): 1509.

Magnetic Actuated Catheterization Robotics

Bok Seng Yeow and Ren Hongliang

Abstract This chapter covers the design principles of magnetic actuated catheter robot and is outlined as follows. Section 1 discusses key fundamental principles to design for an electromagnetic catheter/guide wire type surgical robot. The clinical perspectives are covered in Sect. 1.1 and in Sect. 1.2 the overarching electromagnetic theory is mentioned. Electromagnetic systems can be further decomposed into the stators (stationary wound coils) and actuators (moving part usually consists of permanent magnet), where the stators can be interpreted as the input and the actuator the output. Section 2 will cover the design consideration of stators and Sect. 4 the design principles of the actuators. Sections 2 and 3, aim to provide the reader with an intuitive approach to designing their own electromagnetic system. Section 3 will further exemplify principles covered in Sects. 2 and 3 with a fabricated prototype from our lab. These electromagnetic catheter systems can be classified by many parameters; one important parameter is the bending angle and will be addressed in Sect. 4. The use of this angle is demonstrated for a surgical context. This chapter concludes in Sect. 8, providing an overview of the works presented and the future directions.

1 Medical Background

1.1 AV Fistula

Arteriovenous fistula is a specific treatment support option for patients experiencing renal failure and requiring hemodialysis [24]. During dialysis, a machine replaces the patient's lost kidney function of blood filtration to prevent accumulation of toxic waste products [18]. During dialysis, the blood from the patient has to be rerouted into the machine and this requires venous access. There are other alternatives such as an access catheter or via grafts [54], fistulas allowing an increase in blood volumetric flux which is beneficial to the performance of the procedure. The increase in blood

B.S. Yeow · R. Hongliang (✉)
Department of Biomedical Engineering, National University of Singapore, Singapore, Singapore
e-mail: ren@nus.edu.sg

H. Ren and J. Sun (eds.), *Electromagnetic Actuation and Sensing in Medical Robotics*,
Series in BioEngineering, https://doi.org/10.1007/978-981-10-6035-9_4

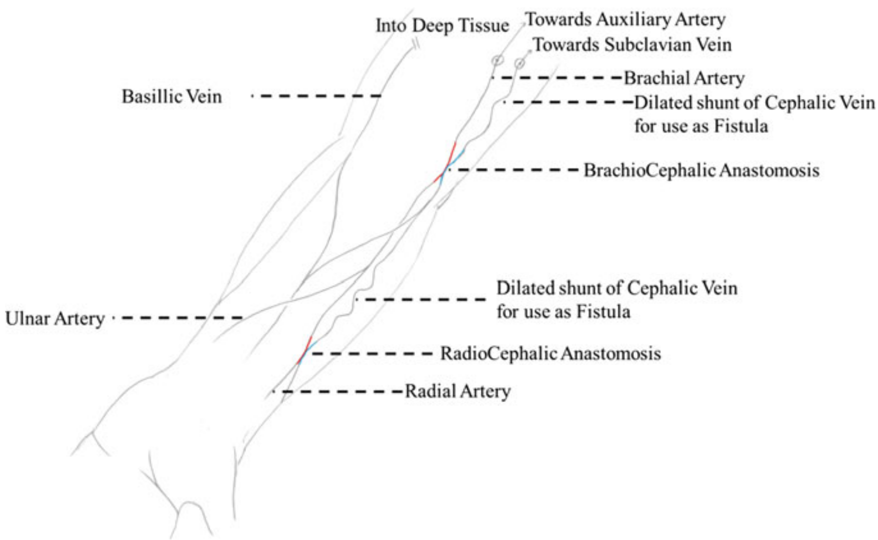

Fig. 1 Vasculature in the upper limbs.

flow comes from rerouting an artery to a vein which is connected via an anastomosis [24]. This causes the vein to build up pressure over time and will dilate. The enlarged vein acts as an easy access for dialysis and this technique can be applied to a wide variety of location. Common sites include the upper limbs using the Radial, Ulnar, Brachial and Cephalic [35], Fig. 1.

The connection technique between arteries and veins can vary depending on the situation such as transposition (the distal drainage network of a vein is replaced with flow from the artery) and interposition (flow from the arteries bifurcates into the vein via a graft connecting the two) [24].

1.2 Stenosis

Utilizing the fistulas overtime will develop into stenosis [1], as there is constant needle access [20, 53]. The constant needle access results in tissue trauma and develops scar tissue; furthermore, there could be fistula thrombosis [11]. These medical issues result in the reduction of volumetric blood flow [17] and should be reopened via angioplasty [25].

Angioplasty involves inserting a surgical balloon or stent into the lumen of the vessel, which expanded to increase the size of the lumen. To reduce surgical trauma and improve surgical success rates, it is common to access the target area via a distal access site. A guide wire is to create an access line connecting the distal access site to the target site. A catheter then run over the guide wire to replace the guide wire.

Surgical tools such as the surgical balloon then traversed through the catheter to react the target site to carry out its functions.

1.3 Challenges and Benefits

In the less ideal and more likely scenario, there will be challenges in performing the procedure. In positioning of the guide wire under the guidance of angiography and ultrasound, visual acuity in trying to place the guide wire is lacking. Further, there is poor transmission of forces to the distal tip as control is mechanically initiated from the proximal end and is expected to traverse the entire insertion length. The transmission is easily compromised with torus environments where the guide wire easily buckles. Physicians utilize various shapes of guide wire [37] and handling techniques [26] to mitigate the current limitations in guide wires. The concepts described in the following chapters intend to provide physicians with a more direct control over the distal tip via electromagnetic coupling. The electromagnetic approach is more direct as the control information outside of the patient is not attenuated along the guide wire path.

1.4 Arteriovenous Fistulas and Electromagnetic Actuation

Minimally invasive surgeries [24] involve teleoperation of surgical equipment and are widely employed in vascular surgeries due to benefits, in patient recovery times, over open surgery [18]. Vascular surgeries typically involve guide wire placement prior to angioplasty (balloon or stent) procedures [54]. There exist a wide variety of vascular targets such as arteriovenous fistulas which are superficial veins/arteries at the dermal surface. This reduces constraints on the design of the system as the magnetic fields need not be as strong to penetrate and reach the deep vasculature. Arteriovenous fistulas are important to hemodialysis patients as access sites for renal therapy; in the 2011 Kidney Dialysis Foundation report, 76.6% of Singapore hemodialysis patients are reliant on arteriovenous fistula [35]. These fistulas, however, tend to close-up over time due to constant needle access [1, 35] inducing tissue trauma and developing stenosis [20]. Angioplasty remains an important surgical option for the management of stenosis in arteriovenous fistulas [53].

The guide wire has to traverse the length of the fistula, mediating across the stenosis. For our problem statement, we assume that complete total occlusion has not occurred. The surgeon is challenged by limited vision and control in the determination of guide wire positions during the navigation phase [11]. Surgeons have to be dexterous and experienced to not over exert pressure which can puncture the vasculature [11] and employ skilful buckling of the different types [17] of guidewires

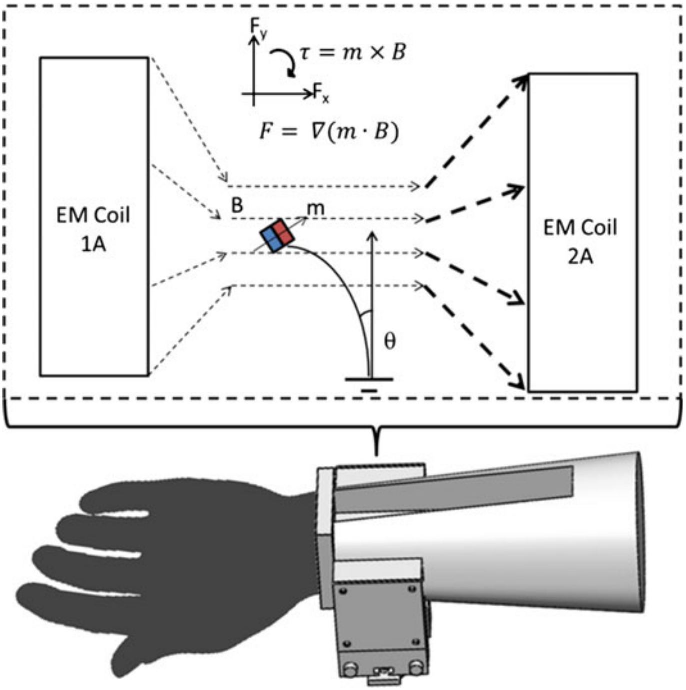

Fig. 2 Overview of the electromagnetic system.

to reach the correct destination. The challenges presented also vary between patient demographics [25] and the type of arteriovenous fistulas [37, 53]. In the case of overly torus routes [26], multiple stagings of catheters guide wires exchanges are needed, consuming time and resources.

Our system utilizes electromagnetic coil pairs that are configured near the stenosis site and defines the magnetic flux density at a region which is operator determined. When the guide wire is at the region of interest and the operator requires the guide wire to deflect in a particular manner (to check for guide wire advancement), the applied magnetic fields can be controllably changed. Changes in the applied magnetic fields interact with the magnetic attachment on the guide wire, inducing mechanical deflection of the guide wire, Fig. 2.

EM coil refers to the electromagnetic coils which generate the magnetic fields (represented by dotted arrows). The guide wire deflects an angle of () due to interaction of the magnetic tip (red and blue box) in the magnetic field. The entire setup is orientated relative to the patient's arm where tele-navigation of the stenosis is deemed necessary.

1.5 Overview and State of the Art

The use of electromagnetic manipulation systems can improve present surgical procedures [45, 55] despite reported risk from magnetic resonance heating [32]. Preexisting tetherless electromagnetic arts are classified here based on the actuator (Particle or Manipulator) or the stators (Electromagnetic coil). Arrangements [31, 33, 40] for the various stators, the control methodology of the magnetic navigation system [4, 6, 8, 10, 43, 47, 48] and the applications of the system [13, 46] can be defined separately. Publications associated with Stereotaxis [9, 21, 27, 36, 38, 39, 44, 49] or claiming novel actuators will be further considered due to the similarity in art.

Novel actuator ideas include converting the associated magnetic responsive elements in the manipulator, which is traditionally ridged, into a fluid [52], nanoparticles [12] or flexible magnets [16]. The magnetic component is also used to grab and advance other instruments [50]. Additional functionalities were associated with the navigation of the manipulator, such as with drilling tasks [5].

Comparing with guide wire actuator-based systems, magnetic micro-robot systems [3, 7, 19, 22, 23, 41] share similar operational mechanics to manipulator-based guide wires [2]. Tetherless magnetic control has also been used to couple the motion of a robotic arm to a magnetic capsule [31]. More recent setups include magnetic actuation of in-vivo cameras [30] or for high-frequency actuation such as in needless injectors [51].

Presently, the prototype holds much similarity in terms of methodology to designs claimed by Stereotaxis. The predetermined position of the magnetic element interacts with the external magnetic field enabling flexion. Our system differs from the above based on the applications to plaque navigation in fistulas and in the portability of the stator magnetic fields generators. Further, this prototype is preliminary and works toward the eventual disposable guide wire attachment for tetherless electromagnetic control. This will enable the angioplasty procedure to move into small clinics as the electromagnetic coils are much smaller and more portable. Additionally, the attachment will allow any type of guide wires to be controlled allowing ease of integration into hospitals.

1.6 Clinical Relevance (In Geographical Context)

Peripheral artery disease (PAD) has been indicated to be a growing problem [28] and is a type of atherosclerosis. In Singapore and many Asian countries, the risk factors associated with PAD are on the rise due to an unhealthy lifestyle and an increase in life expectancy [42]. PAD affects both the mortality and quality of lifestyle of patients and shares similar risk factors with other cardiovascular disease. Common methods for the diagnosis of PAD include the ankle brachial index [14] as PAD usually occurs in extremities of patients especially the lower limbs, affecting mobility. Surgical treatment such as atherectomy or angioplasty via stenting or balloon (US8348858, US8419681) will require a guide wire to deliver the end effector to the desired location [15]. There are many types of catheter-guide wires configurations [34] for a wide range of purposes and control is challenging as complications may arise from perforations and buckling when using a distal controller. It is useful to define some functional definitions [34] of a guide wire.

(1) Wire trackability—is ease in which a wire can be advanced through a tortuous artery without buckling, kinking or prolapsing. This is related to the bend radius, arc length and number of bends of the artery which the guide wire has to traverse. This is similar to the dexterity requirements in the design of manipulators.

(2) Pushability—is the percentage of transmitted force from the shaft to the wire tip and relates to the axial and radial advancement of the guide wire.

(3) Penetration power—is the pressure that the tip can exert without buckling. This is essential when trying to penetrate through occlusions.

(4) Tactile response—is how the operator can comfortably and accurately control changes in movement of the wire tip.

(5) Tip load—quantifies the force to bend the distal tip of a wire. Stiffer wires are harder to bend and consequently easier to pierce through calcified/blocked arteries; but as they are stiffer, they require more force to bend and the forces exerted may cause puncture damage to the surrounding tissue. This is analogous to compliance in a manipulator.

There are further functional aspects of guide wire, which we will not consider as it is less related to the manipulability of the device durability, tip flexibility, tip malleability, etc.

2 Electromagnetic Principles in Magnetic Catheter Actuation

2.1 Magnetic Fields

All electromagnetic designs stem from Maxwell's equations which describe the coupling between electromagnetic fields as well as their spatial representations. While electric fields and magnetic fields are essentially carried by the same boson (photons), their oscillatory interactions with the human body are vastly different. Electric interactions are useful as sensors where the changes in electrical resistances and capacitance are detectable as in the case for ECG, EMG, EEG, etc. While magnetic fields have also been used for sensing (MRI), the magnetic fields required have to be very strong to pick up the atomic spin information. The human body is virtually invisible to weak magnetic fields and thus magnetic fields are a good choice for transmitting information into the body with minimal interference. The generations of magnetic fields are achieved artificially with an electric current which is characterized by Ampere's circuital law. The generated magnetic fields can then be used for subsequent actuation.

2.2 Magnetic Circuit to Generate Magnetic Fields/Magnetomotive Force

Much like Kirchhoff's Law in electrical circuits, the magnetic circuits are the simplified law to model magnetics and are analogous to their electrical counterpart.

The electromagnetic coils (or wire winding/solenoid) act as magnetic dipole sources and generate the potential for magnetic fluxes. The flux density at the regions of interest can then be calculated by considering the integral over the total permeance/reluctances of paths.

The path considered for magnetic circuits can be challenging to define but it gives a good approximation to magnetic flux densities when the flux leakage of the source is small. This approach is best used when the air gap in consideration is small for the magnetic flux path in question. The consideration of the magnetic potential sources on the other hand is quite straight forward. Permanent magnets are characterized by their intrinsic magnetization values and act as fixed dipole sources. Solenoids or wound wires carrying current will generate magnetic fields and also act as magnetic sources. The following example demonstrates the calculations for the magnetic fields at any given point along the axis of a simple solenoid:

$$B = \frac{\mu_0 NI}{2} \int \frac{R^2 dx}{(x^2 + R^2)^{1.5}} \quad \text{where} \quad \begin{Bmatrix} x = rctg\beta \\ dx = -Rd\beta \frac{1}{sin^2\beta} \end{Bmatrix} \tag{1}$$

$$B = \frac{\mu_0 NI}{2}(cos\beta_2 - cos\beta_1), \tag{2}$$

where μ_0 is the permeability of free space, (H/m), and R (not in fig) is the radius of the solenoid (Fig. 3).

2.3 Interpretation of Lorentz Forces

This chapter considers the interactions between ferromagnetic materials in the generated magnetic fields. Two predominant models have been used in the calculation of forces between magnets (Magnetostatics): the Gilbert model and the ampere model. Finite-element models for the numerical derivation of magnetic force on ferromagnetic objects are commonly adopted for experiments handling complex geometries. The details of the Gilbert model and the Ampere model will not be discussed but rather the more general governing equations of (Eqs. (3) and (4)). The reader should still look up on the two models to check if their geometries fall under the classification of either the Gilbert or Ampere model assumptions, in which case the analysis can be simplified. Magnetic fields are controllable via current in electromagnetic coils, and the interaction between the applied magnetic field and a magnetized object is coupled by Lorentz forces which drive the mechanical actuation. By considering

Fig. 3 Models of solenoid.

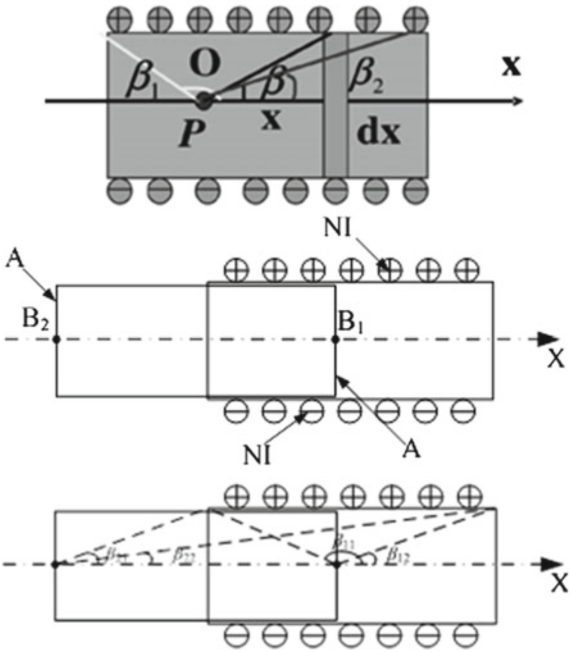

magnetic dipole sources, the net actuation can be split into forces (F) and torques (τ):

$$F = V_{olume}\,(M \cdot \nabla)\,B \tag{3}$$

$$\tau = V_{olume}\,(M \times B)\,. \tag{4}$$

This actuation can be applied to a medical context for manipulating micro-robots, guide wires and catheters. The control over these instruments has a wide array of impact and below we discuss one such impact.

3 Magnetic Stators

3.1 Basic Coil Design

For the magnetic catheter to conduct information, there should be interaction between the external magnetic field generators and the magnetic element, which is inside the patient. For the general setup, the external electromagnetic coils are good targets for controller inputs.

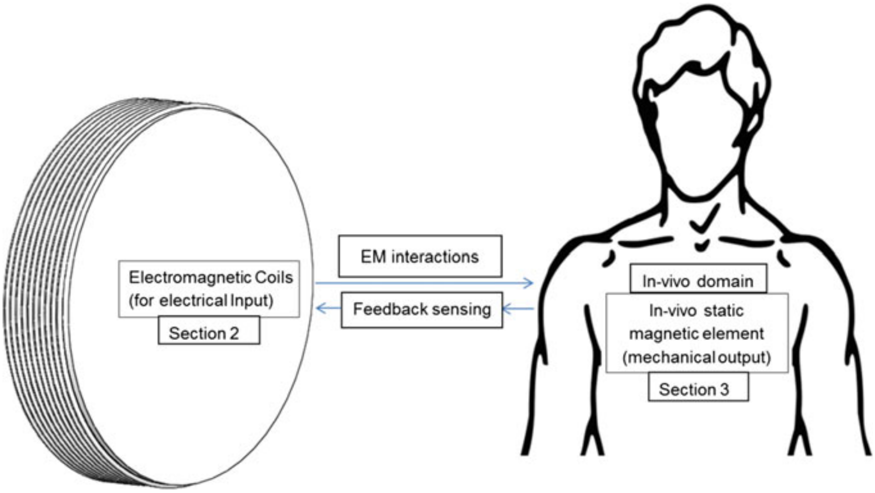

Fig. 4 Relative overview of actuator and stator in practice.

We begin with the design of electromagnetic coils which are the field generators. Varying currents in the EM coils will affect the eventual output position of the in-vivo magnetic elements. The simplest electromagnetic core consists of wound wires around a core material and can take on many designs depending on the requirements. The simplest design is a solid cylindrical core with wires winding coaxially around the core to form a cylindrical shell around the solid core (Fig. 4).

3.2 Electromagnetic Core Parameters

For a given solenoid, we define a region of interest where the generated magnetic fluxes from the solenoid change the magnetic field potentials and gradients for actuation. While it is possible to have an air core system (depending on the design and requirements), the currents may be high (resulting in heating concerns). Thus, incorporating a core material has benefits of concentrating magnetic fluxes and increasing magnetic field strengths at the region of interest. To further enhance the magnetic field, a closed flux path design is recommended to reduce the reluctance of the flux path as much as possible. This is achievable by encasing the solenoid in a magnetic permeable material, thus replacing the external air path with a more permeable material. Magnetic permeable materials will have a BH response curve which is important in the selection of materials [45].

BH curve shows the saturation/max operation for the material and is used to select the appropriate material for the purposes intended. Any material will have a response to the applied/surrounding magnetic fields; here, a magnetic field strength of **H** is applied to the material and the magnetic field **B** (synonymous the magnetic flux density) in the material has a response characteristic to the material composition. Most materials have a saturation limit which should be above the design requirements to reduce losses. Other preferential aspects are the gradient of the operational region (such as optimized linearity, steepness), hysteresis loss (usually minimized via eddy loss minimization common in high-frequency operations) and other physical factors. The approach is to first solve for B field in the homogeneous region based on air coil design. Based on physical parameters for the coil, including I for current, L_{EM} for length, OD for outer diameter, ID for inner diameter, ODwire for wire diameter and Lwire for wire length, we determine the turns per unit length (n):

$$r_{ave} = \frac{\frac{OD}{2} - \frac{ID}{2}}{2} + \frac{ID}{2} \tag{5}$$

$$N = \frac{L_{wire} \times 10^3}{2\pi \times r_{ave}} \times F \tag{6}$$

$$n = N \times \frac{L_{EM}}{OD_{wire}}. \tag{7}$$

The turn per unit length indicates the density of the coils and allows an estimation of the magnetic flux density at the centre of the solenoid (=1 for air core):

$$B = \mu_0 n I. \tag{8}$$

Next, the factoring of changes in the reluctances due to the magnetic permeable core.

B is related to H (magnetic field strength) and thus MMF (magnetomotive force F)

$$B = \mu H \tag{9}$$

$$F = \int H \cdot dl, \tag{10}$$

where *dl* refers to the flux path.

Depending on the cross-sectional area, flux density is usually the better parameter to describe the system as

$$\phi_B = \iint_s B \cdot ds, \tag{11}$$

which is the equation for describing the magnetic flux through a nominal surface S.

When using a soft magnetic core instead of an air coil, the reluctance (Rm) of the magnetic flux path is reduced:

$$\phi \cdot (R_m \downarrow) = (F \uparrow). \tag{12}$$

This will increase the perceivable magnetomotive force at the ROI, which is similar to the electric circuit. The changes to reluctance are determined experimentally to find a factor (μk) which changes the magnetic permeance (μ) of the flux path:

$$\mu = \mu_k \mu_0. \tag{13}$$

By relation to the above equations, the flux density is increased leading to the actuator perceiving stronger electromagnetic field for actuation.

To factor in the spatial position of the region of interest away from the coils, we utilize concepts covered in Sect. 2. The simplified and accessible approach to magnetic field state above does suffer from some limitations. The magnetic fields generated are in many cases not uniform but as EM coil area >> permanent magnet/ROI, this is still a good approximation. However, if the field is nonuniform in the ROI, the above calculations will not be applicable such as when working near the electromagnetic coil surface. If so, alternative computational methods may be preferred.

From the general solenoid Eq. (2), I (current) and n (turns per unit length) are preferably maximized within the physical design limitations. The values of I and n are related inversely, and thus there exist an optimization between the values of n and I. To increase the number of turns, the wire diameter can be decreased:

$$\rho = R\frac{A}{L}. \tag{14}$$

The resistance is a function of the resistivity (R), material property and the geometrical relations of cross-sectional area (A) and length (L). Thin wires can increase the turns per unit length as the diameter of wires decreases and more wires can fit in the same area. However, this will reduce current as the cross-sectional area decreases (A) and resistance of the wire increases. An ideal case should optimize parameters for number of turns per unit length to desired current. This can be done experimentally or via simulation [55].

3.3 Geometrical Configuration

By varying the positions of coils, one can generate unique magnetic fields at the regions of interest. Each coil generates magnetic fields, and the summation of all these effects is translated into the eventual ROI fields. At higher frequencies and magnitudes, the signal can constructively or destructively interact with other coils which can be important to high-frequency and proximity designs. When considering design, start from the simplest level of actuation and move towards desired level of complexity. An example of magnetic translation can include 3 DOFs to translate a permanent magnet in the X, Y and Z axis. We associate one coil pair to each degree of freedom (DOF). Thus, we would have three coil pairs one on each axis. Coil pairs are common in defining 1 DOF; however, this is not always necessary and a single coil is also capable of achieving the same. Coil pairs are, however, commonly used as the magnetic potential falls of greatly when moving away from the coil, and hence a much larger current is required. A coil pair counters this by having an opposite coil to maintain the field strengths. Having Helmholtz or Maxwell coil pairs will allow easier control over the well-modelled dipole field. The differences in input current between the two coils define the gradient and potential along that axis. In addition to field strengths, magnetic field uniformity at the region of interest is also preferred to improve ease of control. This relates to Sect. 3.2 where using a soft iron core which increases field strength will also make the magnetic fields less uniform.

3.4 Unique and More Novel Designs

While it is discussed above that coil pairs are coaxial to define a DOF, many other designs do not follow this. One example being OctoMag [15] which has eight electromagnetic coils but is unique in the layout to achieve 5 DOFs. OctoMag design in which four coils use opposite coil pair designs define the xy plane, while the other four coils rest above the other four coils to provide the additional z-plane motion. The control aspect of such a setup is very much more complicated and by this design 5 DOFs is achievable. Such a complex design is, however, well suited for ocular procedures where it would be difficult to place coils posterior to the eye. This is an example where the number of coil pair does not directly relate to the number of DOFs due to the design restrictions.

Most coils adopt a circular design to capture the symmetry in magnetic fluxes. However, coils need not always be circular; Square coils have been designed [40], and more complicated designs are possible depending on problem specifications. The physical assembly and arrangements of multiple coils (while individually symmetrical) can induce a loss of symmetry in the global system. Square coils can be designed to compensate for this and maintain the global symmetry in magnetic fields [33].

Other designs remove the need for an electromagnetic coil altogether. An actuator with 5 DOFs was achieved in [31] but utilized a single permanent magnet as a stator. Here, a robotic arm is used to provide the DOFs acting as the stator via a permanent magnet attached to the robotic arm. Magnetic forces are used to couple and transfer the position motion, and there are no electromagnetic coils used. The control, however, has to be closed loop, and depending on image feedback the robotic arm has to modulate the signals appropriately to control the positions of the actuator.

4 Magnetic Actuators

4.1 Magnetic Tip Attached to a Guide Wire Modelling

When the guide wire undergoes deformation due to energy input from the external coils, the increased energy state is balanced across the time frames. There are three energy domains for consideration in each time frame where the sum of the internal energies must equal to the energy state in the previous frame plus the energy change from the external system [47, 48]. The three energy domains are (1) magnetic potential energy, (2) strain energy and (3) contact deformation energy. A magnetic dipole in a nonuniform magnetic field will be displaced until it finds a stable low energy state; the energy it must seek out this minimum is the magnetic potential energy and is a result of the interactions between the magnetic field and the magnetic dipole. In our case of guide wire, the deflection in the tip will increase the strain energy in the guide wire. If the external forces acting to deflect the guide wire are interrupted, the strain energy in the guide wire will restore it to its neutral position. This strain energy can be modelled as a spring as a function of changes to neutral curvature or angular displacement. The contact deformation energy is more complex and is applicable to cases where the guide wire is in contact and is deforming a soft body, such as the walls of the vessel. This component can be a simple linear deformation or more complex viscoelastic Kelvin–Voigt deformation [4] and is dependent on the system in question. To keep the analysis, we consider only the magnetic potential energy in the following section.

4.2 Magnetic Forces and Torques on a Magnetic Dipole Point

Starting from the general equation, we reduce it depending on the system in question. For one-dimensional problems, consider a small permanent magnet (a magnetic dipole) moving on the coaxial axis (only By is nonzero, no Mz) between two electromagnetic coils.

The general force Eq. (15) and torque Eq. (16) equation can be reduced to one-dimensional Eqs. (17) and (18) in each component:

$$F = V_{olume}\,(M \cdot \nabla)\,B \tag{15}$$

$$\tau = V_{olume}\,(M \times B) \tag{16}$$

$$F_y = M_x \cdot \frac{dB_y}{dx} + M_y \cdot \frac{dB_y}{dy} \tag{17}$$

Table 1 The derivation of equations.

$\tau = \mathrm{V}(\overrightarrow{\mathrm{M}} \times \overrightarrow{\mathrm{B}})$	$\mathrm{F} = \mathrm{V}(\overrightarrow{\mathrm{M}} \cdot \nabla)\overrightarrow{\mathrm{B}}$
$\begin{pmatrix} \tau_x \\ \tau_y \\ \tau_x \end{pmatrix} = \mathrm{V}\begin{pmatrix} \mathrm{M_y \cdot B_z - M_z \cdot B_y} \\ \mathrm{M_z \cdot B_x - M_x \cdot B_z} \\ \mathrm{M_x \cdot B_y - M_y \cdot B_x} \end{pmatrix}$	$\begin{pmatrix} \mathrm{F_x} \\ \mathrm{F_y} \\ \mathrm{F_x} \end{pmatrix} = \begin{pmatrix} \mathrm{M_x} \cdot \frac{\mathrm{dB_x}}{\mathrm{dx}} + \mathrm{M_y} \cdot \frac{\mathrm{dB_x}}{\mathrm{dy}} + \mathrm{M_z} \cdot \frac{\mathrm{dB_x}}{\mathrm{dz}} \\ \mathrm{M_x} \cdot \frac{\mathrm{dB_y}}{\mathrm{dx}} + \mathrm{M_y} \cdot \frac{\mathrm{dB_y}}{\mathrm{dy}} + \mathrm{M_z} \cdot \frac{\mathrm{dB_y}}{\mathrm{dz}} \\ \mathrm{M_x} \cdot \frac{\mathrm{dB_z}}{\mathrm{dx}} + \mathrm{M_y} \cdot \frac{\mathrm{dB_z}}{\mathrm{dy}} + \mathrm{M_z} \cdot \frac{\mathrm{dB_z}}{\mathrm{dz}} \end{pmatrix}$
$\begin{pmatrix} \tau_x \\ \tau_y \\ \tau_x \end{pmatrix} = \begin{pmatrix} 0 \\ 0 \\ \mathrm{M_x \cdot B_y} - 0^+ \end{pmatrix}$	$\begin{pmatrix} \mathrm{F_x} \\ \mathrm{F_y} \\ \mathrm{F_z} \end{pmatrix} = \begin{pmatrix} \mathrm{M_x} \cdot 0^+ + \mathrm{M_y} \cdot 0^+ + 0 \\ \mathrm{M_x} \cdot \frac{\mathrm{dB_y}}{\mathrm{dx}} + \mathrm{M_y} \cdot \frac{\mathrm{dB_y}}{\mathrm{dy}} + 0 \end{pmatrix}$
$\tau_z = \mathrm{M_x \cdot B_y}$	$\mathrm{F_y} = \mathrm{M_x} \cdot \frac{\mathrm{dB_y}}{\mathrm{dx}} + \mathrm{M_y} \cdot \frac{\mathrm{dB_y}}{\mathrm{dy}}$

$$\tau_z = M_x \cdot B_y\,(x, y)\,. \tag{18}$$

The derivation of Eqs. (15)–(18) is shown in Table 1.

There is no magnetization in Z or magnetic fields in the Z direction when considering motion in a 2D plane (Bz = Mz = 0). Note, however, the torque can exist in the Z plane as a consequence of the orthogonal vector convention. Further, there will not be any gradient variation in the Z direction when considering a 2D plane ($\frac{dB_z}{d(x,y)} = \frac{dB_{(x,y,z)}}{dz} = 0$).

4.3 Application of Forces and Torques to a Cantilever Equation

By ignoring the strain energy and the contact energy, we can consider the system as a point-loaded cantilever. To consider the strain energy, the Young's modulus can be replaced with a strain-dependent equivalent and contact deformation will include another considering term into the differential Eq. (18) (Fig. 5).

The Cantilever equation is given as

$$\frac{d^2y}{dx^2} = \frac{\iint \{F\,(x, y) < x - L >^{-1} - \tau\,(x, y) < x - L >^{-2}\}}{EI}. \tag{19}$$

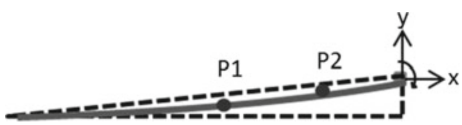

Fig. 5 Relatively small angle deflection P1 & P2 of a modelled cantilever.

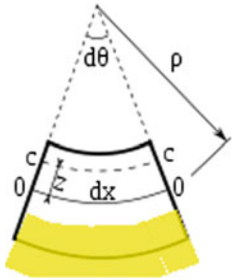

Fig. 6 Model of a bending segment.

For small angle approximations, the following relation holds:

$$\frac{dy}{dx} = tan\left(\theta\right) \sim \theta rad. \tag{20}$$

The curvature is then defined as

$$\frac{d\theta}{ds} = \frac{angle - relative - to - origin}{position - along - curve} = \frac{\theta\left(p2\right) - \theta\left(p1\right)}{s\left(2\right) - s\left(1\right)}. \tag{21}$$

The arc length is formulated by assuming that the plane sections remain plane after bending, where S is the arc length, R is the radius and is the angle in radians. Equation (21) is in differential form:

$$dS = R * d\theta. \tag{22}$$

The curvature is more commonly expressed as a function of the bending radius (Fig. 6),

$$\frac{d\theta}{ds} = \frac{1}{R}. \tag{23}$$

The length of the neutral axis (dx) is

$$dx = ds = \rho * d\theta. \tag{24}$$

Consider strain at the yellow region,

$$\epsilon = \frac{\Delta x}{x} = \frac{(\rho + z) \cdot d\theta - \rho \cdot d\theta}{\rho \cdot d\theta} = \frac{z}{\rho}. \tag{25}$$

For an isotropic material with young's Modulus E, the stress can be expressed as

$$\sigma = E\varepsilon = E\frac{z}{\rho}. \tag{26}$$

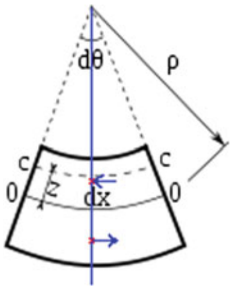

Fig. 7 Bending moment at dx.

Stress is also the force over an area. For this yellow portion, the forces are tensile, and strain is positive:

$$dF = E\frac{z}{\rho}dA. \tag{27}$$

For the opposite side, it will be in compression and we can couple both forces into a moment (Fig. 7).

The bending moment is

$$dM = dF \times z. \tag{28}$$

Substituting Eq. (26) into Eq. (27),

$$dM = E\frac{z^2}{\rho}dA. \tag{29}$$

The integration of Eq. (28) over the area is commonly expressed as

$$\frac{1}{\rho} = \frac{M}{EI}, \tag{30}$$

where I is known as the second moment of area and is the same as R in Eq. (22). Using Eqs. (19), (22) and (29), we can get the beam bending equation:

$$\frac{d^2y}{dx^2} = \frac{M}{EI}. \tag{31}$$

Depending on sign convention, the moment is sometimes written as –M. To solve the equation, we need the support or displacement boundary conditions are used to fix values of displacement (y) and rotations (dy/dx) on the boundary. Such boundary conditions are also called Dirichlet boundary conditions. Load and moment boundary conditions involve higher derivatives of y and represent momentum flux. Flux boundary conditions are also called Neumann boundary conditions.

Shear forces are related to bending moments by

$$\frac{dM}{dx} = -F. \tag{32}$$

A differential load q(x) at a point can be expressed as

$$q\left(x\right) = -\frac{dF}{dx} = \frac{d^2M}{dx^2}. \tag{33}$$

Substituting Eqs. (31) and (32) into Eq. (30), we get

$$EI\frac{d^4y}{dx^4} = q\left(x\right), \tag{34}$$

which can be solved for a point-loaded cantilever with a tip load P:

$$y = -\frac{PL^3}{3EI}. \tag{35}$$

We can also use singularity functions to represent loadings. Singularity functions are indicated with angled brackets $< \;\; >$ in contrast to traditional curved brackets $(\;\;)$. Singularity function differentiates and integrates normally as one would with a standard variable (integrating $< x >^2$ would give us $\frac{1}{3}x^3$) but the unique thing about singularity functions is that if the power is less than 0, we simply ignore the variable ($\int < x >^{-2} = \frac{-1}{2} < x >^{-1} = 0$ but will be apparent to higher degrees of integration). It is also similar to the unit step function in which if the evaluation in between the brackets is less than 0, the term is zero, and it is the variable if it is more than 0, i.e. ($< x - a >^2 = 0 \quad for \quad x < a, \quad and \quad < x - a >^2 = x^2 \quad for \quad x > a$).

(i) Constant load such that the load at m is ω_0 when $L > m > a$:

$$Load(m) = -\omega_0 < m - a >^0 N. \tag{36}$$

(ii) Linear load such that the load at m is b*(m−a) when $L > m > a$. $< x - a >^n$ and n can take on higher orders (Fig. 8):

$$Load(m) = b < m - a >^1 N. \tag{37}$$

(iii) Moment load such that the load at m is M_0 when $L > m > a$. $< x - a >^n$ After each integration, the value of n increases by 1, and thus the moment load is perceived only after two integrations (Fig. 9):

$$Load(m) = M_0 < x - a >^{-2} N. \tag{38}$$

(iv) Impulse load such that the load at m is P when m = a (Fig. 10):

$$Load(m) = P < x - a >^{-1} N. \tag{39}$$

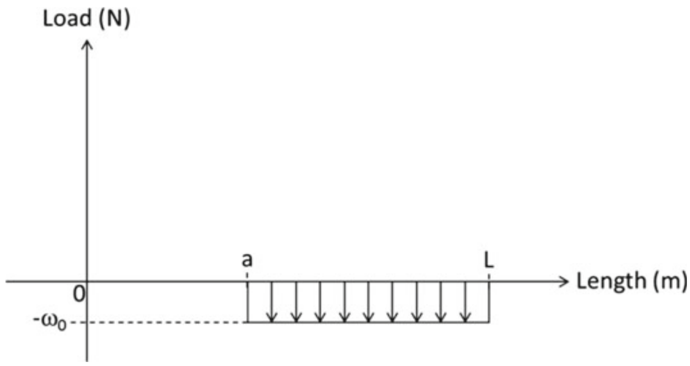

Fig. 8 Constant loading.

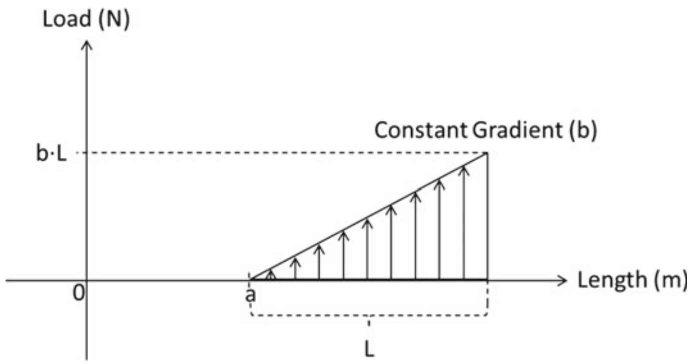

Fig. 9 Linear loading.

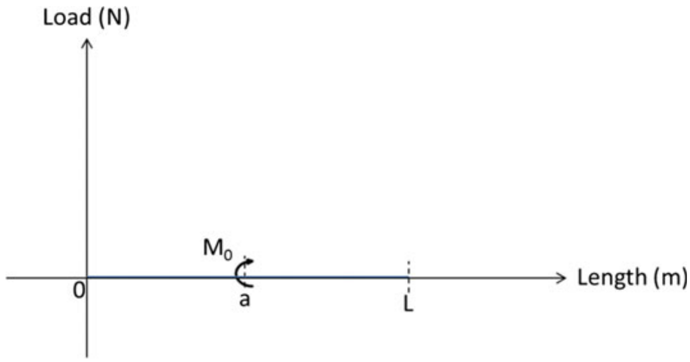

Fig. 10 Moment loading.

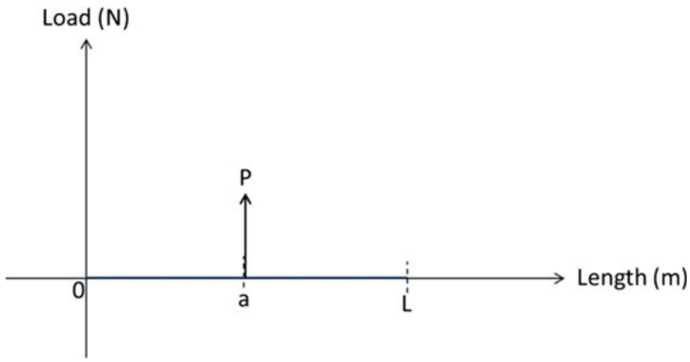

Fig. 11 Impulse loading.

Using free-body diagrams, the load and reaction forces at supports are defined along the length of the rod. The loads(m) are integrated twice to obtain M which is solved for Eq. (30) and is integrated twice again to find the deflection (Fig. 11).

For a magnetic tip experiencing magnetic forces and torques (bending moments),

$$q(x) = \iint F < x - a >^{-1} N + M < x - a >^{-2} Nm^{-1}. \tag{40}$$

This is solved by applying techniques discussed above to determine the deflection from the applied magnetics torques and forces. Additional boundary information such as bending strain can also be considered depending on the requirements.

4.4 Other Applications of Magnetic Tip Actuation

Other than guide wires and catheters, the magnetic navigations of drill, balloon and needles have also been recommended for a wide variety of surgical needs (Table 2).

5 Theory to Prototype

Based on the theory covered in Sects. 4.2 and 4.3, a wide variety of magnetic manipulators (Fig. 12) can be designed, tested and modelled. In the Fig. 12,

- A & B are guide wires with an attached magnetic head.
- C & D are 3D printed design which can be further modified to include a magnetic tip.
- D has multiple magnetic segments.
- E & F are nylon wires with a magnetic tip glued on top.

Table 2 A list of existing applications using magnetic tip actuation.

Surgical/Clinical application	Source
Cardiac ablation	StereoTaxis has developed magnetic catheters for cardiac ablation [6, 8, 10, 13, 43, 46]. By attaching multiple magnetics, the catheter has additional DOFs which allows for more redundancy in actuation. This directly translates to additional positioning of the catheter which is important for cardiac ablation where the heart is still beating and the tip of the catheter has to pulse back and forth in tandem. Stereotaxis has been implemented in a clinical setting [12, 16, 29, 52]
Nasobiliary tube	Placement of a magnetic catheter in a similar fashion [50] to above but for the Gastrointestinal tract
Guide wire control	US20070032746 [38]. A continuous magnetic strip is wrapped around the length of the guide wire for actuation. Such an approach allows for a customizable selection of magnetic elements along the guide wire to tune the magnetic response to various surgical needs
Deep Brain Stimulation electrode implant	Magnetic field is used to guide the insertion of the needle into the deep regions of the brain [36]. The stators utilized here are upscaled versions of OctoMag and the actuators (permanent NdFeB magnets) are hinge supported allowing independent rotation relative to the base. Nitinol wires used to provide translational information while remaining compliant to bending along curvatures. The region of interest is currently 10 cm by 10 cm. Magnetics could also be used to assist needle puncture, making the procedure safer [39]
Angioplasty	A magnetic attachment to surgical balloons for positioning of the stent or balloon during angioplasty [44]
Stenting	Combining guide wire navigation with stenting allows the navigation of the stent to be directly guided to the target location [49]
Alignment of devices	Magnetics could also be used to connect to catheters together in-vivo to create a continuous delivery line. Without the aid of magnetics, this would be a tedious and ardous task for the surgeon to perform in the patient [9]
Drilling	Precise Steering and Unclogging Motions of a Catheter With a Rotary Magnetic Drill Tip Actuated by a Magnetic Navigation System [21]
Drilling and Stenting	Utilizing precession and rotations in magnetic fields, both drilling and release of a sheathed stent are shown [27]
Micro-endoscope	A magnetic ferrofluid suspension rotor is used to turn a small mirror for micro-endoscopy applications [5]

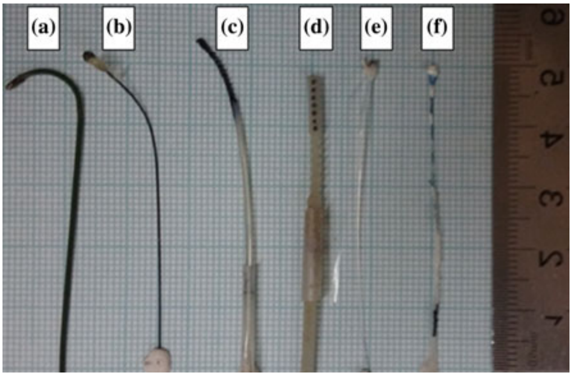

Fig. 12 Flexible manipulators.

5.1 Test Phantom (F)

The outer diameter of the guide wires and nylon wire were similar, 0.35 mm, but the nylon wire is much more flexible than the guide wire. To make the distal region stiffer, we used a polymer (polycaprolactone) coating via immersion coating; equivalently an external catheter which is more ridged can encase the nylon wire. This will constrict the flexible deflection length to about 20 mm. The magnetic attachments are based on polycaprolactone as the adhesive. The attachment can be much more developed and we cover some ideas in the next section. The size of the attached magnetic component should be similar size to the GW itself; in our case fabrication limitations have left it into a cube of $1 \pm 0.5\,\text{mm}^3$. There is a trade-off if the attached magnetic component is too small; the magnetic dipole moment from the dipole will be weak and may have to be compensated by increasing the external magnetic fluxes from the stators.

5.2 3D Printed Designs (C and D)

Given cross-sectional area limitations, we propose two alternative methods to overcome this via 3D rapid prototyping with flexible material, based on the stratasys Objet260 Connex3 and TangoGray FLX950. The idea is to create allowance for magnetic components along the axis of the manipulator such that the summation of forces and torques will be able to compensate the individually small magnetic moments. Additionally, the benefit of 3D printing comes in when the user wants to customize the design. For example, the distances between the magnetic components and the flexible regions can be rearranged to create unique compositions which can cater to the various medical needs (Fig. 13).

A simple model of guide wire will consist of three portions. The relatively ridged rod transmits axial translation forces from the proximal to the distal end. Since the dimensions are usually fixed, the material choice is the key parameter to deciding its

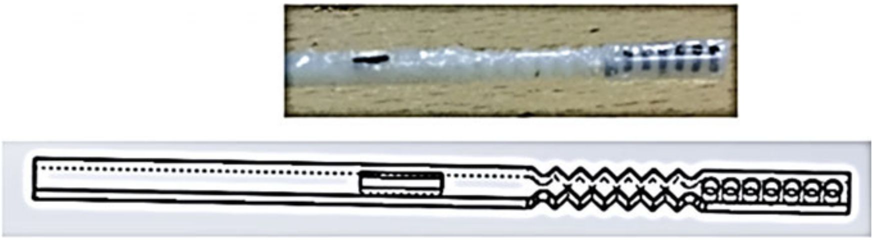

Fig. 13 Flexible manipulator D.

flexibility; notable choices are titanium and steel for small diameters. The sequential segment is the flexible region and defines the bending length. This design removes excess material to induce flexibility relative to the distal end, enhancing bending at this region. Attached to the tip of the flexible region is the magnetically controlled region. This region translates information from the external electromagnetic coils for tetherless actuation. The attachment could come in many forms; here holes for small cylindrical magnets are designed.

There are many methods for magnetic incorporation into the material. Other than a ridged magnetic material, magnetic powder and liquid are also possible means to make a manipulator magnetically responsive. While a simple adhesive solution is possible for ridged permanent magnets, some design may require more sophisticated methods. In extension to the adhesive method, the adhesive can be contained.

Polycaprolactone, a thermo-polymer can be stored in a predefined volume. It is contained in the volume by surface tension and upon heating (water bath); above transition temperature, the guide wire can be inserted into the cavity and the polymer is cooled again to lock the guide wire in place (Fig. 14).

A mechanical tight fit design may also be an option to attaching a magnetic component. In Fig. 15, the threads hold the pieces in place and as it is pushed into the tapered hole. Many other variants are possible with this concept and it is also

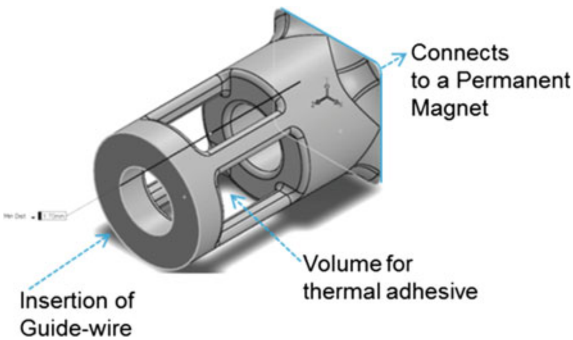

Fig. 14 Connector design for adhesive attachment.

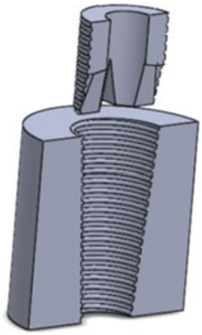

Fig. 15 Connector design for mechanical attachment.

applicable to other fields, such as the luer-lock design. The concept of modular attachment can be beneficial to guide wires which need different types of magnetic attachments. It is also beneficial to the integration of electromagnetic devices into the clinical setting where guide wires are already existent and it is not necessary to custom design a guide wire with the electromagnetic coils. Physicians need only to attach the magnetic tip for magnetic control when needed.

5.3 Control Electronics

Additionally, electronics should be utilized for control such as an Arduino environment. A microcontroller receives joystick bending and translates it into coil currents; refer to Fig. 16 for electronic control. Feedback should also be incorporated for closed-loop control.

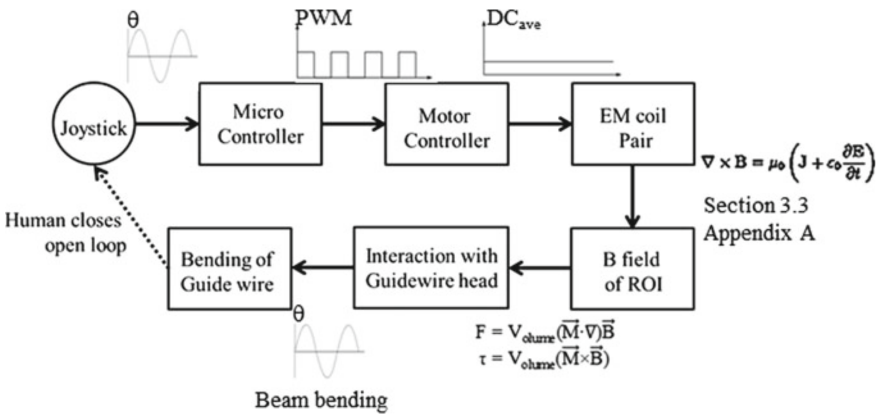

Fig. 16 Information flow of the control electronics.

A joystick or buttons can be used to register user input as an electrical signal. This signal is read by a microcontroller (such as Arduino) and converts the signal into a PWM wave form. PWMs capture the analogue information as a percentage of the duty cycle. A motor controller unit (e.g. L298N) perceives the PWM signal and outputs a DC signal which is an amplification of the initial joystick signal. The motor control unit also defines the maximum voltages and hence the maximum currents. The potential differences across the electromagnetic coils drive a current and by ampere circuital law this generates magnetic fields. The magnetic potentials and gradients in the region of interest interact with the magnetic tip, giving rise to controllable mechanical deflection.

6 Classification of Guide Wire Model

While there are many important parameters to guide wires, we focus here on the bending angle. The bending angle is an important aspect which indicates the type of vessels/blockages it can navigate. We show here a Bézier curve reconstruction to obtain the bending angles. The Bézier curve uses points along the curve to reconstruct the parametric model.

6.1 Bending Angle

To obtain our points, we use colour-coded images (Fig. 17a) to define the centroids (Fig. 17b) along the path of the guide wire. The red line shows the reconstructed curve (Fig. 17). As this is a reconstruction using imaging, errors propagating from any of the processes along the work flow will contribute to some degree of error. These errors can be minimized by using more points along the curve especially at regions when the curvature is high. For guide wire applications, the deflection is relatively small and the bending radius is usually large across the length of deflections, and thus errors perceived do not affect the conclusions drawn significantly. The colour codes translate to cells which break the continuous manipulator into smaller segments.

To locate the centroid, processing software (such as MATLAB) is recommended as it has pre-built functions to handle image processing. The mean/medians of each segment is perceived as a histogram on the X/Y axis and is taken to be the centre. A Bézier function takes in the coordinates of each point in order of progression from base to tip. Each point is connected to subsequent points forming the first-order line. A number of the parametric intervals are then selected. This number represents the segmentation between points on the first-order line, and more parametric point will mean a smooth curve at the cost of computational power. Points on the first-order line corresponding to the parametric integer build the second-order line. The line-forming process is nested until no further lines can be built. On the final-order line, the point corresponding to the parametric integer represents the Bézier curve's value

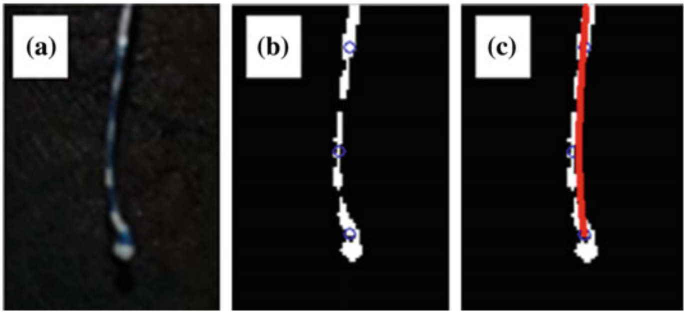

Fig. 17 The image processing for curve reconstruction.

at that parametric integer. The Bézier curve allows a continuous connection between the first and last coordinates, and allows us to interpolate and estimate coordinates for the entire curve.

The bending angle can be taken at any point along the Bézier curve. Here, we compare between the start and end of the curve. Given a joystick input (Fig. 18), we can get bending angles (Fig. 19) and the reconstructed curves at time points of interest (Fig. 20). Other notable parameters that are also extractable are the radius of curvature.

7 System Experiment

In the surgical context, the bending angles achieved can navigate obstacles such as stenosis.

Figure 21a Upon encounter of an obstacle, the bending angle can create different paths for advancement (Fig. 21b, c), and post-selection of path the guide wire can be

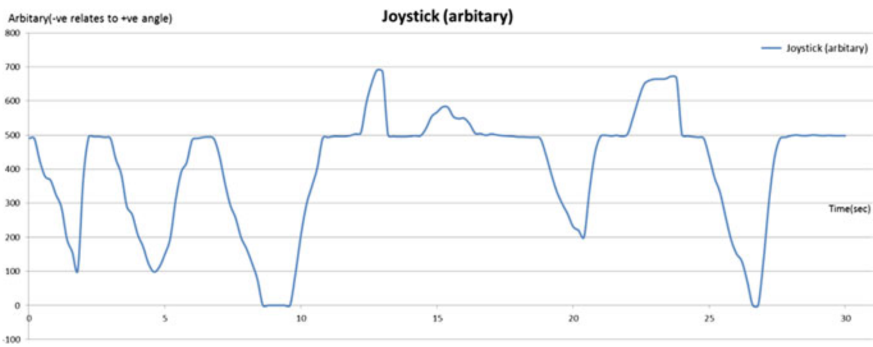

Fig. 18 Input from joystick.

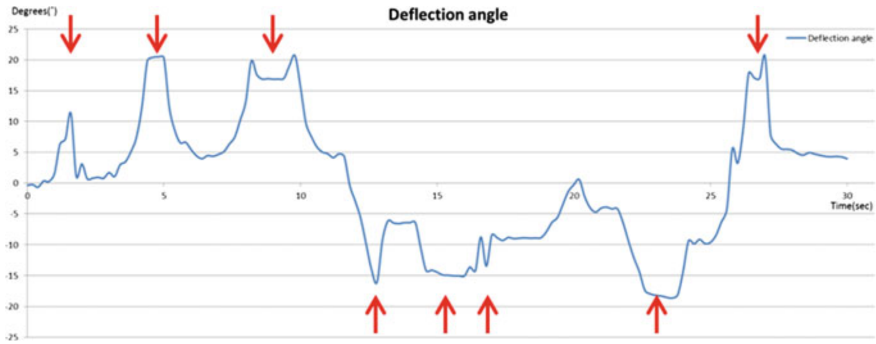

Fig. 19 Output in bending angles.

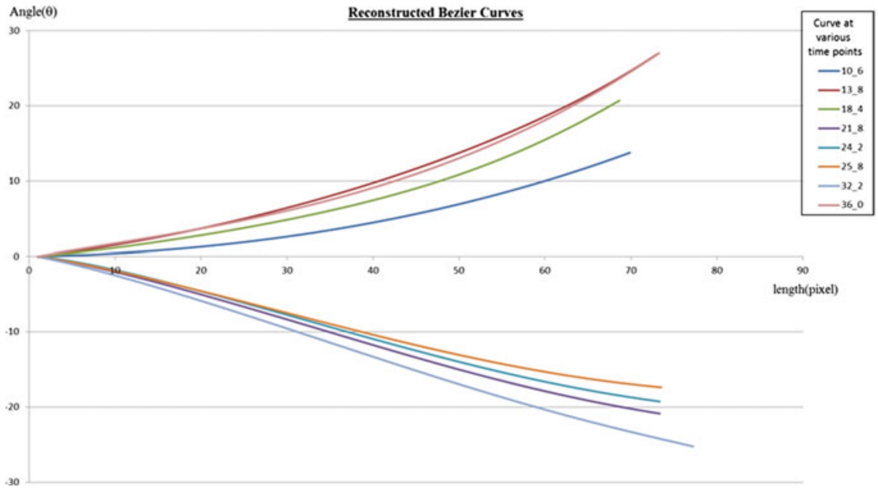

Fig. 20 Bezier curve reconstructions.

advanced to bypass the obstacle (Fig. 21d). In more realistic scenarios, the vision of the operator may be impaired and the actual deflection for advancement is not known. Thus, the operator would constantly sweep through different bending angles at the site to test for advancement; obstruction is detected either through angiography or through ultrasound of tactile information. The deflection shown here is translatable, although to a lesser extent, to more ridged guide wires.

Figure 22b indicates the neutral position of the guide wire. The guide wire is pre-curved and can preferentially bend in one direction (more compliant), while extension in the opposite direction is much more ridged. Compliant bending by electromagnetic interaction is shown in Fig. 22a and extension/straightening of the guide wire is shown in Fig. 22c. As the bending angles are rather small due to the stiffness of the guide wire, Fig. 22a, b and c is superimposed in Fig. 22d. The rigidity in straightening the guide wire is also visible by comparing deflections between Fig. 22a and c. A stronger

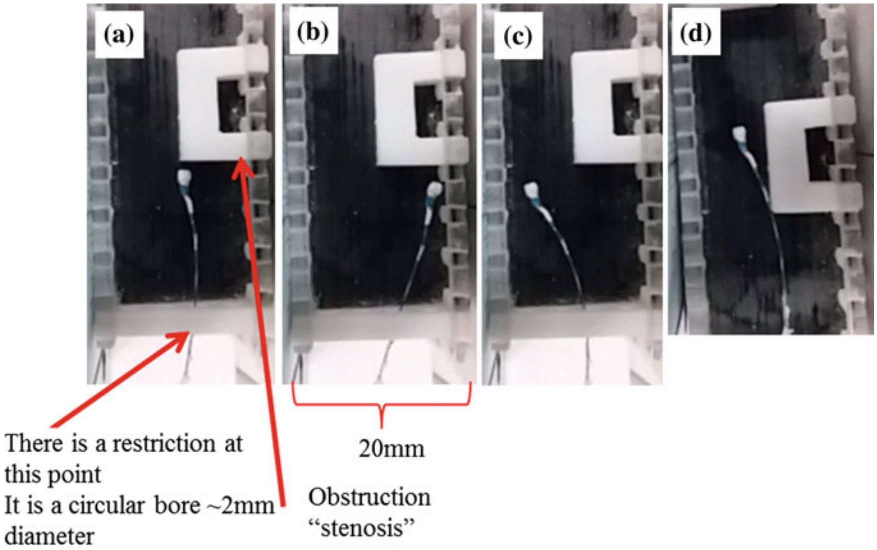

Fig. 21 Prototype navigating a modelled environment.

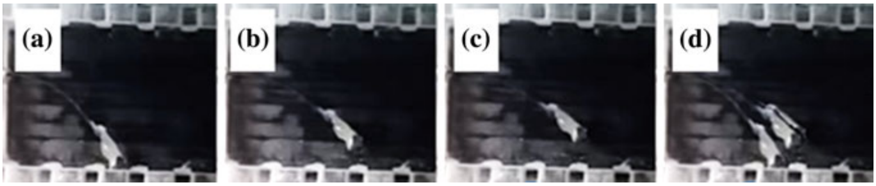

Fig. 22 Guide wire deflection.

magnetic field generated will allow further deflection angles but the concept shown here will allow physicians to direct control over the distal tip which was previously not possible. The reliance on buckling of the guide wire from traditional methods is removed along with the associated risk and uncertainties.

8 Conclusions and Future Direction

Manipulator-based surgical equipment generally suffers from mechanical disturbance during operation and this chapter has illustrated the electromagnetic approach to improve controllability over the distal end. Improving distal end control such as in guide wires for surgical procedures can improve treatment options (angioplasty). The use of untethered electromagnetic interactions consists of two main parts: the actuator and the stator. There are many ways to design and construct the system but ultimately the end goal is to achieve a controllable deflection/bending angle to navigate obstacle and overcome distal mechanical control limitations. We have further shown in this chapter a method to achieve such a system with a simple magnetic tip attachment. From the base design, more complicated features can be added to cater for various needs. From a design stand point, the introduction of electromagnetic control should reduce the mechanical complexity of the procedure. To illustrate, an electromagnetic guide wire can replace a wide range (with different curvatures and bending angles) of guide wire each catering to a specific anatomical region. Therefore, one should consider electromagnetic manipulation as beneficial to distal control and additionally can impact integration at a low-cost implementation.

While electromagnetics provides a good means to actuate, the need for closed-loop control in stability is not covered in this chapter. Present imaging modalities include MRI, NIR and ultrasounds. The acoustic or optical images should be extracted for features to perform real-time tracking such that automation can be achieved. The system which is electromagnetically driven could, in theory, also be used for sensing and position guidance. The domain of transducers and integration with external imaging systems should not be overlooked. The incorporation of electromagnetic sensing capabilities can be achieved with Hall effect sensors, flex sensor, or even inductor-based sensors. However, considering that the use of ultrasound is well established, incorporation of an Ultrasonic system for automated guidance and delivery of guide wire is likely to be the direction in the near future.

8.1 Electromagnetic Actuation in PAD: Future Directions

A notable limitation in current magnetic navigation systems is the use of the external magnetic field generators which are rather bulky in size in order to generate the 0.1–0.15 Tesla fields. Thus if possible the external generators implemented should not increase the bulk of the design to the point where it obstructs movement or vision of the patient or the physician. In an idealized case, the external generators should be eliminated completely and reduce the bulk of the system; this would be favourable in saving the theatre space required to do the procedure.

Present catheters (4 mm) used are also much larger than guide wires (1 mm) and there exists a challenge to minimize the design. However, the magnetic guidance systems were documented to be effective on micro-robots (less than 1 mm), and thus it should be viable for a guide wire design to be magnetically manipulated. There exists a gap in the current implementations for magnetically manipulated guide wires for where there are more stringent requirements on the guide wires as the arteries are much small in the distal positions of the peripherals limbs. Present implementations are focused on the applications in the heart and the brain.

Implementation for the magnetic manipulation poses a viable option for PAD as the magnetic fields to not harm the body and allows for contactless transmission of force/control through human tissue. A concern could exist where the imaging X-rays (CT) or MR imaging could interfere with control of the guide wire, but as Sterotaxis Epoch system is an implemented device, this should be a trivial issue.

An additional note is that current guide wire systems have only used imaging techniques for position sensing, and thus it may be prudent to include force sensing capabilities such as those used in calcific iliac occlusion devices TruePathTM to provide haptic/tactile feedback to the surgeons. Further, while there have been many approaches for magnetic guide wire design, none of them has been tested for implementation for PAD. Thus, there exists a need to design a specific system catered for PAD.

Acknowledgements This work is supported by the Singapore Academic Research Fund under Grant R-397-000-173-133, NUSRI China Jiangsu Provincial Grant BK20150386 & BE2016077 awarded to Dr. Hongliang Ren.

References

1. Aalami, Oliver, et al. 2015. Prevention of Juxta-Anastomotic AV Fistula Stenosis With Implantation of an ePTFE Covered Endograft at Time of AV Fistula Creation. *Journal of Vascular Surgery* 61 (6): 101–102S.
2. J.J. Abbott et al. 2007. Modeling Magnetic Torque and Force for Controlled Manipulation of Soft-Magnetic Bodies. In *IEEE Transactions on Robotics* 23.6, pp. 1247–1252. ISSN: 1552-3098. https://doi.org/10.1109/TRO.2007.910775.
3. Abbott, Jake J., et al. 2009. How Should Microrobots Swim? English. *The International Journal of Robotics Research* 28 (11–12): 1434–1447.
4. Afshin Anssari-Benam, Dan L. Bader, and Hazel R. C. Screen. 2011. A combined experimental and modelling approach to aortic valve viscoelasticity intensile deformation. *Journal of Materials Science: Materials in Medicine* 22.2, pp. 253–262.
5. Assadsangabi, Babak, et al. 2016. Catheter-based microrotary motor enabled by Ferrofluid for microendoscope applications. *Journal of Microelectromechanical Systems* 25 (3): 542–548.
6. Bauernfeind, Tamas, et al. 2011. The magnetic navigation system allows safety and high efficacy for ablation of arrhythmias. *Europace* 13 (7): 1015–1021.
7. Bouchebout, Soukeyna, et al. 2012. An overview of multiple DoF magnetic actuated micro-robots. *Journal of Micro-Nano Mechatronics* 7 (4): 97–113.
8. Jason Bradfield et al. 2012. Catheter ablation utilizing remote magnetic navigation: a review of applications and outcomes. *Pacing and Clinical Electrophysiology* 35 (8): 1021–1034.
9. William D.F Christopher P.S. 2010. *U.S. Patent No.2012,0,089,089*. en. Washington, DC: U.S. Patent and Trademark Office.
10. Julian K. Chun et al. 2007. Remote-controlled catheter ablation of accessory pathways: results from the magnetic laboratory. *European Heart Journal* 28.2, pp. 190–195.
11. Dember, Laura M., et al. 2005. Design of the dialysis access consortium (DAC) clopidogrel prevention of early AV fistula thrombosis trial. *Clinical Trials* 2 (5): 413–422.
12. Ernst, Sabine, et al. 2004. Initial experience with remote catheter ablation using a novel magnetic navigation system: magnetic remote catheter ablation. *Circulation* 109 (12): 1472–1475.
13. Faddis, Mitchell N., and Bruce D. Lindsay. 2003. Magnetic catheter manipulation. *Coronary Artery Disease* 14 (1): 25–27.
14. F.G.R. Fowkes et al. 2013. Comparison of global estimates of prevalence and risk factors for peripheral artery disease in 2000 and 2010: a systematic review and analysis. *Lancet (London, England)* 382.9901, pp. 1329–1340.
15. Anna Franzone et al. 2012. The role of atherectomy in the treatment of lower extremity peripheral artery disease. *BMC surgery 12 Suppl 1. Suppl 1*, S13–S13.

16. Haghjoo, Majid, et al. 2009. Initial clinical experience with the new irrigated tip magnetic catheter for ablation of scar-related sustained ventricular tachycardia: a small case series. *Journal of Cardiovascular Electrophysiology* 20 (8): 935–939.
17. Hod, Tammy, et al. 2014. Factors predicting failure of AV fistula first policy in the elderly: predictors of AVF failure. *Hemodialysis International* 18 (2): 507–515.
18. Walter H. Hörl et al. 2004. *Replacement of renal function by dialysis*. Fifth / by Walter H. Hörl, Karl M. Koch, Robert M. Lindsay, Claudio Ronco, James F. Winchester (-in-chief).;1; 5th; Dordrecht: Springer Science+Business Media. ISBN: 9781402022753; 1402022751;9789401570121; 9401570124.
19. Iacovacci, Veronica, et al. 2015. Untethered magnetic millirobot for targeted drug delivery. *Biomedical Microdevices* 17 (3): 1–12.
20. Ahmed A. Al-Jaishi et al. Patency rates of the arteriovenous fistula for hemodialysis: a systematic review and meta-analysis. *American Journal of Kidney Diseases: The Official Journal of the National Kidney Foundation* 63.3 (2014;2013), p. 464.
21. Jeon, S.M., and G.H. Jang. 2012. Precise steering and unclogging motions of a catheter with a rotary magnetic drill tip actuated by a magnetic navigation system. *IEEE Transactions on Magnetics* 48 (11): 4062–4065.
22. Jeon, Seungmun, et al. 2010. Magnetic navigation system with gradient and uniform saddle coils for the wireless manipulation of micro-robots in human blood vessels. *IEEE Transactions on Magnetics* 46 (6): 1943–1946.
23. Jeong, Semi, et al. 2011. Enhanced locomotive and drilling microrobot using precessional and gradient magnetic field. *Sensors and Actuators A: Physical* 171 (2): 429.
24. K. Konner. 2003. Vascular access in the hemodialysis patient personal experience and review of the literature. en. In *Hemodialysis International* 7.2, pp. 184–190. https://doi.org/10.1046/j.1492-7535.2003.00026.x.
25. Lanzer, P. 2013. *Catheter-Based Cardiovascular Interventions: A Knowledge-based Approach*. New York: Springer.
26. P. Lanzer and Inc Ovid Technologies. *Mastering endovascular techniques: a guide to excellence*. Philadelphia: Lippincott Williams & Wilkins, 2007; 2006; ISBN: 9781582559674; 1582559678.
27. Wonseo Lee et al. 2017. Selective motion control of a crawling magnetic robot system for wireless self-expandable stent delivery in narrowed tubular environments. *IEEE Transactions on Industrial Electronics* 64.2, pp. 1636–1644.
28. Lim, Gregory B. 2013. Peripheral artery disease pandemic. *Nature Reviews Cardiology* 10 (10): 552.
29. Jianhua Liu et al. 2016. Design and fabrication of a catheter magnetic navigation system for cardiac arrhythmias. *IEEE Transactions on Applied Superconductivity* 26.4, pp. 1–4.
30. X. Liu, G.J. Mancini, and J. Tan. 2015. Design and Analysis of a Magnetic Actuated Capsule Camera Robot for Single Incision Laparoscopic Surgery. In *2015 IEEE/RSJ International Conference on Intelligent Robots and Systems (IROS)*, pp. 229–235. https://doi.org/10.1109/IROS.2015.7353379.
31. Arthur W. Mahoney and Jake J. Abbott. 2016. Five-degree-of-freedom manipulation of an untethered magnetic device in fluid using a single permanent magnet with application in stomach capsule endoscopy. *The International Journal of Robotics Research* 35.1-3, 129–147.
32. Hamal Marino, Christos Bergeles, and Bradley J. Nelson. 2014. Robust electromagnetic control of microrobots under force and localization uncertainties. *IEEE Transactions on Automation Science and Engineering* 11.1, 310–316.
33. Misakian, M. 2000. Equations for the magnetic field produced by one or more rectangular loops of wire in the same plane. *Journal of research of the National Institute of Standards and Technology* 105 (4): 557.
34. Mukherjee, Debabrata, et al. 2010. *Cardiovascular Catheterization and Intervention: A Textbook of Coronary, Peripheral, and Structural Heart Disease*. Baton Rouge: CRC Press.
35. J.M.S. Pearce. 2009. Henry gray's anatomy. In *Clinical Anatomy* 22.3, pp. 291–295. issn: 1098-2353. https://doi.org/10.1002/ca.20775.

36. A. J. Petruska et al. 2016. Magnetic needle guidance for neurosurgery: Initial design and proof of concept. In *2016 IEEE International Conference on Robotics and Automation (ICRA)*, pp. 4392–4397. https://doi.org/10.1109/ICRA.2016.7487638.
37. Peter Schneider. *Endovascular skills : guidewire and catheter skills for endovascular surgery*. 3rd ed. CRC Press, 2009;2008; ISBN: 1420069373; 9781420069372.
38. J.C. Sell. 2007. *U.S. Patent No. 2007,0,032,746*. Washington, DC.
39. J.C. Sell. 2005. *U.S. Patent No. 8,419,681*. Washington, DC: U.S. Patent and Trademark Office.
40. S. Song, H. Yu, and H. Ren. 2015. Study on mathematic magnetic field model of rectangular coils for magnetic actuation. In *2015 IEEE 28th Canadian Conference on Electrical and Computer Engineering (CCECE)*, pp. 19–24. https://doi.org/10.1109/CCECE.2015.7129153.
41. Studies from Swiss Federal Institute of Technology Have Provided New Information about Nanoparticles. In *Nanotechnology Weekly* (2012), p. 352.
42. Subramaniam, Tavintharan, et al. 2011. Distribution of ankle-brachial index and the risk factors of peripheral artery disease in a multi-ethnic Asian population. *Vascular Medicine* 16 (2): 87–95.
43. Tamas Szili-torok et al. 2012. Catheter ablation of ventricular tachycardias using remote magnetic navigation: a consecutive case-control study. *Journal of Cardiovascular Electrophysiology* 23 (9): 948–954.
44. Libo Tang, Yonghua Chen, and Xuejian He. 2007. Magnetic force aided compliant needle navigation and needle performance analysis. IEEE, pp. 612–616. ISBN: 1424417619; 9781424417612; 9781424417582; 1424417589.
45. TDK Europe – *EPCOS - Material Data Sheets*.
46. A.S. Thornton et al. 2006. Magnetic navigation in AV nodal re-entrant tachycardia study: early results of ablation with one- and three-magnet catheters. In *Europace : European Pacing, Arrhythmias, and Cardiac Electrophysiology: Journal of the Working Groups on Cardiac Pacing, Arrhythmias, and Cardiac Cellular Electrophysiology of the European Society of Cardiology* 8.4, pp. 225–230.
47. I. Tunay. 2004. Modeling magnetic catheters in external fields, vol. 1. IEEE, pp. 2006–2009. ISBN: 9780780384392; 0780384393.
48. I. Tunay. 2004. Position control of catheters using magnetic fields. In IEEE, pp. 392–397. ISBN: 0780385993; 9780780385993;
49. J.C Viswanathan R.R. and Sell. 2006. *U.S. Patent No.8,348,858*. Washington, DC: U.S. Patent and Trademark Office.
50. Watanabe, Seitaro, et al. 2013. Positioning of nasobiliary tube using magnetloaded catheters. *Endoscopy* 45 (10): 835–837.
51. J.E. White et al. 2012. Development of a lorentz-force actuated intravitreal jet injector. In IEEE, pp. 984–987. ISBN: 1557-170X.
52. Mark, A. Wood, et al. 2008. Remote magnetic versus manual catheter navigation for ablation of supraventricular tachycardias: a randomized, multicenter trial. *Pacing and Clinical Electrophysiology* 31 (10): 1313–1321.
53. Wu, Cong C., et al. 2015. The outcome of the proximal radial artery arteriovenous fistula. *Journal of Vascular Surgery* 61 (3): 802–808.
54. Steven Wu and Sanjeeva P. Kalva. 2015. *Dialysis Access Management*. Cham: Springer International Publishing. ISBN: 3319090933; 9783319090931; 9783319090924; 3319090925.
55. Zhou, H., J. Sun, B.S. Yeow, H. Ren 2016. Multi-objective parameter optimization design of a magnetically actuated intravitreal injection device. In IEEE 14th International Workshop on Advanced Motion Control (AMC). *Auckland, New: Zealand* 2016: 430–435. https://doi.org/10.1109/AMC.2016.7496388.

Design and Analysis of Magnetic Suspension Actuators in Medical Robotics

Jinji Sun and Hongliang Ren

Abstract The introduction of surgical robots improves the quality of healthcare due to the minimal invasiveness, reduced pain of patients, improved efficiency, accuracy, and the efficacy of surgery. The majority of the existing surgical robotic systems are based on master–slave teleoperation mode. The emerging handheld collaborative control modes in robotic systems omit the teleoperation master, and instead use handheld intelligent controls to directly drive its actuator end in order to eliminate motion control uncertainties such as tremors. This chapter puts forward a novel kind of handheld robot system driven by magnetic actuators based on the magnetically suspended technology. The configuration analysis and the design method of magnetic bearing with current bias are presented, and then the analysis and method of the 1-DOF (Degree of Freedom), 3-DOF, and 4-DOF magnetic suspension-based robotic actuator systems are proposed in details.

1 Introduction

1.1 Background

Minimal invasiveness and high accuracy are the two basic characteristics of modern medical science. Information technology, digital medical technology, and intelligent instruments, such as computer and robot, improve the modern medical technology, especially the surgery medical technology [1, 2]. Since 1990s, surgical robot technology has become an international frontier research hotspot, and gradually formed a cross disciplinary with the integration of advanced manufacturing, intelligent control, information technology, medical science, and other fields [3, 4]. The introduction

J. Sun · H. Ren (✉)
Faculty of Engineering, Department of Biomedical Engineering,
National University of Singapore, Singapore 117575, SG, Singapore
e-mail: sunjinji2001@163.com

H. Ren
e-mail: ren@nus.edu.sg

H. Ren and J. Sun (eds.), *Electromagnetic Actuation and Sensing in Medical Robotics*,
Series in BioEngineering, https://doi.org/10.1007/978-981-10-6035-9_5

of surgical robot is the key means to realize and improve the quality of healthcare because it can reduce the wound pain of patients, improve the efficiency, accuracy, and the effect of surgery effectively.

For the main surgical robot system [5], the accuracy and stability of microsurgical operation [6] include micro biological research [7, 8], micro operation for industrial components, and so on. The current manual indirect micro operation mainly depends on the microscopic image guidance and the end actuator action [9]. The general method is solved by using a robot-assisted control system [10], and the novel handheld collaborative control mode robot system which can eliminate the tremor of the actuator itself by intelligent control using handheld device. The biggest advantages of the handheld method are intuitive operation, safety, and economic use of space when compared to the traditional remote operation robot arm system [11]. The doctor can get the same results without auxiliary tools and traditional visual feeling, while retaining the existing surgical techniques. It is helpful to improve the recognition of the robot. The handheld operation also has security advantages compared with the other remote manipulator system. Not only does it need less space to operate, it can also allow the doctor to control the movement of the end actuator. Consequently, the terminal equipment can be removed rapidly at the condition of patients with accidental movement [12]. Although the micro surgical robot technology has recently appeared, the traditional master–slave remote operation robot industry standard system is usually expensive, complex, huge, heavy, and cannot be used in handheld micro-surgery [13].

To solve the problems mentioned above, this chapter puts forward a novel kind of handheld robot system driven by magnetic actuators based on the magnetically suspended technology. The analysis method and design method are presented as well. At first, the primary components and working principles are introduced, second, the configuration analysis and the design method of magnetic bearing with current bias are presented, and then the analysis and method of the 1DOF (Degree of Freedom), 3DOF, and 4DOF magnetic suspension- based robotic actuator systems are proposed in detail. Finally, the expectation of magnetic actuator system, such as small volume magnetic actuator and self-sensing magnetic actuator system and its control method, is introduced.

Cleanliness of medical environment is said to greatly affect the reliability and yield rate of semi-conductor circuits. Since the integration of semi-conductor circuit is increasing and the width of the circuit pattern reaching the order of sub-micron, prevention of dust and oil vapor generation in clean rooms is becoming an even greater necessity. To avoid the dust generation from robots, the ideal one is to develop inherently clean robots by using magnetic bearings and magnetic levitation to eliminate mechanical contacts which are the worst source of dusts. The clean room robot installing magnetic bearings in its joints is more expansive than the conventional sealed robots. And since the robots without mechanical contacts need no lubricant, they are quite suitable for applications in a vacuum and in space. Clean room robots using magnetic bearings are expected to have the advantages and functions beside the cleanliness as friction-free, stiffness-aware, force-sensing, vibration-balancing.

Thanks to the clean actuation capability, magnetically suspended centrifugal rotors have been utilized to pump blood flows for circulation assistance, working in pericardial space. For example, the HeartMate 3 Left Ventricular Assist System (LVAS) function is to bring oxygen-rich blood from the lungs throughout the body.

1.2 Magnetically Suspended Micro-manipulations

Traditional surgical procedures require a very high degree of precision for each action performed by a physician. Complicated surgical procedures can only be carried out in a few specialist hospitals depending on experienced doctors, resulting in imbalances in medical resources. A small number of specialist hospitals overcrowding, and a large number of primary hospitals cannot carry out complex surgery. The application of robotic surgical technique makes operation more minimally invasive, more precise and safer. The current surgical robot system, represented by da Vinci of Intuitive Surgical Inc., USA, uses a robotic arm to simulate the surgeon's arm based on master–slave control, through a number of small, open-ended cavities into the human body and mainly in general surgery, urology etc., to achieve a clinical application. Its main purpose is for minimally invasiveness. While surgical accuracy is mainly dependent on hand–eye coordination, usually up to millimetre level, spot force perception also cannot be applied to sub-millimetre-level micro-operations, such as ophthalmic surgery, neurosurgery micro-nerve anastomosis, and so on.

In response to the challenges of precise and stable micro-manipulation, robot-assisted manipulators are used to stabilize or reduce hand movements. This has demonstrated the advantages of the application and has yielded preliminary results. Current micro-manipulation robotic systems are typically based on master–slave robotic system frameworks or handheld robotic system frameworks. The former master–slave control framework usually includes a main control console for input manipulation, and the operation precision is greatly improved by the process control by filtering out the surgical tremor and enlarging the operation ratio to the slave end. Some early studies include the da Vinci Surgical Robotic System, the Steady Hand system for retinal surgery developed by the team of R. H. Taylor, Johns Hopkins University, and the cell micromanipulator system [14].

The emerging handheld collaborative control mode robotic system omit the teleoperation master, and instead use handheld intelligent controls to directly drive its own actuator end in order to eliminate system control uncertainties such as tremors. This concept is similar to optical images in handheld cameras that are self-stabilizing and do not usually require the use of robotic arms. Compared to traditional teleoperation robotic arm systems, the biggest advantage of handheld approach are intuitive operation, safety and economy. Doctors can get the same intuitive feelings without the aid of the traditional way. Moreover, the doctors can keep the existing surgical skills, but with the simplicity and convenience, of a small space to complete the operation. This will help improve the acceptance of the robot recognition. Handheld operation also has the safety advantage of requiring less operating space than other teleoperation robotic arm systems while allowing the surgeon to maintain control of the end-effector movement.

2 Primary Components and Basic Structures

Nowadays magnetic suspended bearings have advantages over mechanical bearing in terms of wearing-free, lubrication-free and therefore they have been widely used in high-speed actuators or machines including flywheels and turbines. However, the goal is very different between the industry field and the medical field. In the industry field, high speed and large force are the main goals. In the medical field and high precision, small volume and low power loss are the main goals in medical field. Therefore, the structure of magnetic bearing will be different in these fields. At first, the primary components are introduced, and then the basic structure and working principle are presented, leaving the configuration of magnetic actuator is for introduced at last.

2.1 Primary Components

For a magnetically suspended system used in the medical field, it typically includes a rotor component, stator component, magnetic bearing and its control system. The function of each part is as follows:

(1) Rotor component, which is mounted the rotor of magnetic bearing, including the detected ring of displacement sensor if necessary.

(2) Stator component, which is typically the mounted stator of magnetic bearing, including the stator of displacement sensor if necessary, protected bearings and connectors. It not only supports the rotor, but also makes the rotor safe because the protected bearing can prevent the damage of system when it is debugged or overloaded. The electronic circuit can also be mounted to the stator component.

(3) Magnetic bearing and its control system. Magnetic bearing includes its stator component and rotor component, which can allow the rotor system to suspend stably at defined degrees of freedom. In addition, the control system of magnetic bearing includes a controller and power amplifier, and the associated control electronic components.

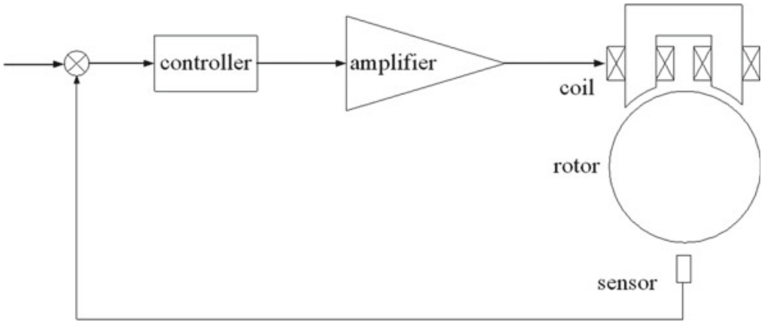

Fig. 1 Composition and working principle of magnetic bearing.

2.2 Basic Structure and Working Principle of Magnetically Suspended Actuators

In general, a magnetic bearing is arising from the attraction forces between stator and rotor, and it comprises of the coil or permanent magnet, rotor, sensor, controller and power amplifier [15].

As shown in Fig. 1, the principle of the a typical magnetic bearing system is as follows. The displacement between the rotor and stator is detected by the displacement sensor, and then it can be converted into control current for the coils through the controller and power amplifier. This allows the rotor to be controlled to the equilibrium position. However, the attraction force is not stable in essence between electromagnetic and ferrite material due to the relationship between current and electromagnetic force. The bias flux of magnetic bearings can be produced by the current and permanent magnet. The latter is of low power loss, so it is widely used for the aerospace application.

Magnetic bearings can be classified by many aspects. For example, it can be classified by radial magnetic bearing and axial magnetic bearing according to the direction of force. It can also be classified by the number of degrees of freedom (DOFs), for example, 1 degree of freedom (DOF), 2DOF, 3DOF, 4DOF, and 5 DOF [16], and by active magnetic bearing versus passive magnetic bearing according to the mode of force application.

In a regular magnetically suspended system, rotary freedom is controlled by the motor and other freedoms are controlled by the magnetic bearings. As mentioned above, the magnetic bearings can be classified by 1DOF $\sim$ 5 DOF according to the quantity of DOF, as shown in Fig. 2. In this figure, A denotes the active DOF and P denote the passive DOF [17].

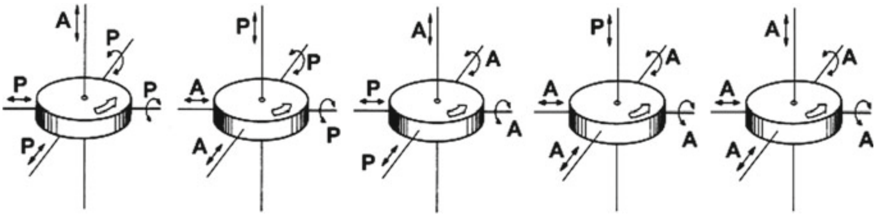

Fig. 2 Degree of freedom of magnetically suspended system **a** 1DOF **b** 2DOF **c** 3DOF **d** 4DOF **e** 5DOF.

3 Configuration Analysis

As mentioned above, the magnetic actuator system can be classified into 1DOF, 2DOF, 3DOF, 4DOF, and 5DOF magnetically suspended system according to the number of DOFs. More DOFs can realize the higher control dexterity, so the 1DOF, 3DOF, and 4DOF magnetic actuator systems are in more common in practice. The detailed contents are as follows.

3.1 Electromagnetic Analysis of Radial Magnetic Bearing with Current Bias

The magnetic bearing with current bias has advantages such as small volume, good controllability, easy to be assembled when compared to the magnetic bearing with permanent magnet bias. The magnetic bearing with current bias consists of radial magnetic bearing and axial magnetic bearing according to the direction of load capacity.

According to the theory of electromagnetism, the electromagnetic force is determined by the coil turns, permeability, magnetic pole area, current, and air gap between the stator and rotor [17], as shown in Fig. 3.

$$F = \frac{B^2 A}{\mu_0} = \frac{\mu_0 A N^2}{4} \frac{I^2}{\delta^2}, \tag{1}$$

where, μ_0 is the permeability of free space, A is the area of magnetic pole, N is the coil turns, I is coil current, and δ is length of the air gap between the stator and rotor.

The relationship between the force and the current is nonlinear according to the Eq. (1).

Force F_x represents the difference of forces between both magnets. Both forces are obtained by inserting the sum $I_0 + i_x$ and the difference $I_0 - i_x$ for current, as shown in Fig. 4. For the air gaps, $\delta + \mathrm{x}$ and $\delta - \mathrm{x}$ are inserted, the Eq. (1) is transformed to,

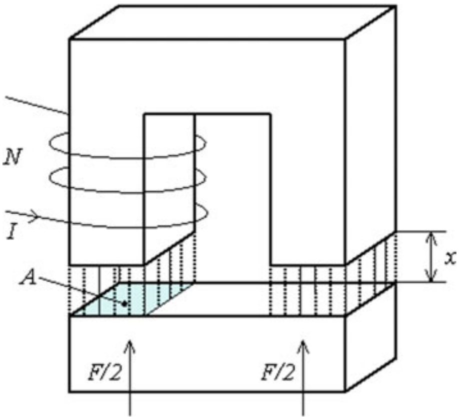

Fig. 3 Schematic of the electromagnetic force.

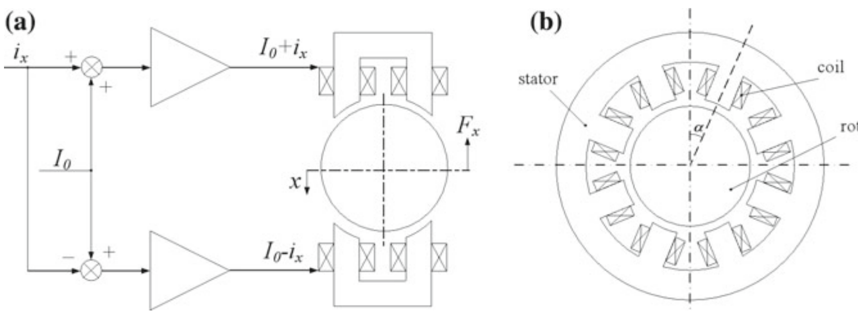

Fig. 4 **a** differential driving mode **b** End view of radial magnetic bearing Differential driving mode of the active magnetic bearing.

$$F_x = F_+ - F_- = k_r[\frac{(I_0 + i_x)^2}{(\delta + x)^2} - \frac{(I_0 - i_x)^2}{(\delta - x)^2}]cos\alpha, \tag{2}$$

where $k_r = \mu_0 N2A/4$, α is the half of magnetic poles angle.

When $x << x_0$ and $i_x << I_0$, the force of the rotor at an operation point can be written in the linearized form in the Eq. (2),

$$F_x = (\frac{4k_r I_0}{\delta^2} i_x - \frac{4k_r I_0^2}{\delta^3} x)cos\alpha = k_i i_x + k_s x \tag{3}$$

In general, k_i is current stiffness, k_s is displacement stiffness,

$$k_s = -\frac{\mu_0 A N^2 I_0^2}{\delta^3} cos\alpha \tag{4}$$

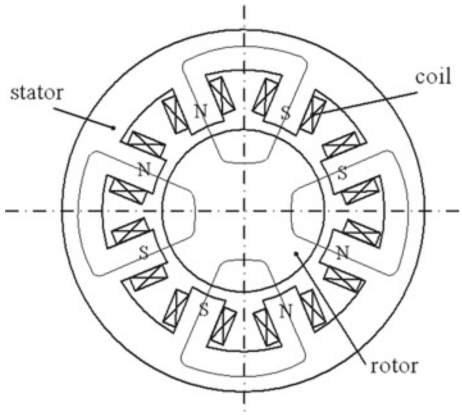

Fig. 5 Structure of radial magnetic bearing and magnetic circuit diagram.

$$k_i = \frac{\mu_0 A N^2 I_0}{\delta^2} cos\alpha \tag{5}$$

The typical radial magnetic bearing structure with eight magnetic poles is shown in Fig. 5, and the force expression is expressed,

$$F_x = (\frac{4k_r I_0}{\delta^2} i_x - \frac{4k_r I_0^2}{\delta^3} x) cos22.5^o \tag{6}$$

3.2 *Electromagnetic Analysis of Axial Magnetic Bearing with Current Bias*

The structure of axial magnetic bearing and magnetic circuit is shown in Fig. 6.

The forces acting on the plate is expressed in the Eq. (7) under the differential driving mode, ignoring the leakage flux.

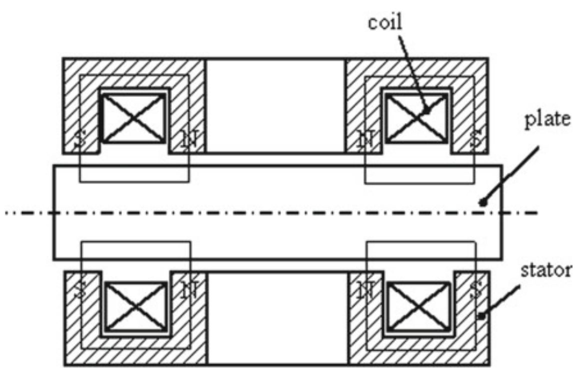

Fig. 6 Structure of axial magnetic bearing and magnetic circuit.

$$F_z = F_{z+} - F_{z-} = k_a[\frac{(I_0 + i_z)^2}{(\delta + z)^2} - \frac{(I_0 - i_z)^2}{(\delta - z)^2}] \tag{7}$$

where,

$$k_a = \frac{N^2}{2(\frac{1}{\mu_0 A_w} + \frac{1}{\mu_0 A_n})}$$

Then the displacement stiffness k_s and current stiffness k_i of the axial magnetic bearing are expressed,

$$k_s = -\frac{2N^2 I_0^2}{\delta^3(\frac{1}{\mu_0 A_w} + \frac{1}{\mu_0 A_n})} \tag{8}$$

$$k_i = \frac{2N^2 I_0}{\delta^2(\frac{1}{\mu_0 A_w} + \frac{1}{\mu_0 A_n})} \tag{9}$$

Especially, when the inner ring area is equal to the outer ring area, that is to say, $Aw = An = A$, the Eqs. (8) and (9) can be simplified:

$$k_s = -\frac{N^2 I_0^2 \mu_0 A}{\delta^3} = -\frac{4kI_0^2}{\delta^3} \tag{10}$$

$$k_i = \frac{N^2 I_0 \mu_0 A}{\delta^2} = \frac{4kI_0}{\delta^2} \tag{11}$$

3.3 Electromagnetic Design of Magnetic Bearing with Current Bias

For the design of magnetic bearing with current bias, the force is determined by the flux density in the air gap between stator and rotor, ampere turns (Ni), which affect the response speed and power loss. For magnetic bearing, ignoring the nonlinearity of magnetic circuit, the equation can be obtained,

$$\frac{dF}{dt} \propto \frac{dB^2}{dt} \propto \frac{d(Ni)^2}{dt} = 2N^2 i \frac{di}{dt} \tag{12}$$

The relationship between current and inductance is in the equation,

$$\frac{di}{dt} = \frac{U}{L} \tag{13}$$

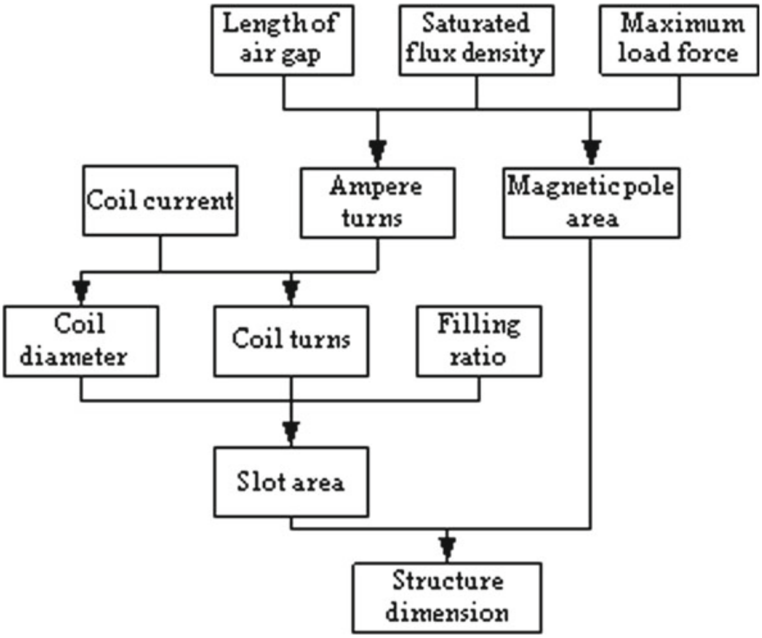

Fig. 7 Design process of magnetic bearing with current bias.

Then,

$$\frac{dF}{dt} \propto i\frac{U}{L/N^2} \tag{14}$$

where L is the inductance of coil, and U is the voltage of the power.

Because the coil inductance is proportional to the square of coil turns, the response speed of electromagnetic force is proportional to the current. As a result, less turns and larger current will be helpful to improve the response speed.

The design process of magnetic bearing with current bias is shown in Fig. 7. The key of design includes the determination of magnetic pole area and ampere turns. They are obtained by the equations as follows:

$$Ni_{max} = 2Ni_0 = 2B_{max}\delta/\mu_0 \tag{15}$$

$$A = \frac{\mu_0 F_{max}}{B_{max}^2 cos\alpha} \tag{16}$$

3.4 Analysis of Relationship Between Structure Parameters and Control System Parameters

The model of magnetically suspended rotor system is built as shown in Fig. 8. In this figure, the magnetically suspended rotor system consists of displacement sensor, controller, power amplifier, magnetic bearing, and rotor. The magnetic poles of magnetic bearing are drawn in the X direction in this figure.

3.4.1 Dynamic Model of Magnetically Suspended Rotor System

According to Fig. 8, the dynamic model of magnetically suspended rotor system is,

$$\begin{cases} m\ddot{x} = f_x + f_{x_d} \\ J_y\ddot{\beta} - H\dot{\alpha} = p_y + p_{y_d} \\ m\ddot{y} = f_y + f_{y_d} \\ J_x\ddot{\alpha} + H\dot{\beta} = p_x + p_{x_d} \end{cases} \tag{17}$$

It can be expressed in matrix form,

$$\boldsymbol{M}\ddot{\boldsymbol{q}} + \boldsymbol{G}_H\dot{\boldsymbol{q}} = \boldsymbol{f} + \boldsymbol{f}_d \tag{18}$$

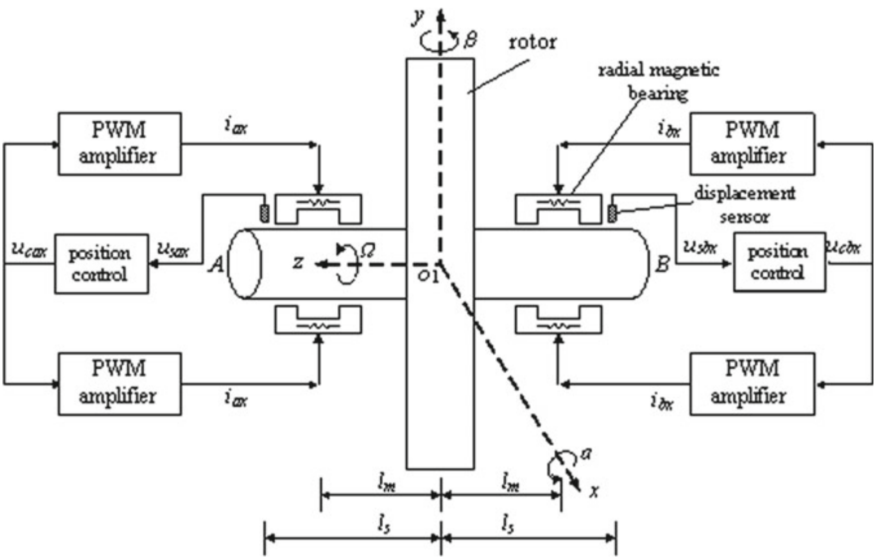

Fig. 8 Model of magnetically suspended rotor system.

where,

$$\mathrm{M} = \begin{bmatrix} m & 0 & 0 & 0 \\ 0 & J & 0 & 0 \\ 0 & 0 & m & 0 \\ 0 & 0 & 0 & J \end{bmatrix}, G_H = \begin{bmatrix} 0 & 0 & 0 & 0 \\ 0 & 0 & 0 & H \\ 0 & 0 & 0 & 0 \\ 0 & -H & 0 & 0 \end{bmatrix}, f = \begin{bmatrix} f_x \\ p_y \\ f_y \\ -p_x \end{bmatrix},$$

$$\mathrm{f}_d = \begin{bmatrix} f_{x_d} \\ p_{y_d} \\ f_{y_d} \\ -p_{x_d} \end{bmatrix}, q = \begin{bmatrix} x \\ \beta \\ y \\ -\alpha \end{bmatrix}$$

3.4.2 Model of Force in HMB

The force and torque of magnetic bearings in X and Y direction are given by,

$$\begin{cases} f_x = f_{ax} + f_{bx} \\ p_y = (f_{ax} - f_{bx})l_m \\ f_y = f_{ay} + f_{by} \\ p_x = -(f_{ay} - f_{by})l_m \end{cases} \tag{19}$$

$$\begin{cases} f_{ax} = K_x h_{max} + K_i i_{ax} \\ f_{bx} = K_x h_{mbx} + K_i i_{bx} \\ f_{ay} = K_x h_{may} + K_i i_{ay} \\ f_{by} = K_x h_{mby} + K_i i_{by} \end{cases} \tag{20}$$

It can be also expressed in matrix form,

$$\boldsymbol{f_m} = \boldsymbol{K_x q_m} + \boldsymbol{K_i i} \tag{21}$$

where,

$$f_m = [f_{a_x} f_{b_x} f_{a_y} f_{b_y}]^T, i = [i_{a_x} i_{b_x} i_{a_y} i_{b_y}]^T, q_m = [h_{max} h_{mbx} h_{may} h_{mby}]^T$$

According to Fig. 8, displacement and angle can be obtained,

$$\begin{cases} x = (h_{m_{a_x}} + h_{m_{b_x}})/2 \\ \beta = (h_{m_{a_x}} - h_{m_{b_x}})/2/l_m \\ y = (h_{m_{a_y}} + h_{m_{b_y}})/2 \\ \alpha = -(h_{m_{a_y}} - h_{m_{b_y}})/2/l_m \end{cases} \tag{22}$$

The formulation is obtained by above expressions (22) and (19),

$$\boldsymbol{q} = \boldsymbol{T}_m \boldsymbol{q}_m \tag{23}$$

$$\boldsymbol{f} = \boldsymbol{T}_m^{-T} \boldsymbol{f}_m \tag{24}$$

3.4.3 Model of Control System in Magnetically Suspended Rotor System

(i) Input and output model of the displacement sensor
Output voltage of displacement sensor model is expressed,

$$\begin{cases} u_{sax} = -k_s h_{sax} \\ u_{sbx} = -k_s h_{sbx} \\ u_{say} = -k_s h_{say} \\ u_{sby} = -k_s h_{sby} \end{cases} \tag{25}$$

It can be shown in matrix form,

$$\boldsymbol{u}_s = \boldsymbol{k}_s \boldsymbol{q}_s \tag{26}$$

where,

$$u_s = [u_{sax} u_{sbx} u_{say} u_{sby}]^T, q_s = [h_{sax} h_{sbx} h_{say} h_{sby}]^T$$

According to Fig. 8, the gap lengths deviation in X and Y direction and the angles of rotation about X and Y can also be indicated,

$$\begin{cases} x = (h_{sax} + h_{sbx})/2 \\ \beta = (h_{sax} - h_{sbx})/2/l_s \\ y = (h_{say} + h_{sby})/2 \\ \alpha = -(h_{say} - h_{sby})/2/l_s \end{cases} \tag{27}$$

Suppose that,

$$T_s = \frac{1}{2l_s} \begin{bmatrix} l_s & l_s & 0 & 0 \\ 1 & -1 & 0 & 0 \\ 0 & 0 & l_s & l_s \\ 0 & 0 & 1 & -1 \end{bmatrix}$$

Matrix form is given by,

$$\boldsymbol{q} = \boldsymbol{T}_s \boldsymbol{q}_s \tag{28}$$

(ii) Input and output model of PWM amplifier
Output voltage of PWM amplifier model is expressed by,

$$g_w = k_w g_{wLPF} \tag{29}$$

According to Fig. 8, output current of PWM amplifier can be obtained,

$$\begin{cases} i_{a_x} = k_w g_{wLPF} u_{cax} \\ i_{b_x} = k_w g_{wLPF} u_{cbx} \\ i_{a_y} = k_w g_{wLPF} u_{cay} \\ i_{b_y} = k_w g_{wLPF} u_{cby} \end{cases} \tag{30}$$

Suppose that $u_c = [u_{cax} u_{cbx} u_{cay} u_{cby}]^T$, it can be shown in matrix form,

$$\boldsymbol{i = k_w g_{wLPF} u_c} \tag{31}$$

Suppose that the controller is decentralized controller, the input and output voltage can be given by,

$$\begin{cases} u_{a_x} = -g_c u_{sax} \\ u_{b_x} = -g_c u_{sbx} \\ u_{a_y} = -g_c u_{say} \\ u_{b_y} = -g_c u_{sby} \end{cases} \tag{32}$$

where g_c is linear operator, then the matrix form is shown,

$$u_c = -G_{dis} u_s \tag{33}$$

$$G_{dis} = g_c \times I_4$$

Consequently, the current is also expressed according to (28), (31) and (33),

$$i = -k_w k_s g_{wLPF} G_{dis} q_s \tag{34}$$

Therefore, Eqs. (23), (28) and (34) are substituted (21), and then the forces can be obtained,

$$f_m = K_x q_m + K_i i = K_x T_m^{-1} q - K_i k_w k_s g_{wLPF} G_{dis} T_s^{-1} q \tag{35}$$

Then the dynamic model of magnetically suspended rotor system based on decentralized controller can be given,

$$M\ddot{q} + G\dot{q} - T_m^{-T} K_x T_m^{-1} q = -K_i k_w k_s g_{wLPF} G_{dis} T_m^{-T} G_{dis} T_s^{-1} q + f_d \tag{36}$$

The whole control system can be shown in Fig. 9.

Consequently, the dynamic model of magnetically suspended rotor system can also be expressed,

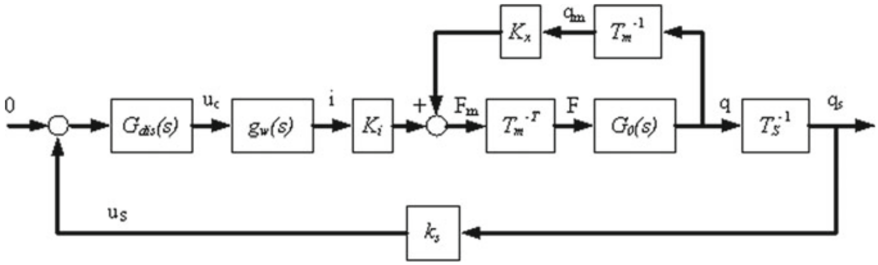

Fig. 9 Diagram of magnetically suspended rotor control system.

$$\begin{cases} m\ddot{x} = (2K_x - 2k_{iws}g_{wLPF}g_c)x + f_{x_d} \\ J_y\ddot{\beta} - H\dot{\alpha} = (2K_x l_m^2 - 2k_{iws}g_{wLPF}g_c l_m l_s)\beta + p_{y_d} \\ m\ddot{y} = (2K_x - 2k_{i_{ws}}g_{w_{LP_F}}g_c)y + f_y d \\ J_x\ddot{\alpha} + H\dot{\beta} = (2K_x l_m^2 - 2k_{iws}g_{wLPF}g_c l_m l_s)\alpha + p_{x_d} \end{cases} \tag{37}$$

where,

$$k_{iws} = K_i k_w k_s.$$

When PID control is used,

$$g_c(s) = k_P + k_I/s + k_D s$$

The formulation (37) can be changed as,

$$\begin{cases} ms^2 + 2(k_{iws}k_P + \frac{k_{iws}k_I}{s} + k_{iws}k_D s - k_h) = \frac{f_{d_x}(s)}{x(s)} = G_x(s) \\ Js^2 + 2k_{iws}k_D l_m l_s s^2 + 2(k_{iws}k_P l_m l_s - K_x l_m^2)s + 2k_{i_{ws}}k_I l_m l_s = \frac{P_{d_y}(s)}{\beta(s)} = G_\beta(s) \\ ms^2 + 2(k_{iws}k_P + \frac{k_{iws}k_I}{s} + k_{iws}k_D s - K_x) = \frac{f_{d_y}(s)}{y(s)} = G_y(s) \\ Js^2 + 2k_{iws}k_D l_m l_s s^2 + 2(k_{iws}k_P l_m l_s - K_x l_m^2)s + 2k_{iws}k_I l_m l_s = \frac{P_{d_y}(s)}{\alpha(s)} = G_\alpha(s) \end{cases} \tag{38}$$

According to Routh criterion, the stability condition of magnetically suspended rotor system is derived according to the Eq. (38),

$$k_p > \frac{\frac{mk_i}{2k_D} + K_x}{k_{iws}} \tag{39}$$

Considering structural parameters, the stability condition can be expressed,

$$K_{pmc} < \frac{1}{1 + \left(\frac{GI_x - 2I_x x \frac{mk_I}{2k_D}}{k_{pws}G\delta - 2I_x\delta\frac{mk_I}{2k_D}}\right)^2} \tag{40}$$

where $k_{p_{ws}} = k_p k_w k_s$.

4 Design 1DOF Magnetic Actuator

As we all know, application of the robotic system for surgical application is getting more and more widely used nowadays [18, 19]. In order to improve its accuracy, variable suspension systems are used in the robotic system [20], especially the electromagnetic suspension system [20]. The 1DOF magnetic actuator system refers that the controllable degree of freedom is axial, and it includes fully active and the combination of passive and active actuation in the axial direction.

4.1 Design of Magnetic Actuator System with Passive and Active Combination

The structure of 1DOF magnetic actuator with passive and active combination is shown in Fig. 10.

This structure consists of housing, coil, plate, inner permanent magnet, outer permanent magnet, shell, and limit device. When electrical current is running through in the coil, the attraction force will be produced between the housing and plate, and then plate will then be moved in the $-z$ direction. At the same time, the outer permanent magnet will misalign with the inner permanent magnet, and an axial force will be produced between them. Because the inner permanent magnet is unable to move in the $+z$ direction by the limit device, the outer permanent magnet will be moved in the $-z$ direction, along with the housing. Commonly, the axial air gap is designed to be $1.5 \sim 2.5$ mm between the housing and the plate, the radial air gap is designed to be $2 \sim 4$ mm between the inner permanent magnet and the outer permanent magnet.

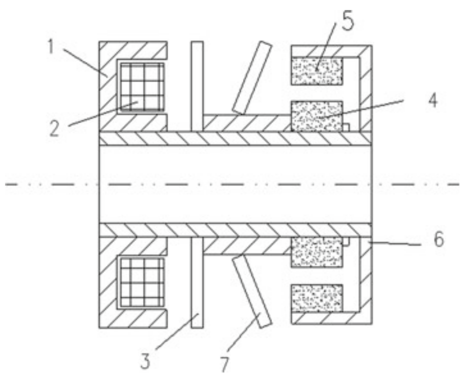

Fig. 10 *1* housing *2* coil *3* plate *4* inner permanent magnet *5* outer permanent magnet; *6* shell *7* limit device. The structure of 1DOF magnetic actuator with passive and active combination.

4.2 Design of Magnetic Actuator System with Active Magnetic Bearing

The structure of 1-DOF magnetic actuator with active combination [21] is shown in Fig. 11.

This structure consists of housing, coils, plates, and stop-limit devices. When electrical current is through in the left coils, the attraction force will be produced between the left housing and the left plate, and then the plate will be moved in the $-z$ direction. Subsequently, current is running through the right coils, and then the attraction force will be produced between the right housing and the right plate. The axial force will be produced between them. Because the plate is unable to move in the $+z$ direction by the limit device, the right housing will be moved in the $-z$ direction. Commonly, the axial air gap is designed $1.5 \sim 2.5$ mm between the housing and the plate.

5 Design of 3-DOF Magnetic Actuator

In order to reduce the volume of magnetic actuator, more degree of freedoms are required. Consequently, the 3-DOF magnetic actuator system is introduced as follows.

- Overall structure design

The structure of 3DOF magnetic actuator [21] is shown in Fig. 12a and the structure of 3DOF housing is shown in Fig. 12b.

This structure consists of 3-DOF housing, coils, plates, and stop-limit device. The 3DOF housing has four poles around the circumference in X and Y directions. When all the coils are across the same current in the left 3DOF housing, the attraction force will be produced between the left 3DOF housing and the left plate, and then the plate

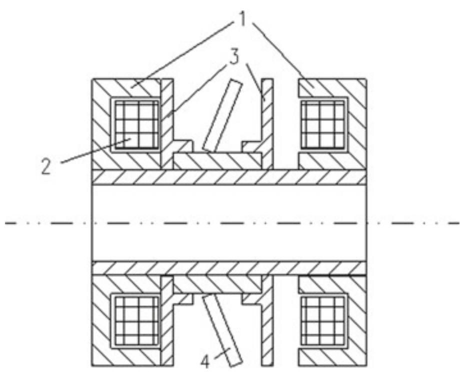

Fig. 11 *1* housing *2* coil *3* plate *4* limit device. The structure of 1-DOF magnetic actuator with active magnetic bearing.

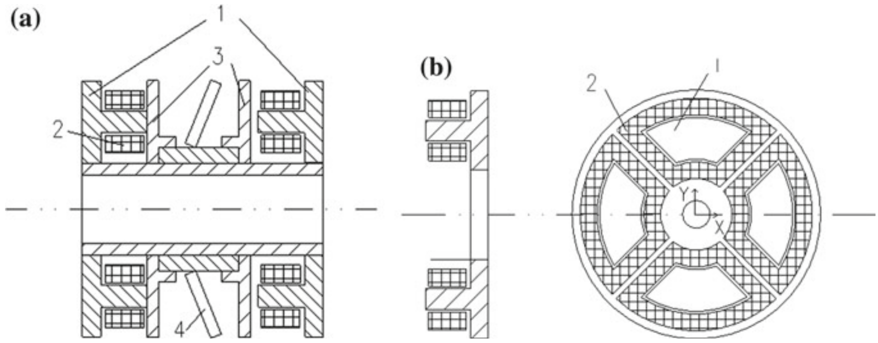

Fig. 12 *1* housing *2* coil *3* plate *4* limit device. The structure of 3DOF magnetic actuator. **a** structure **b** housing.

will be moved in the −z direction. Subsequently, all the coils are across the same current in the right 3DOF housing, and then the attraction force will be produced between the right 3DOF housing and the right plate. The axial force will be produced between them. Because the plate is unable to move in the +z direction by the limit device, the right housing will be moved in the −z direction. On the other hand, when the coils are across the different current in the X and Y direction in the left 3DOF housing, the attraction forces are different in the X and Y directions, as a result, the torque will be produced to realize the tilt movement of the left plate. The right plate will be emerge through the same phenomena when the coils are across the different current in the X and Y direction in the right 3DOF housing. The axial air gap tends to be designed 1.5 ∼ 2.5 mm between the housing and the plate.

6 Control System in Magnetic Bearing System

For the early current integral control method, a novel current integral positive low power loss is proposed for AMB. The proposed current control method diagram is shown in Fig. 13 to solve the problem for uncontrolled coil redundancy [22].

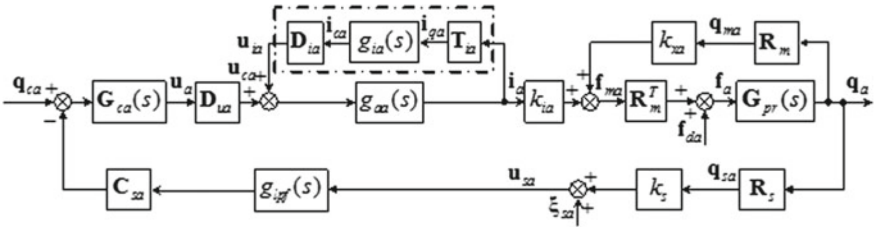

Fig. 13 Low power loss diagram of magnetic bearing.

The new state variable is as follows in magnetic bearing control loop,

$$X_{ag} = [\dot{q}_a^T q_a^T \dot{\tilde{q}}_{ea}^T \tilde{q}_{ea}^T u_{pd} \dot{u}_b^T u_b^T \dot{u}_f^T u_f^T i_a^T i_{ca}^T]^T \tag{41}$$

where $i_{c_a} = [i_{c_{a_\beta}}, i_{c_{a_\alpha}}, i_{c_{a_z}}]^T$ is the output vector of integral.

Then the state equation of magnetic bearing control loop is changed as,

$$\dot{i}_a = \frac{k_{a_a}}{\tau_{a_a}} D_{u_a} u_a - \frac{1}{\tau_{a_a}} i_a + \frac{k_{a_a}}{\tau_{a_a} \tau_{i_a}} D_{i_a} i_{c_a} \tag{42}$$

$$\dot{i}_{a_a} = T_{i_a} i_a \tag{43}$$

Assuming the state equation of the magnetic bearing control loop is,

$$\dot{X}_{a_g} = A_{a_g} X_{a_g} \tag{44}$$

The current of power amplifier is described as differential equation using current integral positive feedback.

$$\dot{i}_a = \frac{k_{a_a}}{\tau_{a_a}} D_{u_a} u_a - \frac{1}{\tau_{a_a}} i_a + \frac{k_{a_a}}{\tau_{a_a} \tau_{i_a}} D_{i_a} \int T_{i_a} i_a dt \tag{45}$$

Given,

$$\begin{cases} T_{i_a} = R_m^T \\ D_{i_a} = (R_m^T)^+ \end{cases} \tag{46}$$

Then the domain solution is,

$$i_a = \begin{bmatrix} 1 & -1 & 1 & -1 \\ -1 & 1 & -1 & 1 \\ 1 & -1 & 1 & -1 \\ -1 & 1 & -1 & 1 \end{bmatrix} \begin{bmatrix} C_{3_1} e^{P^{3^t}} \\ C_{3_2} e^{P^{3^t}} \\ C_{3_3} e^{P^{3^t}} \\ C_{3_4} e^{P^{3^t}} \end{bmatrix} + \begin{bmatrix} 3 & 1 & -1 & 1 \\ 1 & 3 & 1 & -1 \\ -1 & 1 & 3 & 1 \\ 1 & -1 & 1 & 3 \end{bmatrix} \begin{bmatrix} C_{1_1} e^{P^{1^t}} + C_{2_1} e^{P^{2^t}} \\ C_{1_2} e^{P^{1^t}} + C_{2_2} e^{P^{2^t}} \\ C_{1_3} e^{P^{1^t}} + C_{2_3} e^{P^{2^t}} \\ C_{1_4} e^{P^{1^t}} + C_{2_4} e^{P^{2^t}} \end{bmatrix} + \begin{bmatrix} f_1(t) \\ f_2(t) \\ f_3(t) \\ f_4(t) \end{bmatrix} \tag{47}$$

where $p_3 = -\frac{1}{\tau_{a_a}}$.

When the force produced by permanent magnet is equal to the external disturbance, the coil current needs the condition,

$$\begin{cases} (C_{1_1} - C_{1_3}) e^{P^{1^t}} + (C_{2_1} - C_{2_3}) e^{P^{2^t}} = 0 \\ (C_{1_2} - C_{1_4}) e^{P^{1^t}} + (C_{2_2} - C_{2_4}) e^{P^{2^t}} = 0 \\ (C_{1_1} + C_{1_2}) e^{P^{1^t}} + (C_{2_1} + C_{2_2}) e^{P^{2^t}} = 0 \end{cases} \tag{48}$$

$$f_1(t) - f_3(t) = f_2(t) - f_4(t) = f_1(t) + f_2(t) = 0 \tag{49}$$

where,

$$\begin{cases} C_{1_1} = -C_{1_2} = C_{1_3} = -C_{1_4} = C_1 \\ C_{2_1} = -C_{2_2} = C_{2_3} = -C_{2_4} = C_2 \\ f_1(t) = -f_2(t) = f_3(t) = -f_4(t) = f_0(t) \end{cases} \tag{50}$$

Then,

$$i_a = e^{P^{3^t}} \begin{bmatrix} C_{3_1} & +C_{3_3} & -C_{3_2} & -C_{3_4} \\ C_{3_2} & +C_{3_4} & -C_{3_1} & -C_{3_3} \\ C_{3_1} & +C_{3_3} & -C_{3_2} & -C_{3_4} \\ C_{3_2} & +C_{3_4} & -C_{3_1} & -C_{3_3} \end{bmatrix} + f_0(t) \begin{bmatrix} 1 \\ -1 \\ 1 \\ -1 \end{bmatrix} \tag{51}$$

According to the equations above, the stable current in four coils of axial magnetic bearing is as follows because of,

$$\lim_{t \to \infty} i_a = f_0(t) \begin{bmatrix} 1 & -1 & 1 & -1 \end{bmatrix}^T \tag{52}$$

By the analysis root locus of control system, it can be known that the root is existed to trend zero, so the rapidity and stability is improved. Control algorithm is used the gain scheduling cross feedback control algorithm, and incomplete differential PID algorithm is adopted in the PID.

$$H_{PID}(z) = K_P[1 + \frac{T}{T_i(1 - Z^{-1})} + \frac{T_d(1 - Z^{-1})}{T + T_f(1 - Z^{-1})} \tag{53}$$

where Kp is the proportional coefficient, T_i is the integral coefficient, Td is the differential coefficient, T_f is inertial link the time constant of the differential coefficient. T is the sample cycle.

The current control is generated by the difference between control current signal and feedback current signal in DSP. This current control is obtained by DSP modulation, and the coil current will be generated in magnetic bearing coils, then closed-loop current control is realized.

The whole controller includes an interface circuit, DSP system, and power module. In this control system, DSP system is adopted TMS2812, and the signals of eddy-current displacement sensor and current sensor are enlarged by an interface circuit, which transferred the voltage to match the input voltage of A/D. Control values of 3DOF are generated by an algorithm in DSP, which outputs six signals. In addition, there is the interface of RS232 which connects with the monitor computer.

Because the TMS2812 has provided a whole system for designers, the design of DSP system was not expanded on by any peripheral devices to realize the digital of magnetic bearing power amplifier. Consequently, the proposed system can improve the integration level and reliability when compared with an analog amplifier circuit.

7 4DOF Magnetic Actuator

In order to reduce the volume of magnetic actuator system further, the 4DOF magnetic actuator system is presented as follows.

7.1 System Design

A novel configuration of the micro-manipulation surgical robot has been put forward, which is a kind of 4 degrees of freedom (DOFs) active magnetically suspended system [23], as shown in Fig. 14. 4DOFs means radial translational motions along the X-axis and Y-axis and rotational motions around the X-axis and Y-axis. The structure of this active magnetically suspended system is composed of fixtures, the radial displacement sensor module, the radial magnetic bearing module, the shaft, and some guarded blocks. For the radial magnetic bearing module, stators located at both sides are connected by the shell. Rotors are installed on the shaft, which form a magnetic air gap with the stators. Each magnetic pole of stators is winded with coils.

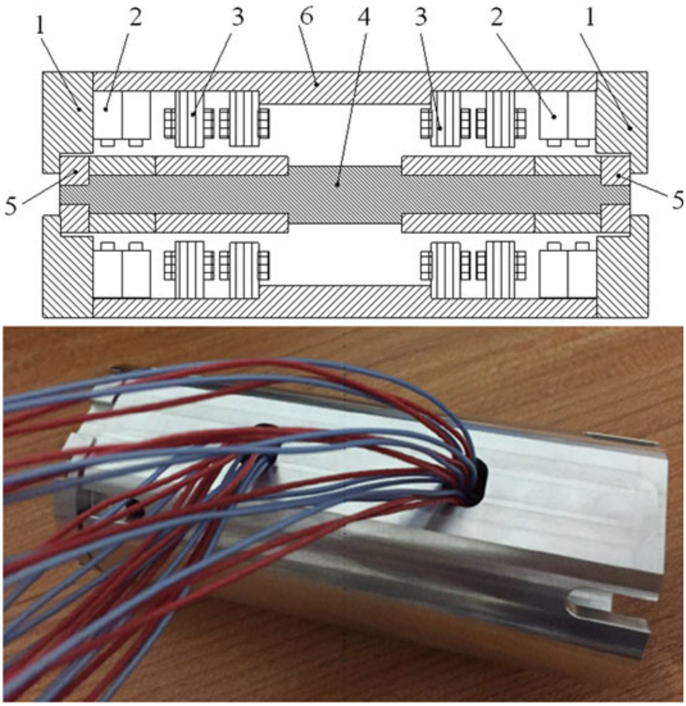

Fig. 14 *1* fixture *2* radial displacement sensor module *3* radial magnetic bearing module *4* shaft *5* guarded block *6* shell 4DOFs active magnetically suspended system.

Located on either side of the magnetic bearing module is the radial displacement sensor module, which consists of the stator, the probe, and the detection ring. For this module, stators are connected to those of the magnetic bearing with their outer sides fixed to the shell. The probes, which locate inside the stators of the sensors module, are placed in four directions: +X, −X, +Y, and −Y. The detection ring is installed on the shaft and located on either side of the rotors magnetic bearing module. A detection air gap is then formed by probes and the detection ring. Outside of the stators sensor module is the fixture, which is fixed to the shell. The guarded blocks, which are fixed in the outer side of the shaft, are utilized to form a protection gap. The size of the protection gap is $0.1 \sim 0.15$ mm.

The working principle is as follows, by detecting the position of the shaft with radial displacement sensors, the independent control of the coils winded on the magnetic bearings can be achieved, which leads to the force-output in the desired degree of freedom. For example, when the shaft gets the disturbance from one direction, the sensor module can detect the variation of the detection gap. The detected variation is then converted to voltage and transferred to the controller. Once receiving the voltage, the controller generates the current according to the predefined control algorithm. The amplified current is then distributed and output to the corresponding coil according to the configuration of the radial magnetic bearings. It is important to note that the variation detected by sensors is the position of the shaft. Therefore, some detection and compensation methods of the rate of change of the shaft position are necessary to improve the control precision of the magnetic bearings. Additionally, in order to reduce the radial dimension of the entire device, two radial displacement sensors and two radial magnetic bearings can be placed on either side. One of two radial displacement sensors uses two probes to detect displacement in the direction of the X-axis. The other adopts two probes to detect displacement in the direction of the Y-axis. One radial magnetic bearing uses two magnetic poles in the direction of the X-axis. The other one adopts two magnetic poles in the direction the Y-axis. With this configuration, two probes, which have the same direction (X-axis), simultaneously perform functions. By detecting the displacement, the translational detection in this direction of X-axis can be achieved. By calculating the difference of displacements detected by these two probes, the deviation displacement around the Y-axis can be obtained. Based on these results, the controller actuates the two radial magnetic bearings in the direction of the X-axis to generate force to eliminate the displacement in this direction. At the same time, the controller actuates the two radial magnetic bearings in the direction of the Y-axis to generate the torsion force to eliminate the deviation displacement around the Y-axis. The other two probes work in the same principle. As a result, displacements in four directions can be detected and eliminated.

The proposed radial magnetic bearing and the radial displacement sensor are shown in Figs. 15 and 16 respectively.

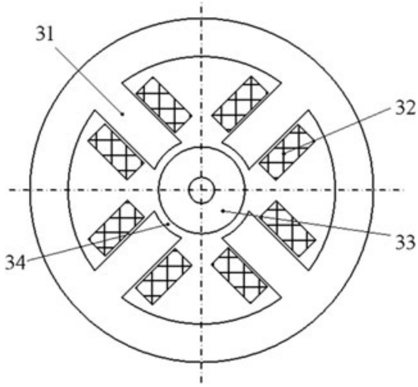

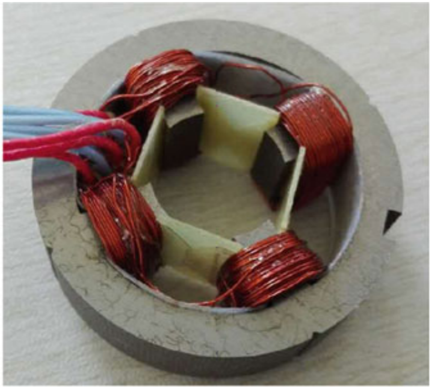

Fig. 15 (Left) *31* stator *32* coil *33* rotor *34* air gap. (Right) The structure of radial magnetic bearing.

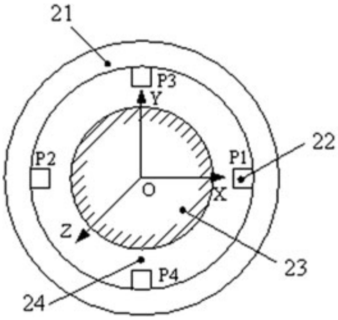

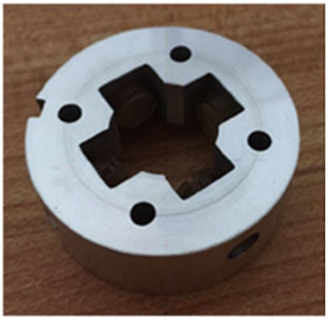

Fig. 16 (Left) *21* stator *22* probe *23* detective ring *24* detective air gap. (Right) The structure of the radial displacement sensor.

7.2 Design and Analysis of the Radial Magnetic Bearing

The equivalent magnetic circuit of the radial magnetic bearing is shown in Fig. 17 and the equivalent magnetic circuit when four coils run is shown in Fig. 18.

In the figures, R_{x1}, R_{x2} are the reluctances of air gaps in the +x and −x directions, R_{y1}, R_{y2} are the reluctances of air gaps in the +y and −y directions, ϕ_{y1x1}, ϕ_{y1x2}, and ϕ_{y1y2} are the air gap fluxes in the +x, −x, and −y directions respectively when the coil current is across in the +y direction. ϕ_{y1} is the total air gap flux in the +y direction when the coil current is across in the y direction. ϕ_{y2x1}, ϕ_{y2x2}, and ϕ_{y2y1} are the air gap fluxes in the +x, −x, and +y directions respectively when the coil current is across in the −y direction. ϕ_{y2} is the total air gap flux in the −y direction when the coil current is across in the y direction. ϕ_{x1y1}, ϕ_{x1y2}, and x1x2 are the air gap fluxes in the +y, −y, and +x directions respectively when the coil current is across in the +x direction. ϕ_{x1} is the total air gap flux in the +x direction when the coil current is across in the x direction. ϕ_{x2y1}, ϕ_{x2y2}, and ϕ_{x2x1} are the air gap fluxes

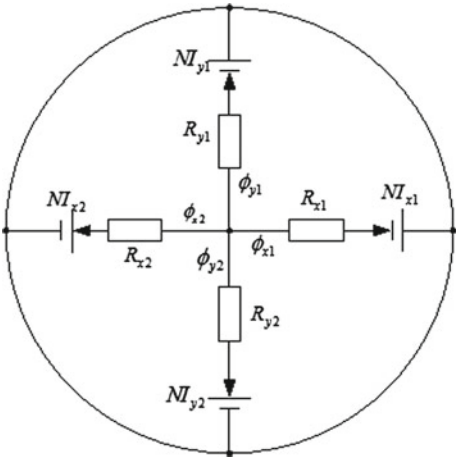

Fig. 17 Equivalent magnetic circuit.

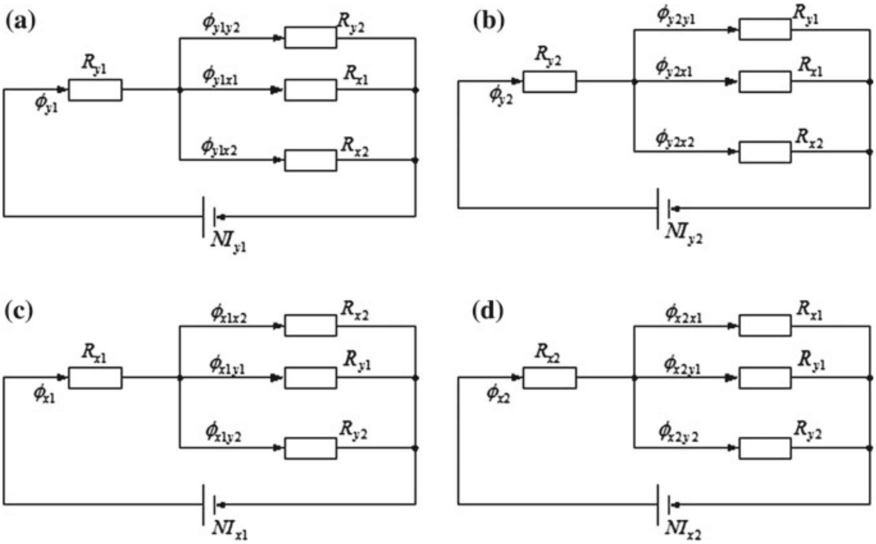

Fig. 18 Equivalent magnetic circuit when four coils run; **a** coil in the +y direction, **b** coil in the −y direction, **c** coil in the +x direction, **d** coil in the −x direction.

in the +y, −y, and +x directions respectively when the coil current is across in the −x direction. x2 is the total air gap flux in the −x direction when the coil current is across in the x direction.

According to the Fig. 18 the total fluxes of every branches in the equivalent circuit of control flux are as follows,

$$\begin{cases} \phi_{y_1} = \frac{NI_{y_1}}{R_{y_1}+R_{y_2}//R_{x_1}//R_{x_2}} \\ \phi_{y_2} = \frac{NI_{y_2}}{R_{y_2}+R_{y_1}//R_{x_1}//R_{x_2}} \\ \phi_{x_1} = \frac{NI_{x_1}}{R_{x_1}+R_{x_2}//R_{y_1}//R_{y_2}} \\ \phi_{x_2} = \frac{NI_{x_2}}{R_{x_2}+R_{x_1}//R_{y_1}//R_{y_2}} \end{cases} \tag{54}$$

Fluxes of every branches are expressed,

$$\begin{cases} \phi_{y_{1_{y_2}}} = \frac{NI_{y_1}-\phi_{y_1}R_{y_1}}{R_{y_2}} \\ \phi_{y_{1_{x_1}}} = \frac{NI_{y_1}-\phi_{y_1}R_{y_1}}{R_{x_1}} \\ \phi_{y_{1_{x_2}}} = \frac{NI_{y_1}-\phi_{y_1}R_{y_1}}{R_{x_2}} \end{cases} \begin{cases} \phi_{y_{2_{y_1}}} = \frac{NI_{y_2}-\phi_{y_2}R_{y_2}}{R_{y_1}} \\ \phi_{y_{2_{x_1}}} = \frac{NI_{y_2}-\phi_{y_2}R_{y_2}}{R_{x_1}} \\ \phi_{y_{2_{x_2}}} = \frac{NI_{y_2}-\phi_{y_2}R_{y_2}}{R_{x_2}} \end{cases} \tag{55}$$

$$\begin{cases} \phi_{x_{1_{x_2}}} = \frac{NI_{x_1}-\phi_{x_1}R_{x_1}}{R_{x_2}} \\ \phi_{x_{1_{y_1}}} = \frac{NI_{x_1}-\phi_{x_1}R_{x_1}}{R_{y_1}} \\ \phi_{x_{1_{y_2}}} = \frac{NI_{x_1}-\phi_{x_1}R_{x_1}}{R_{y_2}} \end{cases} \begin{cases} \phi_{x_{2_{x_1}}} = \frac{NI_{x_2}-\phi_{x_2}R_{x_2}}{R_{x_2}} \\ \phi_{x_{2_{y_1}}} = \frac{NI_{x_2}-\phi_{x_2}R_{x_2}}{R_{y_1}} \\ \phi_{x_{2_{y_2}}} = \frac{NI_{x_2}-\phi_{x_2}R_{x_2}}{R_{y_2}} \end{cases} \tag{56}$$

where,

$$\begin{cases} R_{x_1} = \frac{\delta+x}{\mu_0 A} \\ R_{x_2} = \frac{\delta-x}{\mu_0 A} \\ R_{y_1} = \frac{\delta+y}{\mu_0 A} \\ R_{y_2} = \frac{\delta-y}{\mu_0 A} \end{cases}$$

where x denotes the offset of rotor in the X direction, y denotes the offset of rotor in the Y direction, δ is the length of air gap at the equilibrium position, R denotes the reluctance of magnetic circuit, the subscript $x1$ and $x2$ denote the positive and negative X direction, the subscript $y1$ and $y2$ denote the positive and negative Y direction, and NI_{y1}, NI_{y2}, NI_{x1}, NI_{x2} denote ampere-turns respectively.

$$\begin{cases} \phi_{y_p} = \phi_{y_1} + \phi_{y_{2_{y_1}}} + \phi_{x_{2_{y_1}}} - \phi_{x_{1_{y_1}}} \\ \phi_{y_n} = \phi_{y_2} + \phi_{y_{1_{y_2}}} + \phi_{x_{1_{y_2}}} - \phi_{x_{2_{y_2}}} \\ \phi_{x_p} = \phi_{x_1} + \phi_{x_{2_{x_1}}} + \phi_{y_{2_{x_1}}} - \phi_{y_{1_{x_1}}} \\ \phi_{x_n} = \phi_{x_2} + \phi_{x_{1_{x_2}}} + \phi_{y_{1_{x_2}}} - \phi_{y_{2_{x_2}}} \end{cases} \tag{57}$$

Then the forces in the Y and X directions are described,

$$\begin{cases} F_y = \frac{\phi_{y_p^2} - \phi_{y_n^2}}{2\mu_0 A} \\ F_x = \frac{\phi_{x_p^2} - \phi_{x_n^2}}{2\mu_0 A} \end{cases} \tag{58}$$

So,

$$\begin{cases} F_y = \frac{(P_{y_1} I_{y_1} + P_{y_2} I_{y_2} + P_{x_1} I_{x_1} + P_{x_2} I_{x_2})(P'_{y_1} I_{y_1} + P'_{y_2} I_{y_2} + P'_{x_1} I_{x_1} + P'_{x_2} I_{x_2})}{2\mu_0 A} \\ F_x = \frac{(Q_{y_1} I_{y_1} + Q_{y_2} I_{y_2} + Q_{x_1} I_{x_1} + Q_{x_2} I_{x_2})(Q'_{y_1} I_{y_1} + Q'_{y_2} I_{y_2} + Q'^{x_1} I_{x_1} + Q'_{x_2} I_{x_2})}{2\mu_0 A} \end{cases} \tag{59}$$

where,

$$\begin{cases} P_{y_1} = N\frac{R_{y_2} - R_{y_1} + C_{y_1}}{R_{y_2} C_{y_1}} \\ P_{y_2} = N\frac{R_{y_1} - R_{y_2} + C_{y_2}}{R_{y_1} C_{y_2}} \\ P_{x_1} = N\frac{(R_{y_2} - R_{y_1})(C_{x_1} - R_{x_1})}{R_{y_1} R_{y_2} C_{x_1}} \\ P_{x_2} = N\frac{(R_{y_2} - R_{y_1})(C_{x_2} - R_{x_2})}{R_{y_1} R_{y_2} C_{x_2}} \end{cases} \quad \begin{cases} P'_{y_1} = N\frac{R_{y_2} + R_{y_1} - C_{y_1}}{R_{y_2} C_{y_1}} \\ P'_{y_2} = N\frac{-R_{y_1} - R_{y_2} + C_{y_2}}{R_{y_1} C_{y_2}} \\ P'_{x_1} = N\frac{(R_{y_2} + R_{y_1})(C_{x_1} - R_{x_1})}{R_{y_1} R_{y_2} C_{x_1}} \\ P'_{x_2} = N\frac{(R_{y_2} + R_{y_1})(C_{x_2} - R_{x_2})}{R_{y_1} R_{y_2} C_{x_2}} \end{cases}$$

$$\begin{cases} Q_{y_1} = N\frac{(R_{x_2} - R_{x_1})(C_{y_1} - R_{y_1})}{R_{x_1} R_{x_2} C_{y_1}} \\ Q_{y_2} = N\frac{(R_{x_2} - R_{x_1})(C_{y_2} - R_{y_2})}{R_{x_1} R_{x_2} C_{y_2}} \\ Q_{x_1} = N\frac{R_{x_2} - R_{x_1} + C_{x_1}}{R_{x_2} C_{x_1}} \\ Q_{x_2} = N\frac{R_{x_1} - R_{x_2} + C_{x_2}}{R_{x_1} C_{x_2}} \end{cases} \quad \begin{cases} Q'_{y_1} = N\frac{(R_{x_2} + R_{x_1})(C_{y_1} - R_{y_1})}{R_{x_1} R_{x_2} C_{y_1}} \\ Q'_{y_2} = N\frac{(R_{x_2} + R_{x_1})(R_{y_2} - C_{y_2})}{R_{x_1} R_{x_2} C_{y_2}} \\ Q'_{x_1} = N\frac{R_{x_2} + R_{x_1} - C_{x_1}}{R_{x_2} C_{x_1}} \\ Q'_{x_2} = N\frac{-R_{x_1} - R_{x_2} + C_{x_2}}{R_{x_1} C_{x_2}} \end{cases}$$

where

$$\begin{cases} C_{y_1} = R_{y_1} + R_{y_2} // R_{x_1} // R_{x_2} \\ C_{y_2} = R_{y_2} + R_{y_1} // R_{x_1} // R_{x_2} \\ C_{x_1} = R_{x_1} + R_{x_2} // R_{y_1} // R_{y_2} \\ C_{x_2} = R_{x_2} + R_{x_1} // R_{y_1} // R_{y_2} \end{cases}$$

The 2D FEM model of radial magnetic bearing is built, and the diagram of coil current directions is shown in Fig. 19. The dimension of the radial magnetic bearing is shown in Table 1.

(1) ix1 = ix2 = ix3 = ix4 = 0.2A

When ix1 = 0.2A, ix2 = 0.2A, ix3 = 0.2A, ix4 = 0.2A, the flux distribution is shown in Fig. 20.

(2) ix1 = −ix2 = −ix3 = ix4 = 0.2A

When ix1 = 0.2A, ix2 = −0.2A, ix3 = −0.2A, ix4 = 0.2A, the flux distribution is shown in Fig. 21.

From these figures, it can be seen that the proposed radial magnetic bearing with four magnetic poles can be realized with the 2DOF of the magnetic actuator by controlling every coil currents.

8 Discussions and Future Work

The handheld medical robot is required to have a very small volume of robot body and high precision of localization/tracking, so the requirement of magnetic bearing is also to be small and to have high control precision. The existing structure of displacement

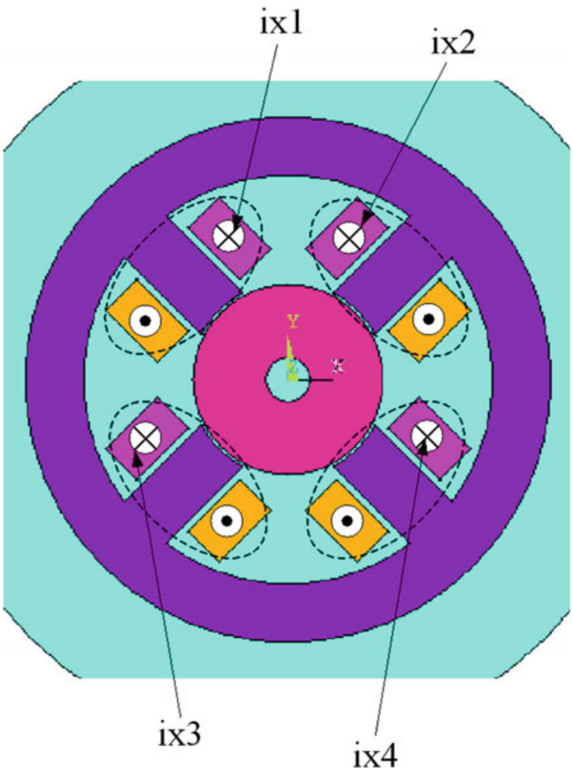

Fig. 19 The diagram of coil current directions.

Table 1 Main parameters of radial magnetic bearing (Inner diameter: ID; Outer diameter: OD).

Item	Value
Stator OD/mm	36
ID of stator /mm	13.4
OD of stator teeth /mm	28
OD of rotor /mm	13
ID of rotor /mm	5
Width of magnetic pole /mm	4
Turns of coil /turn	70

sensors are still too big to be placed in the small volume of magnetic bearing structure. Therefore, it is important to study a new structure of magnetic bearing with a small volume and non-sensor technology in the surgical field. Therefore, this future work includes a novel multiple-DOF integral magnetic bearing configuration and a self-sensing detecting method.

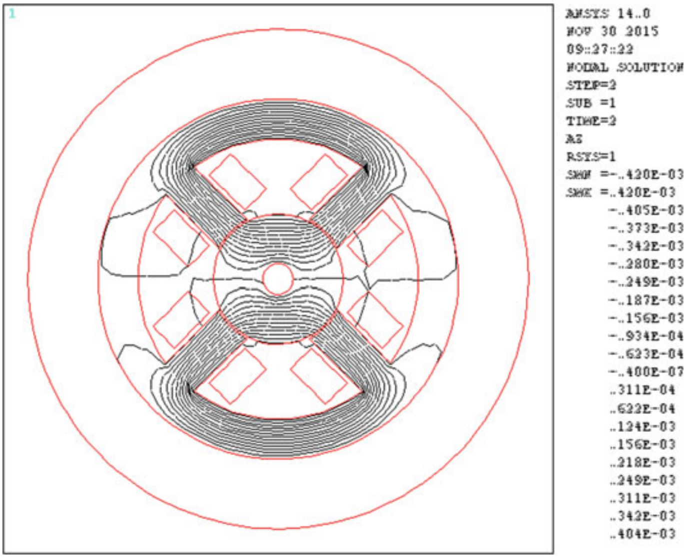

Fig. 20 Flux distribution (ix1 = 0.2A, ix2 = 0.2A, ix3 = 0.2A, ix4 = 0.2A).

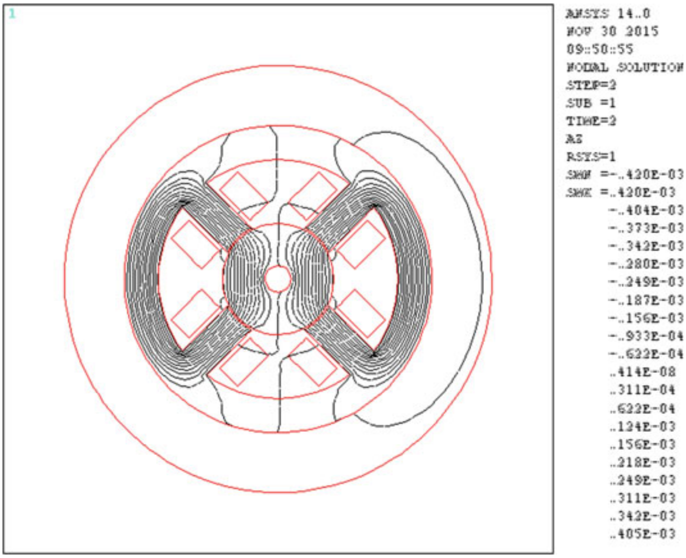

Fig. 21 Flux distribution (ix1 = 0.2A, ix2 = 0.2A, ix3 = 0.2A, ix4 = 0.2A).

8.1 *Design of Magnetic Actuator with Small Volume*

Figure 22 illustrates the flux distribution of the traditional radial magnetic bearing when the coils current in the Y channel is 0.3 A in simulations. From Fig. 22, it is apparent that the magnetic field coupling exists between X and Y channels. In order to decouple the flux between X and Y channels, the field coupling structure is proposed [24], as shown in Fig. 23.

In order to reduce the radial volume of magnetic actuator system, the tradition radial magnetic bearing with four magnetic poles can be designed with two magnetic bearing and two magnetic poles, as shown in Fig. 24. In this figure, one of the radial magnetic bearing is consisted of two magnetic poles which are placed along the Y direction (Fig. 24a), and the other is of two magnetic poles which are placed along the X direction (Fig. 24b).

In addition, the tradition radial displacement sensor with four probes can be designed with two sensors and two probes in order to reduce the radial dimension of the whole magnetic actuator system, as shown in Fig. 25. In this figure, one of the radial displacement sensors is of two probes which are placed along the Y direction (Fig. 25a), and the other is of two probes which are placed along the X direction (Fig. 25b).

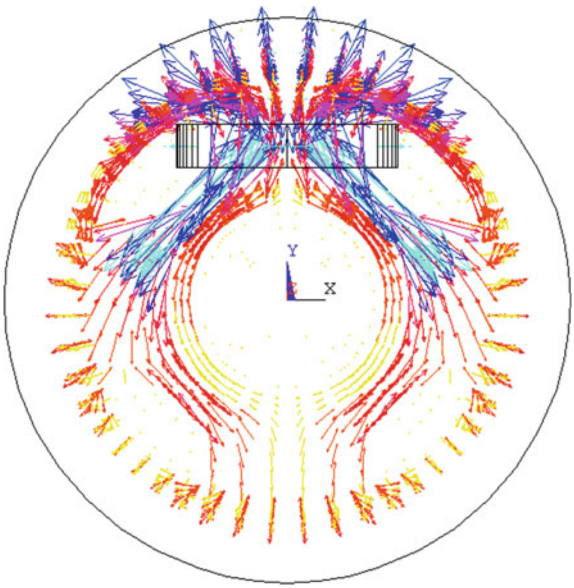

Fig. 22 Flux distribution of traditional radial magnetic bearing.

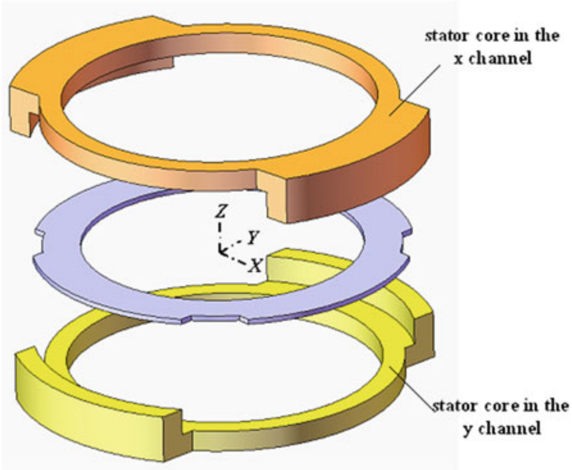

Fig. 23 The proposed structure of field decoupled radial magnetic bearing.

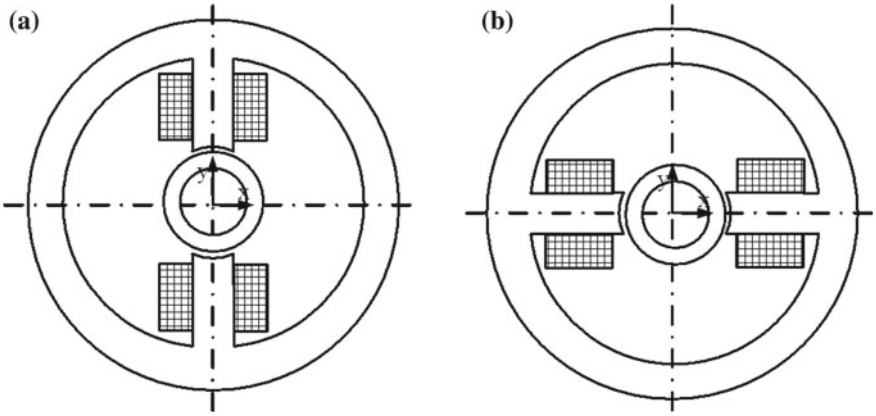

Fig. 24 Radial magnetic bearing with two magnetic poles. **a** two magnetic poles in the Y direction; **b** two magnetic poles in the X direction.

8.2 Research on Control Method of Self-sensing Magnetic Actuator System

Self-sensing is the research emphasis of this project. The magnetically suspended system stability and control precision are determined by the reliability and precise detection of rotor component. The displacement detection device is required to have a small volume and light mass because of the requirement in medical field. Therefore, a novel detected method is needed. Self-sensing needs to be adopted for this

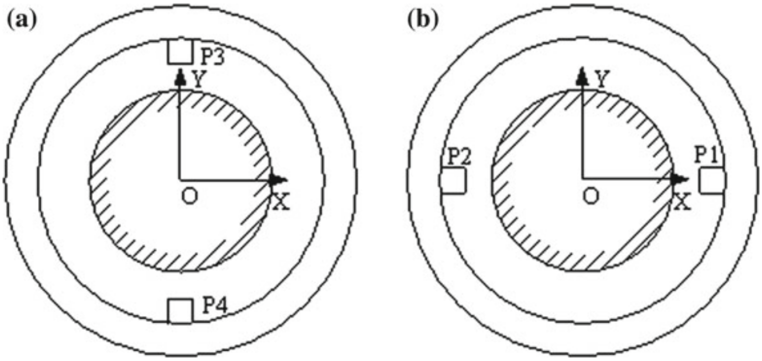

Fig. 25 Radial displacement sensor with two probes. **a** sensor with two probes in the Y direction; **b** sensor with two probes in the X direction.

application. The idea is to detect the rotor displacement by detecting the coil voltage or current in magnetic bearing. It has many advantages such as,

(1) High precision. This method can solve the problem of placement between displacement sensor and magnetic bearing. The signal of self-sensing implies the center of magnetic bearing, so the difficulty of control can be decreased and can be good for high precision active control.

(2) High stability. The dimension of rotor component can be effectively decreased and thus improve the system stability.

(3) High reliability. This method can be separated from the displacement signal demodulation circuit and magnetic bearing coil. Therefore, the magnetically suspended system is away from strong magnetic fields, high temperatures and vibrations. As a result, the system reliability is improved. At the same time, self-sensing detecting method can provide a new idea of sensor redundancy and fault tolerant control of magnetic bearing.

Self-sensing method is usually used for the active magnetic bearing with current biased. This project has proposed a novel self-sensing method to the AMB for micromanipulators. Based on the principle of existing self-sensing method [25], a novel self-sensing method is proposed for two degrees of freedom of rotor based on dual PWM carrier wave. The merit of this method is to avoid the effect of sample processing which is caused by PWM carrier wave on power amplifier performance. So the self-sensing sampling cycle will be shorten.

The following contents introduce the fundamental principle of self-sensing. There are four coils in x or y direction for the radial part of the AMB, and it can be classified six different connection methods according to the coil with series and parallel mode.

To realize the rotor self-sensing using the principle of differential transformer, the coils in positive and negative x direction is in series and the same to the y direction. Besides the self-inductance among coils, mutual inductance is existed because of the magnetic circuit coupling. Consequently, self-sensing method can be realized by detecting the difference of voltage in positive x (or y) direction and negative x (or y) direction.

For the convenience of analysis, leakage, iron core magnetic reluctance, and the magnetic saturation are ignored. According to the equivalent magnetic circuit of radial magnetic bearing, assuming, $i_{x+} = i_{x-} = i_x, i_{y+} = i_{y-} = i_y$, ignoring the voltage caused by coil reluctance, the radial displacement variation is very slow compared with current variation. So the relationship between coil voltage and coil flux linkage is at the equilibrium position. Then the voltages in x and y direction are as follows [26]:

$$v_x = v_{x_+} - v_{x_-} = \frac{d(\psi_{x_1} - \psi_{x_-})}{dt} = \frac{4\mu_0 AN^2}{2g^2 - (x^2 + y^2)}(x\frac{di_x}{dt} - y\frac{di_y}{dt}) \tag{60}$$

$$v_y = v_{y_+} - v_{y_-} = \frac{d(\psi_{y_+} - \psi_{y_-})}{dt} = \frac{4\mu_0 AN^2}{2g^2 - (x^2 + y^2)}(y\frac{di_x}{dt} - x\frac{di_y}{dt}) \tag{61}$$

$$u_x = v_{x_+} - v_{x_-} = \frac{d(\psi_{x_+} + \psi_{x_-})}{dt} = \frac{4\mu_0 AN^2}{g(2g^2 - x^2 - y^2)}[(2g^2 - y^2)\frac{di_x}{dt} - xy\frac{di_y}{dt}] \tag{62}$$

$$u_y = v_{y_+} - v_{y_-} = \frac{d(\Lambda_{y_+} + \Lambda_{y_-})}{dt} = \frac{4\mu_0 AN^2}{g(2g^2 - x^2 - y^2)}[(2g^2 - x^2)\frac{di_y}{dt} - xy\frac{di_x}{dt}] \tag{63}$$

where $v_x(v_y)$ is the voltage difference in positive x (or y) and negative x (or y) direction, $u_x(u_y)$ is the coil voltage in x (y) direction.

Considering the above four equations, it can be solved as follows,

$$v_x = \frac{1}{2g}(u_x x - u_y y) \tag{64}$$

$$v_y = \frac{1}{2g}(u_y y - u_x x) \tag{65}$$

It can be seen from the above equations that the voltage difference in coils with positive and negative directions is proportional to the radial displacement. Because the coil voltages u_x and u_y are known which are controlled by PWM, the radial displacements x and y are obtained by detecting the coil voltages in positive and negative directions $v_x(t_1)$, $v_x(t_2)$ (or $v_y(t_1)$, $v_y(t_2)$) at two adjacent time steps.

Two electric level full-bridges PWM switching amplifier is generally adopted in the controlling of HMB. The amplitude and direction of coils currents are changed by controlling the coils alternating voltages. In order to obtain two adjacent time

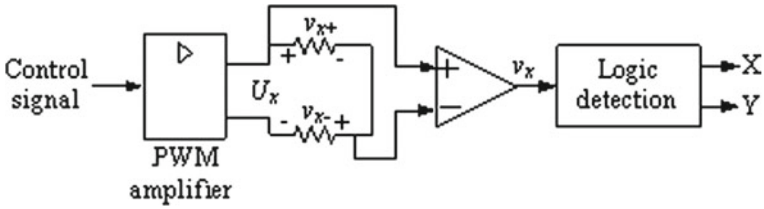

Fig. 26 Principle block diagram of self-sensing of magnetic bearing.

intervals as short as possible, the displacement signals of x and y are detected from the difference of coil voltage v_x. Two triangular wave generators with 90-degree phase act as PWM pulsation of coils in x and y directions, namely carrier signals, in order that two unrelated detected status will be created in a PWM period.

The working principle of PWM switching power amplifier is as follows, the computing of control signals from magnetic bearing control system and signals from current transformer are mixed to send the pulse width modulator to generate PWM square signal. This square signal can make power switch tube output electromagnetic force by optocoupler and drive the circuit, which changes according to the change of the control signal changes.

The principle diagram of self-sensing of magnetic bearing is shown in Fig. 26. It includes orthogonal phase PWM carrier generating circuit, differential comparing circuit, and logic detecting circuit.

As shown in Fig. 26, the voltage v_{x+} in positive coil and v_{x-} in negative coil are exacted using linear optocoupler. Then the detected signals can be obtained by comparing circuit, which is proportional to the displacement of rotor.

In the actual signal detection circuit, it does not require the numerical solution of equations. According to the positive status coil voltage u_x and negative status coil voltage u_y in the x and y directions, the detecting signals which is proportional to rotor displacement can be obtained by these signals through addition and subtractions.

Acknowledgements This work was in part supported by the Singapore Academic Research Fund under Grant R-397-000-173-133 (Magnetically Actuated Micro-robotics) and National Natural Science Foundation of China NSFC grant 51405322.

References

1. Taylor Fisher, Abbi Hamed, and Panagiotis Vartholomeos. 2014. Intraoperative magnetic resonance imaging-conditional robotic devices for therapy and diagnosis. *Proceedings of the Institution of Mechanical Engineers, Part H: Journal of Engineering in Medicine*.
2. Ren, H.L., and R. Denis. 2012. Multi-sensor data fusion in an integrated tracking system for endoscopic surgery. *IEEE Transactions on Information Technology in Biomedicine* 16 (1): 106–111.

3. Abbi Hamed, Sai Chun Tang, Hongliang Ren, et al. 2012. Advances in haptics, tactile sensing, and manipulation for robot-assisted minimally invasive surgery, noninvasive surgery, and diagnosis. *Journal of Robotics* 14.
4. Zhou Y., Ren H. L., and Max Meng Q.-H. 2013. Robotics in natural orifice transluminal endoscopic surgery. *Journal of Mechanics in Medicine and Biology* 13 (2): 1350044.
5. Wang J.L., Ren H.L., Lim C.M. 2014. Assisted transoral surgery with flexible robotics and navigation technologies: A review of recent progress and research challenges. *Critical Reviews in Biomedical Engineering*. (in press).
6. W.Y. Chen, Wu, X. Zhang, et al. 2011. Feasibility study on retinal vascular bypass surgery in isolated arterially perfused caprine eye model. *Eye* 25 (11): 1499–1503.
7. Glauco R Souza, Jennifer R Molina, Robert M Raphael, et al. 2010. Threedimensional tissue culture based on magnetic cell levitation. *Nature Nanotechnology* 5 (4): 291–296.
8. Stephenson, Emma, Laureen Jacquet, and Cristian Miere. 2012. Derivation and propagation of human embryonic stem cell lines from frozen embryos in an animal product-free environment. *Nature Protocols* 7 (7): 1366–1381.
9. Y. Paz. 2011. Ultrasound-guided, video-assisted transdiaphragmatic radiofrequency ablation for primary liver malignancy or metastatic nodules. *Innovations: Technology and Techniques in Cardiothoracic and Vascular Surgery* 6 (5): 337.
10. Tabares. Robert A MacLachlan, Brian C Becker, Jaime Cuevas de. 2012. *IEEE Transactions on Robotics* 28 (1): 195–212.
11. Hongliang Ren Jeffrey Stoll, and Pierre E. Dupont. 2012. Passive markers for tracking surgical instruments in real-time 3d ultrasound imaging. *IEEE Transactions on Medical Imaging*. (in press).
12. Win. Tun Latt, Richard C. de. 2011. *IEEE Transactions on Biomedical Engineering* 58 (9): 2694–2703.
13. Peter, L., Gehlbach Cheol Song and Jin U. Kang. 2012. Active tremor cancellation by a smart handheld vitreoretinal microsurgical tool using swept source optical coherence tomography. *Optics express* 20 (21): 23414–23421.
14. Berk Gonenc et al. 2016. Robot-assisted retinal vein cannulation with forcebased puncture detection: Micron versus the steady-hand eye robot. In *Engineering in medicine and biology society (EMBC), 2016 IEEE Conference of the 38th Annual International*, 5107–5111. IEEE.
15. G. Schweitzer, H. Bleuler, and A. traxler. 1997. *Active magnetic bearing-foundation, performance and Application*. (Yu Lie, Yuan Chongjun). Beijing: New: Times Press.
16. Schlageter, V., et al. 2001. Tracking system with five degrees of freedom using a 2D-array of Hall sensors and a permanent magnet. *Sensors and Actuators A: Physical* 92 (1): 37–42.
17. J.J. and Fan Y.H. 2012. *Magnetically suspended inertial momentum wheel technology, national defense industry*. (in Press).
18. S. Jiang, F. Sun, and J.L. Lou. 2015. Error analysis, and compensation of a high precision tendon-based MRI-compatible robot. *Journal International Journal of Robotics & Automation* 30 (4): 333–344.
19. F.Y. Xu, J.L. Hu, and X.S. Wang. 2014. Helix cable-detecting robot for cablestayed bridge: Design and analysis. *Journal International Journal of Robotics & Automation* 29 (4): 406–414.
20. K. Alipour, S.A.A. Moosavian, and Y. Bahramzadeh. 2008. Dynamics of wheeled mobile robots with flexible suspension: Analytical modeling and verification. *Journal International Journal of Robotics & Automation* 23 (4): 242–250.
21. Ren H.L., Sun J.L., and Yu H.B. 2015. Self-contained active axial drive device for medical applications. (China invention patent201510698290.6).
22. H. Liu. 2010. Study on magnetic bearing control methods and experiment of a novel configuration. Technical report Degree of Freedoms Magnetically Suspended Flywheel (in Chinese). Beijing, BeiHang University.
23. Ren H.L., Sun J.J., and Wu K.Y. 2015. Self-contained active radial drive device for medical application. (China invention patent201510698176.3).
24. X. Wang. 2011. *Research on novel permanent magnet bias and passive magnetic bearings for magnetically suspended inertial actuators*. Beijing.

25. Allaire Paul E. and JiangWei. 2010. *Self sensing integrated system and method for determining the position of a shaft in a magnetic bearing*. USA.
26. Fan Y.H. 2011. Experimental research on high stability and high precision control of magnetic bearing system for magnetically suspended flywheel used. Technical report Space. Beijing, BeiHang University.

Magnetic Tracking in Medical Robotics

Shuang Song and Hongliang Ren

Abstract Biomedical robotic applications with accuracy requirements demand real-time position and orientation tracking, such as in the field of human motion tracking, rehabilitation, surgical instrument tracking, among many others. Among the state-of-the-art tracking technology, magnetic sensing method is an effective technology to provide fast and accurate tracking result without suffering from occlusion drawbacks. Magnetic sensing techniques are used to sense the distribution of a magnetic source field. With the sensing signals, the pose (position and orientation) between the sensor(s) and the source(s) can be estimated according to the magnetic field distribution model. In contrast to other optical tracking technologies in the clinical setup, magnetic sensing has no line-of-sight problem and is easy to be embedded with many instruments. Therefore, it is useful in intracorporeal applications to provide the location information of the tracked targets inside the human body. For this reason, magnetic sensing techniques have potential to further improve the applications of computer assisted surgeries. For example, flexible curvilinear manipulators or endoscopic devices nowadays need to be tracked in real time for better and safer operations. This chapter gives an overview of how the magnetic sensing technology works in the field of medical instrument tracking. After that, the sensing applications will be given in detail. Three typical medical applications will be discussed: (1) magnetic sensing for wireless capsule robots; (2) Current magnetic sensing devices in clinic setups; and (3) magnetic sensing for flexible surgical robots.

1 Overview of Magnetic Tracking

Magnetic tracking has been studied and applied in many areas, such as human motion tracking, human rehabilitation application, virtual reality, human robot interaction [13], guidance [18], surgery [21] and interventions [20], among many others [3, 16, 32].

S. Song · H. Ren (✉)
Faculty of Engineering, Department of Biomedical Engineering,
National University of Singapore, Singapore 117575, Singapore
e-mail: ren@nus.edu.sg

H. Ren and J. Sun (eds.), *Electromagnetic Actuation and Sensing in Medical Robotics*,
Series in BioEngineering, https://doi.org/10.1007/978-981-10-6035-9_6

Based on the way of generating magnetic field sources, two types of magnetic sensing methods are typically utilized, the permanent magnet-based tracking [26–28], which uses permanent magnet as the magnetic field source; and the quasi-static electromagnetic coils-based tracking [27, 28, 31], which uses current to fed on the coil to generate the magnetic field. For both of these two types, the magnetic dipole model can be used to provide an appropriate tracking result. However, for special propose, such as 6-DOF tracking, the dipole model will fail. Therefore, analytical model will be needed. In this section, we will first introduce the magnetic dipole model and the analytical magnetic field model. After that, the magnetic tracking method will be shown, including the permanent magnetic tracking and the electromagnetic tracking methods.

1.1 Magnetic Dipole Model

The magnetic dipole model is the mostly used model for calculating the magnetic field. Figure 1 shows the magnetic dipole model, in which $(a, b, c)^T$ is the position parameter of the magnet in the global coordinate system. $\mathbf{H} = (m, n, p)$ is the direction of the magnetic moment and $m^2 + n^2 + p^2 = 1$. Therefore, the magnetic field at position $(x, y, z)^T$ can be estimated with the following equation

$$\mathbf{B}_D = B_T \left(\frac{3(\mathbf{H} \cdot \mathbf{P}) \times \mathbf{P}}{R^5} - \frac{\mathbf{H}}{R^3} \right), \tag{1}$$

where $B_T = \mu_r \mu_0 M_T / (4\pi)$, and μ_r is the relative permeability of the medium, μ_0 (with unit Tm/A) is the magnetic permeability of the air. M_T (with unit Am^2) is

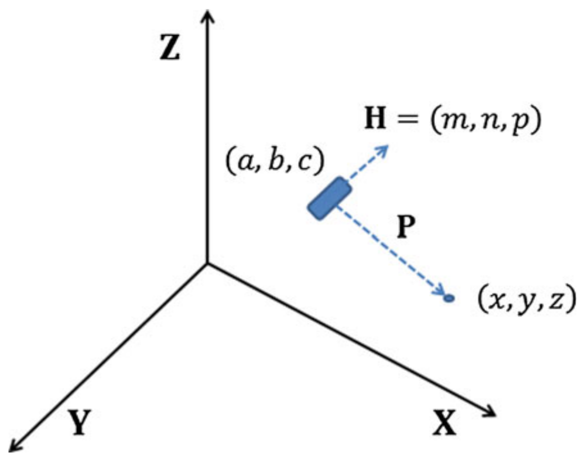

Fig. 1 Magnetic dipole model.

a constant defining the magnetic intensity of the magnet. $\mathbb{P}$ is the vector that from $(a, b, c)^T$ to $(x, y, z)^T$ and R is the distance between these two points.

$$\mathbf{P} = (x - a, y - b, z - c)^T$$

$$R = \sqrt{(x - a)^2 + (y - b)^2 + (z - c)^2}$$

1.2 Integral Based Models

The magnetic dipole model is an approximate model for magnetic field distribution. It has been used in many researches, however, the direction parameter H in the dipole model is a unit vector. Therefore, only 2-DOF orientation information can be obtained. If 3-DOF orientation information is needed, the dipole model will fail. Hence, a closed-form analytical model for special magnet is needed which can provide the 3-DOF position and 3-DOF orientation. In the following part, an example of closed-form analytical model will be shown based on an annular magnet, which can integrate with the capsule endoscope well.

As shown in Fig. 2a, per the Biot–Savart law and the superposition principle, an annular magnet can be regarded as one cylindrical magnet subtracts the other but different radius in terms of the magnetic field. Therefore, we will first present the model of cylinder magnet and then the annular one will then be obtained from the model of the cylinder one.

As shown in Fig. 2b, the cylindrical one has the length parameter as $2a$ and the radius as r. The magnetic moment direction is the same with the Z-axis. Define the origin point of the magnet's coordinate system as the centre of the magnet and the X-axis as the length direction. The magnet can be regarded as surface currents $\mathbf{I}_{ABCDA}$. The surface current $\mathbf{I} = I\mathbf{dl}$ is shown in Fig. 2b using red lines, where $I = J_s dz_0$ is the current magnitude, $\mathbf{dl}$ is the current direction and J_s is the current density (A/m). The magnetic field at the position generated by a surface current with thickness of can be calculated according to the Biot–Savart law. Therefore, the magnetic field at position P generated by the cylinder magnet can be estimated by

$$\mathbf{B} = \int_{-r}^{r} \mathbf{dB} \tag{2}$$

Current can be divided into four segments with different directions. We will first calculate the magnetic field that generated by each segment. After that, can be estimated according to the superposition principle.

The direction of current is. According to the Biot–Savart law, the magnetic field generated by current can be estimated: The direction of current $\mathbf{I}_{AB}$ with segment

(a)

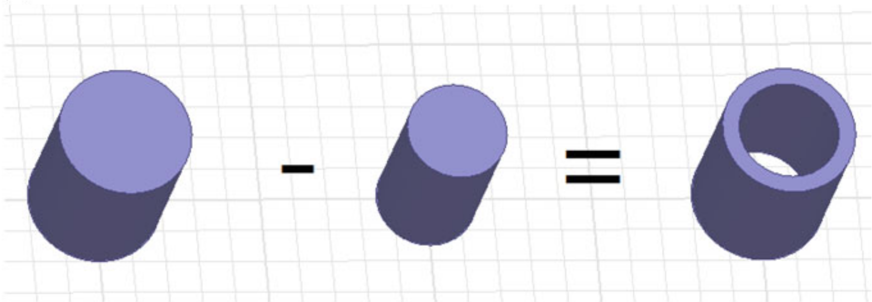

(b)

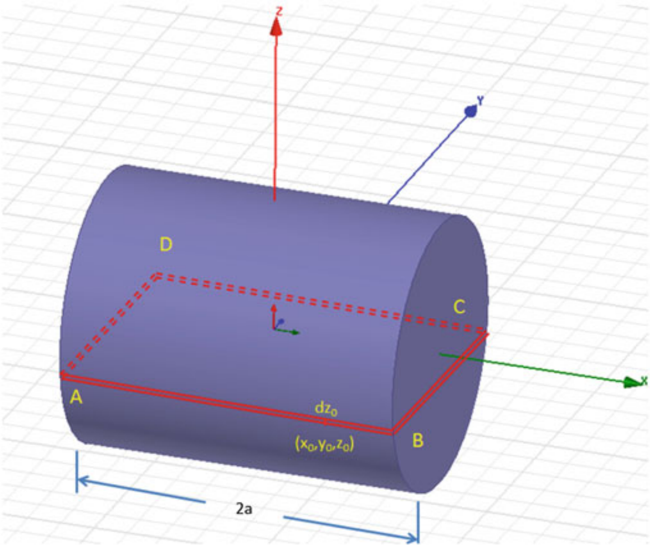

Fig. 2 Modeling of annular magnet. **a** Superposition principle (upper figure) **b** Biot–Savart law (lower figure).

AB is $(1, 0, 0)$. Based on the Biot–Savart law, the magnetic field strength generated by current $\mathbf{I}_{AB}$ can be calculated using the following equation:

$$\mathbf{dB_1} = \frac{\mu_0}{4\pi}\frac{I\mathbf{dl}\times\mathbf{P_0}}{|\mathbf{P_0}|^3} = Kdz_0\int_{-a}^{a}\frac{\begin{vmatrix} i & j & k \\ 1 & 0 & 0 \\ x-x_0 & y-y_0 & z-z_0 \end{vmatrix}}{\left[(x-x_0)^2+(y-y_0)^2+(z-z_0)^2\right]^{3/2}}dx_0 \tag{3}$$

where $K = J_s\mu_0/4\pi$.

For segment BC with current $\mathbf{I}_{BC}$ direction of (0, 1, 0), the magnetic field can be calculated with the subsequent equation

$$\mathbf{dB_2} = \frac{\mu_0}{4\pi}\frac{I\mathbf{dl}\times\mathbf{P_0}}{|\mathbf{P_0}|^3} = Kdz_0\int_{-y'}^{y'}\frac{\begin{vmatrix} i & j & k \\ 0 & 1 & 0 \\ x-a & y-y_0 & z-z_0 \end{vmatrix}}{\left[(x-a)^2+(y-y_0)^2+(z-z_0)^2\right]^{3/2}}dy_0 \tag{4}$$

For current $\mathbf{I}_{CD}$, the direction is $(-1, 0, 0)$ and the magnetic field will be

$$\mathbf{dB_3} = \frac{\mu_0}{4\pi}\frac{I\mathbf{dl}\times\mathbf{P_0}}{|\mathbf{P_0}|^3} = Kdz_0\int_{-a}^{a}\frac{\begin{vmatrix} i & j & k \\ -1 & 0 & 0 \\ x-x_0 & y-y_0 & z-z_0 \end{vmatrix}}{\left[(x-x_0)^2+(y-y_0)^2+(z-z_0)^2\right]^{3/2}}dx_0 \tag{5}$$

For current $\mathbf{I}_{DA}$ with the direction $(0, -1, 0)$, the magnetic field will be

$$\mathbf{dB_4} = \frac{\mu_0}{4\pi}\frac{I\mathbf{dl}\times\mathbf{P_0}}{|\mathbf{P_0}|^3} = Kdz_0\int_{-y'}^{y'}\frac{\begin{vmatrix} i & j & k \\ 0 & -1 & 0 \\ x+a & y-y_0 & z-z_0 \end{vmatrix}}{\left[(x+a)^2+(y-y_0)^2+(z-z_0)^2\right]^{3/2}}dy_0 \tag{6}$$

The magnetic field $\mathbf{dB} = (dB_x, dB_y, dB_z)$ generated by surface current $\mathbf{I}_{ABCDA}$ can then be estimated as follows

$$(dB_x, dB_y, dB_z) = \left(\sum_{i=1}^{4} dB_{xi}, \sum_{i=1}^{4} dB_{y_i}, \sum_{i=1}^{4} dB_{zi}\right) \tag{7}$$

Therefore,

$$\mathbf{B} = (B_x, B_y, B_z) = \left(\int_{-r}^{r} dB_x, \int_{-r}^{r} dB_y, \int_{-r}^{r} dB_z\right) \tag{8}$$

The magnetic field of cylinder magnet can be presented as

$$\mathbf{B_{cylinder}} = (B_x, B_y, B_z) = f_c(x, y, z) \tag{9}$$

Therefore, the solution of the magnetic field generated by an annular magnet will be

$$\begin{aligned}\mathbf{B_{annular}} &= f_{annular}(x, y, z)\\ &= f_c(x, y, z, r_1) - f_c(x, y, z, r_2)\end{aligned} \tag{10}$$

where r_1 and r_2 are the outer and inner radius, respectively.

1.3 Magnetic Tracking Method

One key factor of the magnetic sensing method is how to sense the magnetic field. Two methods are usually used, magnetic sensor and magnetic coils. Principles of these two methods are similar; therefore we take the magnetic sensor method as an example.

A magnetic sensor array is shown in Fig. 3. Each sensor measures the magnetic field at its position and outputs three signals, and, which indicate the field strength on three orthogonal directions parallel to the global coordinate system axes.

Taking i-th sensor as an example: Let its position be $\mathbf{P}_i = (x_i, y_i, z_i)^T$. The output voltages will be $\mathbf{V}_i = (V_{xi}, V_{yi}, V_{zi})^T$. Using the magnetic field model, we can have an estimation of the magnetic field at position $\mathbf{P}_i$, which is $\mathbf{B}_i = (B_{xi}, B_{yi}, B_{zi})^T = f(x, y, z, \alpha, \beta, \gamma, x_i, y_i, z_i)$. $(x, y, z)^T$ is the position parameter of the magnet and $(\alpha, \beta, \gamma)^T$ is the orientation parameter. Define the error function as

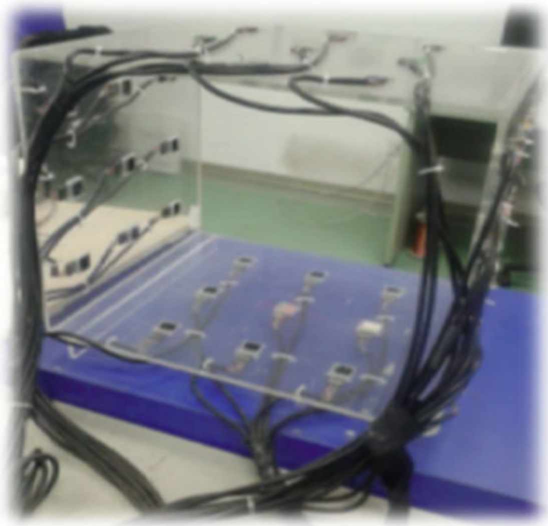

Fig. 3 Magnetic sensor array.

$$f_{e_{rr}} = \sum_{i=1}^{N} ||B_i - s_i V_i||^2 \tag{11}$$

where is a scale factor for the i-the sensor, which relates to the amplifier and the AD chip of the sampling part. By minimizing the error function using an effective optimization algorithm, the position and orientation parameters can be obtained. Here $\mathbf{B}_i$ can be estimated with the magnetic dipole model or the analytic model. We will first introduce the magnetic dipole model-based method in the following part.

1.4 Magnetic Dipole Method Based Methods

There are two methods for the dipole model-based positioning. One is linear algorithm and the other is nonlinear method. We will first introduce the linear algorithm.

Through some vector computation on (1), we can have the following equation

$$(B \times P) \bullet H = 0 \tag{12}$$

This equation can be further simplified as a linear form

$$F \bullet \Gamma = b \tag{13}$$

where

$$F = (B_x, B_y, B_z, B_z y - B_y z, B_x z - B_z x)$$

$$\Gamma = (b - cn', cm' - a, an' - bm', m', n')^T$$

and

$$\begin{cases} m' = \frac{m}{p} \\ n' = \frac{n}{p} \\ b = B_x y - B_y x \end{cases}$$

With the data from the sensor array, a matrix $M = (F_1; F_2; ...; F_N)$ and a vector $B = (b_1, b_2, ..., b_N)$ can be calculated, and then we have

$$\Gamma = (M^T M)^{-1} M^T B \tag{14}$$

Once Γ is solved, the parameters $(a, b, c, m, n, p)^T$ can further be solved.

The nonlinear method generally minimizes the error function (11) by an appropriate nonlinear optimization algorithm, such as LM algorithm. One drawback of the nonlinear method is that the result depends on the initial guess of the parameters. A bad guess can easily lead to a local minima result. One solution is to combine the linear method together with the nonlinear method. The linear method is first used to obtain the initial guess, and then the nonlinear method is performed to find a better global result.

1.5 Integral Model-Based Methods

Since the model of the annular magnet in (10) is established in the local coordinate of the magnet, we have to transform it to the global tracking coordinate system, which is built on the sensor array. Taking i-th sensor as an example, its position is $P_i = (x_i, y_i, z_i)^T$ with output signal $V_i = (V_{ix}, V_{iy}, V_{iz})^T$. The position and orientation parameters of the magnet are $(x, y, z, \alpha, \beta, \gamma)^T$, which can be seen in Fig. 4.

Therefore, the magnetic field at position P_i can be estimated as follows

$$B_i = f_a(x_{il}, y_{il}, z_{il})R^{-1}$$

where

$$(x_{il}, y_{il}, z_{il}) = ((x_i, y_i, z_i) - (x, y, z))R$$

We can then minimize (11) to estimate the unknown position and orientation parameters.

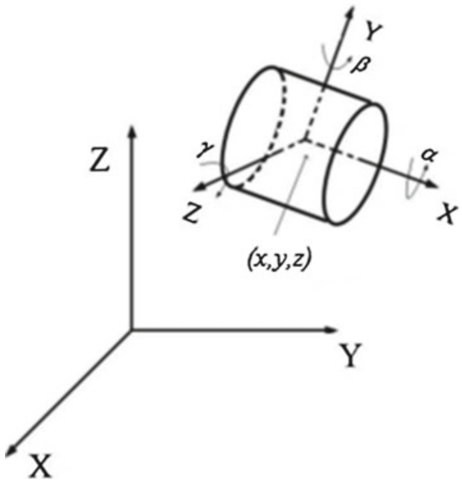

Fig. 4 Coordinate transformation.

2 Electromagnetic Tracking Methods

Compared to the localization approaches based on passive or permanent magnets, the active electromagnetic (EM) localization has better anti-interference performance and a larger sensing range. Usually, three-axis orthogonal transmitting coils are utilized to generate magnetic field seen in Fig. 5. The sensing coils can have different or similar orthogonal structures to the transmitting coils, depending on the design requirements and the applications. In terms of the estimation method, we developed two different methods that can be used, namely direct estimation and rotation-based estimation.

In the direct estimation method, each magnetic field source coil is independent with others. Sensing coils output the signal from every transmitting coil. With an appropriate algorithm, pose information of the sensing coils can be determined.

Raad et al. [11] proposed a tracking method using triaxle transmitting coils and triaxle sensing coils. By processing the sensed signals, small changes of the sensing coils in the coordinates can be detected. Therefore, 3-DOF position and 3-DOF orientation of the sensing coils can be determined. Hu et al. [20] presented an algorithm which is also based on three-axis generating coils and three-axis sensing coils. By expressing the relationship between the transmitting coils and sensing coils with analytic equations, 6-DOF pose information of the sensor coils can be determined directly. Plotkin et al. [10] used a coplanar array consisting of eight transmitting coils to serve as the magnetic field sources. By using the Levenberg–Marquardt (LM) algorithm to solve nonlinear equations, the sensor position can be determined.

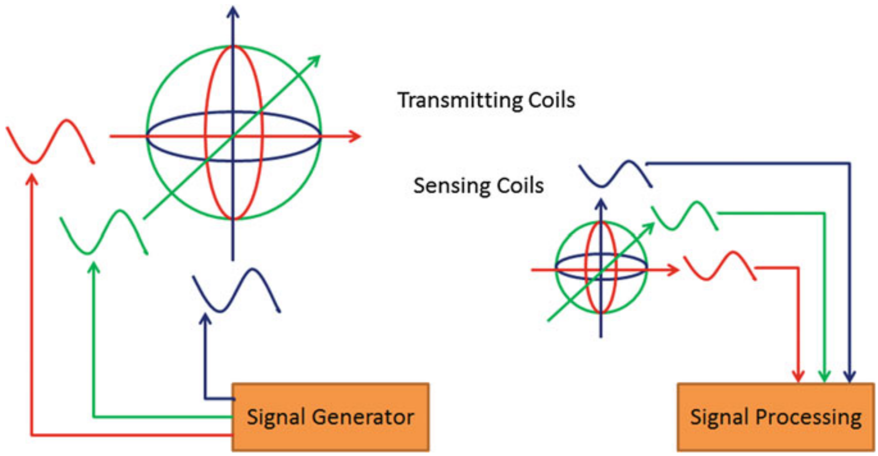

Fig. 5 Electromagnetic tracking method. The magnetic field is generated by the three-axis orthogonal transmitting coils, which are fed with low-frequency alternating current (AC). The sensing coils have the similar structure with the transmitting coils. With the sensing signals, position and orientation of the sensing coils about the transmitting coils can be determined.

The rotation-based method is to rotate the transmitting coil(s) in a particular pattern to generate a rotating dipole field. By extracting features of the rotating field from the sensing signal, position and orientation parameters of the sensing coils can be estimated. Features can be phase, amplitude, maximum value, minimum value and so on. The rotation process can be carried out either mechanically or electrically. For example, a two-axis orthogonal transmitting coils fed with orthogonal sinusoidal signals can be regarded as a single-axis rotating coil. Kuipers et al. [16] proposed a tracking method using a nutating magnetic field. The nutating field is generated by a three-axis coil. Two-axis orthogonal coils fed with orthogonal sinusoidal signals to serve as a rotating coil and the other coil is fed with a direct current (DC) signal. Therefore, a synthetic nutating dipole coil is established. Paperno et al. [9] used two-axis coils fed with the phase quadrature current to serve as a rotating magnetic dipole. By extracting the features such as the phase, maximum and minimum values of the squared total of the AC part of the sensing signal, 3D position and 3D orientation of the sensing coils can be estimated. A similar method was also proposed by Song et al. [28], in which only the amplitude and phase information of the sensing signal are needed.

No matter which estimation method is applied, the tracking method is mainly based on the magnetic dipole. Equations with unknown position and orientation parameters are built based on the dipole model and then can be solved to obtain the pose result. Sometimes, the nonlinear optimization method is used to solve the equation, and in some case the closed-form analytic solution can be found.

As mentioned at the beginning of this chapter, the magnetic tracking method has no line-of-sight problem. In the following part, some applications in medical field will be introduced with the magnetic sensing technology.

3 Magnetic Sensing for Wireless Capsule Robots

First introduced in 2001 by Given Imaging, wireless capsule has provided an easy and comfortable way to diagnosis the gastrointestinal tract. One key limitation factor of the capsule robot is that the image cannot be linked to the position of the GI tract, which makes it hard for physicians to acquire comprehensive clinical information.

One solution is to apply the magnetic sensing method to track the individual capsule endoscope robot. By embedding a magnet into the capsule, real-time tracking can be achieved. As shown in Fig. 6, an annular ring magnet and the associated sensor array can be placed around the capsule, then the real-time position information can be obtained along with the image from the camera. The reason for using annular magnet is that it does not occupy the usable space in the endoscope, and meanwhile will provide enough magnetic field strength for tracking. Figure 7 shows two magnets with different magnetic moment direction. Magnetic moment of magnet “a” is along the length direction of the magnet, which can only provide 3D position and 2D

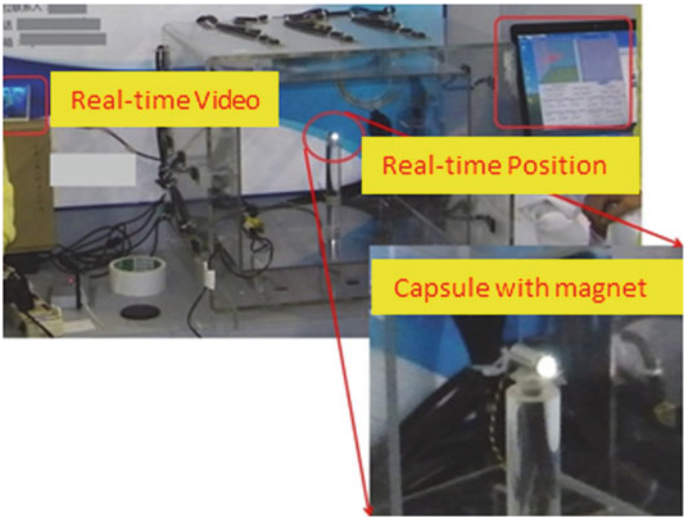

Fig. 6 Endoscope with annular magnet.

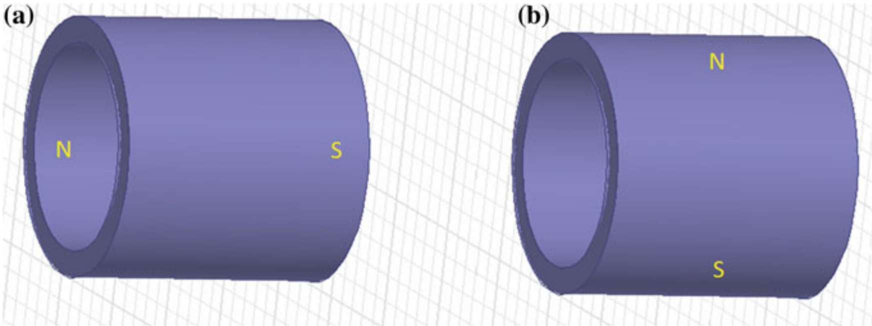

Fig. 7 Different types of annular magnet.

orientation, with the self-rotation information missing. Magnet "b" can provide 6D information, since its magnetic moment it along the height direction, which makes it an asymmetrical structure when rotating about the moment direction. For the tracking with magnet type "a", magnetic dipole model can be used to estimate the 5D position. The method of tracking of magnet type "b" is presented in the previous part of this chapter.

When applying the magnetic sensing method for real life application, the interferences from the movement of the human body should be eliminated, since the coordinate transformation between the tracking sensor array and the human body is varying when movement happens. One feasible solution is to apply a multi-object tracking method [31]. Two magnets fixed on the surface of the human body can serve as a reference coordinate system for the human body. A third magnet is mounted on the capsule and tracked with respect to the reference. Therefore, movement between the human body and the sensor array can be determined in real time and the interferences can be reduced.

4 Electromagnetic Sensing in Clinical Setup

The magnetic sensing system for surgical robots typically includes three parts: the field generator (FG), which creates a magnetic field of known geometry; the EM sensor, which can sense the magnetic field and output signals related to the field. The tracking system unit is designed to control the FG and sample the sensing data to output the position and orientation information.

Usually, the sensor is mounted in the robot and moves with the robot. Therefore, the real-time position information of the robot can be estimated. There are many commercial products that can be used, as shown in Fig. 8.

In-vivo experiments on human body such as the skull [7, 8] and vessels [32] have been performed with actual interventions [12, 22]. These studies provide a practical experience to demonstrate the potential and limitation of EM tracking in in-vivo applications.

It has been shown that EM tracking has potential to be used for catheters, needles, wires and so on. However, tracking accuracy may decrease due to the metal equipment or environment [12, 22]. For example, an increased error due to metal equipment was found during neurosurgical applications [7, 8].

5 Magnetic Sensing for Flexible Robots

Inspired by snakes or other dexterous animals or organs, flexible robots have been well studied for the application of minimally invasive surgery (MIS) with enhanced performance in MIS [13–15, 17, 18]. The flexible robot can deform to unexpected shapes when there is contact with the environment, which may cause damage and hard to detect. Therefore, a real-time shape detection method is needed during the operation for the following reasons.

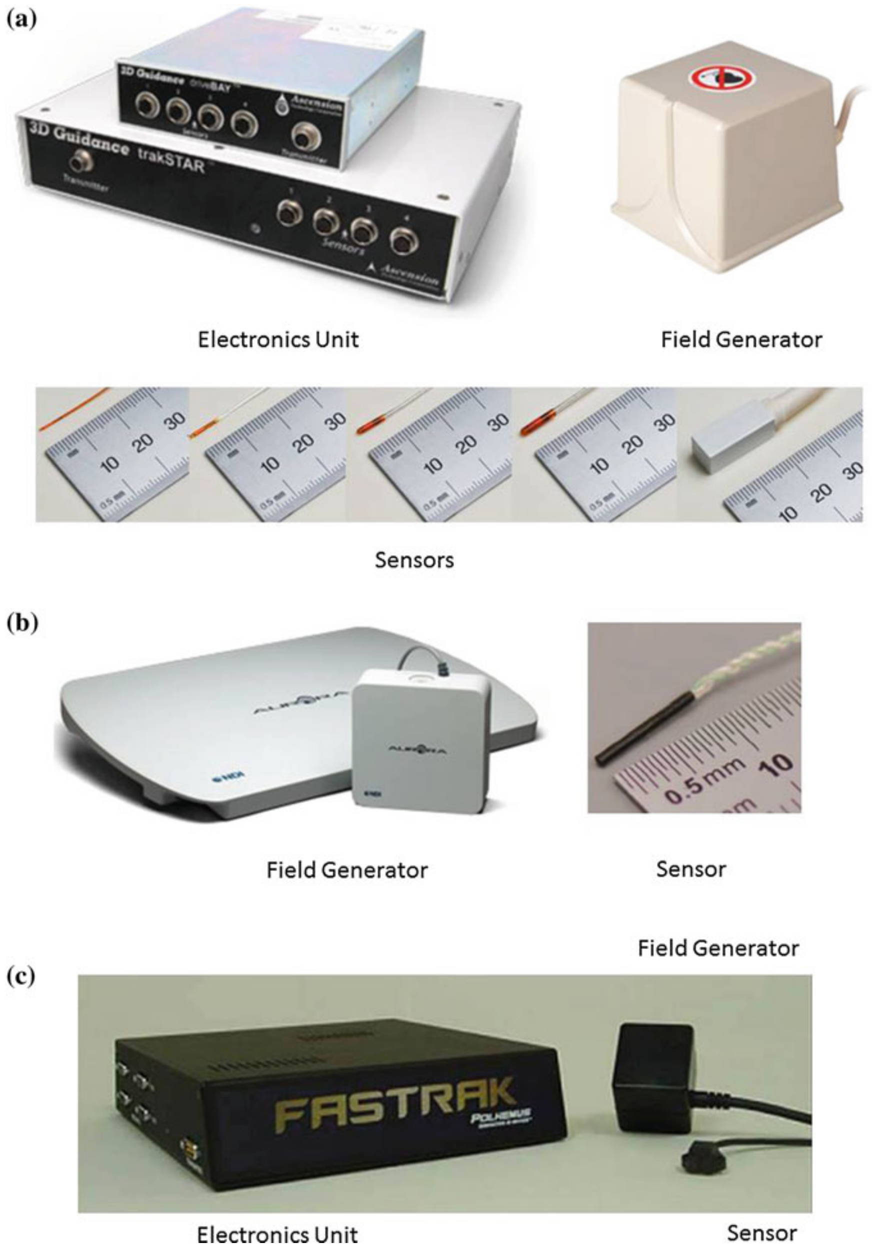

Fig. 8 Commercial electromagnetic tracking products. **a** 3D Guidance **b** Aurora **c** Fastrak.

- Safety issue. During the operation, robot may interact with tissues, which results in not only inaccurate shape estimation, but also potential damage to the tissues. Therefore, positional and shape information of the robot needs to be monitored in real time to detect the contacts and evaluate the scale of the contacts, to provide a safer operation.
- Control issue. Feedback control is required during the operation to provide accurate operation. Therefore, real-time positional and shape information should be provided as feedback to the operator or controller.

Usually, a kinematic model is used to predict the tip and shape information [31]. Under assumptions, such as constant curvature assumption, the shape can be predicted. To achieve more accurate shape estimation, Cosserat Rod Theory [35, 36], geometrically method [34], elliptical integrals [33], Rayleigh-Ritz formulation [23, 28] have also been studied. However, these methods can only estimate the shape only if the external payload is known. In the real operation situation, the contact forces between the robot and the tissues are usually unknown. Therefore, kinematic models may fail to predict the tip position and shape estimation. To overcome the disadvantage, sensor-based shape prediction or reconstruction methods have been studied [31]. Medical images, such as Ultrasound image [32], CT image [19] or Magnetic Resonance Imaging (MRI) [3, 5], have been studied and proved to be feasible to provide shape estimation. Besides the image-based method, Fiber Bragg Grating (FBG)-based technology has been widely studied [6, 32]. This method uses a number of FBG sensors to be mounted in specific positions of the robot. These sensors can provide the axial strain of the placed position. With the axial strain information, curvature of the placed position can be computed. Therefore, 3D robot shape can be estimated from the curvatures of each place position and then the tip pose can also be estimated.

In our previous work, we have demonstrated that Electromagnetic tracking (EMT) method can be used to estimate the shape of multi-segment continuum robots [29–31]. In the following parts, two applications of the shape sensing will be introduced, one is the wire-driven flexible robot and the other is the concentric tube robot.

5.1 Wire-Driven Flexible Robots

Figures 6, 7, 8, 9 and 10 Multi-section wire-driven flexible robot with two bending sections. Each section can be controlled independently to deform as an arc with different curvatures.

The wire-driven flexible robot is a kind of continuum flexible robots developed for minimally invasive surgeries (MIS). As shown in Figs. 6, 7, 8, 9 and 10, the robot contains two parts: the driven part and the bending part. The link between the driven part and the bending part is wire. Each bending section can be controlled independently to deform to a curve.

To achieve better and safer performance, the real-time tip position and shape information are important to provide feedback control. Thanks to its no line-of-sight problem, magnetic sensing method is a good choice to provide the tip tracking results. Based on the tip position and orientation results, real-time shape can be estimated.

The general work flow of the EMT-based shape estimation method is as follows,

- Mount the electromagnetic sensors on the predetermined positions of the robot. These positions are usually the starting points and the ending points of the fitting curves. The order of the curve is decided with the bending of the robot. Generally, both quadratic Bezier curve and cubic Bezier curve [30] can be used and the detailed selection scheme will be presented in the discussion section.
- Use the curve length information to serve as the target function and then perform the optimization algorithm to estimate the unknown parameters of the curve. The curve length is predetermined by the length of the flexible robot.
- Estimate and show the robot's shape based on the Bezier curve. For a wire-driven flexible robot, each joint can have an estimated position from the Bezier curve. For the concentric tube robot, the shape information can be sampled from the Bezier curve with small interval.

An example for shape sensing can be seen in Fig. 9. The robot has two independent sections mounted with three magnetic sensors. One sensor is mounted on the distal end of the robot to perform the tip tracking and shape sensing. One sensor is mounted on the base of the robot is to provide transformation information between EMT coordinate system and robot's coordinate system. The third sensor is mounted on the cross joint of the robot, which is to serve as the reference to evaluate the shape sensing accuracy. Different colours have been used to represent different section.

Figure 10 shows the shape estimation for wire-driven flexible robot in the transoral surgery. A forceps is mounted at the tip of the robot. Once the tip arrives at the desired position, the forceps will grip the tissue for the biopsy experiments. The real-time shape information is shown on screen to monitor the insertion procedure. The tip position information is also displayed in real-time overlaid with the CT image. A sequence of the real-time shape sensing can be seen in Fig. 11.

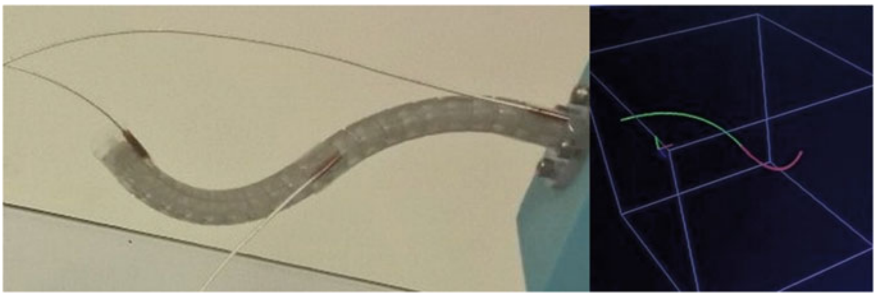

Fig. 9 Experimental platform for the shape sensing with quadratic Bézier curves.

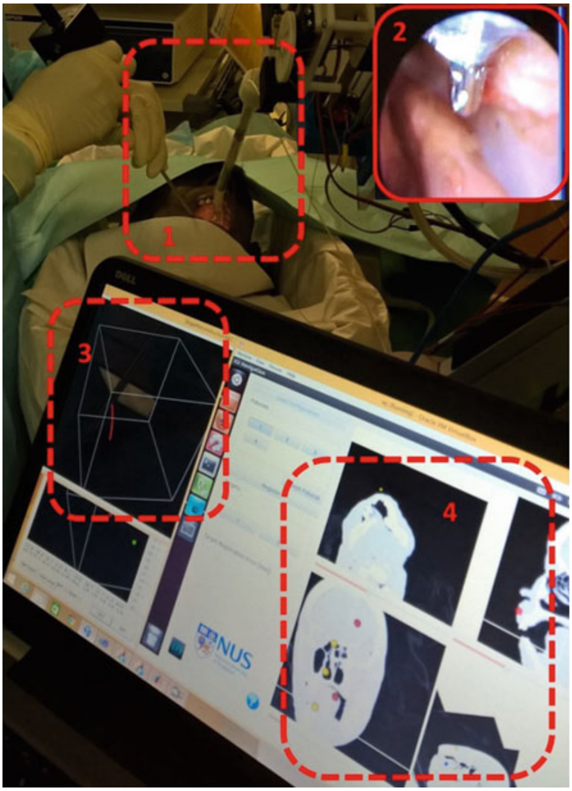

Fig. 10 Shape estimation for wire-driven flexible robot in transoral surgery. *1* The wire-driven flexible robot in the transoral procedure; *2* The image inside the cadaver. It shows the forceps in the tooltip of the robot to grasp the tissue; *3* Real-time shape information and *4* Real-time tip position in the CT image.

5.2 Concentric Tube Robots (CTR)

Concentric tube robots (CTR) [1, 18, 35] are a kind of continuum flexible robots developed for minimally invasive surgeries (MIS). Typically, a CTR contains two or more concentric tubes nested one by one. Each tube can be controlled to rotate and translate independently. With different configurations of tubes' rotation and translation, shape of the robot can be controlled. Therefore, CTR has the potential to follow curved paths into the human body via small open orifices, and meanwhile avoiding collision with tissues due to its controllable curved shape. As a result, more efficient MIS can be achieved.

To achieve better performance, the shape of the tubes is a key factor. Inaccurate estimation of the shape may cause direct contact with the tissues, which may results in unnecessary tissue overload or trauma. Usually, the kinematic model is used to estimate the shape information. However, it may be inaccurate if there are unknown external forces. To solve this problem, we proposed to use magnetic sensing method

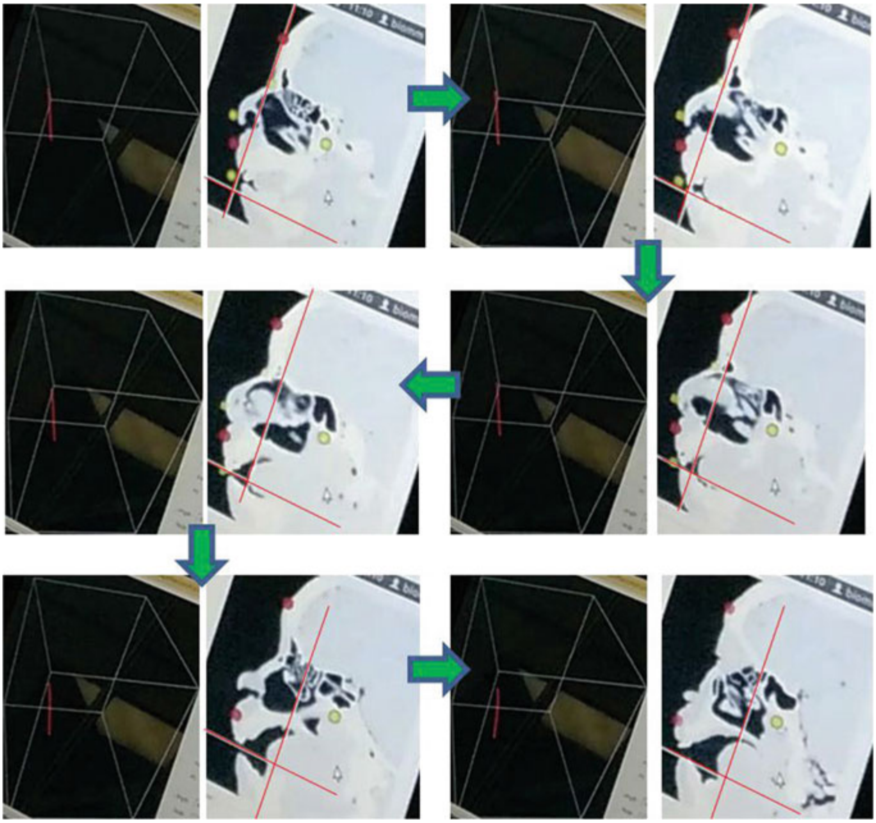

Fig. 11 The sequence shows the inserting procedure during the transoral procedure. For each step, the left figure is the shape estimation result and the right figure is the tooltip position in the CT image. The yellow points in the CT image are the registration points and the red points are the target points to verify the registration precision. The cross point of the two red lines in the CT image indicates the tip position.

to perform the shape sensing. The method is similar with the algorithm used in the shape sensing of wire-driven flexible robot mentioned in the above sections. As shown in Fig. 12, two sensors have been mounted on a CTR with two tubes. For each tube, one sensor has been mounted at the distal end of the tube. Figure 13a shows an experiment of the robot moving inside a plastic mould and the real-time is shown in Fig. 13b. Different colour has been used to represent different tube.

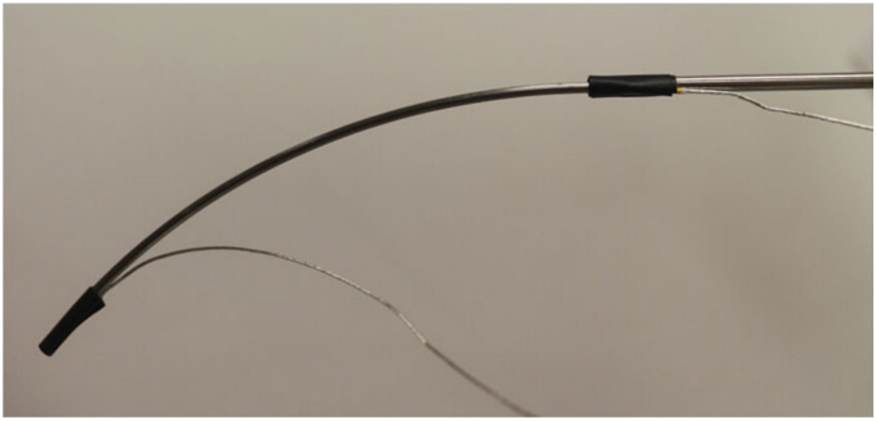

Fig. 12 Shape sensing for a concentric tube robot.

Fig. 13 Shape sensing experiments for concentric tube robot. **a** Shape sensing application **b** Shape sensing results.

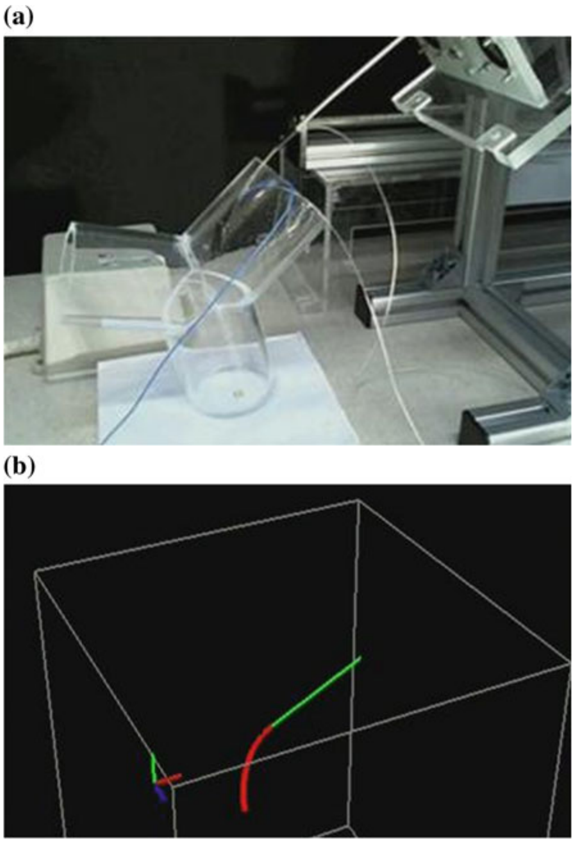

Fig. 14 Motion star and LIBERTY.

6 Magnetic Sensing in Rehabilitation

Magnetic sensing method can be used to provide visual-free tracking results in biomechanics, human motion study and rehabilitation field. To achieve this goal, human motion tracking is necessary as a feedback to correct any undesired motion or behaviour. Usually, sensors are mounted to the human body to collect motion information. Some commercial products have already been used in such filed, such as Motion Star from Ascension Technology, LIBERTY from Polhemus (Fig. 14). The advantage of the sensing method is no line-of-sight problem with low cost. However, the ferromagnetic materials may reduce the accuracy of the tracking results. Moreover, the sensing distance is quite short compared to the optical tracking method.

7 Challenge and Future Work

The electromagnetic tracking method has the following drawbacks:

- Each sensor needs a cable to connect to the control board, which makes it hard to be used in the wireless tracking applications.
- The sensor is kind of expensive and sometimes it cannot be reused due to some health condition.

- The tracking results will be affected by the metal materials in the clinical environment.

One more issue of the EMT and PMT methods is that the tracking range is small compare to the optical tracking. Therefore, in the future developments for better use in the clinical applications, the above issues must be solved, especially the affection from the metal materials, which is the main restriction as the barrier of the widely use of the EMT in clinical applications.

Moreover, shape sensing for flexible surgical robots in minimally invasive surgery is also essential to provide safety and effective procedure. Hence, accurate shape estimation should be well studied, not only for the shape sensing, but also for the force sensing with shape information.

Acknowledgements This work was in part supported by the Singapore Academic Research Fund under Grant R-397-000-173-133 (Magnetically Actuated Micro-robotics) and National Natural Science Foundation of China NSFC grant 51405322, awarded to Dr. Hongliang Ren.

References

1. Dupont, P.E., et al. 2012. Concentric tube robots for minimally invasive surgery. In *Hamlyn Symposium on Medical Robotics*, vol. 7, 8.
2. Dupont, Pierre E., et al. 2010. Design and control of concentric-tube robots. *IEEE Transactions on Robotics* 26 (2): 209–225.
3. Hamed, Abbi, et al. 2012. Advances in haptics, tactile sensing, and manipulation for robot-assisted minimally invasive surgery, noninvasive surgery, and diagnosis. *Journal of Robotics* 14. https://doi.org/10.1155/2012/412816.
4. Hu, Chao, et al. 2010. A cubic 3-axis magnetic sensor array for wirelessly tracking magnet position and orientation. *IEEE Sensors Journal* 10 (5): 903–913.
5. Johnson, Meredith, et al. 2017. Fabricating biomedical origami: a state-of-theart review. *International Journal of Computer Assisted Radiology and Surgery* 1–10, ISSN: 1861-6429. https://doi.org/10.1007/s11548-017-1545-1.
6. Li, Tianliang, and Hongliang Ren. 2017. A diaphragm type fiber Bragg grating vibration sensor based on transverse property of optical fiber with temperature compensation. *IEEE Sensors Journal* PP.99: 1-8, ISSN: 1530-437X.
7. Li, Zheng, et al. 2015. A novel tele-operated flexible surgical arm with optimal trajectory tracking aiming for minimally invasive neurosurgery. In *CIS-RAM 2015, 7th IEEE international conference on cybernetics and intelligent systems (CIS) and the 7th IEEE international conference on robotics, automation and mechatronics (RAM)*.
8. Li, Zheng, et al. 2015. Design and testing of a novel flexible endoscope (Techincal Brief).
9. Paperno, Eugene, Ichiro Sasada, and Eduard Leonovich. 2001. A new method for magnetic position and orientation tracking. *IEEE Transactions on Magnetics* 37 (4): 1938–1940.
10. Plotkin, Anton, et al. 2008. Magnetic tracking of eye motion in small, fastmoving animals. *IEEE Transactions on Magnetics* 44 (11): 4492–4495.
11. Raab, Frederick H., et al. 1979. Magnetic position and orientation tracking system. *IEEE Transactions on Aerospace and Electronic Systems* 5: 709–718.
12. Ren, Hongliang, and Peter Kazanzides. 2012. Investigation of attitude tracking using an integrated inertial and magnetic navigation system for hand- held surgical instruments. *IEEE/ASME Transactions on Mechatronics* 17 (2): 210–217, ISSN: 1083-4435. https://doi.org/10.1109/TMECH.2010.2095504.

13. Ren, Hongliang, and Peter Kazanzides. 2012. Investigation of attitude tracking using an integrated inertial and magnetic navigation system for hand-held surgical instruments. *IEEE/ASME Transactions on Mechatronics* 17 (2): 210–217.
14. Ren, Hongliang, and Max Q.-H. Meng. 2009. Game-theoretic modeling of joint topology control and power scheduling forwireless heterogeneous sensor networks. *IEEE Transactions on Automation Science and Engineering* 6 (4): 610–625, ISSN: 1545-5955. https://doi.org/10.1109/TASE.2009.2021321.
15. Ren, Hongliang, and Max Q.-H. Meng. 2009. Investigation of navigation and robotic system for computer assisted orthopedic surgery: state-of-art and preliminary results. *International Journal of Information Acquisition* 6 (3): 171–179. https://doi.org/10.1142/S0219878909001904
16. Ren, Hongliang, et al. 2013. Computer-assisted transoral surgery with flexible robotics and navigation technologies: A review of recent progress and research challenges. *Critical Reviews in Biomedical Engineering* 41 (4–5): 365–391, ISSN: 0278-940X. https://doi.org/10.1615/CritRevBiomedEng.2014010440.
17. Ren, Hongliang, et al. 2011. Development of a wireless hybrid navigation system for laparoscopic surgery. In *MMVR'11, 18th international conference on medicine meets virtual reality*, Feb 2011. http://www.ncbi.nlm.nih.gov/pubmed/21335843.
18. Ren, Hongliang, et al. 2012. Multi-sensor data fusion in an integrated tracking system for endoscopic surgery. *IEEE Transactions on Information Technology in Biomedicine* 16 (1): 106–111, ISSN: 1089-7771. https://doi.org/10.1109/TITB.2011.2164088.
19. Ren, Hongliang, et al. 2011. Towards fully automatic extraction of the lung field from volumetric images. In *IEEE international conference on information acquisition, accepted*, Feb 2011.
20. Ren, Hongliang, et al. 2014. Treatment planning and image guidance for radiofrequency ablation of large tumors. *IEEE Transactions on Information Technology in Biomedicine (IEEE Journal of Biomedical and Health Informatics)* 18 (3): 920–928, ISSN: 2168-2194. https://doi.org/10.1109/JBHI.2013.2287202.
21. Ren, Hongliang, et al. 2014. Treatment planning and image guidance for radiofrequency ablation of large tumors. *IEEE Journal of Biomedical and Health Informatics* 18 (3): 920–928.
22. Ren, Hongliang, et al. 2010. Wireless hybrid tracking system for image guided therapy. In *IGT 2010, 3rd annual image-guided therapy workshop*, Mar 2010.
23. Rucker, D Caleb, and Robert J Webster. 2011. Statics and dynamics of continuum robots with general tendon routing and external loading. *IEEE Transactions on Robotics* 27 (6): 1033–1044.
24. Rucker, D Caleb, et al. 2010. Equilibrium conformations of concentric-tube continuum robots. *The International Journal of Robotics Research*.
25. Shi, Chaoyang, et al. 2017. Shape sensing techniques for continuum robots in minimally invasive surgery: A survey(in press). *IEEE Transactions on Biomedical Engineering* PP.99: 1–15, ISSN: 0018-9294. https://doi.org/10.1109/TBME.2016.2622361.
26. Song, Eun Kyoo, et al. 2008. Accuracy of navigation: a comparative study of infrared optical and electromagnetic navigation. *Orthopedics* 31 (10): 76.
27. Song, Shuang, et al. 2013. An electromagnetic localization and orientation method based on rotating magnetic dipole. *IEEE Transactions on Magnetics* 49 (3): 1274–1277.
28. Song, Shuang, et al. 2015. Electromagnetic positioning for tip tracking and shape sensing of flexible robots. *IEEE Sensors Journal* 15 (8): 4565–4575.
29. Song, Shuang, et al. 2015. Real-time shape estimation for wire-driven flexible robots with multiple bending sections based on quadratic Bezier curves. *IEEE Sensors Journal* 15 (11): 6326–6334, ISSN: 1530-437X. https://doi.org/10.1109/JSEN.2015.2456181.
30. Song,Shuang, et al. 2015. Shape reconstruction for wire-driven flexible robots based on Bezier curve and electromagnetic positioning. *Mechatronics* 29 (99): 28–35, ISSN: 0957-4158. https://doi.org/10.1016/j.mechatronics.2015.05.003. http://www.sciencedirect.com/science/article/pii/S0957415815000689.
31. Song, Shuang, et al. 2015. Shape reconstruction for wire-driven flexible robots based on Bézier curve and electromagnetic positioning. *Mechatronics* 29: 28–35.
32. Stoll, Jeffrey, Hongliang Ren, and Pierre E. Dupont. 2012. Passive markers for tracking surgical instruments in real-time 3D ultrasound imaging. *IEEE Transactions on Medical Imaging* 31 (3): 563–575. https://doi.org/10.1109/TMI.2011.2173586.

33. Webster III, Robert J., and Bryan A. Jones. 2010. Design and kinematic modeling of constant curvature continuum robots: A review. *The International Journal of Robotics Research* 29 (13): 1661–1683.
34. Wu, Liao, and Hongliang Ren. 2016. Finding the kinematic base frame of a robot by hand-eye calibration using 3D position data. *IEEE Transactions on Automation Science and Engineering* 1–11, ISSN: 1545-5955. https://doi.org/10.1109/TASE.2016.2517674.
35. Wu, Liao, et al. 2017. Development of a compact continuum tubular robotic system for nasopharyngeal biopsy. *Medical and Biological Engineering and Computing* 403–417, ISSN: 1741-0444. https://doi.org/10.1007/s11517-016-1514-9.
36. Wu, Liao, et al. 2016. Simultaneous hand-eye, tool-flange, and robot-robot calibration for comanipulation by solving AXB = YCZ problem. *IEEE Transactions on Robotics* 32 (2): 413–428, ISSN: 1552- 3098. https://doi.org/10.1109/TRO.2016.2530079.

Passive Magnetic Localization in Medical Intervention

Zhenglong Sun, Luc Maréchal and Shaohui Foong

Abstract In the past decade, with continual advancement in the magnetic field sensing technology, passive magnetic tracking has become an emerging trend in the field of medical intervention. By embedding a small permanent magnet in the medical instrument, the passive magnetic tracking approach makes the system possible to have untethered, compact and wearable, even modular design for better ergonomics and lower hardware requirements. In this chapter, an overview of the working principle and methods of the passive magnetic tracking technology was presented. Implementation of the technology in actual medical interventions were also demonstrated. Lastly, the challenges in the development of this technology were explored and discussed.

1 Introduction

Motion tracking and navigation systems are paramount for both safety and efficacy in a variety of medical interventions and procedures. Magnetic field-based tracking technology becomes appealing for such applications. It utilizes the phenomenon that the distance and orientation of the magnetic source will change the amplitude and direction of the local magnetic field in space. By mapping the measurements of the local magnetic field to the distribution of the magnetic source, it is able to estimate up to six degrees-of-freedom (DOFs) positional information (both position

Z. Sun (✉)
School of Science and Engineering, The Chinese University of Hong Kong, Shenzhen,
2001 Longxiang Blvd, Longgang District, Shenzhen, China
e-mail: zhenglong.sun@ieee.org

L. Maréchal
SiMMS (Simulation and Modelling in Medicine and Surgery), Imperial College London,
369 Fulham Road, Chelsea and Westminster Hospital, London, UK
e-mail: l.marechal@imperial.ac.uk

S. Foong
Engineering Product Development, Singapore University of Technology and Design,
8 Somapah Road, Singapore, Singapore
e-mail: foongshaohui@sutd.edu.sg

H. Ren and J. Sun (eds.), *Electromagnetic Actuation and Sensing in Medical Robotics*,
Series in BioEngineering, https://doi.org/10.1007/978-981-10-6035-9_7

and orientation). Because the magnetic fields are of a low field strength and can safely pass through human tissue with least interference, it can be used for tracking instruments/tools inside the human body without line-of-sight restrictions.

In general, based on the type of the magnetic source, the tracking techniques can be divided into two groups: active electromagnetic (EM) tracking and passive magnetic tracking. In active electromagnetic tracking, the magnetic source is generated by excitation coils; while in passive magnetic tracking, the magnetic source is from a permanent magnet. Although both groups are often referred as *magnetic tracking*, the underlying principles are fundamentally different [4]. Several tracking systems based on the active approach have been commercially available. It requires sending a small sensor coil (e.g. AURORA system, NDI Medical, US) or an EM transmitter (e.g. CORTRAK system, Corpak Medsystems, US) together with the medical instrument into the human body. The source will generate controlled, varying electromagnetic field. Small voltage signals will be induced in the sensor coil, and therefore be characterized to calculate the position and orientation of the sensor. In this process, tethering wires are usually indispensable for power supply as well as electrical signal transmission. In comparison to that, the passive magnetic tracking provides a less-invasive option. It only requires associating a small permanent magnet with the medical instrument as the passive source, and all electronic components (such as the magnetic sensors) can be left outside the human body. By measuring the magnetic fields at fixed points in space, the position, and orientation of the permanent magnet can be calculated. In such manner, the system can be designed to be completely untethered and wireless. Because of this feature, passive magnetic tracking approach has been adopted in many medical research studies, such as the wireless capsule endoscope [14, 22], heart valve prostheses [1], ventriculostomy [11] and nasogastric intubation [2, 20].

Therefore, in this chapter, the magnetic field model often used in passive magnetic tracking is first reviewed. Then two different localization methods are described, namely the inverse optimization method and the direct ANN (artificial neural network) method; the advantages and disadvantages of the two methods are discussed using two actual medical intervention procedures for practical illustration. Lastly, some limitations and challenges faced by the passive magnetic tracking are discussed.

2 Modeling the Magnetic Field of Permanent Magnet

2.1 Dipole Model

Same as in the active EM tracking technique, the magnetic source is often modeled by a magnetic dipole as shown in Fig. 1. The Dipole Model (originally suggested by Fitz Gerlad in 1883) is commonly adopted in these works for its simplicity. Schlageter et al. first presented a 5-DOFs tracking system with 4×4 2D-array of Hall sensors [15]. Hu et al. evaluated different nonlinear optimization methods in

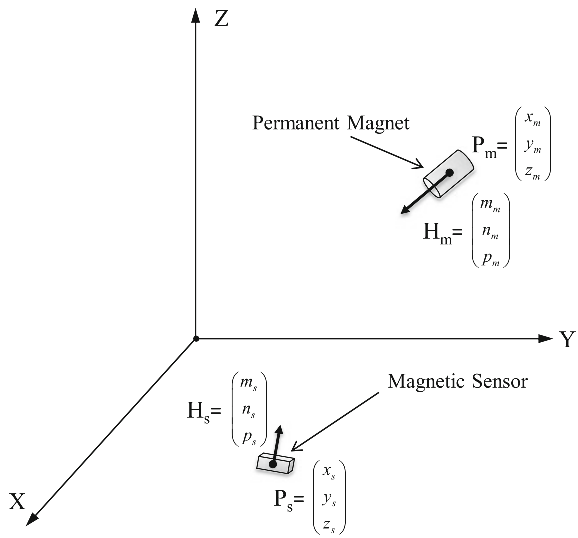

Fig. 1 Illustration of modeling the permanent magnet as a single magnetic dipole.

tracking 3D location and 2D orientation of the capsule endoscope movement [7]. Yao et al. demonstrated the detection of magnetic object with a fixed three-axial Hall probe for tracking control [26]. Lee et al. developed a magnetic gradient tensor method to detect ferromagnetic objects for guiding the visually impaired [8, 9]. Researches have also been done in the sensor arrangement and optimization to achieve higher tracking accuracy [6, 12, 13].

In Dipole Model, the total magnetic flux density at ith observation point (magnetic sensor) due to the magnetic dipole is modeled as

$$\mathbf{B}(\mathbf{P}_{s_i}) = \frac{\mu_r \mu_0 \cdot M}{4\pi} \left(\frac{3(\mathbf{H}_m \cdot \mathbf{P}_i)\mathbf{P}_i - R_i^3 \cdot \mathbf{H}_m}{R_i^5} \right), \tag{1}$$

where μ_r is the relative permeability of the medium, μ_0 is the magnetic permeability of free space (mT· mm/A), M is the constant strength of the dipole moment (A· mm^2) measured from the permanent magnet, $\mathbf{H}_m$ is a unit vector along the magnet magnetization axis. and $\mathbf{P}_i$ is a vector from the magnet $\mathbf{P}_m$ pointing to the ith sensor $\mathbf{P}_s^i$, and R_i is the magnitude of the vector $\mathbf{P}_i$,

$$\mathbf{P}_i = \mathbf{P}_{s_i} - \mathbf{P}_m. \tag{2}$$

Dipole model is known for its simplicity, since it has only one unknown parameter, the dipole moment strength M. Usually it is considered to be constant, and can be decided by the material magnetic field strength and the magnetic object volume.

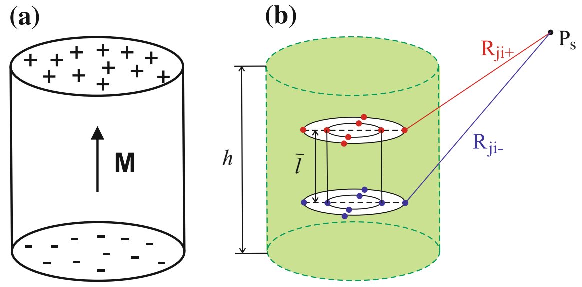

Fig. 2 Illustration of **a** the Charge Model and **b** the Distributed Multipole Model of a cylindrical permanent magnet.

2.2 *Charge Model*

While the dipole model has been widely adopted, it ignores the geometry of the permanent magnet and it gives poor approximation of the near field of the magnet. In general, it is often studied best for needle-like magnets, or the distance is sufficiently larger than the dimension of the magnet. To account for the geometry of a permanent magnet, the Charge Model can be used. In the Charge Model, the magnet is modeled as a distribution of equivalent "*magnetic charge*" as shown in Fig. 2a. It is derived from the magnetostatic field equations, and the fields are obtained using standard methods [5]. It defines two parameters

$$\begin{aligned} \rho_m &= -\nabla \cdot \mathbf{M} \ \ (A/m^2) \qquad \text{(volume charge density)} \\ \sigma_m &= \mathbf{M} \cdot \hat{\mathbf{n}} \ \ (A/m) \qquad \text{(surface charge density)}, \end{aligned} \tag{3}$$

where $\mathbf{M} = M_s \mathbf{H}_m$ is the magnetization, and $\hat{\mathbf{n}}$ is the outward unit normal vector. Considering a magnet is free space, the magnetic flux density at observation point $\mathbf{P}_s$ can be written as

$$\mathbf{B}(\mathbf{P}_s) = \frac{\mu_0}{4\pi} \int_V \frac{\rho_m(\mathbf{P}_c)(\mathbf{P}_s - \mathbf{P}_c)}{|\mathbf{P}_s - \mathbf{P}_c|^3} dv' + \frac{\mu_0}{4\pi} \oint_S \frac{\sigma_m(\mathbf{P}_c)(\mathbf{P}_s - \mathbf{P}_c)}{|\mathbf{P}_s - \mathbf{P}_c|^3} ds', \tag{4}$$

where $\mathbf{P}_c = [x_c, y_c, z_c]^T$ is the source point (the surface magnetic charge).

For a constant magnetization in a magnet, the volume charge density ρ_m equals to zero, and the magnetic field can be calculated by integration of the surface charge density. In such manner, both the shape and the magnetization of the magnet will contribute to the magnetic field calculation.

2.3 *Distributed Multipole Model*

Distributed Multipole (DMP) model is another method that is often used to account for the shape and magnetization of a permanent magnet. It was firstly proposed and generalized in [10]. In the DMP model, a *dipole* is defined as a pair of source and sink separated by a distance $\bar{l}$. And it may contain multiple k loops (or columns) of n dipoles distributed within the magnet volume, as shown in Fig. 2b.

The magnetic flux density at any point $\mathbf{P}_s$ contributed by all the dipoles (in terms of the ith dipole in the jth loop) is thus given by

$$\mathbf{B}(\mathbf{P}_s) = \sum_{j=0}^{k} \sum_{i=0}^{n} M_{ji} \beta_{ji}, \tag{5}$$

Here M_{ji} is the strength of the jith dipole, and the term β_{ji} represents

$$\beta_{ji} = -\frac{\mu_0}{4\pi} \left(\frac{\mathbf{a}_{R_{ji+}}}{R_{ji+}^2} - \frac{\mathbf{a}_{R_{ji-}}}{R_{ji-}^2} \right), \tag{6}$$

where $\mathbf{a}_R = \mathbf{R}/R$, and R_{ji+} and R_{ji-} expressed in terms of distance $\bar{l}$ are the distances from the source and sink of the jith dipole to the observation point $\mathbf{P}_s$.

The unknown parameters in (5) are the number of dipoles per loop n, the loop number k, the separation distance between the source and sink $\bar{l}$, and the strength of the moment for each dipole m_{ji}. Given more degrees of freedoms, the DMP model outperforms the Dipole Model in depicting the magnetic field of a permanent magnet of random shape and magnetization; but all the parameters have to be calculated accordingly through proper calibrations, since there is no physical meaning behind the distributed dipoles.

2.4 Hybrid Model

Although the model accuracy deteriorates as it approaches the surface of the magnet, the Dipole Model is still able to adequately characterize the magnetic field at large distances from the source for many applications. Therefore, a hybrid model has been proposed by Wu et al. to keep the simplicity of the model while compensating for the incompetence of the Dipole Model at near field [23].

In this hybrid model, non-parametric Artificial Neural Network (ANN) model is employed to depict the magnetic field in spatial areas at close proximity to the magnet; and the parametric Dipole model is employed at spatial locations sufficiently far away from the magnetic source. By exploiting the magnetic field of an axisymmetric permanent magnet in cylindrical coordinates as elaborated in Fig. 3, the workload for data collection and training for the ANN model can be reduced significantly. In order to ensure smooth transition between the two models in the hybrid model, the magnetic equipotential (region in free space where every point is at the same potential, i.e., B = constant) is used. The concept of the hybrid model is as shown in Fig. 4.

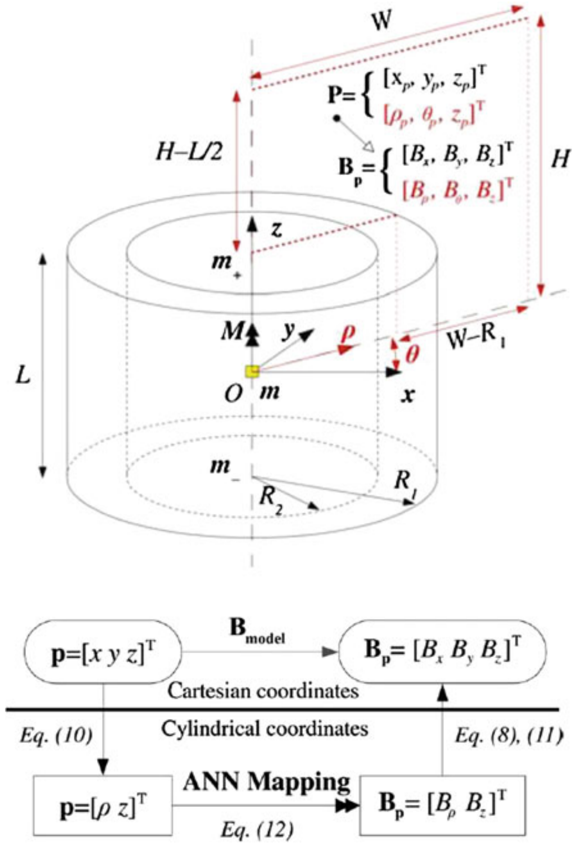

Fig. 3 Schematic illustration of the magnetic field of an axisymmetric cylinder/annular magnet (above) and the ANN mapping process with conversions between Cartesian and Cylindrical Coordinates (below). W and H representing the width and height of the field, while L and R representing the length and radius of the magnet respectively.

Here a potential threshold B_{th} is introduced. By observing the magnetic field B_p as measured at location **p**, the ANN model will be used if $B_p \geq B_{th}$ (closer to the magnet) and Dipole model will be used if $B_p \leq B_{th}$ (further away from the magnet). A sigmoid function is used together to determine the percentage of contribution from the two models as shown below,

$$B_{hybrid} = B_{ANN} \times y + B_{Dipole} \times (100 - y), \tag{7}$$

where the percentage y is expressed as

$$y = 50 \left[\frac{B_p - B_{th}}{\sqrt{A + (B_p - B_{th})^2}} + 1 \right]. \tag{8}$$

In such manner, the hybrid model is able to maintain the modeling accuracy at locations near the magnet, and retain the capability of extrapolating the fields using

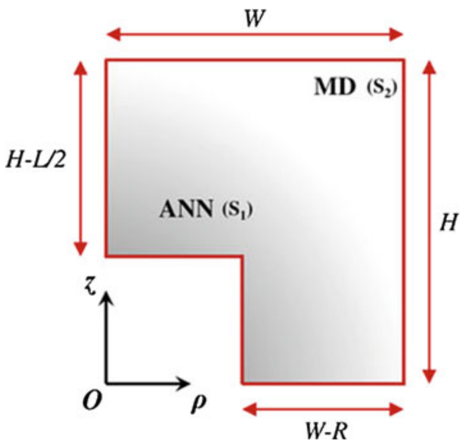

Fig. 4 Illustration of the hybrid model of a cylindrical magnet in the transverse plane. ANN model region (S_1) and Magnetic Dipole (MD) model region (S_2) segregate along the equipotential line.

the simple parametric Dipole model. The hybrid model is also able to account for the geometry and size of the permanent magnet, but the method discussed here is only optimized for axisymmetric magnetic object. It is worthy to note that it can be easily generalized to arbitrary geometry and magnetization if needed. Still pre-calibration procedure is required for the ANN model, and re-calibration of the Dipole model might be necessary for best performance.

3 Principle of the Passive Magnetic Tracking

Previous section demonstrated some of the mathematical models that are often adopted to depict the magnetic field of a permanent magnet. The inputs to these models are the positional information (both position and orientation) of the magnetic source (e.g. the permanent magnet) and the observation point (e.g. the sensor) in space, while the outputs are the magnetic field at the observation point (e.g. the sensor measurement). However, due to the non-linearity of the models, there is no analytical solution to the inverse function to retrieve the positional information directly from the sensor measurement. In the following, two distinct tracking principles are reviewed and discussed.

3.1 Inverse Optimization Method

Inverse optimization method requires solving an inverse problem as illustrated in Fig. 5. The sensors measurements are used to compare with the estimation results by feeding positional information into the magnetic field models. A cost function *C*

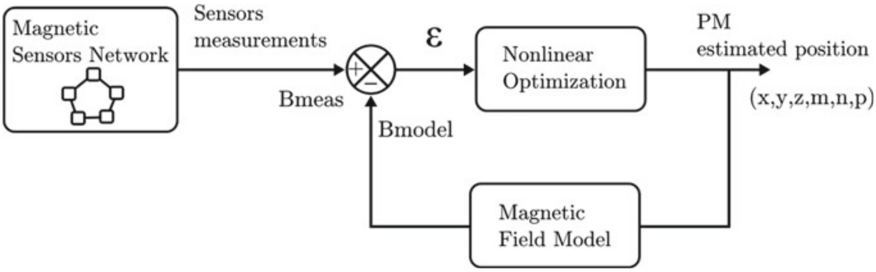

Fig. 5 Principle of passive magnetic localization with inverse optimization method.

is then defined to quantify the differences between the measured and the modeled magnetic field at all k sensors in the sensor array:

$$C = \sum_{i=1}^{k} ||\mathbf{B}_{modeled}(\mathbf{P}_{s_i}) - \mathbf{B}_{measured}(\mathbf{P}_{s_i})||^2. \tag{9}$$

Then the positional information of the magnetic source can be calculated through nonlinear optimization in a least-square manner. By minimizing this cost function through iterative optimization, the position vector $\mathbf{P}_m$ and orientation $\mathbf{H}$ of the permanent magnet can be estimated.

As illustrated in Fig. 1, $\mathbf{H}$ represents a unit vector along the magnetized axis of the permanent magnet, so the three components of $\mathbf{H}$ are actually correlated:

$$m^2 + n^2 + p^2 = 1. \tag{10}$$

Therefore, at least five sensor measurements are required in order to solve the position and orientation information of the permanent magnet. Often more sensors are used to increase the system redundancy for better resilience against environment and hardware noises. It is noted that only five DOF information can be retrieved as elements in the orientation vector $[m, n, p]$ are coupled. This is because the magnetic field models are in particular axis-symmetric about the magnetization axis of the permanent magnet.

The inverse optimization method is widely adopted in a number of research and applications. It is easily to be implemented, with no or little pre-procedural preparation is required, and no specified workspace is needed. The accuracy of the tracking depends on the adequacy of the magnetic field model used, the convergence of the optimization algorithm adopted, and the robustness of the magnetic sensors employed. In general, complexity of the field model and computational expensiveness of the optimization algorithm may lead to a compromise between the requirements of tracking accuracy and processing speed.

3.2 Direct ANN Method

Contrary to a physical model, the ANN model is a non-parametric model that is inspired by biological neural networks. It consists of artificial neuron as a fundamental information processing unit in the neural network structure. At each neuron, it contains one or more input signals $(x_1, x_2, \cdots, x_n)$ associating with weights $(w_1, w_2, \cdots, w_n)$ and one output signal y. Mathematical representation of this model at kth neuron can be written as

$$y_k = g(\sum_{j=1}^{n} w_{ki}x_i), \tag{11}$$

where function g is a nonlinear activation function, such as a sigmoid function [3].

The output of each neuron is computed and propagated through all the hidden layers. In practice, the implementation of direct ANN method accepts n magnetic sensors field data as inputs $(B_{x1}, B_{y1}, B_{z1}, ..., B_{xn}, B_{yn}, B_{zn})$ and directly produces the position and orientation of the permanent magnet (x, y, z, m, n, p) as outputs as illustrated in Fig. 6. Basically, the ANN consists of sets of adaptive weights, which requires supervised learning from pre-procedural training. Once the training is done, the outputs can be directly obtained by performing linear transformation of the inputs. Compared to the traditional inverse optimization method, the direct ANN method bypasses the solving of the challenging inverse problem. Moreover, it can directly incorporate the intrinsic characteristics of the sensors, such as the sensor precision and noise. In such a manner, the direct ANN method is able to provide straightforward and fast calculation with high accuracy. But on the other hand, the direct ANN method also poses the requirement of pre-procedural data collection and training within the region-of-interest (ROI). Therefore, for each medical intervention, determining an *ad hoc* ROI for training is crucial for the direct ANN method in order to reduce the workload for the pre-procedural data collection and training process. In a nut shell,

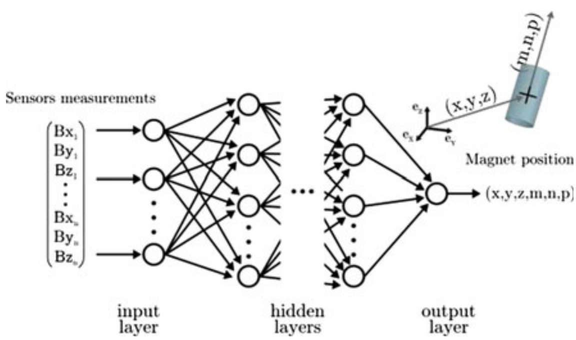

Fig. 6 Principle of passive magnetic localization with direct ANN method.

the direct ANN method provides an ideal solution for those medical interventions with relatively low variance in trajectory but requirements of high accuracy and real-time tracking.

4 Implementation of the Passive Magnetic Tracking in Medical Applications

In this section, two medical intervention procedures are presented to illustrate the implementation of the passive magnetic tracking in practical medical applications:

- The Ventriculostomy, also known as External Ventricular Drain (EVD), which requires inserting a catheter through a burr hole on the skull into the brain tissue to access brain ventricles.
- The Nasogastric (NG) intubation, which consists of inserting a flexible hollow tube through the nose, past the throat and down into the stomach.

Illustrations of two medical intervention procedures are shown in Fig. 7. The problem in the conventional routines for both procedures is that they are manually performed "blind" by clinicians without any visual aids or indications. Without real-time instrument tracking, it may result in safety risks in identifying erroneous insertions, which could potentially cause significant complications and even morbidity. By embedding a small permanent magnet at the tip of the catheter, the passive magnetic tracking could be applied to provide real-time monitoring of the position and orientation information of the magnet at the tip of the catheter. In such manner, the system would allow untethered instrument tracking. It is expected that potential erroneous insertions could be prevented and corrected right away; thus, the success rate of the intervention procedures could be improved.

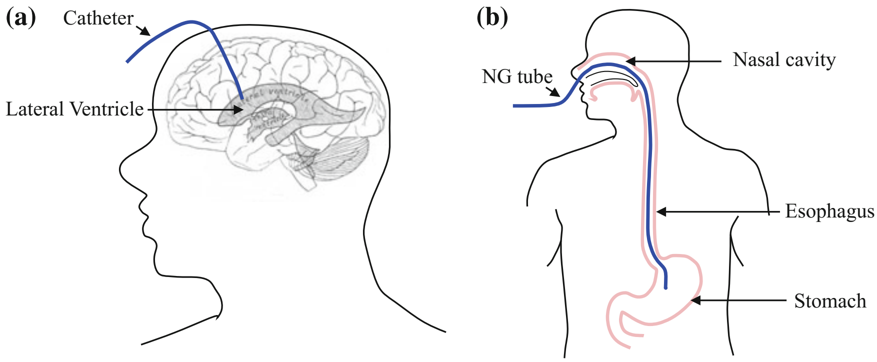

Fig. 7 **a** The Ventriculostomy **b** the Nasogastric (NG) intubation.

In the following, implementation of the passive magnetic tracking in these two procedures are presented. Experiments were carried out on specifically designed localization systems. Both the traditional inverse optimization method and the direct ANN method were applied in tracking random conical-helix paths and representative medical specific trajectories. Tracking performance of the two distinct methods was then assessed and compared.

4.1 Localization Systems and Experimental Setup

For each application, a customized localization system with embedded sensor array was designed and built. As shown in Fig. 8, for the Ventriculostomy procedure, eight sensors were used and arranged in a specific pattern on a flat circular board around the burr hole on the skull for the catheter to go through; for the NG intubation, eleven sensors were used and distributed inline on a semi-circular neck attachment (radius 65 mm with sensor spacing 15°), where the center sensor laid on the thyroid cartilage with its surface perpendicular to the neck.

To experimentally test the localization performance, a bench test was set up, as featured in Fig. 9. A Grade N52 Neodymium (Nd-Fe-B) magnet from K&J Magnetics (Jamison, PA, USA) was mounted at the end-effector of a 6-axis articulated robotic arm (VS-068, Denso Robotics, Aichi, Japan). The dimensions of the permanent magnet (3.2 mm diameter and 9.5 mm length) were chosen to fit the inner diameter of the catheter. An off-the-shelf digital 3-axis magnetic sensor, MAG3110 (Freescale Semiconductor, Austin, USA) was employed for its high sensitivity to low magnetic field measurement, with a resolution of 0.10 μT and a range of $\pm$1000 μT. The sensors measurements were then acquired by a real-time controller cRIO 9082 (National Instruments, Austin, USA). With a positional repeatability of $\pm$0.02 mm, the robotic arm was commanded to accurately move the magnet along reference trajectories in designed configuration (both position and orientation).

Same sets of experimental data were concurrently tested on the two methods: the inverse optimization method and the direct ANN method. For the direct ANN method, a ROI for pre-procedural data collection and training was firstly decided based on the specifications of corresponding medical application. For example, for Ventriculostomy procedure the catheter is inserted through a small hole in the skull. Consequently, the whole expected tracking ROI for Ventriculostomy can be reasonably defined as a cone. The possible orientations of the magnet can also be limited regarding the physical constrains of the catheter, which is unlikely to bend an angle exceeding 45° from the axial plane. The same approach can be applied for NG intubation where the ROI can be represented by a tube encompassing the esophagus and trachea. Hence, the orientation of the magnet is highly limited around the sagittal axis. The spatial resolution within the ROI was set at 1 mm. At each position, instead of testing different configurations, a random orientation $[m, n, p]$ of the magnet about its magnetization axis was assigned within a designed range, in order to include as much as variations without significantly increasing the number of training data sets.

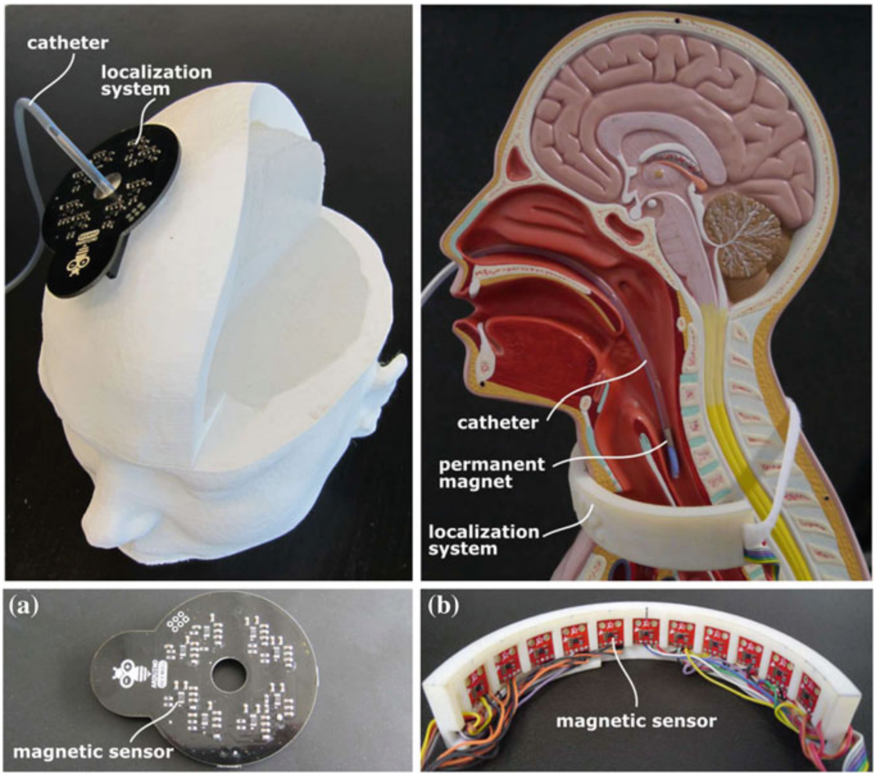

Fig. 8 Design and installation of the localization systems for two different medical interventions **a** Ventriculostomy **b** the Nasogastric (NG) intubation.

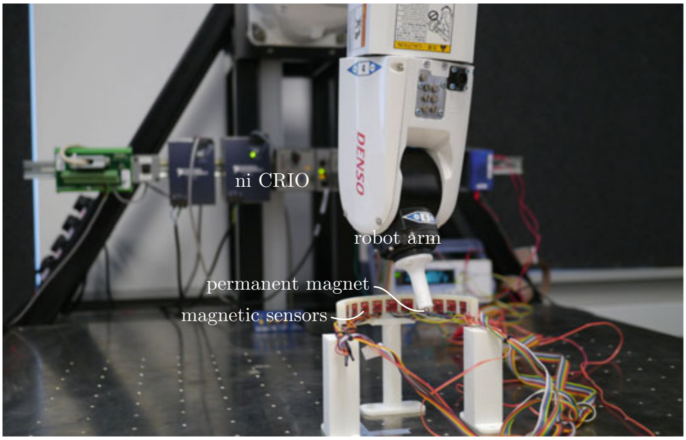

Fig. 9 Experimental setup for tracking performance tests. The six-axis robotic arm provides the ground truth localization of the permanent magnet.

Table 1 ROI parameters for two medical applications.

Parameters	Ventriculostomy	NG Intubation
Volume (cm^3)	90	60
Number of points	52811	19530
Range m	[0, 0.4]	[−0.1, 0.3]
Range n	[−0.2, 0.2]	[−0.1, 0.1]
Range p	[−1, −0.6]	[−1, −0.8]
Calibration time (hour)	13	5

The detailed parameters of the ROI for both applications are shown in Table 1. Neural network toolbox from MATLAB (Mathworks, USA) was used to train the data sets with ten hidden layers and Levenberg-Marquardt back propagation algorithm. For the inverse optimization method, the Dipole model was used for its simplicity and fast calculation processing speed; and Levenberg-Marquardt Algorithm was used as the optimization algorithm.

4.2 Experimental Results

The tracking performance of both methods can be visualized in Figs. 10 and 11, where the true reference trajectory in solid line, the estimated trajectory in colored dots. In Fig. 10, non-application specific conical-helix paths were tested for both procedures. For the Ventriculostomy procedure, the center of the circular sensor board was placed at (0, 0, 0); for the NG intubation procedure, the center of the semi-circular attachment was placed at (0, 0, 0) with the opening towards the positive X-axis direction. In Fig. 11, medical representative trajectories based on *in situ* data from either real patient or realistic manikin dummy were tested. In this case, the coordinates of the localization system were planned according to the actual settings. For the Ventriculostomy procedure, the sensor board was placed on the top right corner where the trajectory went through the center hole; for the NG intubation procedure, the center of the attachment remained at (0, 0, 0) but the attachment was placed perpendicular to the neck with 20° above the positive X-axis direction.

Table 2 summarizes the RMSE (root mean square error) and the maximum localization error along different paths tested. It can be seen that both methods are able to track the reference trajectories. It can be seen that the direct ANN method outperforms the traditional inverse optimization method in terms of localization accuracy in all cases. The RMSE of the tracking error using the direct ANN method can be as small as less than 2 mm. Higher errors were seen in the NG intubation system for both localization methods. That is because the Euclidean distance between the passive source (permanent magnet) and the sensors are generally farther in the NG intubation system, resulting in lower Signal-to-Noise Ratio (SNR). This can be seen

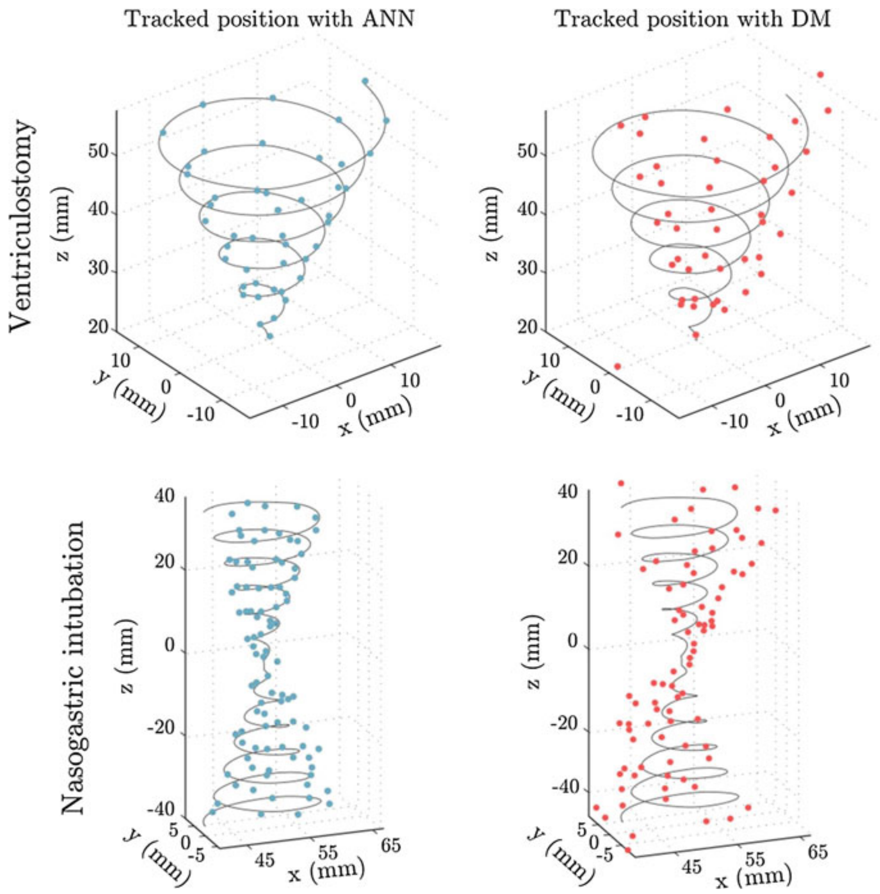

Fig. 10 Performance of the passive magnetic tracking of non-application specific conical-helix path in two different medical applications using the direct ANN method (left) and the inverse optimization method (right).

from Fig. 12, where the localization errors for all trajectories were plotted against the Z-axis (considering as the penetration direction). It is also shown that the SNR has much higher influences on the inverse optimization method than on the direct ANN method. Significantly increases in the localization error can be observed as the source moved away from the sensors when the inverse optimization method was used, but the localization error remained on the same level throughout the range for the direct ANN method. However, such robustness requires pre-procedural data collection and training within the defined ROI.

It is also noted that in Fig. 11, when the inverse optimization method was used in Ventriculostomy procedure, the first few points were off the reference trajectory. That is because some of the sensors readings were saturated as the magnet passing through the center hole and getting too close to the sensors. Such adverse sensor readings

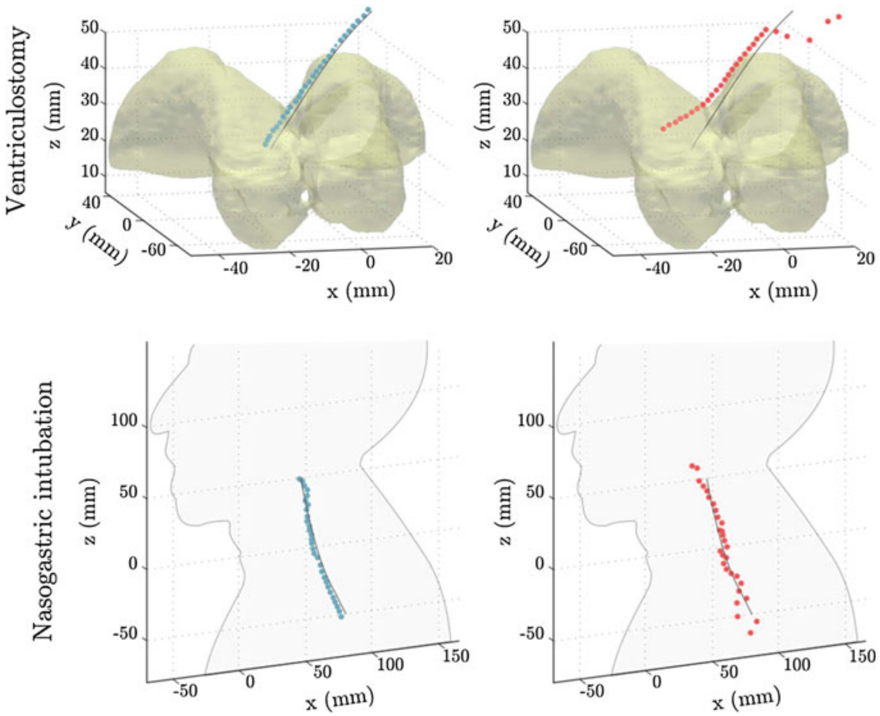

Fig. 11 Performance of the passive magnetic tracking of medical representative trajectories in two different medical applications using the direct ANN method (left) and the inverse optimization method (right).

Table 2 Tracking performance of two methods in different medical applications.

Tracking paths	Methods	Inverse optimization method		Direct ANN method	
	Procedures	Ventriculostomy	NG Intubation	Ventriculostomy	NG Intubation
Non-specific conical-helix	RMSE (mm)	9.8	6.4	0.8	1.5
	Max (mm)	14.3	17.2	1.2	5.3
Representative trajectory	RMSE (mm)	5.8	6.8	1.1	1.8
	Max (mm)	12.9	15.4	1.6	4.5

could affect the convergence in the optimization algorithm, resulting in erroneous estimation. Thus, it requires control algorithm for real-time sensor fault detection and correction [16, 21]. In comparison, as long as the trajectory was covered by the trained ROI, the direct ANN method was able to take account of the adverse sensor readings such as saturation.

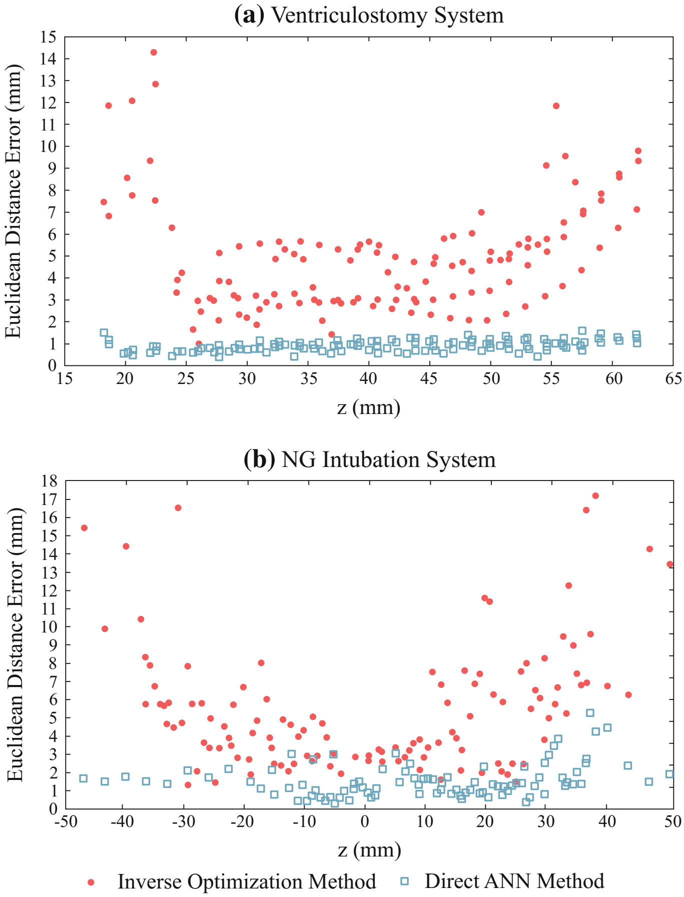

Fig. 12 Euclidean distance errors for conical-helix path and representative trajectory altogether along the insertion direction **a** Ventriculostomy System **b** NG Intubation System.

4.3 Discussions on the Method Selection

Implementation of the passive magnetic tracking has been demonstrated in two medical intervention examples. Both the inverse optimization method and the direct ANN method were used. In general, the direct ANN method provides higher tracking accuracy, at the cost of pre-procedural training. Thanks to its non-parametric nature, the direct ANN method is able to take account of the sensor characteristics; but also because of that, the direct ANN method can only be implemented within the ROI where the pre-procedural calibration was performed in. In order to have larger tracking region, more data points have to be measured for training, resulting in prolonged data collection process and increased training complexity. But once the preparation work is done, the computation of the ANN would be linear transformation from the inputs to the outputs; implementation of the method would be straightforward and fast. In comparison, the inverse optimization method is based on a physical model of the permanent magnet. It only requires calibration of the model parameter(s), then it can be implemented at any point in space. However, the tracking accuracy would be greatly affected by the modeling errors. More sophisticated models can be used to increase the model accuracy, but the model complexity would greatly affect the processing speed as the inverse optimization algorithm requires iterative computations.

In a nutshell, both methods could be used in realization of untethered medical instrument tracking. The selection of the methods for the tracking is driven by the variation of the intervention trajectory, the size of the ROI, the requested tracking accuracy and the refresh rate. Generally speaking, the direct ANN method is more accurate and versatile, requiring application specific pre-procedural training but offering fast processing in real-time; the inverse optimization method is more adaptive but more computationally intensive. If the ROI is relatively small, the required accuracy is high and most importantly the measurement conditions are consistent, the direct ANN method is preferable. Though when the tracking area is large, the path has high variance or the accuracy is less critical, the inverse optimization method is better to be considered.

5 Challenges and Outlook of the Passive Magnetic Tracking

There are quite a number of advantages of adopting passive magnetic tracking technology in medical applications. The passivity of the magnetic source makes it possible to have untethered tracking of the medical instrument. The localization system for passive magnetic tracking technology only requires arrays of magnetic sensors, which are widely used in the consumer products and consume much less power than the commercially available electromagnetic tracking system. Therefore, the localization system using passive magnetic tracking technology could be designed in a compact and wearable package with battery powered and wireless feature.

As aforementioned, the feasibility of the passive magnetic tracking in medical intervention has been experimentally validated. Comparing with those commercially available Electromagnetic tracking system (e.g. NDI Aurora), the developed passive magnetic tracking system has been proven capable of delivering comparable performance in terms of tracking accuracy and refresh rate, for example using the direct ANN method. However, the lacking of multiple objects tracking and 6-DOF tracking capabilities in the passive magnetic tracking technology is still criticized and considered as technical barriers in implementation. In the following, some of the recent development in these two areas in passive magnetic tracking are introduced.

5.1 *Multiple Objects Tracking*

One of the features of the commercial electromagnetic system is the capability of simultaneous tracking multiple sensors. Through a controlled varying electromagnetic field, voltages induced in the sensor coils can be differentiated and identified individually. For example, the NDI Aurora $V3$ System can be customized to provide simultaneous tracking of up to 16 sensors. On the opposite, in passive magnetic tracking, the system has less controlled variables to manipulate with since the magnetic sources are fixed. The identification of the multiple magnetic objects (sources) will depend on the algorithm only, as discussed in the following.

In general, when multiple magnetic objects coexist in free space, the principle of superposition applies. This concept simply means that the magnetic field in space is the sum of the contribution due to each magnetic source. Therefore, each magnetic object can be modeled as a single dipole as shown in Fig. 13. Although it is impossible to directly decouple the contributions from each magnetic source out of the total MFD measurements, the inverse optimization method can still be used by constructing a combined magnetic field model to calculate the most appropriate positions and orientations of each magnetic source. Based on Dipole Model, the total magnetic field at ith observation point due to N magnetic objects can be described as

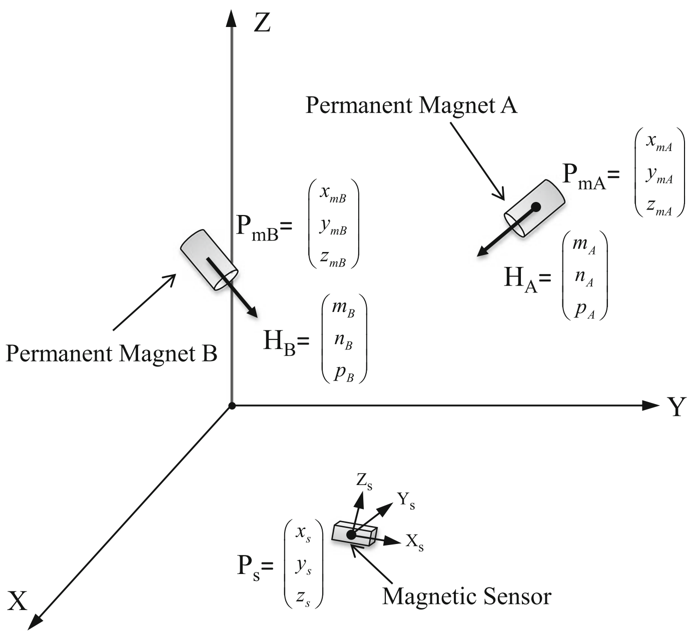

Fig. 13 Illustration of modeling each object as a single magnetic dipole.

$$\mathbf{B}(\mathbf{P}_{s_i}) = \sum_{j=1}^{N} \frac{\mu_r \mu_0 \cdot M_j}{4\pi} \left(\frac{3(\mathbf{H}_j \cdot \mathbf{P}_{ij})\mathbf{P}_{ij} - R_{ij}^3 \cdot \mathbf{H}_j}{R_{ij}^5} \right), \tag{12}$$

where μ_r is the relative permeability of the medium, μ_0 is the magnetic permeability of free space (mT· mm/A), M_j is the constant strength of the dipole moment (A· mm^2) for jth magnetic object, and $\mathbf{P}_{ij}$ is a vector from the jth magnetic object $\mathbf{P}_{m_j}$ pointing to the ith sensor $\mathbf{P}_s^i$, and R_{ij} is the magnitude of the vector $\mathbf{P}_{ij}$,

$$\mathbf{P}_{ij} = \mathbf{P}_{s_i} - \mathbf{P}_{m_j}. \tag{13}$$

A cost function C is then defined to quantify the differences between the measured and the modeled magnetic field at all k sensors in the sensor array:

By minimizing this cost function through iterative nonlinear optimization, the position vector $\mathbf{P}_m = [\mathbf{P}_{m_1}, \mathbf{P}_{m_2}, \ldots, \mathbf{P}_{m_N}]$ and orientation $\mathbf{H} = [\mathbf{H}_1, \mathbf{H}_2, \ldots, \mathbf{H}_N]$ of all N magnetic objects can be estimated from the sensor measurements.

Following the same definition as in (refeq:H), H_j represents a unit vector along the magnetized axis of the jth magnetic object, so the three components of H_j are actually correlated:

$$m_j^2 + n_j^2 + p_j^2 = 1. \tag{14}$$

Therefore, there are total of five independent variables in each dipole model (12), corresponding to the 5-DOFs tracking. Because of the axis-symmetric nature of the Dipole Model, only the Yaw and Pitch motions are represented. The Roll motion about the magnetized axis makes no differences in the magnetic field distribution.

Yang et al. first explored this method to simultaneously localize three identical magnets [24], such that the optimization problem could be simplified by sharing the same magnetic dipole strengths for all objects. But in such settings, it was difficult to distinguish the objects from each other, unless the initial positions of all objects were previously known. Recently, Song et al. used the same localization system to localize three magnets with different magnetic strength parameters [17]. The idea was verified in both simulations and experiments; but the magnets were assumed to be fixed in static.

At the current stage, only inverse optimization method could be applied due to the high uncertainties introduced by multiple objects. And the number of magnets also needs to be pre-defined and fixed; otherwise the likelihood of the optimization cost function converging to local minimum increases with the increasing number of unknown parameters. Due to such complexity, the processing time would also be affected. Along this research direction, it is expected to have a fast and robust algorithm to identify the number of objects as well as to estimate their positional information (both position and orientation) with reasonable accuracy.

5.2 6-DOF Tracking

As stated previously, 5-DOF tracking in magnetic tracking is the most common one since the magnetic field is usually symmetric about the magnetization axis of the magnet. In order to have 6-DOF tracking to include the roll motion, the commercial electromagnetic tracking system incorporates two sensor coils perpendicularly to each other; thus, by tracking the positional information of both sensor coils simultaneously, all 6-DOF parameters could be recovered.

Similar concept could be used in passive magnetic tracking to enable 6-DOF tracking. Song et al. reported using assembly of two identical perpendicular aligned permanent magnets inside a wireless capsule endoscopy (WCE) [19]. Dipole model was used and two magnets were localized separately with constraints on the parameters. However, due to the limitation of the dipole model, there would be no unique solutions if two magnets are too close to each other; the estimated orientation errors would be large. Thus, the two perpendicular aligned magnets have to be kept at a distance. For example, in [19], the two magnets were placed 10cm apart from each other.

Another method to enable 6-DOF tracking in passive magnetic tracking is to adopt a better physical model that is able to take account of the geometry rather than dipole model. Then an odd geometric shaped magnet can be used to bring asymmetry in the magnetic field about the magnetization axis. For example, Yang et al. suggested using a thin rectangular shape magnet [25] and Song et al. suggested using a diametrically magnetized long annular shape magnet [18]. But only simulation results were presented as concept verification. But in their work, the simulation also shown that the differences in the magnetic field asymmetry caused by the geometry of the magnet could be quite limited; compared to the dipole model, the differences at a distance away from the magnet could be only in $10^{-}2\mu$T level which could be hardly picked up by the magnetic sensors.

Following the idea used in the active electromagnetic tracking, one novel idea to amplify such asymmetry in the magnetic field is to use magnet assembly. As shown in Fig. 14, three different assembly designs are presented to form two mutually orthogonal magnetic fields by using axially and diametrically magnetized magnets.

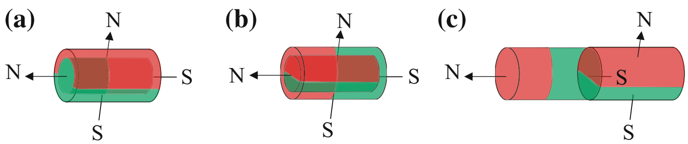

Fig. 14 Three different magnet assembly designs **a** Axially magnetized cylindrical magnet inside diametrically magnetized annular magnet **b** Diametrically magnetized cylindrical magnet inside axially magnetized annular magnet **c** Two cylindrical magnets with axially and diametrically magnetized each.

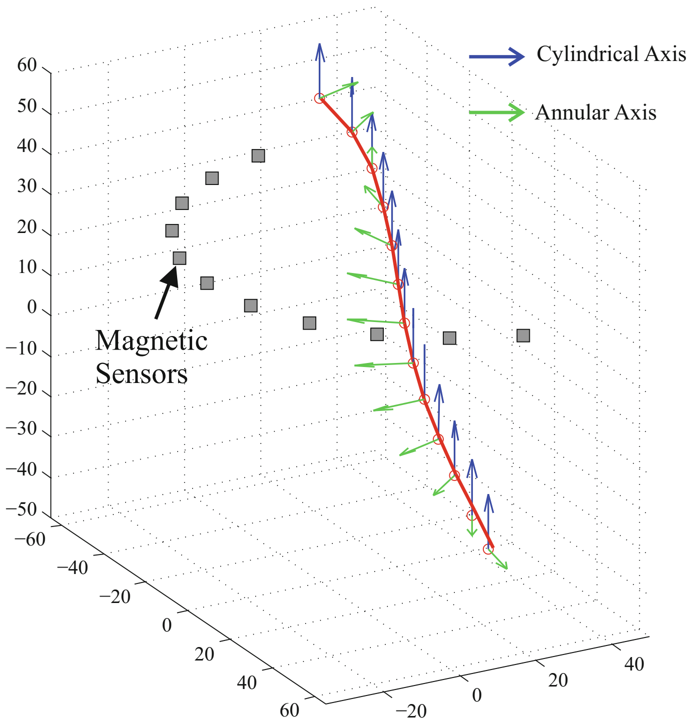

Fig. 15 Performance of 6-DOFs tracking using Charge Model.

- An axially magnetized cylindrical magnet inside a diametrically magnetized annular magnet.
- A diametrically magnetized cylindrical magnet inside an axially magnetized annular magnet.
- An axially magnetized magnet in serial with a diametrically magnetized magnet.

Then the charge model could be used to represent the actual magnetic field of the assembly. The derivation of the magnetic field of a cylindrical/annular magnet using the charge model can be found in the Appendix. Taking the assembly design A as an example, a simulation is performed as follows. Based on the specifications from magnet manufacturer K& J Magnetics, one axially magnetized cylindrical magnet (D28-N52), and one diametrically magnetized annular magnet (R424-DIA) are chosen. The radius of the cylindrical magnet is the same as the inner diameter of the annular magnet. Using the nasogastric intubation application as reference, the simulation is performed with the cylindrical magnet pointing upward straight with magnetization at [0, 0, 1], while the annular magnet rotating around the Z-axis. The results are shown in Figs. 15 and 16.

As shown in Fig. 15, the proposed method is able to detect three positions as well as the three orientation of the assembly. Figure 16 shows the position and orientation

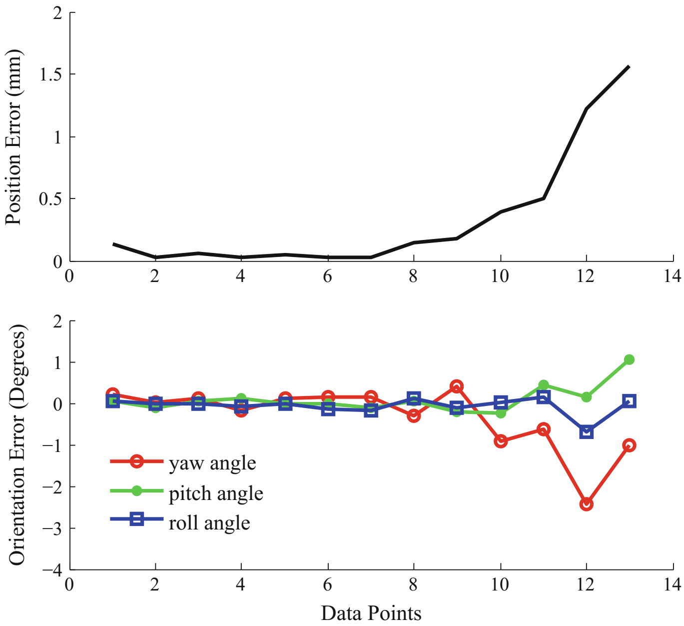

Fig. 16 Tracking errors of 6-DOFs tracking using Charge Model (top) position error (bottom) orientation error.

errors at each data point. It is noted that the error becomes larger as the assembly moves further away from the sensor array. That is expected as the further away from the sensor array, the larger the Signal-to-Noise Ratio (SNR); thus, the tracking accuracy will be affected.

The concept of 6-DOF tracking in passive magnetic tracking has been theoretically verified. The next step is to validate this method using experimental data. One foreseen limitation would be the processing time due to the iterative calculation using the complex physical models. For example, adoption of the charge model would result in hectic computation load of the integration in the optimization stage. A computationally inexpensive model would be desired to solve this problem.

6 Conclusion

In this chapter, the concept of passive magnetic tracking technology has been presented. The advantages of using permanent magnets as passive magnetic source for medical intervention localization are explored. Comparing with the commercially available active electromagnetic tracking systems, it is shown that the passive magnetic tracking technology is able to provide comparable performance in terms of the tracking accuracy and refresh rate. The challenges and limitations in the current development of this technology were also discussed. It is expected that the passive magnetic tracking technology could open a new era in the design and development for instrument localization in medical interventions, This would allow for less modification and invasiveness in the current routine, enable untethered / mobile system design and target better ergonomics and cost-efficiency.

Acknowledgements The work is supported by SUTD-MIT International Design Center (IDC) Research Grant IDSF1200107OH, and partially support by the State Joint Engineering Lab on Robotics and Intelligent Manufacturing (2015[581], 2015[955]), and Shenzhen Engineering Lab on Robotics and Intelligent Manufacturing (2014[1722]).

Appendix

Magnetic Field of a Cylindrical Magnet Using the Charge Model

In order to calculate the surface integration of a cylindrical magnet, the variables are first transformed into cylindrical coordinates by

$$\begin{aligned} x_c &= r \cdot cos(\theta) \\ y_c &= r \cdot sin(\theta) \\ z_c &= z. \end{aligned} \tag{15}$$

For a cylindrical axially magnetized magnet, only the top and bottom surfaces are considered since the outward surface vector of the lateral surface is perpendicular to the magnetized vector, thus $\mathbf{M} \cdot \hat{\mathbf{n}} = 0$. Let the magnetization be $\mathbf{M} = M_s \hat{\mathbf{z}}$, then it can be obtained $\sigma = M_s$ for the top surface ($z_{c_{top}} = h/2$), $\sigma = -M_s$ for the bottom surface ($z_{c_{bottom}} = -h/2$). The magnetic field at observation point $\mathbf{P}_s$ can be written as

$$\begin{aligned} \mathbf{B}(\mathbf{P}_s) =& \frac{\mu_0 M_s}{4\pi} \int_0^{2\pi} \int_0^R \frac{\mathbf{P}_s - \mathbf{P}_{c_{top}}}{|\mathbf{P}_s - \mathbf{P}_{c_{top}}|^3} r dr d\theta \\ &- \frac{\mu_0 M_s}{4\pi} \int_0^{2\pi} \int_0^R \frac{\mathbf{P}_s - \mathbf{P}_{c_{Bottom}}}{|\mathbf{P}_s - \mathbf{P}_{c_{Bottom}}|^3} r dr d\theta. \end{aligned} \tag{16}$$

For a cylindrical diametrically magnetized magnet, only the lateral surface is considered. Let the magnetization be $\mathbf{M} = M_s \hat{\mathbf{y}}$. The outward normal vector at the lateral surface can be written as

$$\hat{\mathbf{n}} = cos(\theta)\hat{\mathbf{x}} + sin(\theta)\hat{\mathbf{y}}. \tag{17}$$

Then the surface charge density equals to

$$\begin{aligned} \sigma &= \mathbf{M} \cdot \hat{\mathbf{n}} \\ &= M_s \hat{\mathbf{y}} \cdot (cos(\theta)\hat{\mathbf{x}} + sin(\theta)\hat{\mathbf{y}}) \\ &= M_s\, sin(\theta). \end{aligned} \tag{18}$$

The magnetic field at point $\mathbf{P}_s$ can be calculated

$$\mathbf{B}(\mathbf{P}_s) = \frac{\mu_0 M_s}{4\pi} \int_0^{2\pi} \int_{-h/2}^{h/2} \frac{\mathbf{P}_s - \mathbf{P}_c}{|\mathbf{P}_s - \mathbf{P}_c|^3} R dz d\theta \tag{19}$$

For an annular magnet, its magnetic field can be obtained by the principle of superposition. It is equivalent to the magnetic field of a cylindrical magnet with the size of the outer diameter subtract that of a cylindrical magnet with the size of the inner diameter.

References

1. Baldoni, J.A., and B.B. Yellen. 2007. Magnetic tracking system: Monitoring heart valve prostheses. *IEEE Transactions on Magnetics* 43 (6): 2430–2432.
2. Bercik, P., et al. 2005. Noninvasive verification of nasogastric tube placement using a magnet-tracking system: A pilot study in healthy subjects. *Journal of Parenteral and Enteral Nutrition* 29 (4): 305–310.
3. Bishop, C.M. 1996. *Neural networks for pattern recognition*, 1st ed. Oxford University Press.
4. Franz, A.F., et al. 2014. Electromagnetic tracking in medicine-a review of technology, validation and applications. *IEEE Transactions on Medical Imaging* 33 (8): 1702–1725.
5. Furlani, Edward P. 2009. *Permanent magnet and electromechanical devices: Materials, analysis and applications*, 1st ed. Academic Press.
6. Hu, C., T. Ma, and M.Q.-H. Meng. 2007. Sensor arrangement optimization of magnetic localization and orientation system. In *IEEE International Conference on Integration Technology*, pp. 311–315.
7. Hu, Chao, M.Q.-H. Meng, and Mrinal Mandal. 2005. Efficient magnetic localization and orientation technique for capsule endoscopy. *International Journal of Information Acquisition* 2 (1): 23–36.
8. Lee, K.-M., and Min Li. 2013. Magnetic field localization method for guiding visually impaired applications. In *IEEE/ASME International Conference on Advanced Intelligent Mechatronics*, pp. 542–547.
9. Lee, K.-M., Min Li, and Chun-Yong Lin. 2015. A novel way-finding method based on geomagnetic field effects and magnetic tensor measurements for visually impaired users. In *IEEE/ASME International Conference on Advanced Intelligent Mechatronics*, pp. 232–237.
10. Lee, K.-M., and H. Son. 2007. Distributed multipole model for design of permanentmagnet-based actuators. *IEEE Transaction on Magnetics* 43 (10): 3904–3913.
11. Maréchal, L., et al. 2016. Design optimization of a magnetic field-based localization device for enhanced ventriculostomy. *Journal of Medical Devices* 10 (1).
12. Maréchal, L., et al. 2015. Design optimization of the sensor spatial arrangement in a direct magnetic field-based localization system for medical applications. In *IEEE International Conference on Engineering in Medicine and Biology Society*, pp. 897–900.

13. Maréchal, L., et al. 2014. Optimal spatial design of non-invasive magnetic field-based localization systems. In *IEEE International Conference on Robotics and Automation*, pp. 3510–3516.
14. Meng, M.Q.-H., et al. 2004. Wireless robotic capsule endoscopy: state-of-the-artand challenges. In *World Congress on Intelligent Control and Automation*, pp. 5561–5565.
15. Schlageter, V., et al. 2001. Tracking system with five degrees of freedom using a 2D-array of Hall sensors and a permanent magnet. *Sensors and Actuators A: Physical* 92 (1–3): 37–42.
16. Sharma, A.B., L. Golubchik, and R. Govindan. 2010. Sensor faults: Detection methods and prevalence in real-world datasets. *ACM Transactions on Sensor Networks* 6 (3).
17. Song, S., C. Hu, and M.Q.-H. Meng. Multiple objects positioning and identification method based on magnetic localization system. *IEEE Transactions on Magnetics*. https://doi.org/10.1109/TMAG.2016.2583408.
18. Song, S., et al. 2014. 6-D magnetic localization and orientation method for an annular magnet based on a closed-form analytical model. *IEEE Transactions on Magnetics* 50 (9): 1–11.
19. Song, S., et al. 2009. Two-Magnet-based 6D localization and orientation for wireless capsule endoscope. In *IEEE International Conference on Robotics and Biomimetics*, pp. 2338–2343.
20. Sun, Z., et al. 2015. A non-invasive real-time localization system for enhanced efficacy in nasogastric intubation. *Annals of Biomedical Engineering* 43 (12): 2941–2952.
21. Sun, Z., et al. 2016. Real-time sensor fault detection and compensation in a passive magnetic field-based localization system. In *IEEE/ASME International Conference on Advanced Intelligent Mechatronics*, pp. 1040–1046.
22. Wang, X., M.Q.-H. Meng, and Y. Chan. 2006. A localization method using 3-axis magnetoresistive sensors for tracking of capsule endoscope. In *IEEE International Conference on Engineering in Medicine and Biology Society*, pp. 2522–2525.
23. Wu, F., S.H. Foong, and Z. Sun. 2015. A hybrid field model for enhanced magnetic localization and position control. *IEEE Transactions on Mechatronics* 20 (3): 1278–1287.
24. Yang, W., et al. 2010. A new tracking system for three magnetic objectives. *IEEE Transactions on Magnetics* 46 (12): 4023–4029.
25. Yang, W., et al. 2009. A six-dimensional magnetic localization algorithm for a rectangular magnet objective based on a particle swarm optimizer. *IEEE Transactions on Magnetics* 45 (8): 3092–3099.
26. Yao, W.-S., et al. 2012. Detection of magnetic object movements by flux density tracking control. *IEEE/ASME Transactions on Mechatronics* 17 (4): 709–716.

Tracking Magnetic Particles Under Ultrasound Imaging Using Contrast-Enhancing Microbubbles

KaiTing Loh and Hongliang Ren

Abstract In this chapter, motion of magnetic particles were captured using ultrasound imaging with contrast-enhanced microbubbles. Ultrasound videos were captured and analyzed by the created tracking algorithm to determine the efficiency and accuracy of the algorithm. It is necessary to ensure an efficient and accurate tracking method of the particles in order to evaluate future in vitro or in vivo applications of the microbubbles, when implanted into an enclosed system and imaged using ultrasound. First, it was found that the porous structure of the magnetic microbubbles could be successfully fabricated based on a gas foaming technique, using alginate (low viscosity, 2% (w/v)) as the polymer, mixed homogeneously with sodium carbonate (4%) solution. The reaction between sodium bicarbonate and hydrogen peroxide (32 wt%) in the collecting solution allowed the creation of encapsulated microbubbles. The alginate went under crosslinking in the collecting calcium chloride (25% w/v) solution. Second, it was proven that the encapsulated microbubbles enhanced the resultant ultrasound images, with the air bubbles appearing as bright white spots. In contrast, the solid spheres appeared dull and at times could not be seen under ultrasound. The contrast enhancing properties of the microbubbles allowed the microbubbles to be detected by the tracking algorithm, as compared to the solid spheres which could not be detected at all. Third, ground truth of the (x, y) coordinates of the microbubble centroids were determined using manual selection by the user mouse. Based on the accuracy analysis done, the accuracy of the tracking algorithm was 3.33 pixels, or 0.0354 cm, between the algorithm detected and the manually selected (x, y) coordinates of the centroids. Also, the optimal number of particles to be tracked was up to five particles with an accuracy studies.

K. Loh · H. Ren (✉)
Department of Biomedical Engineering, National University of Singapore, Singapore, Singapore

H. Ren and J. Sun (eds.), *Electromagnetic Actuation and Sensing in Medical Robotics*, Series in BioEngineering, https://doi.org/10.1007/978-981-10-6035-9_8

1 Introduction

1.1 Purpose

Magnetic particles which can be controlled by an external magnetic field have been explored as a method for precise and efficient drug delivery. With the increased usage of microbubbles as a system for drug delivery using ultrasound imaging, there is an interest to develop a tracking algorithm to locate the in vivo position of the microbubbles once delivered. In this chapter, ultrasound imaging of magnetic particles with encapsulated microbubbles is further studied. The objective of this chapter is to optimize the tracking of microbubbles from the ultrasound images and to perform image analysis to identify the location of the microbubbles.

1.2 Problem

Currently, clinical use of microbubbles are being visualized by methods such as ultrasound Particle Image Velocity or Echo particle image velocimetry, which return velocity vectors of the particles under flow conditions. The literature review shows a limited number of studies on microbubble localization under ultrasound imaging when using external controlled manipulation of the magnetic particles. As such, this chapter aims to create a tracking algorithm for tracking of magnetic particles with encapsulated microbubbles under controlled conditions.

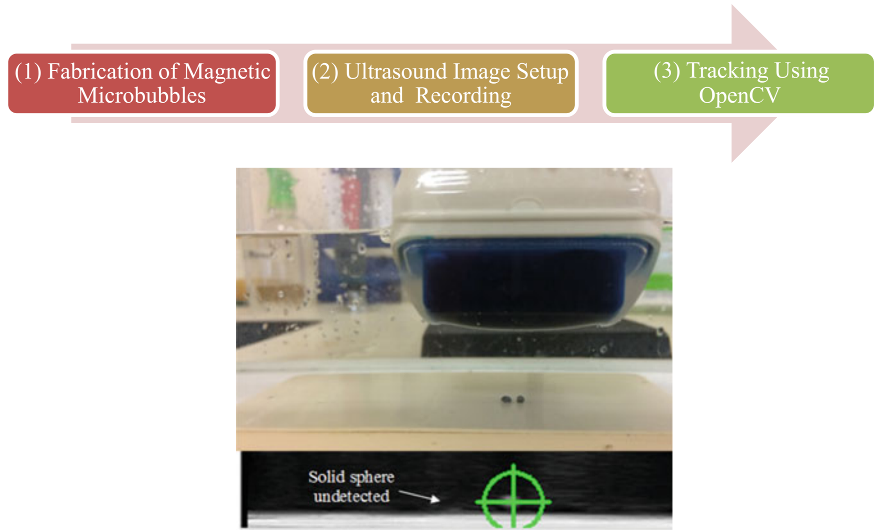

Fig. 1 Overview of chapter.

1.3 Scope

Figure 1 shows the overview of this chapter. First, a suitable technique to fabricate the required microbubble encapsulated magnetic particles for imaging under ultrasound was investigated. Second, the most suitable experimental setup for obtaining the required ultrasound images was used. Third, the tracking algorithm to locate the microbubbles was applied. After which, the results from the experiments and future works for the chapter are discussed.

2 Literature Survey

2.1 Microbubbles as Ultrasound Contrast Agents

Microbubbles as contrast agents for ultrasound imaging [1] typically consist of a gas core (filling gas) encapsulated by a coating (shell) normally made from a protein, lipid or polymer [2]. When the compressible gas bubbles are smaller than the wavelength of incidental ultrasound signals, the microbubbles oscillate in the ultrasound acoustic field, causing the resulting backscattered ultrasound signal to be detected and differentiated from tissue [3]. In addition, ultrasound imaging is advantageous as ultrasound imaging allows capturing of dynamic moving targets inside human body noninvasively [4].

Recent growing researches shed lights on the fabrication of magnetic microbubbles by infusing magnetic nanoparticles into the microbubble shell. Research done by Yang et al. (2009) on superparamagnetic iron oxide (SPIO) particles incorporated into the microbubble polymer shell demonstrated that embedding magnetic nanoparticles into bubble shells enhanced the stability of microbubbles, preventing premature destruction of microbubbles during ultrasound imaging [5]. Magnetic particles may be further developed for diagnostic and therapeutic drug delivery.

2.2 Clinical Applications of Magnetic Microbubbles

2.2.1 Diagnostic Applications: Magnetic Microbubbles as Dual Contrast Agents

Research done by Stride et al. (2008) showed that addition of magnetic nanoparticles to the microbubble encapsulating layer enhanced ultrasound imaging contrast due to increased asymmetric bubble oscillations [6]. Furthermore, the close way of packing the magnetic particles limits bubble compression, causing increased harmonic components of the scattered ultrasound signal. Consequently, the microbubbles can be imaged at lower ultrasound power levels, minimizing the risk of high-power complications. In addition, lower ultrasound intensity used for imaging reduces unwanted premature bubble break, which is advantageous for drug or gene delivery [7]. Specific applications of microbubbles for ultrasound diagnostic include cardiac ultrasonography. Microbubbles allow for improved visualization of beating heat chambers [8] and also for the evaluation of microvascular perfusion as its similar rheology to red blood cells [9].

2.2.2 Therapeutic Applications: Targeted Drug Delivery

Magnetic robotic microbubbles can be designed as a drug delivery vehicle and delivered to the target site driven by external magnetic fields. Upon reaching the target site, robotic microbubbles can be destroyed by local application of high transmitted ultrasound acoustic powers [10], releasing the loaded drug. Targeted drug delivery by magnetic microbubbles prevents exposure of surrounding tissue to harmful side effects, and may be especially useful for cancer treatment [11]. Furthermore, microbubbles may improve effectiveness of drug delivery due to the phenomenon of sonoporation [12]. The transient cell permeability during low-intensity ultrasound was found enhanced with microbubbles [13] and thus regulating the drug release rate.

2.2.3 Therapeutic Applications: Gene Delivery

Both ultrasonically and magnetically-mediated transfection improves uptake of DNA by target cells interacting with phospholipid coated microbubbles with magnetic nanoparticles, which enhanced the transfection of the target cells [14].

2.3 Ultrasound Microbubble Tracking

Microbubbles currently used in clinical applications such as echocardiography or imaging of angiogenesis are visualized by contrast pulse sequencing [15]. The velocity of the microbubble under ultrasound imaging can be estimated by *Echo Particle Image Velocimetry (EPIV)*, which has been utilized for measurement of local hemodynamics and wall shear rate [16] and intracavitary blood flow 2-D velocity vectors [17].

Table 1 Comparison of moving object detection methods.

Technique	Technique description	Applications
1. Background subtraction	Assumes that background is static [20] The most frequently used technique of object foreground segmentation by performing image subtraction by threshold to obtain the foreground	• Traffic monitoring • Human action recognition • Object tracking
2. Optical flow	Assumes that brightness of tracked image patches do not change, consistent appearance and spatial smoothness [21]. Determination methods include differential methods such as the Lucas-Kanade method or the Horn-Schunck method	• Feature tracking
3. Frame difference	Assumes that object to be tracked is constantly in motion Algorithm checks for difference between two consecutive video frames [22]	• Vehicle tracking • Human tracking

2.4 Optical Tracking of Microbubbles

The literature review here compares three methods for moving object detection: *background subtraction, optical flow* and *frame difference* [18], as indicated in Table 1. Furthermore, studies on moving object detection demonstrate that there is no fixed method in developing a tracking algorithm, as the approach taken depends largely on the application, imaging setup and contrast agents being used [19].

3 Methodology

3.1 Fabrication of Encapsulated Microbubbles

The methods of producing gas microbubbles include sonication, high shear emulsification, inkjet printing, and microfluidic processing and the later two can better control over stability, uniformity, size and composition of microbubbles [23]. Dharmakumar et al. (2005) characterized three different constructs of magnetic microbubbles [24]. Fabrication techniques which can be used to achieve the three different magnetic microbubble constructs have been classified accordingly as shown in Table 2.

Of the three magnetic microbubble structures, the second structure (B) was chosen for fabrication due to ease of reproducibility as additional gas source and equipment were not required. The magnetic microbubbles were fabricated using gas foaming; a simple, inexpensive and easy to operate method to generate a porous structure [27].

Table 2 Schematic diagram of three magnetic microbubble constructs.

Magnetic microbubble constructs	Method description	Fabrication technique
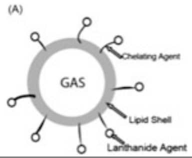	– Magnetic nanoparticles incorporated onto encapsulating surface	• Electrostatic coupling [25] • Chelating agent [25] • Microfluidics [26]
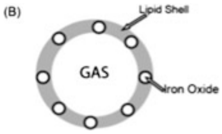	– Magnetic particles embedded in microbubble shell – Porous	• Gas foaming [27] • Air pressure-driven injection [28] • Porogen elimination [29] • Emulsion/freeze drying [30, 31] • Expansion in super critical fluids [32] • Inkjet printing [33, 34] • Coaxial electrohydrodynamic atomisation (CEHDA) [35]
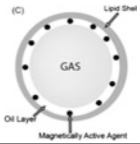	– Nanoparticles embedded within oil layer of multi layered structure microbubble	• Double emulsion procedure [5] • One-pot emulsion polymerization [36]

3.1.1 Materials

Polymer was chosen as the encapsulating material due to its advantage of mechanical stability. Alginate was the chosen polymer as alginate is biocompatible, biodegradable and is easily fabricated to gelated capsules by crosslinking [37]. Other polymers which have been used to fabricate microbubbles, such as poly (lactic-glycolic) acid (PLGA) [38], polyvinyl alcohol (PVA) and poly (DL-lactide) (PLA) [2] require a more complex multiple emulsion method. Furthermore, alginate allows for the fabrication of more 'air-tight' biopolymer shells, reducing the outward diffusion of air-filled microbubbles.

3.1.2 Methods

The encapsulated microbubbles were prepared according to a modified protocol by Huang et al. (2013) [39]. The solution was first prepared by mixing sodium bicarbonate (4%) homogeneously in Na-alginate (low viscosity, 2% (w/v)) solution.

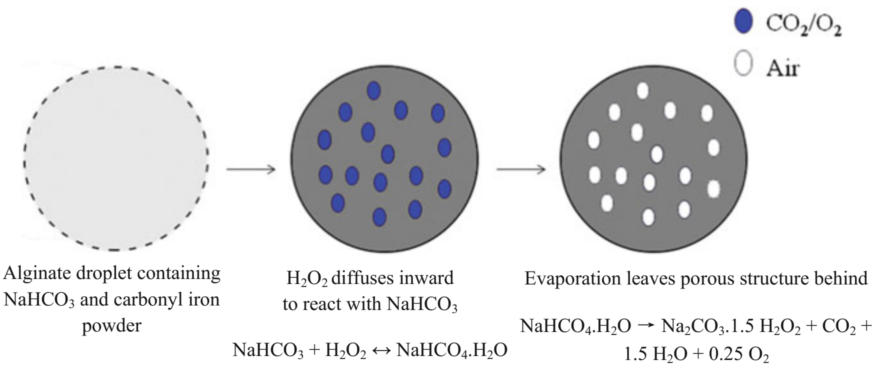

Fig. 2 Porous structure formation by inward diffusion of H_2O_2 to react with $NaHCO_3$.

4% sodium bicarbonate concentration was chosen as it gave the most desired structure of porous spheres. 1 ml of the homogeneous Na-Alginate mixture was mixed with 0.05 g of carbonyl iron powder and loaded in a syringe (TERUMOR® Syringe, 1 cc/mL). The mixture was manually extruded from the needle tip (25G, 0.50 × 25 mm). The drops of Na-alginate solution were collected in a solution of 25% w/v calcium chloride solution mixed with H_2O_2 (32 wt%) for gelation of the alginate.

The collected Na-alginate-iron spheres measured in the range of about 2–3 mm in diameter. The Na-alginate-iron spheres were left in the collecting solution for 10 min, undergoing the chemical reactions. Figure 2 illustrates the diffusion of hydrogen peroxide into the Na-alginate spheres to react with sodium bicarbonate, creating the resultant porous structure.

After the reaction went on for 10 min, the desired porous Na-alginate-iron spheres (group B) were removed and rinsed with distilled water. The procedure was repeated to prepare two more sets of spheres: (group A) Na-alginate porous spheres with no iron particles and (group C) control solid magnetic spheres with no encapsulated microbubbles as distilled water was used in place of hydrogen peroxide.

3.2 Imaging Setup

After the encapsulated microbubbles were fabricated, an imaging setup as shown in Fig. 3 was used to capture the preliminary videos for image processing. Imaging was done using an Ultrasonix machine, with a 4DL14-5/38 Linear 4D probe. The probe allows for applications such as abdominal, MSK, nerve block, small parts and vascular imaging. The bandwidth for the probe is 14–5 MHz with a depth range of 2–9 cm and a geometric focus of 28 mm [40]. The ultrasound probe was immersed in a water tank, to minimize attenuation of the ultrasound waves in air.

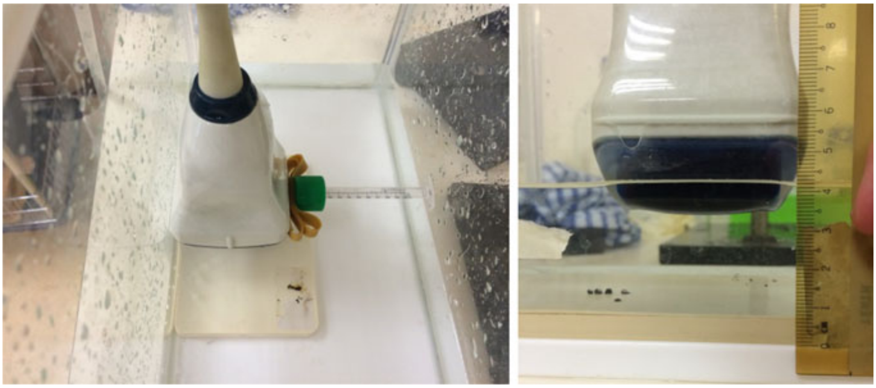

Fig. 3 Stabilized ultrasound probe immersed in water tank setup.

The magnetic spheres were aligned on a MISSION® ExpressMag® Super Magnetic Plate measuring 127.8 by 85.5 cm. The ultrasound probe was placed directly above the tube to be imaged and was kept in a fixed position by exerting force via an external structure. Stabilizing the ultrasound probe was critical in obtaining consistent images and prevent swaying of the probe as the magnetic field from the moving magnetic plate interfered with the magnetic field of the probe. Stabilization also prevented false detections caused by disturbances in the tracking algorithm [41]. The ultrasound videos were captured by moving the Super Magnetic Plate in the x direction, as shown in Fig. 4.

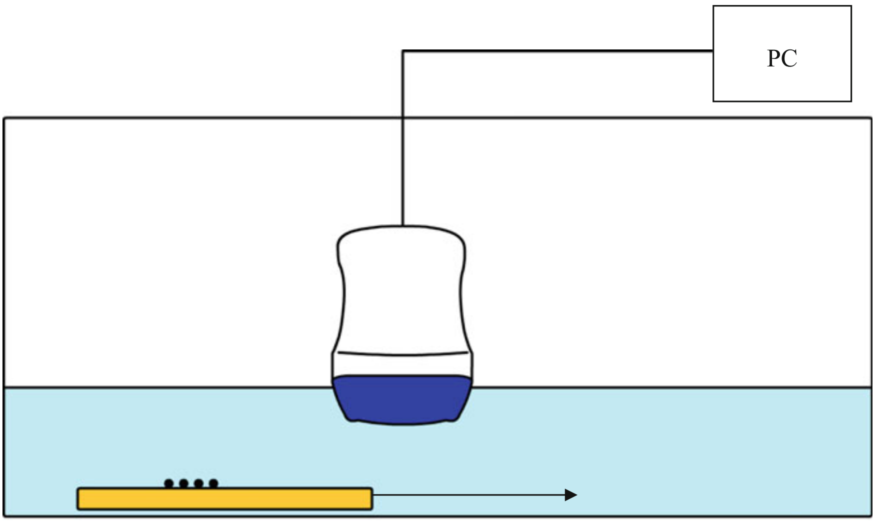

Fig. 4 Experimental setup for capturing of ultrasound videos.

3.3 Image Analysis by Frame Difference Algorithm

After the ultrasound videos of the moving microbubbles were captured, the tracking algorithm used to analyze the videos was created in C++, using libraries from Open Source Computer Vision (OpenCV). OpenCV contains a library of programming functions specifically for the use for real-time computer vision.

From Table 1 in Sect. 2.4, the frame difference algorithm was found to be the most suitable in detecting the moving microbubbles. Figure 5 shows an overview of the frame difference algorithm. First, the tracking algorithm reads in the input video, which can also be programmed to allow for live input from the ultrasound probe. Second, the ultrasound video is converted to grayscale. Third, a difference image is computed by using two consecutive frames from the video. Fourth, the frame difference images are thresholded by binary threshold, where the resultant image is converted to either black or white. Fifth, the thresholded image is smoothened to increase whitespace between the two consecutive frames. Last, the function to detect the centroids of the microbubbles is called, finding the contours in the image. The output of the total number of microbubbles detected in each frame is given, with the respective (x, y) coordinates of each microbubble and the centre of the microbubbles highlighted with a crosshair and circle.

Table 3 details the OpenCV functions that were used in the tracking algorithm.

3.4 Ground Truth Validation

For the purposes of this chapter, the ground truth for the (x, y) coordinates of the centroids of the moving spheres were manually selected. The following adjustments were made to the tracking algorithm: First, the user mouse was adjusted to allow the (x, y) coordinates to be the output upon clicking (Fig. 6). Second, the crosshair and

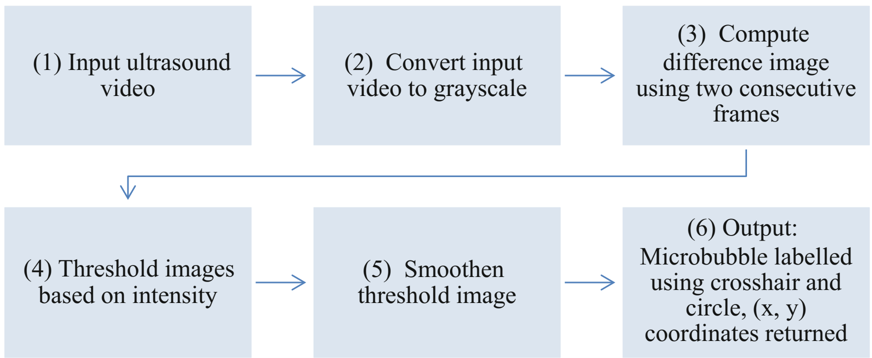

Fig. 5 Outline of tracking analysis of ultrasound videos.

Table 3 Overview of OpenCV functions used in tracking algorithm.

Function name	Purpose of function
1. cv::cvtColor(frame1, grayImage1, COLOR_BGR2GRAY)	cvtColor is used to convert the videos to grayscale, in order to use the absdiff function. Hence, both frame1 and frame2 inputs are converted to grayscale prior to using the absdiff function
2. cv::absdiff(frame1, frame2, output) void absdiff(InputArray src1, InputArray src2, OutputArray dst)	absdiff function compares the images in both frames and takes the absolute difference between the pixels on the images, giving resultant threshold image. The threshold image shows the pixels which have changed between the compared two images. The output is stored in the matrix: differenceImage, which contains values between 0 and 1 s
3. cv::threshold(differenceImage, thresholdImage, SENSITIVITY_VALUE)	Binary threshold was used to convert the faint grey pixels to white. SENSITIVITY_VALUE was a predefined value used to control the amount of noise allowed. If the object to be detected was too small, a lower sensitivity value was used
4. cv::blur(thresholdImage, thresholdImage, cv::size(BLUR_SIZE)	BLUR_SIZE was another predefined value to be inputed into the function cv::size. The blur function was used to increase the amount of white space (in the third window) as compared to the second window. Blurring allows for smoothing of the image, by reducing noise or camera artefacts. The blur function allows the threshold image path, which is almost closed, to be effectively closed
5. findContours(temp, contours, hierarchy, CV_RETR_EXTERNAL, CV_CHAIN_APPROX_SIMPLE)	The findContours function was used in the created MicrobubbleSearch tracking function. The function returns a bounding rectangle which is drawn around the detected centroid

circle labelling were removed to prevent prejudice during the manual selection of the centre of the spheres (Fig. 7). Third, the video playback speed was reduced by increasing the waitKey switch to 400 (Fig. 8), to allow for a sufficient pause

Adjustment 1: CallBackFunc to allow return of (x,y) location with mouse click

```
void CallBackFunc(int event, int x, int y, int flags, void* userdata)
{
    if (event == EVENT_LBUTTONDOWN)
    {
        cout << "Left button of the mouse is clicked - position (" << x << ", " << y << ")" << endl;
    }
    else if (event == EVENT_RBUTTONDOWN)
    {
        cout << "Right button of the mouse is clicked - position (" << x << ", " << y << ")" << endl;
    }
    else if (event == EVENT_MBUTTONDOWN)
    {
        cout << "Middle button of the mouse is clicked - position (" << x << ", " << y << ")" << endl;
    }
}
```

Fig. 6 Using CallBackFunction for manual selection of microbubble centroids.

Adjustment 2: Remove crosshair and circle labelling to remove obstruction and prevent prejudice when labelling

```
//Crosshair labelling around centroid
//circle(cameraFeed, Point(x, y), 20, Scalar(0, 255, 0), 2);
//line(cameraFeed, Point(x, y), Point(x, y - 25), Scalar(0, 255, 0), 1);
//line(cameraFeed, Point(x, y), Point(x, y + 25), Scalar(0, 255, 0), 1);
//line(cameraFeed, Point(x, y), Point(x - 25, y), Scalar(0, 255, 0), 1);
//line(cameraFeed, Point(x, y), Point(x + 25, y), Scalar(0, 255, 0), 1);
```

Fig. 7 Crosshairs and circle labelling of code commented away.

Adjustment 3: Increase waitKey value to 400 to reduce frame speed

```
        switch (waitKey(400)){
```

Fig. 8 Playback speed of ultrasound videos slowed down via waitKey value.

Adjustment 4: Using cv::resizeWindow to expand size of output video for more accurate selection

```
setMouseCallback("4) Final Tracking Video", CallBackFunc, NULL);
namedWindow("4) Final Tracking Video", WINDOW_NORMAL);
cv::resizeWindow("4) Final Tracking Video", 784, 588); //Expanded Window
imshow("4) Final Tracking Video", frame1);
```

Fig. 9 Code to expand window size of video.

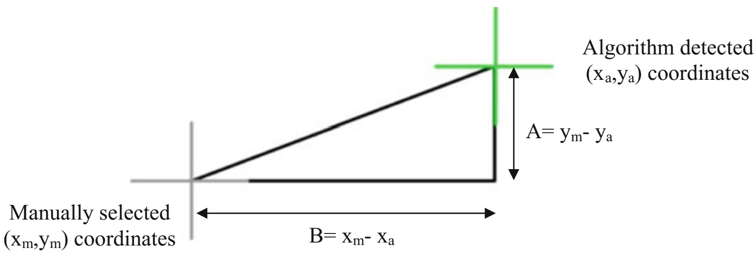

Fig. 10 Calculation of distance between detected and manually selected centroids by Pythagoras' Theorem.

duration between each frame. Lastly, the video was enlarged for clearer selection of the centroid (Fig. 9). The ground truth readings were taken when all the moving spheres were in the frame.

The Ground Truths were calculated using Pythagoras' Theorem. By calculating the pixel difference in both the x and y coordinates, the distance between the actual and detected centroid locations was calculated using $\sqrt{A^2 + B^2}$ (Fig. 10).

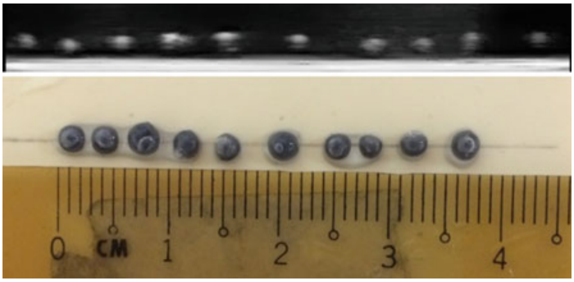

Fig. 11 Corresponding ultrasound image of 10 aligned magnetic spheres and measured physical distances.

3.5 *Pixel Resolution Calculation*

The resolution of the ultrasound probe was calculated by taking physical measurements of the distance between the magnetic spheres and the corresponding pixel distance in the resultant ultrasound image obtained. Figure 11 shows the physical measurement of the distance between the edges of the spheres and the corresponding measurement of pixel distance through manual selection of the edges via the manual mouse selections.

From the results in Table 4, the average calculated resolution was 0.0106 cm/pixel for the ultrasound probe. This value would be used in Sect. 4.4 to calculate the tracking accuracy of the algorithm.

4 Results

4.1 *Properties of Magnetic Microbubbles*

Following the methodology in Sect. 3.1, the three sets of collected 2–3 mm spheres were observed under the microscope (x4 magnification). Figure 12 shows group A, the control Na-alginate only spheres with distinct microbubbles but without iron particles. Figure 13 shows group B, the desired Na-alginate-iron spheres with encapsulated microbubbles. Figure 14 shows group C, the control solid spheres, with no encapsulated microbubbles.

Furthermore, to verify that the fabricated magnetic particles contained encapsulated microbubbles, the Na-alginate-iron spheres with encapsulated microbubbles (group B) and the solid iron spheres (group C) were placed inside eppendorf tubes filled with water. Figure 15 shows that the magnetic microbubbles (group B) floated to the surface, while the control solid spheres (group C) sunk to the bottom. In addition, Fig. 16 shows that the magnetic microbubbles were attracted to a strong magnet.

The microscopic images and experimental tests clearly prove the magnetic properties and presence of encapsulated microbubbles in the desired group B spheres.

Table 4 Resolution calculation based on pixel and corresponding physical distance.

Sphere number	2nd	3rd	4th	5th	6th	7th	8th	9th	10th
Pixel distance	42	80	119	156	204	259	292	326	374
Distance/cm	0.50	0.90	1.30	1.60	2.20	2.65	2.95	3.30	3.80
Resolution: cm/px	0.01191	0.01125	0.01092	0.01026	0.01078	0.01023	0.01010	0.01012	0.01016

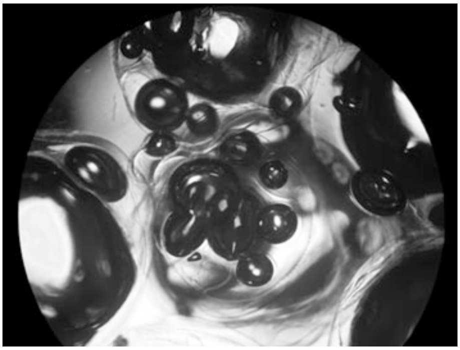

Fig. 12 (Group A) Na-alginate spheres with encapsulated microbubbles, no carbonyl iron.

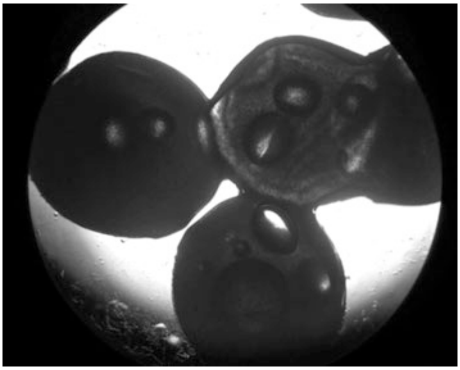

Fig. 13 (Group B) Na-alginate-iron spheres with encapsulated microbubbles.

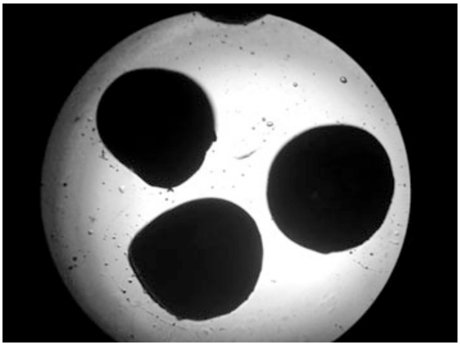

Fig. 14 (Group C) Control solid iron spheres with no encapsulated microbubbles.

4.2 Ultrasound Contrast Results

Upon successful encapsulation of the microbubbles, the effects of the encapsulated microbubbles as ultrasound contrast agents was tested using the setup as shown in Fig. 17. Four of the microbubble encapsulated spheres (group B) and four of the solid magnetic spheres (group C) were lined on the MISSION® ExpressMag®

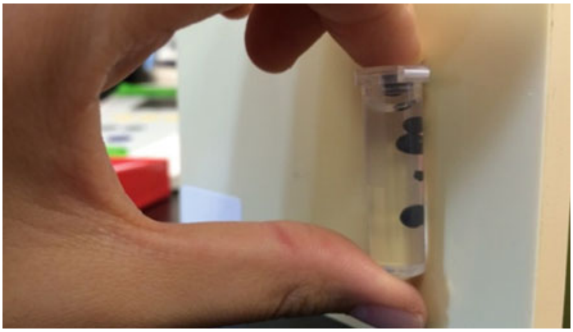

Fig. 15 Magnetic Microbubbles floated to the surface while solid control spheres sunk.

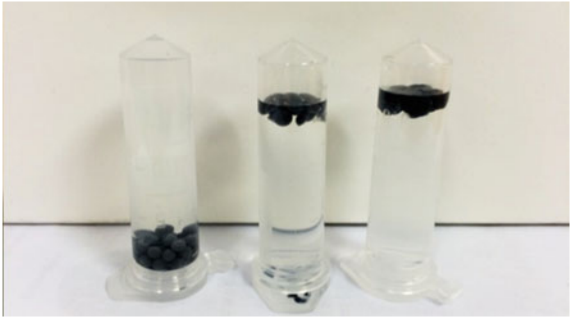

Fig. 16 Fabricated magnetic microbubbles attracted to a magnet.

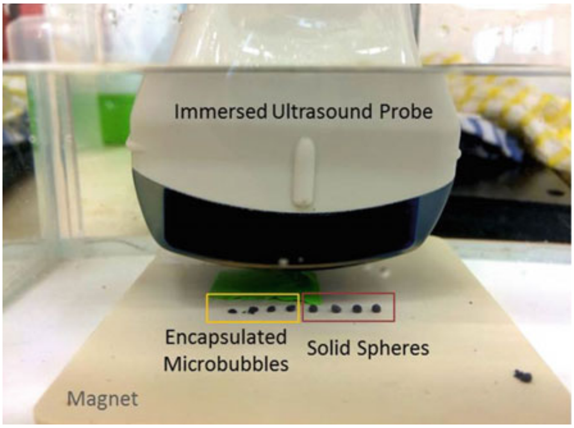

Fig. 17 Experimental setup to compare the contrast enhancement properties of microbubbles.

Super Magnetic Plate. The magnet was placed at the bottom of the water tank with the ultrasound probe positioned vertically above the magnetic particles.

The obtained ultrasound images in Fig. 18 show that at equal distance from the ultrasound probe, the encapsulated microbubbles (group B) were distinctively clearer, appearing as bright white spots. However, the solid magnetic spheres

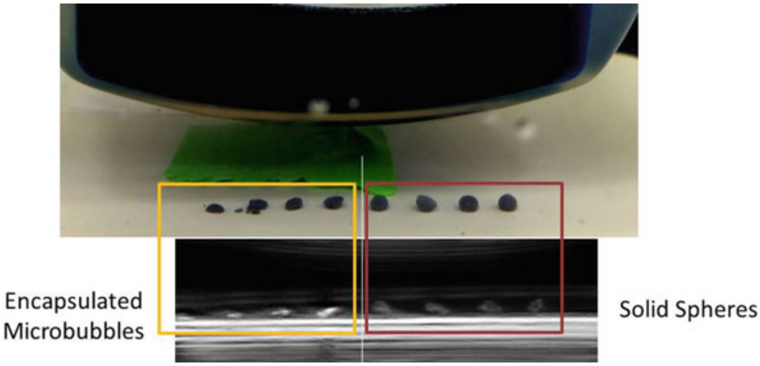

Fig. 18 Encapsulated microbubbles compared with solid spheres under ultrasound imaging.

(group C) appeared duller. Hence, the experimental results obtained verify the expected contrast enhancing properties of microbubbles as explained in Sect. 2.1.

4.3 Tracking Results by Frame Difference Algorithm

From the experiments conducted, it was found that the tracking algorithm worked best for up to five magnetic spheres. For six magnetic spheres and onwards, the algorithm could not track each sphere as consistently. Figure 19 shows the results of the applied tracking algorithm for 1 sphere (a), 2 (b), 3 (c), 4 (d) and 5 (e) spheres, with complete windows shown in Appendix 1. The results show that the algorithm could successfully detect the movement of the microbubbles, and give the (x, y) coordinates of the centroids of the microbubbles with a and a crosshair and circle used to label the position of the microbubble.

Furthermore, the algorithm returns the total number of particles detected at each frame and the respective (x, y) coordinates of each particle, as shown in Fig. 20.

4.4 Tracking Accuracy

Table 5 shows the calculated difference in pixels and actual distance between the detected centroids from the algorithm and the manually selected centroids, based on the method described in Sect. 3.5.

From Table 4, the total average difference between the algorithm detected and manually selected centroids of the five tracking experiments was 3.33 pixels, or 0.0354 cm.

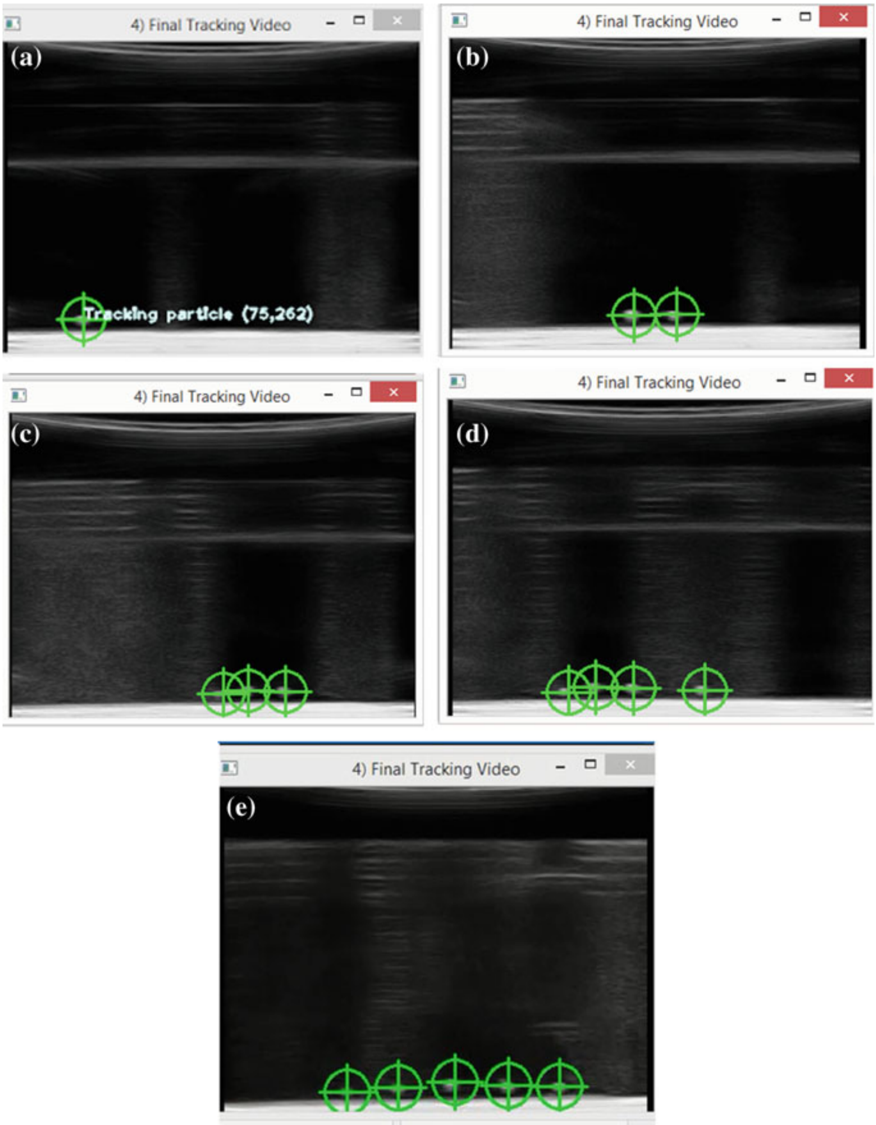

Fig. 19 Results of applied frame difference algorithm on captured ultrasound videos for 1 sphere (**a**), 2 (**b**), 3 (**c**), 4 (**d**) and 5 (**e**) spheres.

4.5 Tracking Results of Solid Spheres Compared to Microbubbles

Furthermore, when the tracking algorithm was applied to both the solid sphere and microbubble encapsulated sphere under the same conditions, only the microbubble

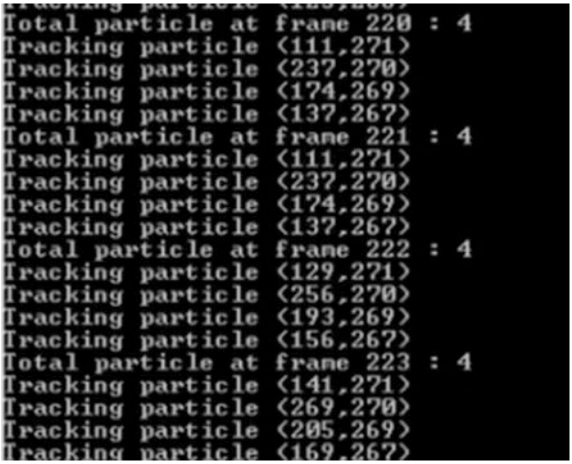

Fig. 20 Tracking algorithm returns total number of particles detected and respective (x, y) coordinates.

Table 5 Calculated difference in pixels and actual distance between detected and manually selected centroids.

Number of particles	Number of frames captured	Average difference in pixel difference/px	Actual difference in distance/cm
1	34	3.286	0.03496
2	25	2.966	0.03155
3	17	2.917	0.03103
4	14	4.688	0.04987
5	12	2.779	0.02956

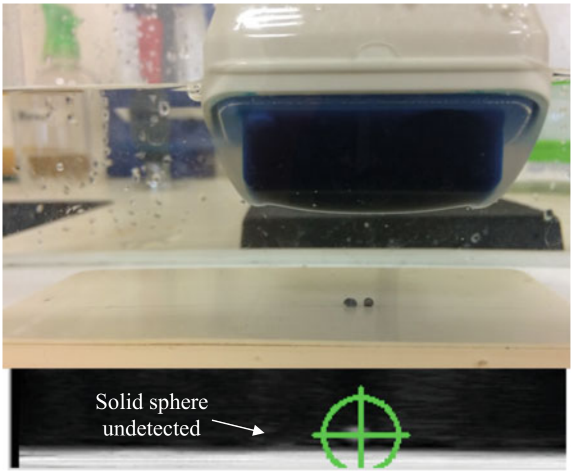

Fig. 21 Comparison of tracking results of moving solid and microbubble encapsulated spheres.

encapsulated sphere was detected by the tracking algorithm. Figure 21 shows the crosshair labelled microbubble sphere whereas the solid sphere was barely visible and was left undetected.

5 Discussion

The goals of this study were to fabricate magnetic spheres with encapsulated contrast enhancing microbubbles and to create an experimental setup to capture ultrasound videos to analyze the position of the spheres using a tracking algorithm. The results obtained above demonstrate an alternative to the current state of the art of ultrasound microbubble imaging and the application of OpenCV functions for biomedical tracking purposes.

5.1 Ultrasound Imaging Setup

From the experiments conducted, it was found that the resultant OpenCV tracking approach used depended largely on the ultrasound imaging setup used to obtain the ultrasound videos. Appendix 2 shows a comparison of the various imaging setups that were tested to obtain the ultrasound videos.

After experimental trials with the different setups, it was found that setup 5, using a large planar magnet, was the most suitable setup for the purposes of this chapter. Furthermore, the purpose of this chapter was to track the particles in controlled motion for targeted drug delivery, and not in specific flow conditions such as that used for vascular applications. However, additional precautions have to be taken.

First, it was also observed that the large magnet created magnetic fields that would interfere with the ultrasound video, as shown in Fig. 22. As such, the tracking algorithm used had to be able to remove the interfering magnetic field in order to track the moving microbubbles.

Second, the magnetic field created also interfered with the ultrasound probe, causing the ultrasound probe to swing with the change in magnetic field caused by movement of the magnet. As such an external force had to be exerted to stabilize and keep the ultrasound probe in a fixed position.

Last, it was found that the hollow magnetic spheres were fragile and had to be handled with care. When positioning on top of the magnet, the spheres were easily crushed and destroyed. A dropper was used to position the spheres on the magnet linearly.

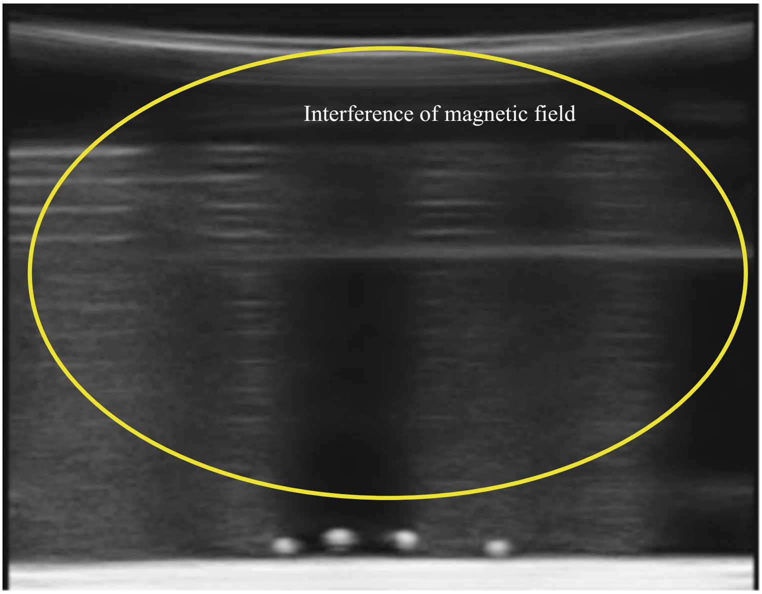

Fig. 22 Interference of magnetic field with ultrasound image.

5.2 *Tracking Algorithm*

As the purpose of the tracking moudule is to return the coordinates of the microbubble location, the EPIV or PIV methods discussed in Sect. 2.3, which incorporates velocity of the microbubbles, were not applied.

One of the challenges faced in developing the tracking algorithm was the irregular shape of the magnetic spheres. Due to its hollow structure, the magnetic spheres were easily deformed. Figure 23 shows a flattened magnetic particle on the

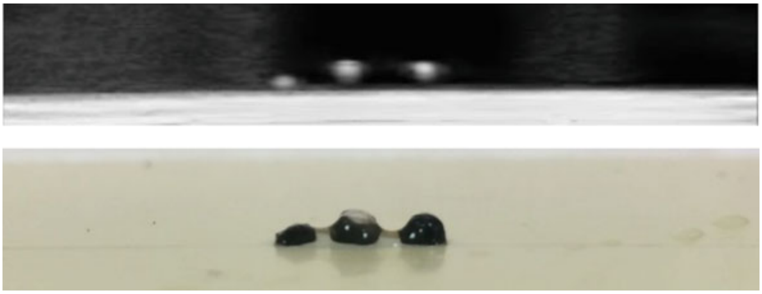

Fig. 23 Irregular shape of magnetic particles affects resultant ultrasound image.

planar magnet with the corresponding ultrasound image above. Therefore, under ultrasound imaging, the magnetic particles did not always appear as a spherical white spot and at times had irregular shapes. As such the frame difference tracking algorithm used allowed for more robust detection, as compared to methods such as Hough transform which detects more spherical shaped artefacts.

5.3 Future Works

Towards integrating the tracking approach here for further drug delivery, future tests would have to be done using a magnetic system, such as an actuation system consisting of a pair of Helmholtz and Maxwell coils [42]. By using an external magnetic system, the capturing of the ultrasound videos could be more realistic and allow for tracking as well in the x, y and z directions. Furthermore, the experimental conditions can be adjusted to include more in vivo like conditions, such as the presence of red blood cells, white blood cells to test the versatility of the methods in more realistic conditions.

6 Conclusion

In this project, the use of ultrasound contrast enhancing microbubbles was tested in an experimental setup inducing the motion of microbubbles through moving a large planar magnet in the x direction. The tracking algorithm used, based on frame difference, proved capable of tracking and returning the (x, y) coordinates of the moving microbubbles. The optimal number of particles to be tracked was up to five particles with an accuracy of 3.33 pixels, or 0.0354 cm, between the algorithm detected and the manually selected (x, y) coordinates of the centroids. The limitations of the project include the lack of use of in vivo like conditions, such as the presence of other particles, for example, red blood cells. The fabricated magnetic microbubbles could be further used as test particles for external manipulation systems for drug delivery studies.

Acknowledgements The authors would like to thank the support from NUS teams in Dr H. Ren's, Dr J. Li's and Dr C. Yap's lab.

Appendices

Appendix 1: Algorithm Results

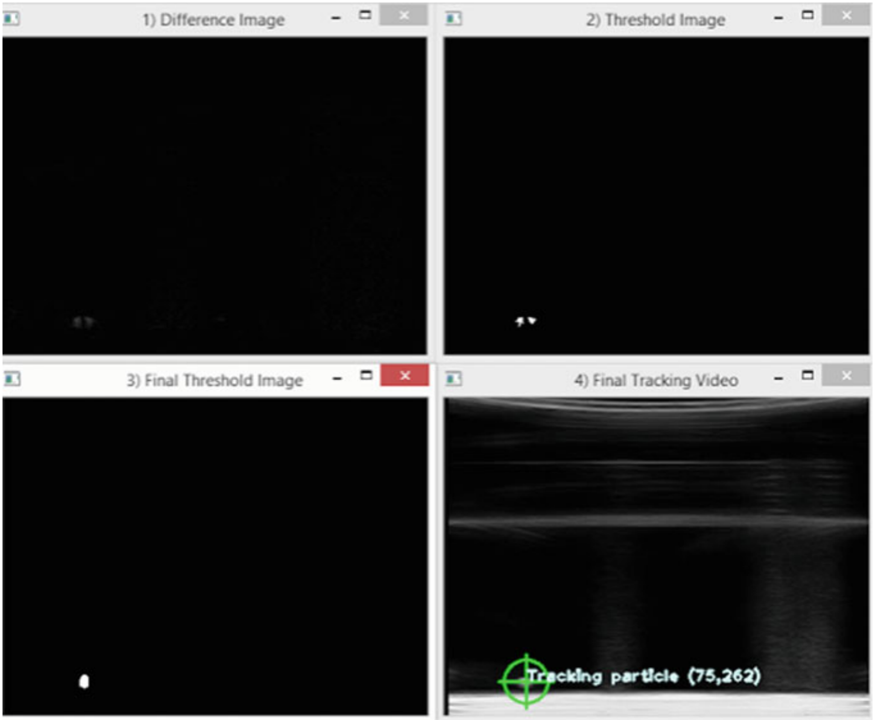

Tracking of 1 detected particle

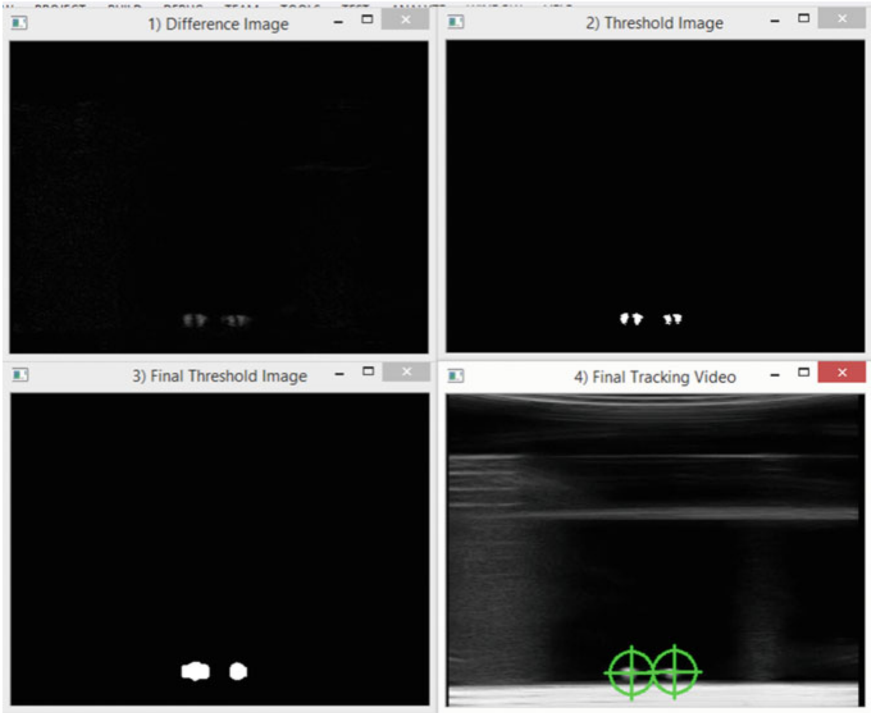

Tracking of 2 detected particle

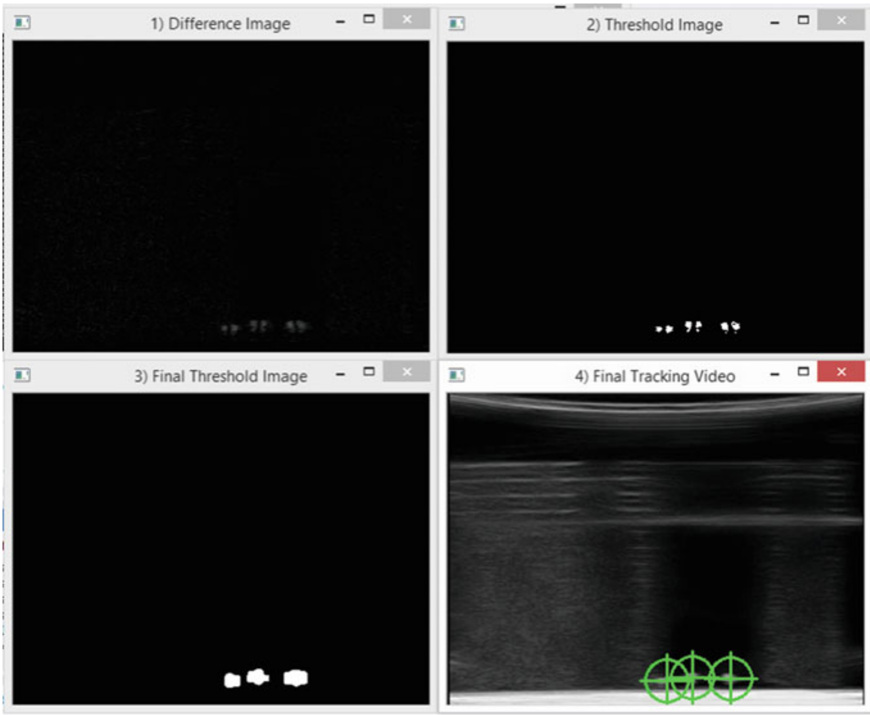

Tracking of 3 detected particles

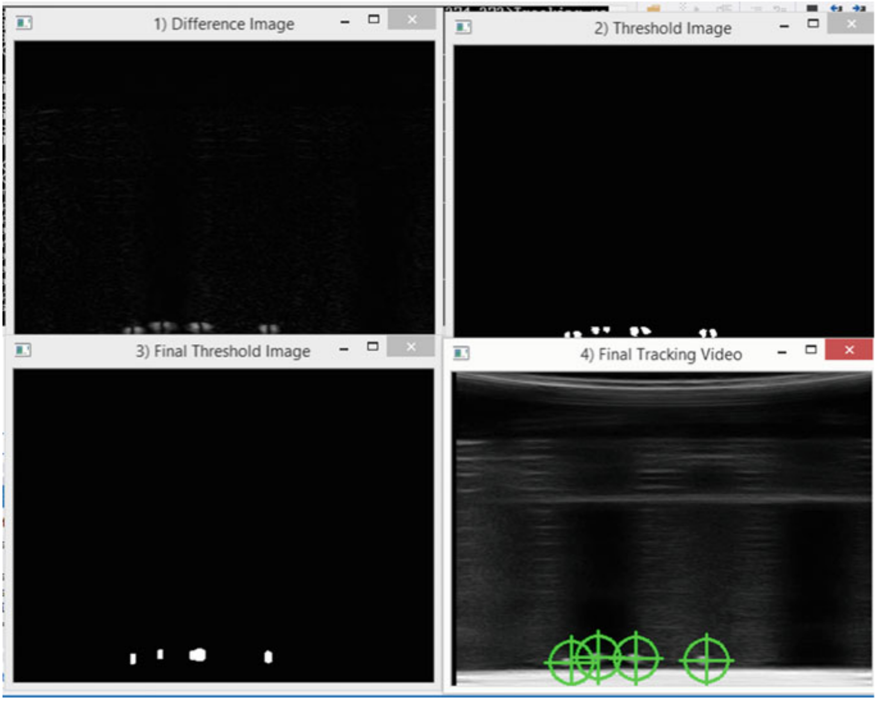

Tracking of 4 detected particles

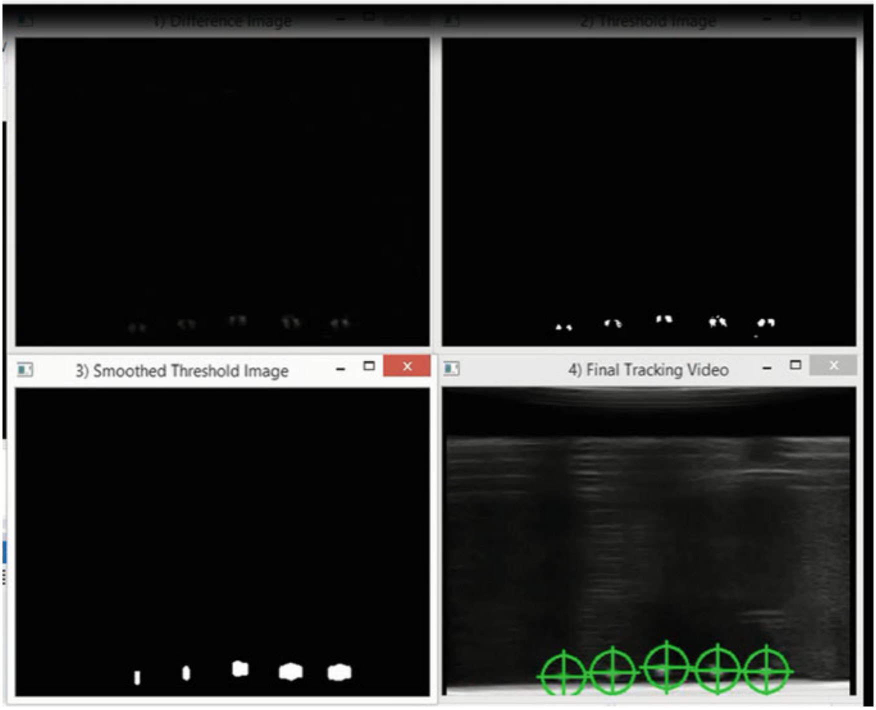

Tracking of 5 detected particles

Appendix 2: Comparison of Various Ultrasound Imaging Setups

Tested ultrasound imaging setups

1. Flow of microbubbles through rubber tubes

Movement of microbubbles induced through flow

Advantages	Disadvantages
(+) Setup mimics flow of microbubbles in vessel-like conditions	(–) Magnetic particles do not appear spherical (–) Ultrasound intensity attenuated by rubber tube

2. Floating particles

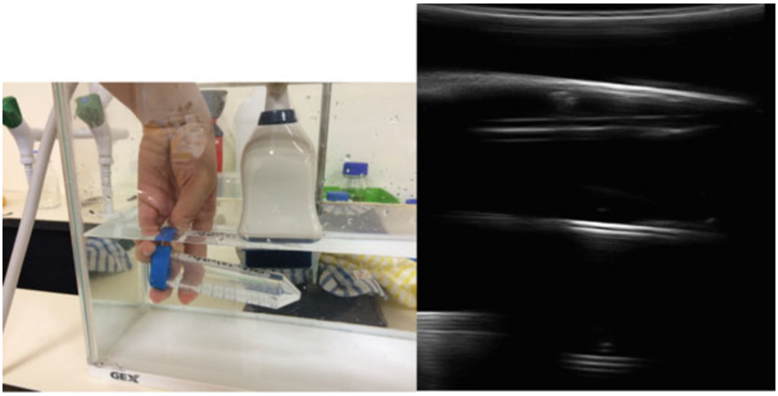

Advantages	Disadvantages
(+) Particles appear spherical (+) Movement is in both x and z direction	(–) Ultrasound attenuation at plastic-water interface

3. Magnetic Particles in Dish

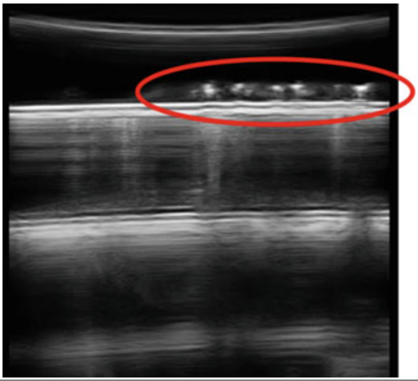

Advantages	Disadvantages
(+) Movement of multiple magnetic spheres can be recorded	(–) Magnetic spheres do not appear as distinct particles with clustering of spheres

4. Small magnet used to control movement of magnetic spheres

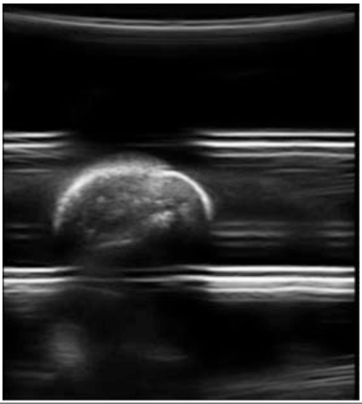

Advantages	Disadvantages
(+) Easy control (+) No attenuation from interface, direct observation	(–) Magnet interferes with ultrasound imaging

5. Large magnet planar magnet

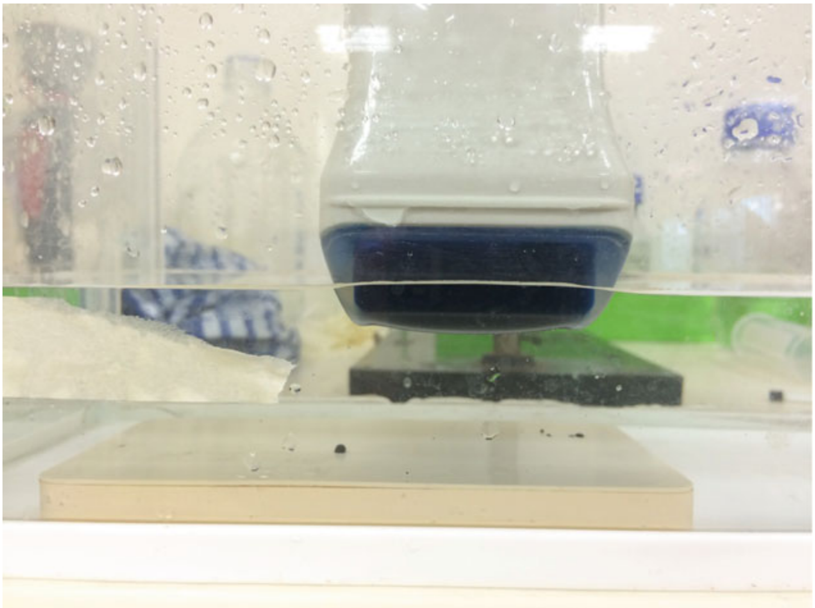

Advantages	Disadvantages
(+) Direct observation of microbubbles without attenuation from interface (+) Movement along x axis captured	(–) Magnetic field from magnet interferes with ultrasound probe (–) Movement of particle in z direction is not captured

References

1. Cosgrove, D. 2006. Ultrasound contrast agents: an overview. *European Journal of Radiology* 3: 324–330.
2. Sirsi, S., and M. Borden. 2009. Microbubble compositions, properties and biomedical applications. *Bubble Science Engineering and Technology* 1–2: 3–17.
3. Qin, S., C.F. Caskey, and K.W. Ferrara. 2009. Ultrasound contrast microbubbles in imaging and therapy: physical principles and engineering. *Physics in Medicine and Biology* 6: R27–R57.
4. Cootney, R.W. 2001. Ultrasound Imaging: Principles and applications in rodent research. Institute for Laboratory Animal Research Journal.
5. Yang, F., Y. Li, Z. Chen, Y. Zhang, J. Wu, and N. Gu. 2009. Superparamagnetic iron oxide nanoparticle-embedded encapsulated microbubbles as dual contrast agents of magnetic resonance and ultrasound imaging. *Biomaterials* 23–24: 3882–3890.

6. Stride, E., K. Pancholi, M.J. Edirisinghe, and S. Samarasinghe. 2008. Increasing the nonlinear character of microbubble oscillations at low acoustic pressures. *Journal of the Royal Society, Interface/the Royal Society* 24: 807–811.
7. Harvey, C.J., J.M. Pilcher, R.J. Eckersley, M.J. Blomley, and D.O. Cosgrove. 2002. Advances in ultrasound. *Clinical Radiology* 3: 157–177.
8. Heath, K., and P. Dayton. 2013. Current status and prospects for microbubbles in ultrasound theranostics. Nanomedicine and Nanobiotechnology.
9. Hernot, S., and A.L. Klibanov. 2008. Microbubbles in ultrasound-triggered drug and gene delivery. *Advanced Drug Delivery Reviews* 60 (10): 1153–1166.
10. Wei, K., D.M. Skyba, C. Firschke, A.R. Jayaweera, J.R. Lindner, and S. Kaul. 1997. Interactions between microbubbles and ultrasound: in vitro and in vivo observations. *Journal of the American College of Cardiology* 5: 1081–1088.
11. Perera, R.H., C. Hernandez, H. Zhou, P. Kota, A. Burke, and A.A. Exner. 2015. Ultrasound imaging beyond the vasculature with new generation contrast agents. Wiley Interdisciplinary reviews: Nanomedicine and Nanobiotechnology.
12. Keravnou, C., C. Mannaris, and M. Averkiou. 2015. Accurate measurement of microbubble response to ultrasound with a diagnostic ultrasound scanner. *IEEE Transactions on Ultrasonics, Ferroelectrics, and Frequency Control* 1: 176–184.
13. Unger, E.C., E. Hersh, M. Vannan, and T. McCreery. Gene delivery using ultrasound contrast agents. Echocardiography.
14. Stride, E., C. Porter, A.G. Prieto, and Q. Pankhurst. 2009. Enhancement of microbubble mediated gene delivery by simultaneous exposure to ultrasonic and magnetic fields. *Ultrasound in Medicine and Biology* 5: 861–868.
15. Phillips, P.J. 2001. Contrast pulse sequences (CPS): Imaging nonlinear microbubbles. In *2001 Ultrasonics symposium*, Atlanta, GA.
16. Zhang, F., C. Lanning, L. Mazzaro, A.J. Barker, P.E. Gates, W.D. Strain, J. Fulford, O.E. Gosling, A.C. Shore, N.G. Bellenger, B. Rech, J. Chen, J. Chen, and R. Shandas. 2011. In vitro and preliminary in vivo validation of echo particle image velocimetry in carotid vascular imaging. *Ultrasound in Medicine and Biology* 3: 450–464.
17. Westerdale, J., M. Belohlavek, E.M. McMahon, P. Jiamsripong, J.J. Heys, and M. Milano. 2011. Flow velocity vector fields by ultrasound particle imaging velocimetry: in vitro comparison with optical flow velocimetry. *Journal of Ultrasound in Medicine: Official Journal of the American Institute of Ultrasound in Medicine* 2: 187–195.
18. Zhang, Y., X. Wang, and B. Qu. 2012. Three-frame difference algorithm research based on mathematical morphology. Procedia Engineering.
19. Chenouard, N., I. Smal, F. de Chaumont, M. Maška, I.F. Sbalzarini, Y. Gong, J. Cardinale, C. Carthel, S. Coraluppi, M. Winter, A.R. Cohen, W.J. Godinez, K. Rohr, Y. Kalaidzidis, L. Liang, J. Duncan, H. Shen, Y. Xu, K.E. Magnusson, J. Jaldén, H.M. Blau, P. Paul-Gilloteaux, P. Roudot, C. Kervrann, F. Waharte, J.Y. Tinevez, S.L. Shorte, J. Willemse, K. Celler, G. P. van Wezel, H.W. Dan, Y.S. Tsai, C. Ortiz de Solórzano, J.C. Olivo-Marin, and E. Meijering. 2014. Objective comparison of particle tracking methods. *Nature methods 3*, 281–289.
20. Stauffer, C., and W.E.L. Grimson. 1999. Adaptive background mixture models for real-time tracking. *Computer Vision and Pattern Recognition*.
21. Sun, D., S. Roth, J.P. Lewis, and M.J. Black. 2008. Learning optical flow. Computer vision—ECCV 2008. *Lecture Notes in Computer Science* 5304: 83–97.
22. Prabhakar, N., V. Vaithiyanathan, A.P. Sharma, A. Singh, and P. Singha. 2012. Object tracking using frame differencing and template. Research Journal of Applied Sciences, Engineering and Technology.
23. Cai, X., F. Yang, and N. Gu. 2012. Applications of magnetic microbubbles for theranostics. *Theranostics* 2 (1): 103–112.

24. Dharmakumar, R., D.B. Plewes, and G.A. Wright. 2005. A novel microbubble construct for intracardiac or intravascular MR manometry: A theoretical study. *Physics in Medicine and Biology* 20: 4745–4762.
25. Soetanto, K., and H. Watarai. 2000. Development of magnetic microbubbles for drug delivery system (DDS). *Japanese Journal of Applied Physics* 39: 3230–3232.
26. Park, J.I., D. Jagadeesan, R. Williams, W. Oakden, S. Chung, G.J. Stanisz, and E. Kumacheva. 2010. Microbubbles loaded with nanoparticles: a route to multiple imaging modalities. *ACS Nano* 11: 6579–6586.
27. Bae, S.E., J.S. Son, K. Park, and D.K. Han. 2008. Fabrication of covered porous PLGA microspheres using hydrogen peroxide for controlled drug delivery and regenerative medicine. *Journal of Controlled Release: Official Journal of the Controlled Release Society* 1: 37–43.
28. Wang, X.L., X. Li, E. Stride, J. Huang, M. Edirisinghe, C. Schroeder, S. Best, R. Cameron, D. Waller, and A. Donald. 2010. Novel preparation and characterization of porous alginate films. *Carbohydrate Polymers* 79: 989–997.
29. Chevalier, E., D. Chulia, C. Pouget, and M. Viana. 2008. Fabrication of porous substrates: a review of processes using pore forming agents in the biomaterial field. *Journal of Pharmaceutical Sciences* 3: 1135–1154.
30. Cui, W., J. Bei, S. Wang, G. Zhi, Y. Zhao, X. Zhou, H. Zhang, and Y. Xu. 2005. Preparation and evaluation of poly (L-lactide-co-glycolide) (PLGA) microbubbles as a contrast agent for myocardial contrast echocardiography. Journal of biomedical materials research. *Part B, Applied biomaterials* 1: 171–178.
31. Zhang, H., X.J. Ju, R. Xie, C.J. Cheng, P.W. Ren, and L.Y. Chu. 2009. A microfluidic approach to fabricate monodisperse hollow or porous poly (HEMA-MMA) microspheres using single emulsions as templates. *Journal of Colloid and Interface Science* 1: 235–243.
32. Butler, R., C.M. Davies, and A.I. Cooper. 2001. Emulsion templating using high internal phase supercritical fluid emulsions. *Advanced Materials* 13: 1459–1463.
33. Yang, S., K.F. Leong, Z. Du, and C.K. Chua. 2002. The design of scaffolds for use in tissue engineering. *Tissue Engineering Part II: Rapid Prototyping Techniques* 1: 1–11.
34. Tsang, V.L., and S.N. Bhatia. 2004. Three-dimensional tissue fabrication. *Advanced Drug Delivery Reviews* 11: 1635–1647.
35. Stride, E., and M. Edirisinghe. 2009. Novel preparation techniques for controlling microbubble uniformity: a comparison. *Medical and Biological Engineering and Computing* 8: 883–892.
36. Liu, Z., T. Lammers, J. Ehling, S. Fokong, J. Bornemann, F. Kiessling, and J. Gätjens. 2011. Iron oxide nanoparticle-containing microbubble composites as contrast agents for MR and ultrasound dual-modality imaging. *Biomaterials* 26: 6155–6163.
37. Gurruchaga, H., L. Saenz Del Burgo, J. Ciriza, G. Orive, R.M. Hernández, and J.L. Pedraz. 2015. Advances in cell encapsulation technology and its application in drug delivery. *Expert Opinion on Drug Delivery* 1–17.
38. Pareta, R., and M.J. Edirisinghe. 2006. A novel method for the preparation of biodegradable microspheres for protein drug delivery. *Journal of the Royal Society, Interface* 3 (9): 573–582.
39. Huang, K.S., Y.S. Lin, W.R. Chang, Y.L. Wang, and C.H. Yang. 2013. A facile fabrication of alginate microbubbles using a gas foaming reaction. *Molecules* 18 (8): 9594–9602.
40. Ultrasonix Transducer Guide. 2015.
41. Ihnatsenka, B., and A.P. Boezaar. 2010. Ultrasound: Basic understanding and learning the language. International Journal of Shoulder Surgery.
42. Kwon, J.O., S.Y. Ji, B.C. Jeong, and K.C. Sang. 2013. A novel drug delivery method by using a microrobot incorporated with an acoustically oscillating bubble. In *2013 IEEE 26th International Conference Micro Electro Mechanical Systems (MEMS)*, Taipei.